

A Thesis Submitted for the Degree of PhD at the University of Warwick

Permanent WRAP URL:

<http://wrap.warwick.ac.uk/173556>

Copyright and reuse:

This thesis is made available online and is protected by original copyright.

Please scroll down to view the document itself.

Please refer to the repository record for this item for information to help you to cite it.

Our policy information is available from the repository home page.

For more information, please contact the WRAP Team at: wrap@warwick.ac.uk



Multinuclear Solid-State NMR of Ceria Zirconia
and Hybrid Perovskite Systems

By

Adam John Carver

Thesis

Submitted to the University of Warwick

For the degree of

Doctor of Philosophy in Physics

Supervised by Prof. John Hanna and Dr. David Thompsett

Department of Physics

December 2021



Contents

List of figures	v
List of Tables	xi
Acknowledgements.....	xii
Declarations	xiii
COVID-19 impact statement.....	xiv
Abstract.....	xv
Abbreviations	xvii
Chapter 1: Introduction.....	1
1.1 Material Characterisation	1
1.2 Thesis Overview	3
Chapter 2: Solid-State NMR Theory	5
2.1 NMR Theory.....	5
2.1.1 The Classical Description	5
2.2 The Quantum Mechanical Description	6
3.2.1 The Zeeman Effect	7
2.3 Spin excitation in the rotating frame	7
2.4 NMR Interactions.....	9
2.4.1 The Internal Nuclear Spin Hamiltonian	9
2.4.2 Rotational Frames and the Hamiltonian.....	10
2.4.3 Chemical shift and shielding	11
2.4.4 The dipolar interaction	13
2.4.5 The quadrupolar interaction.....	14
2.4.6 Scalar Coupling	18
2.4.7 Paramagnetic interaction	20
2.4.8 Magic Angle Spinning.....	21
Chapter 3: Experimental Methods	23

3.1 NMR Spectroscopy	23
3.1.1 One-Dimensional Techniques	23
3.1.2 T_1 relaxation	25
3.1.3 $T_{1\rho}$ relaxation in the rotating frame	25
3.1.4 Cross-polarisation	27
3.1.5 Nuclear Overhauser-Effect Spectroscopy	29
3.1.6 Single-Quantum Double-Quantum Methods	29
3.1.7 Heteronuclear Correlation	30
3.2 Raman Spectroscopy	30
3.3 DFT, CASTEP and AIRSS	33
Chapter 4: An investigation of ordered and disordered ceria-zirconia	34
4.1 Introduction	34
4.1.1 Ceria and its uses in autocatalysis	34
4.1.2 Ceria Zirconia	37
4.1.3 Ordered Ceria Zirconias	37
4.2 Materials and Methods	38
4.2.1 Materials and ^{17}O enrichment	38
4.2.2 Methods	39
4.2.2.1 $^{17}\text{O}_2$ Straight Exchange and $^{17}\text{O}_2$ Redox Experiments	39
4.3 Results	43
4.3.1 PXRD and SAXS studies of disordered ceria-zirconia	44
4.3.2 Raman studies of disordered ceria-zirconia	44
4.3.3 ^{17}O MAS NMR studies of disordered ceria-zirconia	46
4.3.4 PXRD and SAXS studies of ordered ceria-zirconia	49
4.3.5 Raman study of straight exchange labelled κ-phase $\text{Ce}_2\text{Zr}_2\text{O}_8$	52
4.3.6 ^{17}O MAS NMR studies of κ-phase $\text{Ce}_2\text{Zr}_2\text{O}_8$	54
4.3.7 ^{17}O MAS NMR studies of redox labelled κ-phase $\text{Ce}_2\text{Zr}_2\text{O}_8$	56

4.3.8 Oxidation comparison of ordered ceria-zirconia.....	62
4.3.9 ^{91}Zr static NMR studies of ordered and disordered ceria-zirconia	66
4.4 Conclusion.....	69
Chapter 5: An investigation of hybrid perovskites used as LEDs	73
5.1 Introduction	73
5.2 Materials and Methods	76
5.2.1 Materials	76
5.2.2 Methods.....	77
5.3 Results	79
5.3.1 FTIR, Raman, single-crystal and powder XRD studies.....	79
5.3.2 AIRSS modelling and DFT calculations.....	84
5.3.3 1D ^1H and ^{13}C MAS NMR studies	85
5.3.4 HETCOR, BABA and NOESY studies.....	94
5.3.5 T_1 , $T_{1\rho}$ relaxation and ^{207}Pb MAS NMR studies	94
5.3.6 EXSY studies	98
5.4 Conclusion.....	99
Chapter 6: An investigation of hybrid perovskites with optoelectronic properties	102
6.1 Introduction	102
6.2 Materials and Methods	104
6.2.1 Materials	104
6.2.2 Methods.....	105
6.3 Results	106
6.3.1 FTIR and Raman Spectroscopy.....	107
6.3.2 1D ^1H MAS NMR studies	108
6.3.3 HETCOR studies.....	111
6.3.4 NOESY and BABA studies.....	115
6.3.5 Relaxation studies.....	123

6.3.6 ^{207}Pb NMR studies	126
6.4 Conclusion	127
Chapter 7: Summary	129
7.1 An investigation of ordered and disordered ceria-zirconia	129
7.2 An investigation of hybrid perovskites used as LEDs	130
7.3 An investigation of hybrid perovskites with optoelectronic properties	131
References	132
Appendix	140

List of figures

Figure 2.1 The effect of the Zeeman interaction on a spin $\frac{1}{2}$ nucleus in a finite magnetic field (adapted from Multinuclear Solid-State NMR of Inorganic Materials).	7
Figure 2.2 Frame rotations from the PAS frame to the LAB frame using the Euler angles α, β, γ	10
Figure 2.3 A schematic of shielding and deshielding in an NMR spectrum in comparison to a reference compound (black bar).	11
Figure 2.4 Above are examples of the powder patterns that can be produced due to CSA effects. a) is the typical chemical shift anisotropy (CSA) line shape with shielding parameters, b) is the Pake doublet for a powder under dipolar coupling and c) is the CSA line shape for different symmetries with respect to the external magnetic field.	12
Figure 2.5 A series of quadrupolar lineshapes that are produced for changing (a) CQ , (b) ηQ and (c) I	15
Figure 2.6 An energy level diagram for a nucleus of $I=3/2$ showing the energy level perturbations from the quadrupolar interaction. $HQ(1)$ does not further perturb the central transition, however both the central and satellite transitions are perturbed by $HQ(2)$	16
Figure 2.7 An experimental schematic showing the magic angle used to rotate a sample in an NMR experiment in order to minimise internal interactions.	21
Figure 3.1 Pulse sequence diagrams of some one-dimensional NMR (a) single pulse, (b) solid-echo and (c) Hahn-echo.	24
Figure 3.2 In the rotating frame under the influence of B_0 inhomogeneity there is an effective spin-lock strength and direction $\Delta\omega_{eff}$. (Adapted from Wang et. al.)	26
Figure 3.3 (a) A schematic of how Rayleigh and Raman scattering arises due to the transition between the electronic ground state and two virtual states and (b) a Raman spectra that contains low frequency Stokes emissions and high frequency anti-Stokes emissions.	31
Figure 4.1 (a) ceria structure showing the OCe_4 tetrahedra and (b) the CeO_{2-x}	35
Figure 4.2 The three step process to producing ordered ceria-zirconia. The step from pure ceria to the disordered solid-solution is unknown but by reducing the disordered system and reoxidising; the ordered κ -phase system can be synthesised.	39
Figure 4.3 The two $^{17}O_2$ gas labelling experiments used on the ordered and disordered ceria-zirconia samples. a) is the straight exchange method and b) the redox method.	40

Figure 4.4 PXRD of the as prepared disordered ceria-zirconia and the 300 °C 500°C, 500 °C 500 °C and 700 °C 500 °C $^{17}\text{O}_2$ redox labelled samples.....	43
Figure 4.5 Raman spectra of the as prepared sample of (a) the as prepared disordered CeZrO_2 and a series $^{17}\text{O}_2$ redox labelled CeZrO_2 (b) 300 °C 300 °C, (c) 300 °C 500 °C, (d) 500 °C 300 °C, (e) 500 °C 500 °C, (f) 700 °C 300 °C and (g) 700 °C 500 °C. The inset shows the expanded region of the $\text{F}_{2\text{G}}$ band.....	45
Figure 4.6 ^{17}O MAS NMR of a range of $^{17}\text{O}_2$ redox labelled disordered CeZrO_2 . A 4 mm zirconium rotor spectrum has been added for comparison with the zirconium coordinated oxygen region of the samples. These data were acquired in a 4 mm zirconia rotor with $\nu r = 14$ kHz on a spectrometer operating at 14.1 T. Asterisks (*) denote spinning sidebands. The red dashed line marks out the broad Ce^{3+} site.	47
Figure 4.7 ^{17}O MAS NMR of $^{17}\text{O}_2$ redox labelled disordered CeZrO_2 . These data were acquired in a 2.5 mm zirconia rotor with $\nu r = 31$ kHz on a spectrometer operating at 9.4 T. Asterisks (*) denote spinning sidebands. The red dashed line marks out the broad Ce^{3+} site.	48
Figure 4.8 PXRD of the as prepared κ -phase ceria-zirconia and the 200 °C, 300°C, 350 °C and 400 °C $^{17}\text{O}_2$ straight exchanged labelled samples.	50
Figure 4.9 A SAXS spectrum of the 350 °C $^{17}\text{O}_2$ straight exchanged sample highlighting the Bragg peak at $\sim 0.08 \text{ \AA}^{-1}$. The right of the figure shows the plane that this peak is attributed to.	51
Figure 4.10 Comparison of Raman spectra of the disordered CeZrO_2 and the ordered κ -phase $\text{Ce}_2\text{Zr}_2\text{O}_8$	52
Figure 4.11 Comparison of the as prepared κ -phase $\text{Ce}_2\text{Zr}_2\text{O}_8$ against a range of $^{17}\text{O}_2$ straight exchange labelled samples using temperatures of 200 °C, 300 °C, 350 °C and 400 °C.	53
Figure 4.12 ^{17}O MAS NMR comparison of (a) the disordered CeZrO_2 and (b) the κ -phase $\text{Ce}_2\text{Zr}_2\text{O}_8$. Each spectrum was measured at 9.4 T but (a) was acquired in a 2.5 mm rotor spinning at 31 kHz and (b) in a 3.2 mm rotor spinning at 20 kHz.	54
Figure 4.13 ^{17}O MAS NMR spectra of $^{17}\text{O}_2$ straight exchange labelled κ -phase $\text{Ce}_2\text{Zr}_2\text{O}_8$. These were acquired in a 4 mm rotor spinning at 8 kHz in a 9.4 T field. A recycle delay of 45 s was used. Asterisks denote spinning sidebands.....	55
Figure 4.14 The ceria region of the κ -phase $\text{Ce}_2\text{Zr}_2\text{O}_8$ showing the increasing intensity of the resonance at 840 ppm. This was acquired on a spectrometer operating at 9.4 T in a 3.2 mm rotor with spinning speeds of 20 kHz. Asterisks denote spinning sidebands.....	56
Figure 4.15 (Top) ^{17}O MAS NMR spectrum of $^{17}\text{O}_2$ 700 °C 500 °C redox labelled κ -phase $\text{Ce}_2\text{Zr}_2\text{O}_8$. (Bottom) The ceria, mixed ceria-zirconia and zirconia regions of the κ -phase spectrum with DMfit simulations in red and the convolutions of these simulations in various colours offset below. This spectrum was obtained in a 3.2 mm rotor spinning at 20 kHz at a field of 9.4 T. The	

black bars are predicted isotropic shifts from DFT calculations. Asterisks denote spinning sidebands and the R is the signal from the rotor.	58
Figure 4.16 The two unique ceria sites, C1 and C2, in the κ -phase structure. The top row shows the x-axis orientation and the bottom row the z-axis. The table on the right shows the Ce-O bond lengths as well as the mean and standard deviation of each site.	59
Figure 4.17 EELS images of the κ -phase $\text{Ce}_2\text{Zr}_2\text{O}_8$. (a) shows the interior of the crystal (b) shows the exterior.	60
Figure 4.18 Photos of various oxidation states of the κ -phase $\text{Ce}_2\text{Zr}_2\text{O}_8$ powder.	62
Figure 4.19 pXRD of the reduced κ -phase $\text{Ce}_2\text{Zr}_2\text{O}_8$ and a two phase Rietveld refinement. The blue line shows the difference between the refinement and the experimental data.	63
Figure 4.20 Raman spectra of the 700 °C 500 °C redox blue and green ordered ceria-zirconia samples as well as the 600 °C exchange sample.	64
Figure 4.21 ^{17}O NMR comparison of the three different coloured ordered ceria-zirconia samples. The blue sample was measured on a spectrometer operating at 11.7 T, the other two at 9.4 T. All samples were in a 3.2 mm rotor spinning at 20 kHz. The blue sample required 13000 scans due to very low S/N. Asterisks denote spinning sidebands.	65
Figure 4.22 ^{91}Zr NMR spectra of (a) the disordered CeZrO_2 , (b) the 700 °C 500 °C redox blue ordered sample, (c) the 700 °C 500 °C redox green ordered sample, (d) the 600 °C straight exchange ordered sample and (e) the BaZrO_3 reference. All measurements were static and recorded on an 11.7 T spectrometer apart from (a) which was on a spectrometer operating at 9.4 T.	67
Figure 4.23 The two unique zirconia sites, Z1 and Z2, in the κ -phase structure. The top row shows the x-axis orientation and the bottom row the z-axis. The table on the right shows the Zr-O bond lengths as well as the mean and standard deviation of each site.	68
Figure 5.1 (a) a basic representation of an exciton and (b) an energy level diagram showing how free and self-trapped excitons can exchange before energy emission back to the ground state.	74
Figure 5.2 Schematics of the organic MBA molecules placed in the inorganic lead bromide lattice.	75
Figure 5.3 Raman and FTIR spectra of the 2-MOP, 3-MOP and 4-MOP systems. Section a) FTIR of all three systems, showing the fingerprint region and stretching region of N-H and O-H, b) a Raman spectra showing the full range from the prominent organics up to the O-H stretching region, and c) zoomed in spectra showing only the prominent vibrational modes from the organic region.	80
Figure 5.4 A comparison of experimental pXRD patterns and calculated powder patterns from scXRD for (a) 2-MOP, (b) 3-MOP and (c) 4-MOP. These data suggest that the content of the	

single-crystal data is not entirely accounted for, discrepancies are shown with a red asterisk. AIRSS modelling has been used to add the missing water molecules to each crystal structure (see crystal structures to the right).	81
Figure 5.5 The binding energy of the last added water molecule using AIRSS is shown here, the water molecules are added sequentially before the systems are relaxed.	84
Figure 5.6 1D ^1H and ^{13}C NMR of 2-MOP (a) 3-MOP (b) and 4-MOP (c). Each ^1H spectrum has an associated simulation and deconvolution showing the individual sites which match up with the adjacent schematic molecules. H_2O is present in all three systems, but 2-MOP does not have a resonance at ~ 7 ppm like 3-MOP and 4-MOP.	86
Figure 5.7 2-MOP 2D spectra (a) ^1H - ^{13}C HETCOR using 2 ms contact times, (b) ^1H - ^1H NOESY using a contact time of 500 ms and (c) SQ-DQ BABA using 1 recoupling loop. The black dotted line in (a) is used as a guide to indicate a lack of major correlations and the blue dotted lines in (b) and (c) show the same.	91
Figure 5.8 3-MOP 2D spectra (a) ^1H - ^{13}C HETCOR using 2 ms contact times, (b) ^1H - ^1H NOESY using a contact time of 500 ms and (c) SQ-DQ BABA using 1 recoupling loop. The black dotted line in (a) is used as a guide to indicate a lack of major correlations and the blue dotted lines in (b) and (c) show water-water correlations.	92
Figure 5.9 4-MOP 2D spectra (a) ^1H - ^{13}C HETCOR using 2 ms contact times, (b) ^1H - ^1H NOESY using a contact time of 1 s and (c) SQ-DQ BABA using 1 recoupling loop. The black dotted line in (a) is used as a guide to indicate a lack of major correlations and the blue dotted lines in (b) and (c) show water-water correlations.	93
Figure 5.10 T_1 and $T_{1\rho}$ data for 2-MOP, 3-MOP and 4-MOP, the lines going through each data set are guides to show the difference in times clearly and are not lines of best fit.	95
Figure 5.11 ^{207}Pb NMR spectra of the MOP series at 14.1 T and 7.05 T. At the higher field a faster spinning speed was employed as the spinning sidebands are more visible. Due to the J -coupling present in 2-MOP the sidebands could not be displaced from the central transition (marked with an asterisk). The 7.05 T spectra have been magnified to better display the extent of J -coupling present; a J -manifold has been fitted for each.	96
Figure 5.12 Exchange rates calculated from EXSY experiments. The red dotted line shows the starting rate for efficient CEST experiments. The x-axis labels show the NOESY correlations taken from experiment, see Table A.1.	99
 Figure 6.1 Organics used in hybrid perovskite systems (a) the NMA organic used by Hu <i>et. al.</i> , (b) the NMA organic used by Du <i>et. al.</i> (c) the NEA organic, (d) the PMA organic and (e) the PEA organic.	103

Figure 6.2 Raman and FTIR spectra of the NMABr organic and the slow and fast preparation NMA based perovskites systems. Section a) FTIR of all three systems, showing the fingerprint region and stretching region of N-H and O-H, b) zoomed in spectra showing only the prominent vibrational modes from the organic region c) a Raman spectra showing the full range from the prominent organics up to the O-H stretching region.	107
Figure 6.3 1D ^1H NMR of a) the NMABr organic, b) the fast preparation perovskite and c) the slow preparation perovskite. The red lines show the simulated spectra from DmFit and the blue lines are the components of those simulations. The two molecules shown are the NMABr organic (top) and the NMA organic in the perovskites (bottom). The perovskite organic has two NH^{3+} groups to indicate that it displays conformerism.	110
Figure 6.4 HETCOR spectra of the NMABr organic. The left diagram is focussed around the aliphatic region and the right is focussed on the aromatic region. Black dots denote direct correlations between the protons and carbons whereas the red asterisks denote long range correlations.	112
Figure 6.5 HETCOR spectra of the $(\text{NMA})_2\text{PbBr}_4$ fast preparation perovskite. The left diagram is focussed around the aliphatic region and the right is focussed on the aromatic region. Black dots denote direct correlations between the protons and carbons whereas the red asterisks denote long range correlations.	113
Figure 6.6 HETCOR spectra of the $(\text{NMA})_2\text{PbBr}_4$ slow preparation perovskite. The left diagram is focussed around the aliphatic region and the right is focussed on the aromatic region. Black dots denote direct correlations between the protons and carbons whereas the red asterisks denote long range correlations.	114
Figure 6.7 NOESY spectra of the NMABr organic. The left spectrum uses a 10 ms mixing time and the right a 50 ms mixing time. Red dotted lines indicate correlations between resonances and the distances in brackets are the distances in space between atoms from the NMABr crystal structure.	116
Figure 6.8 NOESY (Left) and BABA (Right) spectra of the NMABr organic. The NOESY uses a 100 ms mixing time and the BABA uses 1 recoupling loop. Red dotted lines indicate correlations between resonances and the distances in brackets are the distances in space between atoms from the NMABr crystal structure.	117
Figure 6.9 NOESY spectra of the $(\text{NMA})_2\text{PbBr}_4$ fast preparation. The left spectrum uses a 10 ms mixing time and the right a 100 ms mixing time. Red dotted lines indicate correlations between resonances.	118
Figure 6.10 NOESY (Left) and BABA (Right) spectra of the $(\text{NMA})_2\text{PbBr}_4$ fast preparation. The NOESY uses a 500 ms mixing time and the BABA uses 1 recoupling loop. Red dotted lines indicate correlations between resonances.	119

Figure 6.11 NOESY spectra of the (NMA) ₂ PbBr ₄ slow preparation. The left spectrum uses a 10 ms mixing time and the right a 100 ms mixing time. Red dotted lines indicate correlations between resonances.	120
Figure 6.12 NOESY (Left) and BABA (Right) spectra of the (NMA) ₂ PbBr ₄ slow preparation. The NOESY uses a 500 ms mixing time and the BABA uses 1 recoupling loop. Red dotted lines indicate correlations between resonances.....	121
Figure 6.13 <i>T</i> ₁ and times of the NMABr organic and the fast and slow prep. (NMA) ₂ PbBr ₄ perovskites. The lines through the data are used to guide the eye and are not lines of best fit. ..	125
Figure 6.14 ²⁰⁷ Pb MAS NMR of the fast and slow prep. (NMA) ₂ PbBr ₄ perovskites and PbBr ₂ . The asterisks denote spinning sidebands.....	126
Figure A.1 EXSY fits used to produce exchange rates for 2-MOP.....	141
Figure A.2 EXSY fits used to produce exchange rates for 3-MOP.....	142
Figure A.3 EXSY fits used to produce exchange rates for 4-MOP.....	143
Figure A.4 <i>T</i> ₁ fits for NMABr organic.....	144
Figure A.5 <i>T</i> ₁ fits for (NMA) ₂ PbBr ₄ fast preparation perovskite.....	145
Figure A.6 <i>T</i> ₁ fits for (NMA) ₂ PbBr ₄ slow preparation perovskite.	146
Figure A.7 SAXS measurements and fits including particle size distribution data of the disordered ceria-zirconia system.....	147
Figure A.8 SAXS measurements and fits including particle size distribution data of the κ -phase ceria-zirconia.....	148

List of Tables

Table 4.1 Particle size and particle distribution values taken from fits to SAXS data for the as prepared and various redox $^{17}\text{O}_2$ labelled ceria-zirconias.	44
Table 4.2 Particle size and particle distribution values taken from fits to SAXS data, Figure A.8, for the as prepared and various straight exchange $^{17}\text{O}_2$ labelled κ -phase ceria-zirconia.....	50
Table 4.3 A list of the <i>δiso</i> and relaxation times of the resonances from the κ -phase $\text{Ce}_2\text{Zr}_2\text{O}_8$. The resonance numbers match to the numbers seen in Figure 4.15.	59
Table 4.4 The percentage contribution from the two structures used in Rietveld refinements of a series of κ -phase $\text{Ce}_2\text{Zr}_2\text{O}_8$ with varying levels of oxidation.....	62
Table 5.1 Single crystal XRD cell parameters of the three MOP systems. The parameters excluding crystal are from experiment and the parameters including water are from the structures generated by AIRSS.	83
Table 5.2 ^1H T_1 relaxation times for 2-MOP, 3-MOP and 4-MOP taken on 600 MHz and 800 MHz spectrometers. In general, the T_1 times increase when increasing in field strength. Also shown are the relative intensities of the ^1H simulations shown in Figure 5.6	87
Table 5.3 ^{13}C NMR isotropic shifts and comparative DFT values from the incomplete MOP structures and the complete, water containing, structures. $T_{1\rho}$ relaxation times were also measured for 2-MOP, 3-MOP and 4-MOP. The relaxation for the 2-MOP system is on average three times slower than its narrowband LED counterparts.	90
Table 5.4 J -manifold parameters and T_1 data from the ^{207}Pb NMR measurements.	97
Table 6.1. ^1H NMR shifts of the NMABr organic and the two NMA based perovskite structures. Also included are the ^1H shifts from DFT calculations of the NMABr, the T_1 times for all three systems and the relative intensity of the simulation components.....	109
Table 6.2 ^{13}C shifts for the NMABr organic and the fast and slow $(\text{NMA})_2\text{PbBr}_4$ preparations. NMABr has comparative values from the DFT calculations using CASTEP17.....	124
Table A.1 EXSY exchange rate data from ^1H - ^1H NOESY correlations of 2,3 and 4-MOP.	140

Acknowledgements

I would like to thank my academic supervisor Professor John V. Hanna as without his support and guidance I would not have had the opportunity to begin or complete this research.

Also I am thankful for all the help and guidance from all the members of the clean air group at Johnson Matthey Sonning, especially my industry supervisor Dr. David Thompsett for offering his scientific input when I presented results. This can very much be extended to Loredana Mantarosie, Dr. Maria Vlachou and Dr. Stephen Day. Without them I would not have achieved much, if any, research at the Johnson Matthey site.

I would like to acknowledge and thank all of the members of the solid-state NMR group at Warwick for their support and needed conversation between work in the office. I would especially like to thank Dr. Sam Page and Dr. Nicole Kelly for their perseverance with me, both because they proofread my thesis and put up with my bad jokes. A special thanks goes to Benjamin Griffith, without him my 8 years of university would have lacked that special charm.

I would also like to thank my family, my mum Toni, brother Jack and sister Alex for their constant support throughout my degree.

Last but not least, I would like to acknowledge Megan Sambrook who through the good times and the bad has kept me on the right path, encouraged my work and kept me sane throughout the pandemic and beyond.

Declarations

The experimental work contained in this thesis is original research carried out by myself at the University of Warwick between October 2017 and September 2021 in support of my application for Doctor of Philosophy in Physics. It has not been submitted in any previous application for any other degree.

The 0.7 mm solid-state NMR measurements were recorded by Dr. Xiangyan Shi (Nanyang Technological University).

Dr. Albert Bartok (University of Warwick) acquired the majority of the density functional theory calculations and AIRSS data.

The as prepared ordered Ceria Zirconia samples were prepared by Dr. Amy Kolpin (JMTC). Amy also collected the EELS data.

The hybrid perovskite systems were prepared by Hongwei Hu (Nanyang Technological University).

SAXS measurements of these samples were acquired by Dr. Stephen Hubband.

Results from other authors have been referenced in the text in the usual manner.

COVID-19 impact statement

Throughout the pandemic a significant portion of my research with Johnson Matthey was affected. The work shown here is roughly half of what was envisioned, the original plan had been to investigate 1:3 and 3:1 ratio ceria-zirconia solid solutions for both the ordered and disordered systems. Unfortunately, this could not go ahead as to make and label the samples, visits to the Johnson Matthey site are required. Their site was not and is still not receiving visiting students and due to the need for laboratory booking, no one onsite was available to assist.

The first lockdown meant that no laboratory work could be conducted at Warwick for ~3 months, this meant any NMR or other characterisation methods had to be put on hold. This first lockdown did however allow me to thoroughly analyse the work presented in Chapter 6 of this thesis.

The lack of data for Chapter 4 has led to subsequent holes in some series of labelling conditions, this has been addressed in the work. Altering the order and flow of the data presented has allowed for a coherent story to still be presented.

Abstract

Solid-state NMR has been applied alongside other characterisation techniques such as Raman spectroscopy and pXRD, and with the aid of DFT calculations via CASTEP to investigate ceria-zirconia materials and a variety of organic-inorganic hybrid perovskites. NMR is a technique that has not widely been utilised before on these materials but has proved to further elucidate their properties.

Ceria (CeO_2) is a very sought after material due to its broad range of uses in the medical field, as a catalyst, and as a non-inert support, particularly in catalytic converters. This is largely due it being able to reversibly change the oxidation state of the cerium nucleus from Ce^{4+} to Ce^{3+} . This leads to these systems having an oxygen storage capacity (OSC) which is ideal in autocatalysis when reducing or oxidising emission gases. To avoid sintering and degradation at high temperatures, CeO_2 is stabilised with ZrO_2 , to form a CeO_2 - ZrO_2 solid solution. These systems, both disordered and ordered, have been labelled with $^{17}\text{O}_2$ gas using a range of redox and straight exchange conditions such that ^{17}O NMR can be utilised. In the disordered ceria-zirconia, solid-state NMR has confirmed that the Zr-O bonds are weaker as they exchange oxygen more readily at lower temperatures. These weak bonds facilitate the improved OSC of this system.

Ordered, κ -phase ($\text{Ce}_2\text{Zr}_2\text{O}_8$), ceria-zirconia has been synthesised by using a high temperature (1200 °C) reduction and is then reoxidised in air. The κ -phase has greatly increased OSC due to very distant Zr-O bonds which are a product of the distortion of the crystal structure upon synthesis. At low temperature labelling conditions, ^{17}O NMR has shown that oxygen non-selectively moves through the κ -phase structure when it exchanges. At higher temperatures, additional OCe_4 sites begin to exchange oxygen. Rietveld refinements of pXRD have proven a useful tool to quantify the presence of multiple phases within the κ -phase when at different levels of oxidation.

Hybrid perovskites have many uses in LEDs, solar cells and data storage devices – this is owing to their ease of manufacture and low raw material cost. The main drawback of these materials is that water can lead to or speed up degradation. The two studies here both show that the MOP and NMA series contain crystallographic water

but show no evidence of degradation. The water molecules however, do hinder broadband LED properties in the 3-MOP and 4-MOP system. 1D and 2D NMR techniques have aided in assignment and complete characterisation of these systems with the aid of AIRSS paired with DFT calculations. 2D NMR was particularly key to the identification of conformerism in the NMA perovskite systems, which explains why it was not possible to grow large enough stable crystals for XRD measurements.

Abbreviations

AIRSS	Ab initio random structure search
B_0	External magnetic field in the z-axis
B_1	Induced magnetic field from a radiofrequency pulse
BABA	Back-to-back
CASTEP	Cambridge Serial Total Energy Package
CEST	Chemical exchange spectroscopy
CMOS	Complementary Metal-Oxide-Semiconductor
CP	Cross polarisation
CT	Central transition
DFT	Density functional theory
DOR	Double rotation
EELS	Electron energy loss spectroscopy
EFG	Electric Field gradient
EM	Electromagnetic
EXAFS	Extended X-ray absorption fine structure
EXSY	Exchange spectroscopy
FC	Fermi contact
FID	Free induction decay
FT	Fourier Transform
FWHM	Full-width half-maximum
GIPAW	Guage Including Projector Augmented Waves
HETCOR	Heteronuclear correlation
IR	Infrared
MAS	Magic angle spinning
MEMS	Micro-Electro-Mechanical Systems
MQ	Multiple Quantum
NMR	Nuclear Magnetic Resonance
NOESY	Nuclear Overhauser Effect Spectroscopy
OSC	Oxygen storage capacity
OTF	On-the-fly
PAS	Principle axis system

PCS	Pseudocontact shift
PGM	Platinum group metal
ppm	Parts per million
PXRD	Powder x-ray diffraction
QM	Quantum mechanics
RF	Radio Frequency
RTP	Room temperature phosphorescence
SAXS	Small-angle x-ray scattering
scXRD	Single-crystal x-ray diffraction
SQ	Single Quantum
ST	Satellite transition
T_1	Spin-lattice relaxation
$T_{1\rho}$	Spin-lattice relaxation in the rotating frame
T_2	Spin-spin relaxation
ω_0	Larmor frequency
ω_1	Frequency of an applied radiofrequency pulse

Chapter 1: Introduction

1.1 Material Characterisation

To conduct a complete characterisation of a material or series of materials a multi-technique approach is paramount. This is now the industry standard, in which an individual will either possess in depth knowledge of a number of techniques and apply them or they will collaborate with members of other departments. These techniques can be either experimental or computational in nature, but by bringing all of this analysis together additional information may be gleaned about a particular material or system.

In this work the major techniques employed are solid-state nuclear magnetic resonance (NMR), powder X-ray diffraction (pXRD), Raman and FTIR spectroscopy and density functional theory (DFT) calculations via CASTEP. These are used to investigate three different series of systems, the first are ordered and disordered ceria-zirconia solid solutions, the second organic-inorganic hybrid perovskite systems used as LEDs and finally another series of hybrid perovskites which have room-temperature phosphorescent (RTP) properties. None of these systems have been thoroughly analysed using solid-state NMR before, and so to combine this with more standard techniques will provide a more robust characterisation.

For the systems investigated here solid-state NMR can provide a number of different insights. Firstly NMR can be used as a structural tool to confirm the expected functional groups and overall structure of a material. This is particularly useful in the case of the hybrid perovskites in which multiple different nuclei (e.g. ^1H , ^{13}C and ^{207}Pb) can be observed. Both 1D and 2D techniques can provide this information, in

the case of 2D NMR multiple nuclei can be observed and correlated. ^1H and ^{13}C correlation experiments are used here. Pairing this with chemical shift positions from both 1D NMR and CASTEP shift predictions, provides a conclusive assignment for the functional groups in the organic components of the hybrid perovskite systems. Information on the dynamics of the system can also be gained from solid-state NMR. Relaxation measurements can be used to help explain the properties of a system, and how each nucleus interacts with either local or slightly distant nuclei.

Powder X-ray diffraction is excellent for providing long range structural information, and by using refinement techniques phase purity or multiple phases can be indentified. Even without refinement, lattice parameters and space groups can still be gleaned. If a system is sufficiently disordered or amorphous pXRD is less useful for determining these parameters, however it can confirm the disordered nature. One of the ceria-zirconia systems is disordered, but still possess enough local order of the various sites to produce distinct reflections. However small changes to the system can not be identified using this method.

Raman spectroscopy is excellent at observing small changes to bond stretching and vibrations. Whilst it can be difficult to assign all Raman bands, certain ones can be analysed and compared to give information on changes to crystallinity, order and lattice expansion or contraction. This is particularly useful in the ceria-zirconia systems as small changes to the isotope ratio of ^{16}O and ^{17}O after the ^{17}O labelling process can be seen and quantified.

DFT calculations via CASTEP are an excellent pairing for solid-state NMR as isotropic shifts can be predicted, provided there is a starting crystal structure to work from. These predicted shifts are key in aiding the assignment of functional groups, as well as showing that systems might not be phase pure. The role in assignments was very important for the LED based hybrid perovskites as the shift predictions aided in confirming the presence and nature of crystallographic water molecules.

These methods were applied to two different organic-inorganic hybrid perovskite systems. Hybrid perovskites are of particular interest for use in modern devices such as flexible solar cells and broadband LEDs. They offer cheap manufacture both due to

the readily available materials and the lack of need for clean rooms to produce high grade silicon. They are also favoured due to the tunability of their optoelectronic properties by making slight alterations to the organic components. Understanding the structure of these systems via solid-state NMR can reveal features such as conformers which generally cannot be observed via single-crystal XRD, and can also reveal additional components such as water within the structure. Having evidence for either of these factors would certainly aid in the design of these materials and how they are utilised in devices.

Ceria-zirconia materials in this context will be thought of as a non-inert support for use in autocatalysis. They do however have many uses beyond this, such as trapping soot in diesel exhaust, being used as a catalyst to produce phenol and catechol and also as thermally resistant catalysts used at high temperatures. Having knowledge of the oxygen mobility and phases of these systems can aid in better understanding how they behave when used in catalytic converters – with the final aim of improving their efficiency.

It is the aim of this work to robustly characterise and investigate these systems using a multi-technique approach, with the novel approach of using solid-state NMR to shed more light on the origin of each materials properties.

1.2 Thesis Overview

Chapter 2 gives the fundamental background theory of NMR and the interactions that can occur in the solid-state, particularly those observed in the systems in this work.

Chapter 3 outlines the experimental techniques and approaches used in both solid-state NMR as well as pXRD, Raman spectroscopy and CASTEP.

Chapter 4 is a study of both disordered and ordered ceria-zirconia materials. NMR, pXRD and Raman feature heavily in this work. There are shortcomings in each method when attempting to explain changes to the crystal structure based on changes in oxidation levels. The aim is to understand the oxygen mobility of the systems and any phase changes they undergo.

Chapter 5 is an investigation into LED based organic-inorganic hybrid perovskites called the MOP series. NMR and CASTEP are the driving forces into attempting to understand the broadband emission nature of one of the systems and the lack of this in the other two.

Chapter 6 is an insight into possible conformerism of hybrid perovskites with RTP properties. Solid-state NMR is the main source of structural elucidation in this chapter due to a lack of single-crystal XRD data, this was because crystals of sufficient size and stability could not be grown.

Chapter 2: Solid-State NMR Theory

2.1 NMR Theory

Nuclear magnetic resonance (NMR) is a technique used to investigate the local structure of a system by giving detailed information of the electronic environment of individual atoms. In short this is achieved by placing a sample in a strong magnetic field, applying a radiofrequency (RF) pulse and then after the pulse has stopped, an additional RF signal is produced by the sample as it relaxes back to equilibrium in the magnetic field. A Fourier transform (FT) can then be performed on this raw data to produce an NMR spectrum.

The bulk of the theory presented here comes from the following texts: Multinuclear Solid-State NMR of Inorganic Materials (Mackenzie and Smith, 2002) [1]; Solid-State NMR in Materials Science: Principles and Applications (Bakhmutov, 2016) [2] and Solid-State NMR: Basic Principles and Practice (Apperley, Harris and Hodgkinson, 2012) [3].

2.1.1 The Classical Description

Nuclei have an intrinsic angular momentum property called nuclear spin, I , which can be defined as $I = \hbar\sqrt{I(I+1)}$, where I is the spin quantum number (0, 1/2, 1, 3/2,...). This spin defines the nuclear magnetic moment, μ , when paired with the gyromagnetic

ratio, γ ($\text{rads}^{-1}\text{T}^{-1}$) – a constant for each element. This leads to the equation for the magnetic moment of a single spin:

$$\boldsymbol{\mu}_i = \gamma \mathbf{I}_i. \quad 2.1$$

The $\boldsymbol{\mu}_i$ are randomly orientated in a system, however when they are placed in a strong magnetic field, B , they will either align (low energy state) or anti-align (high energy state). In this context the direction of this field is thought of as the z -axis. The difference between these two states is called the population difference and is the key part to an NMR experiment. A greater number of magnetic moments are aligned with the field leading to a bulk magnetisation M for multiple spins:

$$M = \frac{N\gamma^2 B I(I+1)\hbar^2}{3kT}. \quad 2.2$$

Where N is the number of spins, k is the Boltzmann constant and T is the temperature.

The magnetic field induces a torque on the system:

$$\boldsymbol{\tau} = \mathbf{M} \times \mathbf{B}_0. \quad 2.3$$

Which causes a precession about the z -axis at the Larmor frequency $\omega_0 = -\gamma B_0$, which is dependent on both the magnetic field strength and the element in question.

Using Newton's 2nd law $\boldsymbol{\tau} = \frac{d}{dt}\mathbf{I}$ it can be determined that the motion of the bulk magnetisation can be given by:

$$\frac{d}{dt}\mathbf{M}(t) = \gamma \mathbf{M}(t) \times \mathbf{B}_0(t). \quad 2.4$$

2.2 The Quantum Mechanical Description

NMR deals with systems consisting of a large ensemble of spins, the previous section only offers a simplistic view of how a smaller spin system would act in a magnetic field. What is required is the use of quantum mechanics (QM) to fully describe larger scale systems with the use of wavefunctions, probabilities, discrete values and operators.

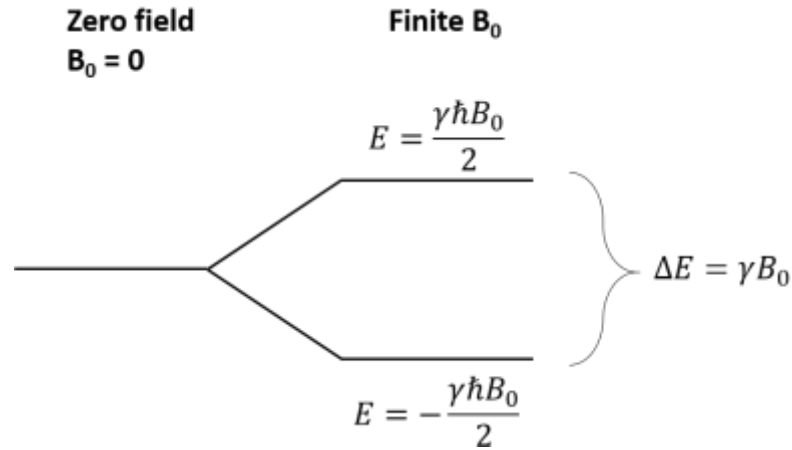


Figure 2.1 The effect of the Zeeman interaction on a spin $\frac{1}{2}$ nucleus in a finite magnetic field (adapted from Multinuclear Solid-State NMR of Inorganic Materials).

3.2.1 The Zeeman Effect

The Zeeman effect requires a strong magnetic field of the form $B = (0, 0, B_0)$. The quantum mechanical description of the interaction between the magnetic moment and this field is defined as:

$$\hat{H}_z = -\gamma B_0 \hat{I}_z. \quad 2.5$$

Where $\hat{I}_z = m\hbar|I, m\rangle$. The magnetic field lifts the degeneracy of the $2I + 1$ spin states leading to a splitting of their energies (Figure 2.1 [1]). Using the time-independent Schrödinger equation, $\hat{H}\psi = E\psi$ for a system where we are observing spin $\frac{1}{2}$ nuclei the eigenvalues in a finite B_0 field would be:

$$E_{1/2} = -\frac{\hbar\omega_0}{2}, E_{-1/2} = \frac{\hbar\omega_0}{2}. \quad 2.6$$

These energies correspond to the eigenvalues of the free-precession Hamiltonian. If an RF pulse of frequency ν is applied it will be absorbed and induce a spectroscopic transition provided $\Delta E = E_{upper} - E_{lower} = h\nu$ is satisfied.

2.3 Spin excitation in the rotating frame

To conduct an NMR experiment an RF pulse is applied in order to manipulate the nuclear magnetisation. The applied RF pulse has a field denoted as $B_1 = \omega_1/\gamma$ which

is several orders of magnitude smaller than the B_0 field and consists of two counter-rotating components. Each component rotates at a frequency ω_{RF} and has superposed amplitudes of $B(t) = 2B_1 \cos(\omega_{rf}t + \phi)$ where ϕ is the phase of an EM wave. In the laboratory frame a nuclear spin will experience a static B_0 field in the z direction and an oscillating $B_1(t)$ field as described above. In this case the applied pulse will be thought of as being along the x-axis which leads to a Hamiltonian of the form:

$$\hat{H} = -\gamma(\hat{I}_z B_0 + \hbar \hat{I}_x B_1 \cos(\omega_{rf}t + \phi)). \quad 2.7$$

Changing the frame of reference from the laboratory to the rotating frame and assuming $-\gamma$, where \mathbf{M} precesses anticlockwise, the B_1 field will appear stationary. Precession will now be at the offset frequency Ω which is defined as:

$$\Omega = \omega_0 - \omega_{rot.f.} = \omega_0 - \omega_{rf}. \quad 2.8$$

where $\omega_{rot.f.}$ is the rotating frame frequency. Hence the Hamiltonian is now defined as:

$$\hat{H}' = ((\gamma B_0 - \omega_{rf})\hat{I}_z + \hbar \hat{I}_x B_1).$$

When $\omega_{rf} = \omega_0$ then $\Omega = 0$, this is the on-resonance case. The general case leads to a reduction of B_0 leading to the residual field:

$$\Delta B = -\frac{\Omega}{\gamma}. \quad 2.10$$

In the rotating frame ΔB and B_1 are now linear fields in the z and x axes respectively, this causes an effective field to be applied to the system:

$$B_{eff} = \sqrt{B_1^2 + \Delta B^2}. \quad 2.11$$

Following this, a precession about the effective field occurs at $\omega_{eff} = |\gamma|B_{eff}$ which corresponds to the B_1 field, provided that either the offset is small or that the RF is much greater than the offset.

The flip angle defines the extent of the rotation of the net magnetisation of a system from the z-axis to the x-y plane. It is defined as $\theta_f = \omega_1 t_p$ where ω_1 is the nutation

frequency of an RF pulse and t_p is the duration of that pulse. Maximum signal is reached at a 90° flip angle.

The evolution of the magnetisation can be redefined in the rotating frame to be:

$$\frac{d}{dt}\mathbf{M} = \gamma\mathbf{M} \times \mathbf{B}_{eff}. \quad 2.12$$

The Bloch equations can be defined from this as the three directional components in the x,y and z axes. They fully describe the evolution of magnetisation over time in an NMR experiment.

2.4 NMR Interactions

In a homogenous external magnetic field, the evolution of nuclear magnetisation is solely defined by its internal interactions. It is these interactions that can be used to investigate the local structure of a system. These interactions can be viewed as perturbations of the Zeeman energy splitting and are generally either isotropic or anisotropic in nature. The anisotropic terms have an orientation dependence between the nuclear spin states and the external magnetic field. In a solid-state NMR experiment, using a powder, all possible orientations will be sampled in the magnet, the sum of which will produce a powder pattern.

2.4.1 The Internal Nuclear Spin Hamiltonian

The internal Hamiltonian is the sum of the interactions arising from the nucleus being investigated and its surroundings:

$$\hat{H}_{int} = \hat{H}_D + \hat{H}_{CS} + \hat{H}_K + \hat{H}_J + \hat{H}_P + \hat{H}_Q^{(1)} + \hat{H}_Q^{(2)} + \dots \quad 2.13$$

Diamagnetic insulating solids that are spin-1/2 experience many of these interactions including the magnetic dipolar interaction through space (\hat{H}_D), chemical shielding (\hat{H}_{CS}), and indirect spin-spin coupling (\hat{H}_J), also called J-coupling. The other interactions are the Knight shift (\hat{H}_K), the paramagnetic interaction (\hat{H}_P) and the 1st

and 2nd order electric quadrupole interaction ($\hat{H}_Q^{(1)}, \hat{H}_Q^{(2)}$). Most of these will be discussed in more detail in the following sections.

2.4.2 Rotational Frames and the Hamiltonian

These interactions are reported as diagonalised tensors; these diagonal tensors are said to be in the principal axis system (PAS). This system is subject to its three diagonal components, the principle values, and the local environment of the nucleus. Since the NMR experiment takes place in the LAB frame and not the PAS frame a set of rotations must be performed. The Euler angles are used to describe this frame rotation and as seen in Figure 2.2 are conventionally labelled α, β, γ . Here the Rose convention [4] is applied, a rotation about the z-axis by α , then a rotation about the y-axis by β and finally another rotation about the z-axis by γ .

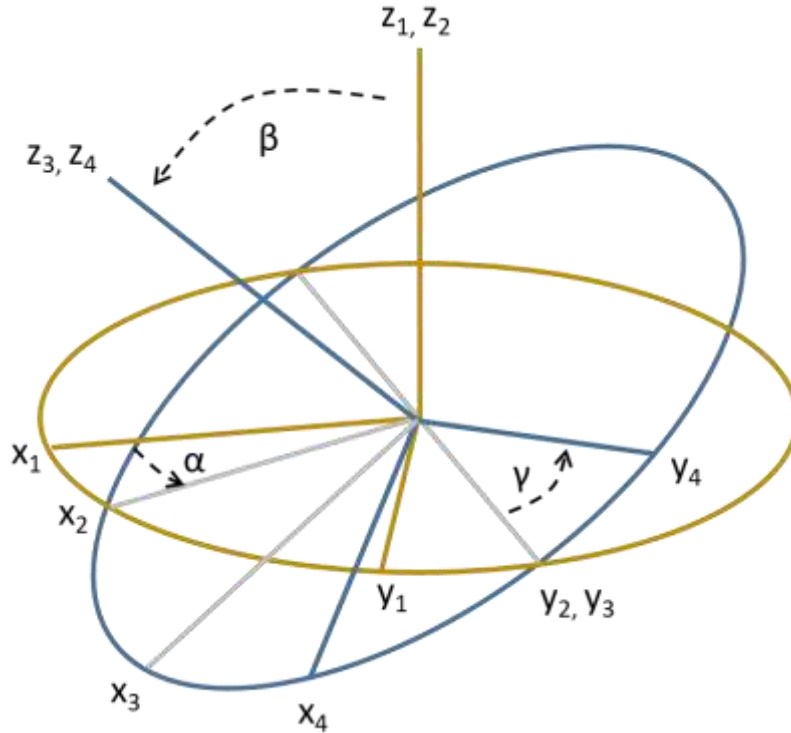


Figure 2.2 Frame rotations from the PAS frame to the LAB frame using the Euler angles α, β, γ .

2.4.3 Chemical shift and shielding

All the previous theory presented has assumed a bare nucleus, however in a real system the nucleus would be surrounded by electrons. These electrons produce a local field that alters the effect of the applied field to the nucleus, thus shielding or deshielding it. The local field at the nucleus is given by:

$$\mathbf{B}_{loc} = (\mathbf{1} - \boldsymbol{\sigma}) \cdot \mathbf{B}_0 = \begin{pmatrix} 1 - \sigma_{xx} & -\sigma_{xy} & -\sigma_{xz} \\ -\sigma_{yx} & 1 - \sigma_{yy} & -\sigma_{yz} \\ -\sigma_{zx} & -\sigma_{zy} & 1 - \sigma_{zz} \end{pmatrix} \begin{pmatrix} 0 \\ 0 \\ B_0 \end{pmatrix} = \begin{pmatrix} -\sigma_{xz}B_0 \\ -\sigma_{yz}B_0 \\ (1 - \sigma_{zz})B_0 \end{pmatrix}. \quad 2.14$$

Where $\boldsymbol{\sigma}$ is the second-rank tensor that describes the electron density of a material, called the magnetic shielding tensor. The perturbation of the Zeeman interaction is described by:

$$\hat{H}_{CS} = \gamma \hat{\mathbf{I}} \boldsymbol{\sigma} \mathbf{B}_0 = -\gamma \begin{bmatrix} \hat{I}_x & \hat{I}_y & \hat{I}_z \end{bmatrix} \begin{bmatrix} \sigma_{xx} & \sigma_{xy} & \sigma_{xz} \\ \sigma_{yx} & \sigma_{yy} & \sigma_{yz} \\ \sigma_{zx} & \sigma_{zy} & \sigma_{zz} \end{bmatrix} \begin{bmatrix} 0 \\ 0 \\ B_0 \end{bmatrix}. \quad 2.15$$

Since the strength of the chemical shift is directly proportional to the magnetic field strength, direct comparisons of chemical shifts (in Hz) are hard to make across different fields. A universal standard is therefore used, by converting chemical shielding values into chemical shift leads to a field-independent parameter, δ . These values must be compared to a standard, or reference, compound with a known response in an NMR experiment:

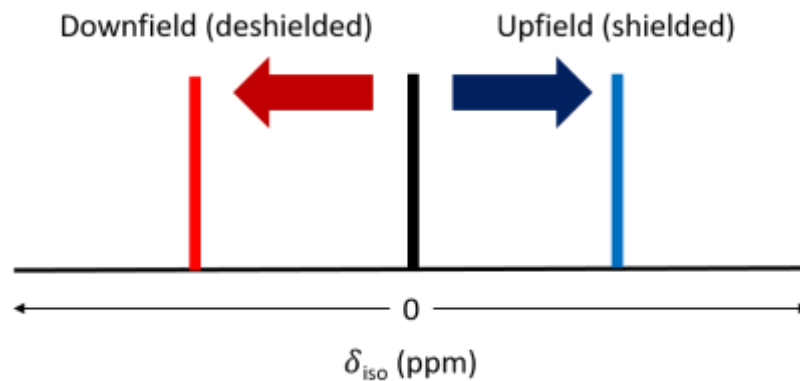


Figure 2.3 A schematic of shielding and deshielding in an NMR spectrum in comparison to a reference compound (black bar).

$$\delta_{sample} = \frac{\nu_{sample} - \nu_{ref}}{\nu_{ref}} \times 10^6. \quad 2.16$$

The isotropic chemical shift is a field-independent value quoted in parts per million (ppm). Any δ_{iso} value greater than the reference is less shielded than the reference and more shielded if it is a smaller value, see Figure 2.3. δ_{iso} is defined by the trace of the diagonalised chemical shielding tensor:

$$\delta_{PAS} = \begin{bmatrix} \delta_{xx} & 0 & 0 \\ 0 & \delta_{yy} & 0 \\ 0 & 0 & \delta_{zz} \end{bmatrix} \xrightarrow{Trace} \delta_{iso} = \frac{\delta_{xx} + \delta_{yy} + \delta_{zz}}{3}. \quad 2.17$$

There are a number of conventions for assigning the components of this tensor, the Haeberlen convention [5] is used here such that $|\delta_{zz} - \delta_{iso}| \geq |\delta_{xx} - \delta_{iso}| \geq |\delta_{yy} - \delta_{iso}|$. From this the chemical shift anisotropy, $\Delta\delta$, is defined as the largest

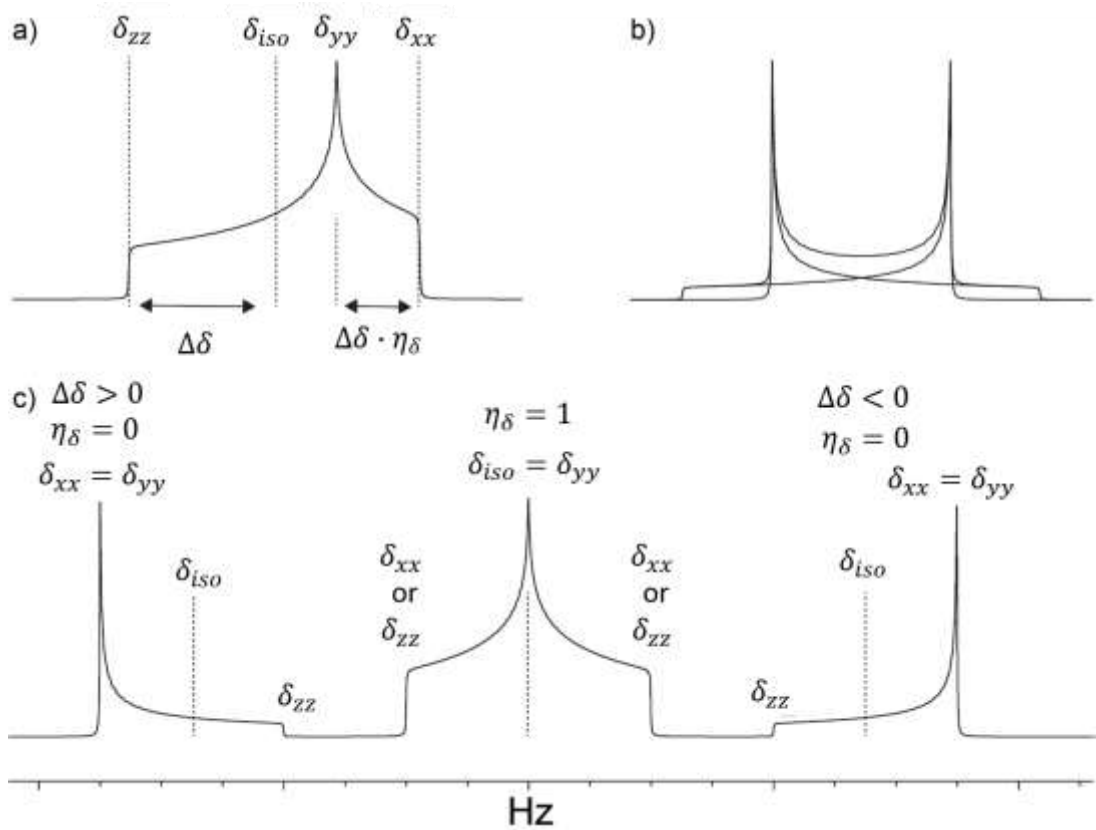


Figure 2.4 Above are examples of the powder patterns that can be produced due to CSA effects. a) is the typical chemical shift anisotropy (CSA) line shape with shielding parameters, b) is the Pake doublet for a powder under dipolar coupling and c) is the CSA line shape for different symmetries with respect to the external magnetic field.

frequency difference from δ_{iso} , and the asymmetry parameter η_δ is a measure of axial symmetry in the local electron environment:

$$\Delta\delta = \delta_{zz} - \delta_{iso} \quad \text{and} \quad \eta_\delta = \frac{\delta_{yy} - \delta_{xx}}{\Delta\delta}.$$

A chemical shift line shape from an experiment can be defined by the anisotropic and isotropic components arising from the chemical shielding interaction. For a powder sample all orientations of the system are represented which leads to a broad line consisting of many different overlapping crystallite orientations. Examples of the line shapes these produce can be seen in Figure 2.4 and are dependent on $\Delta\delta$ and η_δ .

2.4.4 The dipolar interaction

The dipolar interaction stems from the coupling between two magnetic dipoles, the Hamiltonian describing two dipoles interacting $\boldsymbol{\mu}_1 = \gamma_1 \hbar \mathbf{I}_1$ and $\boldsymbol{\mu}_2 = \gamma_2 \hbar \mathbf{I}_2$ a distance r apart is given by:

$$H_D = \frac{\mu_0}{4\pi} \frac{\gamma_1 \gamma_2 \hbar^2}{r^3} \left(\mathbf{I}_1 \cdot \mathbf{I}_2 - \frac{3(\mathbf{I}_1 \cdot \mathbf{r})(\mathbf{I}_2 \cdot \mathbf{r})}{r^2} \right). \quad 2.19$$

In Cartesian coordinates $\mathbf{I}_1 \cdot \mathbf{r} = \hat{I}_{1x}x + \hat{I}_{1y}y + \hat{I}_{1z}z$ which can be rewritten in polar coordinates as:

$$x = r \sin\theta \cos\phi, \quad y = r \sin\theta \sin\phi, \quad z = r \cos\theta. \quad 2.20$$

These conventions and techniques leads to what is referred to as the ‘alphabet expression for the dipolar Hamiltonian:

$$H_D = \frac{\mu_0}{4\pi} \frac{\gamma_1 \gamma_2 \hbar^2}{r^3} (A + B + C + D + E + F) \quad 2.21$$

$$A = \hat{I}_{1z} \hat{I}_{2z} (3 \cos^2\theta - 1) \quad 2.22$$

$$B = -\frac{1}{4} [\hat{I}_{1+} \hat{I}_{2-} + \hat{I}_{1-} \hat{I}_{2+}] (3 \cos^2\theta - 1) \quad 2.23$$

$$C = -\frac{3}{2} [\hat{I}_{1+} \hat{I}_{2z} + \hat{I}_{1z} \hat{I}_{2+}] (\sin\theta \cos\theta) \exp(-i\phi) \quad 2.24$$

$$D = -\frac{3}{2}[\hat{I}_{1-}\hat{I}_{2z} + \hat{I}_{1z}\hat{I}_{2-}](\sin\theta\cos\theta)\exp(+i\phi) \quad 2.25$$

$$E = -\frac{3}{4}[\hat{I}_{1+}\hat{I}_{2+}](\sin^2\theta)\exp(-2i\phi) \quad 2.26$$

$$E = -\frac{3}{4}[\hat{I}_{1-}\hat{I}_{2-}](\sin^2\theta)\exp(+2i\phi). \quad 2.27$$

Of the terms A-F only A and B commute with \hat{I}_z , this is the secular part of the dipole Hamiltonian which is time-independent and is expressed as:

$$H_D^{sec} = \frac{\mu_0}{8\pi} \frac{\gamma_1\gamma_2\hbar^2}{r^3} \left[2\hat{I}_{1z}\hat{I}_{2z} - \frac{1}{2}[\hat{I}_{1+}\hat{I}_{2-} + \hat{I}_{1-}\hat{I}_{2+}] \right] (3\cos^2\theta - 1). \quad 2.28$$

The $(3\cos^2\theta - 1)$ can be reduced to zero if $\theta = 54.74^\circ$, this is the magic angle which is used under MAS conditions. It is the angle subtended from the magnetic field to the internuclear vector. The strength of the interaction is dependent upon the distance between spins, r , and the gyromagnetic ratio γ .

2.4.5 The quadrupolar interaction

For nuclei with $I > 1/2$ the electrical charge distribution is non-spherical, leading to an electric quadrupole moment \mathbf{Q} . The surrounding charge of a quadrupolar nucleus is a three-dimensional ellipsoid that establishes an electric field gradient (EFG), it is this that couples to \mathbf{Q} to produce the quadrupolar interaction.

The energy of a charge distribution $\rho(r)$ in an electrostatic potential $V(r)$ is:

$$E = \int \rho(\mathbf{r}) \cdot V(\mathbf{r}) d\tau. \quad 2.23$$

$V(r)$ can be expanded as a Taylor series such that:

$$V(\mathbf{r}) = V(0) + \sum_{i=x,y,z} i \frac{\partial V}{\partial i} \Big|_{r=0} + \sum_{i,j} ij \frac{\partial^2 V}{\partial i \partial j} \Big|_{r=0} + \dots \quad 2.24$$

The zero-order term here is the electrostatic energy and so isn't orientation dependent and thus has no influence on an NMR spectrum. The first-order term is the electric dipole moment and is zero for all nuclei due to its inherent symmetry. This leaves the second order term representing the electric quadrupolar moment which gives a system its orientation dependence. The variation of Q is determined by the deviation of charge distribution from spherical symmetry and is given as:

$$Q = \int \rho(\mathbf{r}) (3z^2 - r^2). \quad 2.25$$

Laplace's equations states that an electrostatic potential in free space should equal zero meaning that the principal components of the EFG centred about a nucleus sum to zero leading to the definition of two new parameters:

$$C_Q = \frac{eQV_{zz}}{h} \quad \text{and} \quad \eta_Q = \frac{V_{xx} - V_{yy}}{V_{zz}}. \quad 2.26$$

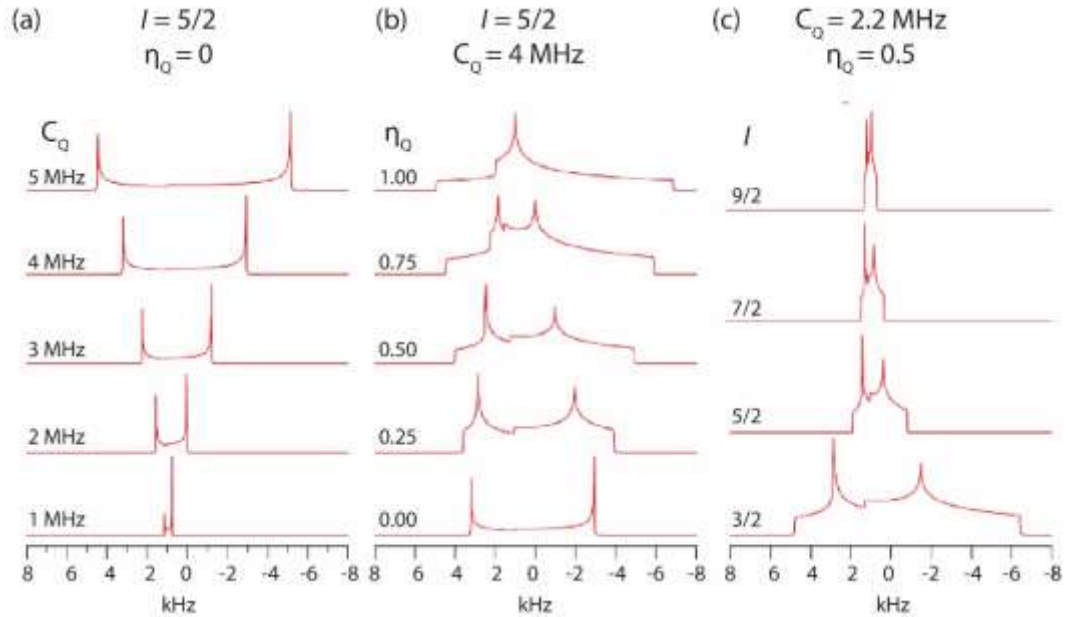


Figure 2.5 A series of quadrupolar lineshapes that are produced for changing (a) C_Q , (b) η_Q and (c) I .

C_Q is the quadrupole coupling constant, a measure of the strength of the quadrupole interaction, and η_Q is the asymmetry parameter which has values between 0 and 1. η_Q

describes the axial symmetry of the EFG and is a major contributing factor to the shape of a powder pattern, Figure 2.5. As will be seen in the later chapters here, a low C_Q shows that a site has high spherical symmetry.

The full quadrupole Hamiltonian is given as:

$$\hat{H}_Q = \frac{eQ}{2I(2I-1)\hbar} \hat{\mathbf{I}} \cdot \mathbf{V} \cdot \hat{\mathbf{I}}, \quad 2.27$$

the field gradient \mathbf{V} is a second rank tensor. When expanded into Cartesian coordinates using the Wigner-Eckhart Theorem and positioned in the PAS by using the EFG components V_i , defined as $V_0 = \sqrt{3/2}eq$, $V_{\pm 1} = 0$ and $V_{\pm 2} = 1/2 eq\eta_Q$ the Hamiltonian takes on the form:

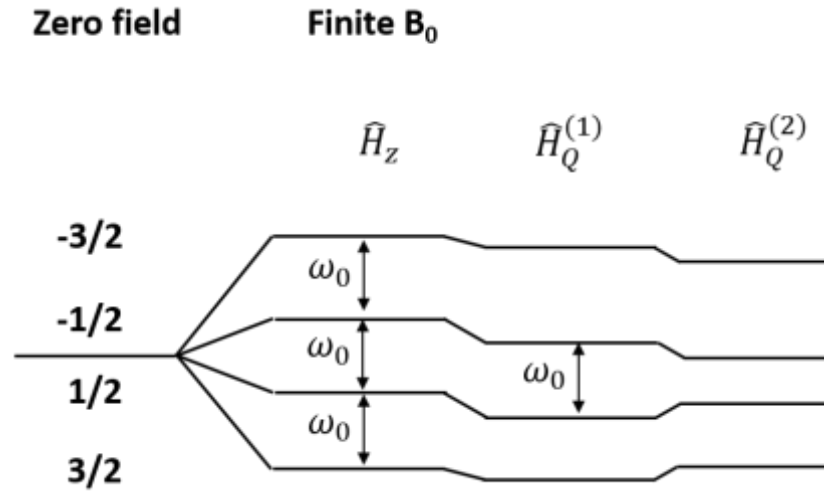


Figure 2.6 An energy level diagram for a nucleus of $I=3/2$ showing the energy level perturbations from the quadrupolar interaction. $\hat{H}_Q^{(1)}$ does not further perturb the central transition, however both the central and satellite transitions are perturbed by $\hat{H}_Q^{(2)}$.

$$\hat{H}_Q = \frac{eQh}{4I(2I-1)\hbar} \left(\sqrt{\frac{3}{2}} [3\hat{I}_z - \hat{I}^2] V_0 + [\hat{I}_z \hat{I}_+ + \hat{I}_+ \hat{I}_z] V_{-1} - [\hat{I}_z \hat{I}_- + \hat{I}_- \hat{I}_z] V_1 + \hat{I}_+^2 V_{-2} + \hat{I}_-^2 V_2 \right). \quad 2.28$$

Using time-dependent perturbation theory on the total energy Hamiltonian under the secular approximation, the effect of the quadrupolar interaction on spin states already experiencing the Zeeman interaction can be calculated. A half integer quadrupolar nucleus retains the Zeeman energy spacing for the central transition (CT) ($m = 1/2$ and $m = -1/2$) see Figure 2.6 . For the satellite transitions a shift of the frequency is seen which is dependent on the quadrupole frequency ν_Q which is related to the quadrupolar coupling constant by:

$$\nu_Q = \frac{3C_Q}{2I(2I - 1)}. \quad 2.29$$

If the quadrupolar interaction is strong relative to the Zeeman interaction (5% or more) then a significant energy correction occurs to the central and satellite transitions:

$$E_m^{(2)} = \sum_{m \neq n} \left(\frac{\langle n | \hat{H}_Q | m \rangle \langle m | \hat{H}_Q | n \rangle}{E_n^{(0)} - E_m^{(0)}} \right). \quad 2.30$$

This perturbation broadens and shifts the energy of the CT, if \hat{H}_Q is substituted into this equation the correction becomes:

$$E_m^{(2)} = -\frac{2}{\nu_0} \left[\frac{eQ}{4I(2I - 1)\hbar} \right]^2 \left[V_{-1}V_1(24m(m - 1) - 4I(I + 1) + 9) \right. \\ \left. + \frac{V_{-2}V_2}{2}(12m(m - 1) - 4I(I + 1) + 6) \right]. \quad 2.31$$

The V_i components now need to be transformed from the PAS to the Laboratory frame. Using the previously defined Euler angles and performing this transformation using the Wigner rotation matrices $D_{ji}^{(n)}$ [3]:

$$V_i^{Lab} = \sum_{j=-2}^2 D_{ji}^{(2)}(\alpha, \beta, \gamma) V_j^{PAS} \quad 2.32$$

which therefore gives the components:

$$V_1V_{-1} = -\frac{3}{4}e^2q^2 \left[\left(-\frac{1}{3}\eta^2 \cos^2 2\alpha + 2\eta \cos 2\alpha - 3 \right) \cos^4 \beta \right. \\ \left. + \left(\frac{3}{2}\eta^2 \cos^2 2\alpha - 2\eta \cos 2\alpha - \frac{1}{3}\eta^2 + 3 \right) \cos^2 \beta + \frac{1}{3}\eta^2(1 - \cos^2 2\alpha) \right] \quad 2.33$$

and

$$V_2V_{-2} = -\frac{3}{2}e^2q^2 \left[\left(\frac{1}{24}\eta^2\cos^2 2\alpha - \frac{1}{4}\eta\cos 2\alpha - \frac{3}{8} \right) \cos^4 \beta \right. \\ \left. + \left(-\frac{1}{12}\eta^2\cos^2 2\alpha - \frac{1}{6}\eta^2 - \frac{3}{4} \right) \cos^2 \beta + \frac{1}{3}\eta^2\cos^2 2\alpha + \frac{1}{4}\eta\cos 2\alpha \right. \\ \left. + \frac{3}{8} \right]. \quad 2.34$$

Using these components and substituting them into Equation 2.30 allows for the calculation of the second order perturbation energy shift. This leads to the quadrupolar frequency of the CT being given by:

$$v_{\frac{1}{2},-\frac{1}{2}}^{(2)} = -\frac{1}{6v_0} \left[\frac{3C_Q}{2I(2I-1)} \right]^2 \left[I(I+1) - \frac{3}{4} \right] \left(\frac{A(\alpha,\eta)\cos^4 \beta + B(\alpha,\eta)\cos^2 \beta + C(\alpha,\eta)}{B(\alpha,\eta)\cos^2 \beta + C(\alpha,\eta)} \right), \quad 2.35$$

where

$$A(\alpha,\eta) = -\frac{27}{8} + \frac{9}{4}\eta\cos 2\alpha - \frac{3}{8}\eta^2\cos^2 2\alpha \\ B(\alpha,\eta) = \frac{30}{8} - 2\eta\cos 2\alpha + \frac{3}{4}\eta^2\cos^2 2\alpha \\ C(\alpha,\eta) = -\frac{3}{8} + \frac{\eta^2}{3} - \frac{1}{4}\eta\cos 2\alpha - \frac{3}{8}\eta^2\cos^2 2\alpha. \quad 2.36$$

2.4.6 Scalar Coupling

Scalar coupling (or spin-spin, indirect or J -coupling) is caused by the indirect interaction of nuclear moments mediated via electrons in the chemical bonds between nuclei. The first nucleus perturbs the surrounding electrons and this produces an additional magnetic field at a second nucleus, this is a through-bond interaction. For multiple coupled spins the total scalar Hamiltonian is:

$$H_J = \sum_{i,j} hJ_{ij}m_i m_j. \quad 2.37$$

The powder pattern produced by this coupling gives information about the local spin network; whilst this is an interaction mostly seen in solution NMR in this work an example of scalar coupling in solids is seen.

If a spin, I , is coupled to several spins S and the Zeeman interaction is taken into account this Hamiltonian becomes:

$$H = H_Z + H_J = h\nu_0 I_z + J_{IS} h I_z S_{1z} + J_{IS} h I_z S_{2z}. \quad 2.38$$

This manifests as a splitting of what would otherwise be a single resonance, this splitting is dependent on the rule $2nI + 1$ where n is the number of coupled spins and I is the spin of the coupled nucleus. The number of resonances and their intensity follow a binomial distribution. The magnitude of the scalar coupling depends on the degree of covalency in bonding, the number of bonds between the nuclei, the gyromagnetic ratio and the degree of orbital overlap.

Scalar coupling can have both isotropic and anisotropic components. The J -coupling is normally taken to be directed along the internuclear vector as this is where the tensor is likely to have axial symmetry. The J -anisotropy is therefore described by $\Delta J = J - J_\perp$ which makes the complete J -Hamiltonian:

$$H_J = J \hat{I}_z \hat{S}_z + \frac{\Delta J}{3} [3 \hat{I}_z j_z (\mathbf{S} \cdot \mathbf{j}) - \hat{I}_z \hat{S}_z]. \quad 2.39$$

Here j_z is a projection of the unique axis of the J -tensor onto the z -direction. As the anisotropic component interaction is identical in form to the direct through-space dipolar coupling it is non-trivial to separate the contributions, therefore a pseudo-dipolar Hamiltonian is written that describes the bilinear coupling between spins I and S . Here the dipolar coupling is replaced by an effective dipolar coupling:

$$D' = \frac{\mu_0 \gamma_I \gamma_S \hbar}{8\pi^2 r_{IS}^3} - \frac{\Delta J}{3}. \quad 2.40$$

This effective dipolar coupling therefore leads to a frequency shift for the $(m, m-1)$ transition:

$$\Delta v_m = -mJ + mD'(3\cos^2\theta - 1) \quad 2.41$$

where θ is the direction of the internuclear vector in space.

2.4.7 Paramagnetic interaction

If a material contains a localised unpaired electron, these paramagnetic centres can induce an additional magnetic field at the nucleus. These local fields are described by:

$$B_{eff} = \frac{2\pi A\mu_B g B_0 I(I+1)}{3\gamma_N kT} + \frac{\mu_0 \mu_B^2 B_0 I(I+1)(3\cos^2\theta - 1)}{3kTr^3 + B_{BMS}} + BMS \quad 2.42$$

where A is the isotropic electron-nucleus hyperfine coupling constant, μ_B is the Bohr magneton, r is the electron-nucleus distance, θ is the angle between the electron-nucleus vector and B_0 and g is the electron g-factor. The B_{BMS} term represents a demagnetisation field that appears in the sample due to bulk magnetic susceptibility (BMS). This is an effect that is often ignored. These local fields can be significantly stronger than previously mentioned couplings and can mask other interactions.

The paramagnetic interaction is governed by two mechanisms - the Fermi contact shift (FC) and the pseudocontact shift (PCS), these are through-bond and through-space interactions respectively. The first term in Equation 2.42 describes the FC shift, for a bond between an observed nucleus and a paramagnetic centre. The second term is the dipolar interaction generated between a nucleus and an electron. For a spin rate ν_r , under MAS conditions, that is less than the magnitude of the interaction, the term appears as an intense spinning sideband manifold in an NMR spectrum. The PCS is described by:

$$\delta(PCS) = \left(\frac{1}{12\pi}\right)r^{-3} \left\{ \Delta\chi_{AX}(3\cos^2\theta - 1) + \left(\frac{3}{2}\right)\chi_{RH}\sin^2\theta\cos 2\phi \right\} \quad 2.43$$

where r is the paramagnetic centre-nucleus distance and θ and ϕ orientate the nucleus relative to the PAS of the magnetic susceptibility tensor χ of the axial (AX) and rhombic (RH) elements, respectively (with the paramagnetic centre being at the origin).

In addition to the broadening from the paramagnetic interaction, the strength of the interaction also effects the amount a resonance is shifted from its δ_{iso} position.

2.4.8 Magic Angle Spinning

In solution NMR there is rapid tumbling of molecules so many of the interactions previously described are inconsequential due to averaging. The dipolar and quadrupolar interaction share the same term, $3\cos^2\theta - 1$, which comes to zero if a

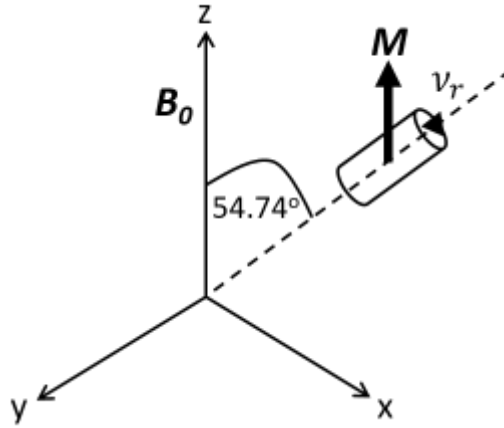


Figure 2.7 An experimental schematic showing the magic angle used to rotate a sample in an NMR experiment in order to minimise internal interactions.

sample is rotated with the frequency ν_r on an axis titled at $\theta = 54.74^\circ$ with respect to the \mathbf{B}_0 field, see Figure 2.7. This approach leads to the CSA being averaged to the isotropic value and the ST from the quadrupolar interaction are reduced to zero in the first-order and are narrowed greatly in the case of second-order lineshapes.

The main purpose of MAS is to improve spectral resolution and narrow resonances. If the spinning speed of the rotor does not satisfy the fast condition (the spinning frequency is not greater than the linewidth/strength of the interaction) then there is spectral dispersion of the anisotropy resulting in spinning sidebands that are separated by the spinning frequency.

The sample, see Figure 2.7, is fixed within the rotor frame. To understand the second order perturbation in the quadrupolar interaction the terms $V_{-1}V_1$ and V_2V_{-2} must be rotated to the rotor frame before the lab frame. Using the Wigner-Eckhart Theorem once more this leads to a second-order perturbation defined as:

$$E^{(2)} = \frac{1}{\nu_0} \left[\frac{3C_Q}{2I(2I-1)\hbar} \right] \begin{bmatrix} C_0(I, m)F_0(\eta) \\ +C_2(I, m)P_2(\cos\theta)F_2(\beta, \gamma, \eta) \\ +C_4(I, m)P_4(\cos\theta)F_4(\beta, \gamma, \eta) \end{bmatrix}. \quad 2.44$$

From here there are two important terms, the second and fourth order terms of the Legendre polynomials:

$$P_2(\cos\theta) = \frac{1}{2}(3\cos^2\theta - 1) \text{ and } P_4(\cos\theta) = \frac{1}{8}(35\cos^4\theta - 30\cos^2\theta + 3). \quad 2.45$$

Under MAS, $P_2(\cos\theta) = 0$ but the fourth order polynomial requires two spinning angles to be significantly reduced, 30.6° and 70.1° . Spinning at both of these angles can be achieved using a technique called double rotation (DOR), whereby one rotor is spinning inside of another and each rotor is spinning at one of the two afore mentioned angles. This technique will however not be used in this work as the contribution of the quadrupolar interaction in the investigated systems is minimal.

Chapter 3: Experimental Methods

3.1 NMR Spectroscopy

In this work a multitude of one-dimensional and two-dimensional NMR techniques were utilised to aid in the structural and dynamic characterisation of the systems investigated. These techniques and the parameters used will be outlined in the following pages.

3.1.1 One-Dimensional Techniques

The simplest case of an NMR pulse sequence is the single pulse experiment. For a system with $I = 1/2$ a single 90° ($\pi/2$) RF pulse is applied along the x axis which rotates the bulk magnetisation into the x-y plane. Once the pulse stops, the system begins to relax and a free induction decay (FID) is measured, Figure 3.1a. The decay of this magnetisation in all three axes is described by the Bloch equations:

$$\frac{dM_x}{dt} = \gamma(\mathbf{M} \times \mathbf{B}(t))_x - \frac{M_x}{T_2} \quad 3.1$$

$$\frac{dM_y}{dt} = \gamma(\mathbf{M} \times \mathbf{B}(t))_y - \frac{M_y}{T_2} \quad 3.2$$

$$\frac{dM_z}{dt} = \gamma(\mathbf{M} \times \mathbf{B}(t))_z - \frac{M_o - M_z}{T_1}. \quad 3.3$$

T_1 and T_2 are the longitudinal and transverse relaxation times respectively. For quadrupolar nuclei the flip angle θ_f used is generally between 30° - 50° . This is to

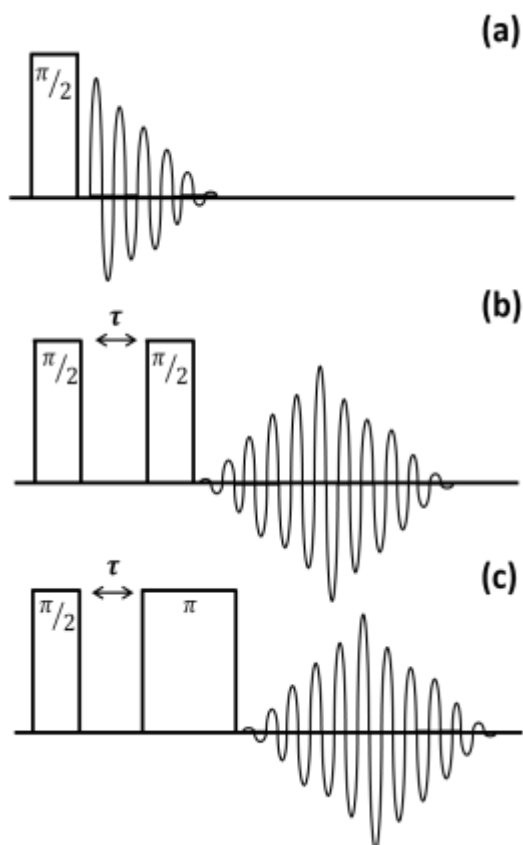


Figure 3.1 Pulse sequence diagrams of some one-dimensional NMR (a) single pulse, (b) solid-echo and (c) Hahn-echo.

ensure that for an environment with a large C_Q there is equal excitation of all resonances.

In single-pulse experiments narrow lineshapes are easily acquired, but due to issues with deadtime, the time between stopping an RF pulse and acquisition, broader features may not be represented in the NMR spectrum. An echo experiment solves this by forming a signal that has an effective time-zero deadtime. Thus any broad or fast decaying species in a system will also be shown in the FID.

The Hahn-echo and solid-echo experiments utilise T_2 relaxation to refocus the NMR signal. In a Hahn-echo this is done by an initial $\pi/2$ pulse into the x-y plane, after a fixed delay a π pulse then flips the precessing spins into the parallel plane where they refocus to a maximum signal, Figure 3.1c. In a solid-echo both pulses are the same length but the secondary refocusing pulse has an additional 90° phase shift, Figure

3.1b. The solid-echo experiment is generally applied to system with large C_Q 's as the second pulse has a larger bandwidth of excitation.

3.1.2 T_1 relaxation

Spin-lattice, longitudinal or T_1 relaxation is the process by which the longitudinal component of the bulk magnetisation exponentially relaxes to equilibrium aligning with the z-axis. This relaxation parameter is defined by equation 3.3. T_1 gives an indication to the dynamics of a system, and is dependent on the nuclei and system under investigation as there will be significant differences in the local environments and therefore interaction strength between the spins and the lattice. This relaxation time is also dependent on external factors such as heating and the strength of the external magnetic field. If a sample is heated the fluctuations at ω_0 are more frequent leading to a reduced T_1 time. It will be shown in this work that increasing the external magnetic field strength will lead to an increase in T_1 times, this is simply because $\omega_0 = -\gamma B_0$. For a quadrupolar nucleus the quadrupole interaction dominates the relaxation mechanisms which lead to significantly reduced T_1 relaxation times.

3.1.3 $T_{1\rho}$ relaxation in the rotating frame

Spin lattice relaxation in the rotating frame, $T_{1\rho}$, is the recovery of magnetisation to equilibrium in the presence of an RF field B_1 . $T_{1\rho}$ times are significantly longer than transverse relaxation, T_2 , and are used to investigate slower fluctuations; in this study they are used to investigate hybrid perovskites as the longitudinal relaxation of a range of these systems are very similar. $T_{1\rho}$ experiments use a spin-lock pulse which suppresses the free evolution of transverse magnetisation, essentially locking it in a particular orientation in the rotating frame.

In an ideal case the spin-lock magnetisation decays according to a single exponent at a rate of $1/T_{1\rho}$, however contributions from inhomogeneties in both the B_0 and B_1 will lead to a deviation from the ideal. When there are B_0 inhomogeneties the

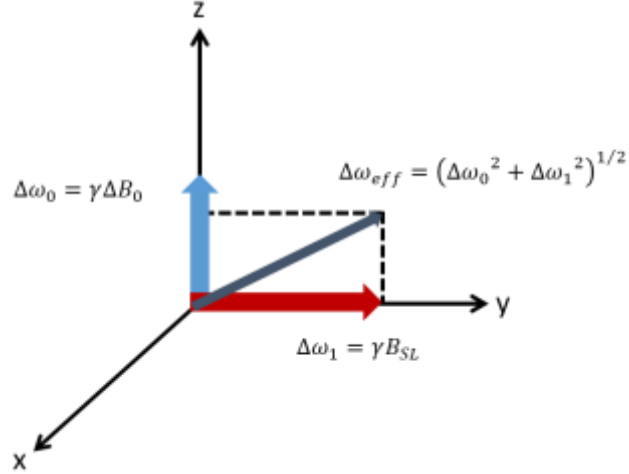


Figure 3.2 In the rotating frame under the influence of B_0 inhomogeneity there is an effective spin-lock strength and direction $\Delta\omega_{eff}$. (Adapted from Jurga et. al.)

magnetisation nutates about an effective spin lock frequency which deviates from the z direction at the angle:

$$\theta = \tan^{-1}\left(\frac{\Delta\omega_1}{\Delta\omega_0}\right) = \tan^{-1}\left(\frac{\text{FSL}}{\gamma\Delta B_0}\right) \quad 3.4$$

where FSL is the spin lock frequency. B_0 inhomogeneities lead to a deviation of this FSL. The effective spin-lock field strength is visualised in Figure 3.2 and can be calculated as:

$$\Delta\omega_{eff} = (\Delta\omega_0^2 + \Delta\omega_1^2)^{1/2}. \quad 3.5$$

The influence of these inhomogeneities can be combatted by using a spin-lock pulse with a strong spin-lock field strength and a large FSL such that θ is close to 90° hence $\Delta\omega_{eff} \approx \Delta\omega_1$ [6].

A simplification to the full Bloch analysis whilst still being held to an acceptable degree of accuracy is to ignore the transient relaxation effect. This will allow a precise trace of the evolution of the magnetisation using the multiplication of a series of rotations and relaxation matrices that represent each RF component of a composite spin-lock pulse. If an instantaneous RF pulse is defined as a rotation matrix with φ being the pulse field orientation and ϕ being the flip angle, $R_\varphi(\phi)$, then the evolution of magnetisation under an RF pulse is given by:

$$M_{t1} = R_\varphi(\phi)M_{t0}. \quad 3.6$$

Where M_{t0} and M_{t1} is the magnetisation before and after the pulse. The rotation matrix for each orientation for x, y and z are:

$$R_x = \begin{bmatrix} 1 & 0 & 0 \\ 0 & \cos\phi & \sin\phi \\ 0 & -\sin\phi & \cos\phi \end{bmatrix}, R_y = \begin{bmatrix} \cos\phi & 0 & -\sin\phi \\ 0 & 1 & 0 \\ \sin\phi & 0 & \cos\phi \end{bmatrix}, \quad 3.7$$

$$R_z = \begin{bmatrix} \cos\phi & \sin\phi & 0 \\ -\sin\phi & \cos\phi & 0 \\ 0 & 0 & 1 \end{bmatrix}.$$

Under a spin-lock pulse with duration T , assuming it is applied along the y direction, the spin-lock relaxation matrix can be given as:

$$E_\rho(T) = \begin{bmatrix} e^{-T/T_{2\rho}} & 0 & 0 \\ 0 & e^{-T/T_{1\rho}} & 0 \\ 0 & 0 & e^{-T/T_{2\rho}} \end{bmatrix} = \begin{bmatrix} E_{2\rho}(T) & 0 & 0 \\ 0 & E_{1\rho}(T) & 0 \\ 0 & 0 & E_{2\rho}(T) \end{bmatrix} \quad 3.8$$

here $T_{2\rho}$ is the decay rate of the magnetisation perpendicular to the spin lock pulse.

For a normal spin-lock pulse assuming a tip-down pulse, P_1 , and a tip-up pulse, P_2 with flip angles β and a flip angle α for the spin-lock component SL where $\alpha = 2\pi \cdot FSL \cdot TSL$, where TSL is the spin-lock time, the magnetisation evolution is given by:

$$M(TSL) = R_x(\beta) \cdot R_y(\alpha) \cdot E_\rho(TSL) \cdot R_x(\beta) \cdot M(t_0). \quad 3.9$$

Were $M(t_0) = [0 \quad 0 \quad M_0]^T$. As P_1 and P_2 are much shorter in duration than SL the relaxation during P_1 and P_2 can be ignored. By substituting equations 3.7 and 3.8 into 3.9 the final longitudinal magnetisation can be derived:

$$M_z = (\sin^2\beta \cdot e^{-TSL/T_{1\rho}} + \cos^2\beta \cdot \cos\alpha \cdot e^{-TSL/T_{2\rho}})M_0. \quad 3.10$$

Provided $\beta = 90^\circ$ then M_z will follow an exponential decay, if not then M_z will be a composite function of $T_{1\rho}$, $T_{2\rho}$ and α .

3.1.4 Cross-polarisation

Cross-polarisation (CP) is the transfer of magnetisation from one element to another, usually from abundant ^1H or ^{19}F spins to dilute X spins (in this work ^{13}C); X can however be any other $I = 1/2$ nucleus. As two different nuclei with different

gyromagnetic ratios are involved in CP, the system must be observed using the doubly rotating frame. One frame where effective magnetic fields from ^1H pulses appear static and another where effective magnetic fields from X pulses appear static.

The experiment consists of a ^1H $\pi/2$ pulse directed along the x-axis which rotates the ^1H bulk magnetisation onto the y-axis. A second pulse is then applied, phase-shifted by $\pi/2$, which spin-locks the magnetisation. During the spin-lock pulse, another pulse is simultaneously applied at the X frequency, this is the contact pulse. The time that these pulses are applied is the contact time. Provided the Hartmann-Hahn matching condition is met, the magnetisation will transfer from the ^1H nuclei to the X nuclei. This condition is given as:

$$\gamma^H B_1^H = \gamma^X B_1^X. \quad 3.11$$

This condition essentially says that if the nutation frequency of the ^1H and X nuclei are equal then a redistribution of the spin states occurs; there is a net gain for the X spins and hence an increase in signal. Following the contact pulse, ^1H decoupling is applied, this removes dipolar coupling during acquisition of the signal from the X spins. Decoupling is done to remove the broadening effects of this dipolar coupling which can either be heteronuclear or homonuclear. This is achieved by irradiating the protons with an RF pulse which leads the proton magnetisation to rotate from the z-axis to the xy-plane and then to the $-z$ -axis, such that the proton spin has gone from $I_z \rightarrow -I_z$. If this is done sequentially, the dipolar Hamiltonian will rapidly oscillate between $\pm I_z S_z$, and provided this oscillation is rapid compared to the timescale of the experiment it will time-average to zero.

Under MAS the net cross polarisation averages to zero, thus an additional matching condition needs to be used that accounts for the rotor MAS frequency:

$$\gamma^H B_1^H - \gamma^X B_1^X = \pm n \omega_r. \quad 3.12$$

With n being an integer. This is the sideband match condition. In this work the majority of CP experiments will adhere to this condition as $\omega_r = 110$ kHz was used.

3.1.5 Nuclear Overhauser-Effect Spectroscopy

Nuclear Overhauser-effect spectroscopy (NOESY) is a powerful method of 2D NMR structural determination. Cross-relaxation via dipolar couplings between proximate nuclei (in this case ^1H 's) can aid in assigning sites in 1D ^1H NMR. It can also observe conformers and stereochemistry not seen in single-crystal x-ray diffraction (scXRD) and can corroborate data from heteronuclear correlation (HETCOR) experiments and density functional theory (DFT) calculations. Cross-peaks that appear in a NOESY spectrum with a relatively short mixing time e.g. 100 ms correspond to nuclei that are within ~ 2.5 Å through space. As the mixing time is increased so is the distance from the site being observed. In this work the NOESY experiment used consists of a 90° RF pulse followed by an evolution time τ , during this time the ^1H spin precession will be characterised by their chemical shifts and couplings. Another 90° RF pulse is then used and the bulk magnetisation of the system nutates into the $-z$ axis, the z -magnetisation is then exchanged between proximate nuclei via cross-relaxation. After a preselected mixing time the magnetisation is finally detected with a 90° pulse. The basis of the 2D experiment arises from using a fixed mixing time for each experiment and each slice of the experiment will increment τ , thus collecting all aspects of the cross-relaxation occurring in the system.

3.1.6 Single-Quantum Double-Quantum Methods

A multiple quantum analogue to the NOESY pulse sequence, back-to-back (BABA) pulse sequences transfer multiple quantum (MQ) coherences to single quantum (SQ) modes such that they are observable. This observable magnetisation then leads to a spectrum showing dipolar couplings between nuclei in a structure, these are seen as either auto-correlation peaks or cross-peaks, the latter of which are a result of anisotropic dipole-dipole interactions. Broadband BABA spectroscopy is more commonly used than the original sequence due to the robust nature of the numerous 90° RF pulses implemented [7]. As a MQ analogue to NOESY experiments BABAs are used to confirm chemical structures, in the literature this largely pertains to ^{31}P structural measurements [8–10]. The broadband BABA sequence implemented here

begins with a 90° RF pulse creating transverse magnetisation, this is followed by a series of three 90° phase cycled pulses which prepare the spin system such that spins oscillate with “forbidden” double quantum (DQ) transition frequency. A double quantum evolution period τ then elapses (like the NOESY this increments with each slice) and then three more phase cycled 90° pulses occur which recombine the DQ coherences with the SQ coherences. A final 90° RF pulse occurs and the signal is then observed. The 90° RF pulses which create and recombine the DQ coherence can be looped, this looping allows for imperfections in the optimization of the pulse sequence. This technique gives information of atoms through bond, the maximum distance it can observe is $\sim 3.5 \text{ \AA}$.

3.1.7 Heteronuclear Correlation

Numerous structural studies employing high resolution 2D NMR techniques use NOESY and HETCOR experiments together to confirm the structure and assignments of their systems [11–13]. The same approach is taken here, however in this case an inverse HETCOR experiment is used. Data from a HETCOR spectrum shows cross-peaks relating ^1H 's and their directly bonded ^{13}C atom. In this study an inverse hCH HETCOR experiment is deployed. By detecting on the ^1H channel an 8-fold increase in signal intensity is achieved compared with a 4-fold increase seen when detecting on the ^{13}C in standard experiments. This is realised by first exciting the ^1H 's with a 90° RF pulse and then transferring magnetisation from the ^1H to the ^{13}C using a contact pulse. After an evolution time, τ , a second 90° pulse on the ^{13}C channel flips the magnetisation vector into the transverse plane which is then transferred back with another contact pulse; now ready for detection on the ^1H channel.

3.2 Raman Spectroscopy

Raman spectroscopy is a technique used to investigate the vibrational modes of bonds within a sample. This is achieved by irradiating a sample with monochromatic light from a laser between the visible to near infrared part of the spectrum. Ground state electrons within a molecule are excited to the ‘virtual state’, Figure 3.3a, after

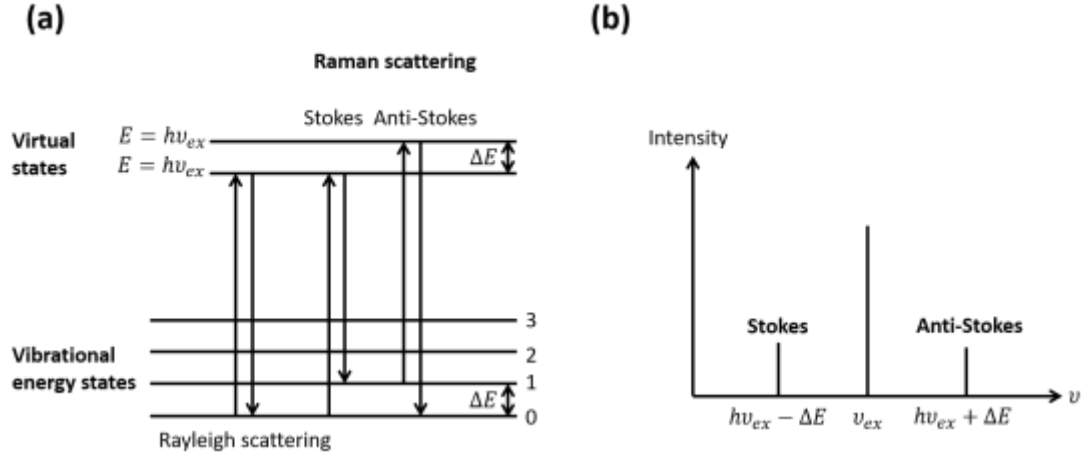


Figure 3.3 (a) A schematic of how Rayleigh and Raman scattering arises due to the transition between the electronic ground state and two virtual states and (b) a Raman spectra that contains low frequency Stokes emissions and high frequency anti-Stokes emissions. Adapted from Czernuszewicz and Zaczek (2011).

absorbing a photon; leading to three scattering methods after photon reemission. These are Stokes, anti-Stokes and Rayleigh scattering. Stokes and anti-stokes scattering are inelastic scattering that occurs when either the reemitted photon is of lower energy (Stokes), or higher energy (anti-Stokes). Rayleigh scattering is elastic scattering such that the reemitted photon is of the same energy and frequency of the incident radiation.

Due to the relative population of the two virtual state energy levels Stokes emission is favoured over anti-Stokes. Rayleigh scattering also has a much greater occurrence as the probability of energy transfer to molecules in the ground state and the subsequent reemission back is very high. The energy difference between Rayleigh scattering and Stokes and anti-Stokes is $\pm\Delta E$, which is the energy of the first ground state vibrational level. A wave model can be used to describe the two types of Raman scattering and Rayleigh scattering. An incident beam of radiation with frequency ν_{ex} has an electric field E :

$$E = E_0 \cos(2\pi\nu_{ex}t) \quad 3.13$$

E_0 here is the amplitude of the wave. Once the field interacts with the bond of a sample, and thus its corresponding electron density, a dipole moment, m , is induced:

$$m = \alpha E = \alpha E_0 \cos(2\pi\nu_{ex}t) \quad 3.14$$

α is the polarizability of the bond i.e. a measure of its deformability within an electric field. It is dependent upon the distance between the bonded nuclei:

$$\alpha = \alpha_0 + (r - r_{eq}) \left(\frac{d\alpha}{dr} \right). \quad 3.15$$

Here α_0 is the polarizability of the bond at r_{eq} which is the equilibrium internuclear distance and r is the internuclear separation. This difference in separation varies with a vibrational frequency ν_v as defined below:

$$r - r_{eq} = r_m \cos(2\pi\nu_v t). \quad 3.16$$

Here r_m is the maximum nuclear separation relative to an equilibrium position. By substituting equations 3.15 and 3.16 into equation 3.14 the induced dipole moment is now defined as:

$$m = \alpha_0 E_0 \cos(2\pi\nu_{ex} t) + E_0 r_m \left(\frac{d\alpha}{dr} \right) \cos(2\pi\nu_v t) \cos(2\pi\nu_{ex} t). \quad 3.17$$

If the trigonometric identity for the product of two cosines, $\cos x \cdot \cos y = [\cos(x + y) + \cos(x - y)]/2$, is used to reinterpret equation 3.17 then the induced dipole moment now becomes:

$$\begin{aligned} m = \alpha_0 E_0 \cos(2\pi\nu_{ex} t) + \frac{E_0}{2} r_m \left(\frac{d\alpha}{dr} \right) \cos[2\pi(\nu_{ex} - \nu_v) t] \\ + \frac{E_0}{2} r_m \left(\frac{d\alpha}{dr} \right) \cos[2\pi(\nu_{ex} + \nu_v) t]. \end{aligned} \quad 3.18$$

This equation now describes the three types of scattering in Raman spectroscopy. The first term describes Rayleigh scattering and the second and third terms describe Stokes and anti-Stokes scattering respectively. Raman spectra generally show multiple vibrational modes which is due to the excitation frequency being modified by the bonds in a sample. Not all modes are said to be Raman active and this is decided by the selection rules for Raman scattering that require a change in polarizability, $\frac{d\alpha}{dr}$, that is greater than zero.

3.3 DFT, CASTEP and AIRSS

Density functional theory (DFT) is an approach to first principles calculations that uses quantum-mechanical theory to calculate the cohesive properties of solids using the electron density as the fundamental variable. This is done by using pseudopotentials calculated from theory devised by Kohn and Sham [14], this theory presents the full solution of the Schrodinger many body problem as a set of non-interacting particles. By then using an exchange functional which attempts to simulate interactions between these particles, a sensible pseudopotential is produced. Here DFT is used to calculate NMR parameters, specifically chemical shielding values. These chemical shielding values are realised by utilising the software CASTEP [15] which can subsequently be converted to isotropic chemical shift using:

$$\delta(r) = -\sigma_r - \sigma_{ref} \quad 3.19$$

where σ_r is the shielding and σ_{ref} a reference shielding from a known compound or series of compounds.

To further supplement these calculations an approach called AIRSS (*Ab Initio* Random Structure Search) [16–18] was implemented. This method was first proposed to explore the stable region of the potential energy surface of atomic systems with a minimal bias. It is a method based on a number of geometry relaxations each of which start from a randomly generated configuration corresponding to the composition of the system in question. These configurations are driven by forces obtained from first-principle quantum mechanics calculations. AIRSS has been successful in predicting new phases [19], understanding the structure of interfaces [20] and defects in complex materials [21]. The full experimental details for each of these computational approaches will be outlined in later chapters.

Chapter 4: An investigation of ordered and disordered ceria-zirconia

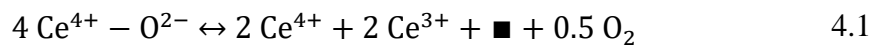
4.1 Introduction

Since the inception of the combustion engine and automobiles, toxic exhaust gases have been a threat to public health and thus a method to process these emissions became necessary [22]. Recent reports regarding the 2025 transportation status predictions revealed that the future of light-duty emission standards can be met using a wide range of advanced gasoline technologies [23–25]. The implication is that the future of the emission control technologies obliges for the development of new innovative catalyst materials and non-inert supports; those of which are suitable for low temperature operation under three-way catalyst (TWC) conditions with very high efficiency.

4.1.1 Ceria and its uses in autocatalysis

Since the introduction of the TWC converter in 1981, ~26000 characterisation studies of its components have been undertaken [26]. Cerium dioxide (Ceria, CeO_2) is one of these components and in TWC converters, acts as a non-inert support. Ceria is used in a wide variety of disciplines such as intracellular drug delivery [27], a support for stem cells in vitro [28], solid oxide fuel cells [29] and gas sensors [30]. The reason for the versatility of ceria lies in the unique redox property of Cerium which allows it to change its oxidation state between Ce^{3+} and Ce^{4+} . The electronic configuration of Cerium is $[\text{Xe}]4f^1 5d^1 6s^2$ and it is this 4f electron that is the root of this redox property. Amongst the range of oxides that ceria forms there are two extreme compositions CeO_2 (Ce^{4+}) and Ce_2O_3 (Ce^{3+}), the latter has a $P\bar{3}m1$ hexagonal structure. CeO_2 has a

face-centred cubic (fcc) fluorite-type structure (space group $Fm3m$ [31]). As the coordination number of oxygen is four the structure contains OCe_4 tetrahedra, Figure 4.1(a). The Ce^{4+} has a coordination number of eight and therefore consists of CeO_8 which will be demonstrated later in the Raman spectroscopy studies. The reduction of cerium to Ce^{3+} allows oxygen to be released from the structure Figure 4.1(b), this reversible process is the origin of ceria's oxygen storage capacity (OSC). Ceria releases oxygen and becomes disordered, however up until a deficiency of $\text{CeO}_{1.714}$ [32] the $Fm3m$ structure is maintained. This reduction can be expressed using the following equation:



where \blacksquare is a vacancy. The two electrons from the oxygen are transferred to the cerium cations which reduces them.

The OSC property of ceria is caused by defects in the lattice. Here these defects come in the form of Ce^{3+} cations, intrinsic and extrinsic vacancies. Extrinsic defects are largely a product of doping ceria with cations such as Zr^{4+} which in this case is used to stabilise Ce^{3+} cations and to introduce more vacancies to the system. The main focus of this chapter is to investigate these solid-solutions. Intrinsic defects result from

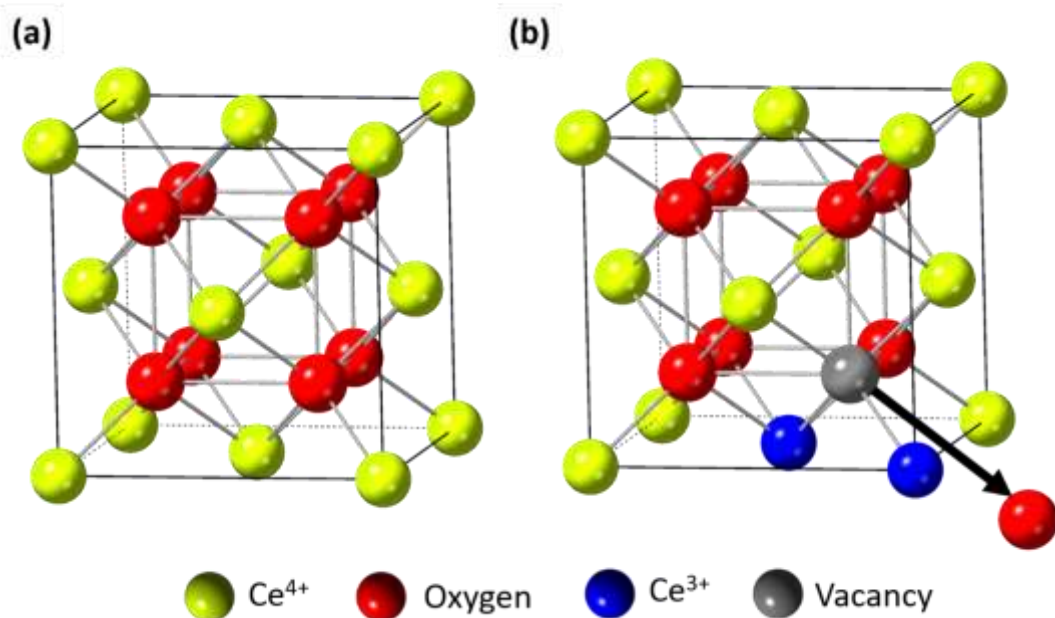
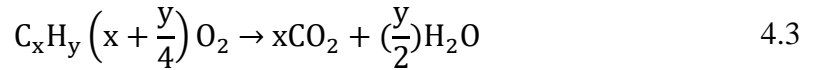


Figure 4.1 (a) ceria structure showing the OCe_4 tetrahedra and (b) the CeO_{2-x} . (Graphics are from the program CrystalMaker).

movement of oxygen within the system, such as the Frenkel-type point defect [33–36]. This is a defect in which the centre of the octahedral lattice is occupied by the adjacent oxygen anion from the structure. This is then balanced by leaving a vacancy. This defect is thought to vastly contribute to ceria's OSC as it leads to improved oxygen mobility and maintains additional intrinsic vacancies. Defects are more stable at the surface of ceria [37] and so a reduction of surface area (which in this work will be seen by heating the system) decreases the defect concentration.

Petrol engines rely on a TWC to convert harmful CO, hydrocarbons and NO_x emissions into CO₂, H₂O and N₂ gas via:



Ceria in the form of a washcoat is coated onto a ceramic honeycomb cordierite monolith which comprises of long parallel channels to allow exhaust gases to pass through the catalytic converter. Platinum group metal (PGM) nanoparticles are dispersed throughout the channels and act as the catalyst. In this case the ceria would be replaced with either an ordered or disordered ceria-zirconia solid solution. The main goal of ceria is to mediate the oxygen partial pressure within the exhaust such that these gases are converted as efficiently as possible, this is done by the reaction:



To maintain maximum efficiency of both reducing and oxidising the necessary emission gases, ceria releases oxygen in oxygen-lean conditions (creating vacancies throughout the system) and adsorbs oxygen in oxygen-rich conditions (refilling the vacancies). Pure ceria sinters and therefore thermally ages relatively easily. In a catalytic converter, without doping, the exhaust gases which can reach temperatures in excess of 1100 °C [38] would easily lead to this decay. A thermally stable ceria-zirconia support was revealed in 1987 [39], this consisted of a ceria-zirconia solid

solution, this system possesses a greater OSC due to improved reduction properties. Ceria-zirconia supports are the industry standard for supports used in modern TWCs.

4.1.2 Ceria Zirconia

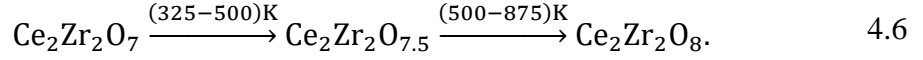
As previously stated, ceria-zirconia solid solutions are used in three-way catalysis due to their improved thermal stability and increased OSC. These ceria-zirconia supports come in the form $\text{Ce}_x\text{Zr}_{1-x}\text{O}_2$, in the systems investigated in this work $x = 0.5$; the powder sample is yellow in colour. When x is between 0.2 and 0.6 the structure takes on the tetragonal (t') phase with the space group being $P4_2/nmc$ [40–42]. To form these solid solutions, the Zr^{4+} cations (0.84 Å) replace some of the Ce^{4+} cations (0.97 Å) in the cubic lattice. This leads to a disordered system in which domains of cerium and zirconium coordinated oxygen atoms exist that are randomly distributed throughout the structure. The addition of Zr^{4+} cations causes a lattice contraction that is readily observable using routine characterisation techniques such as pXRD and Raman spectroscopy. For a 1:1 composition, significant distortion around the Zr atoms has been observed using extended X-ray absorption fine structure (EXAFS) spectroscopy [43,44]. The local environment around the Zr is described as 4 O atoms at 0.2115 nm, 2 O atoms at 0.2312 nm and 2 O atoms at a distance exceeding 0.26 nm. By comparison 8 O atoms at the distance of 0.2312 nm are present around the Ce. These longer Zr-O bonds are weaker and offer an excellent explanation for the greater oxygen mobility in ceria-zirconia solid solutions [45].

Whilst these systems have excellent OSC properties and are thermally stable they can be improved by creating a structurally ordered system.

4.1.3 Ordered Ceria Zirconias

A number of structurally ordered 1:1 ceria-zirconia solid solutions have been discovered. In 1996 the first non-stoichiometric system, a pyrochlore, was reported by Thomson *et. al.* [45]. In 1998, Otsuka-Yao-Matsuo *et. al.* [46] reported the κ -phase system and from these two discoveries a number of intermediates between these two phases emerged [47,48]. The pyrochlore structure $\text{Ce}_2\text{Zr}_2\text{O}_7$ is an fcc system, space group $Fd3m$, and is black in colour. It has oxygen occupying 7 of the 8 tetrahedral sites between the two different cations. There is a fine balance between CeO_2 and

Ce₂O₃ in this system and because of this it has relatively low thermal stability in air at above 325 K. The system begins to oxidise in a two-step process seen below:



In the first step the pyrochlore gains a total mass of 1.35%, measured by thermogravimetric analysis (TGA) and another 1.40% in the second step. These mass gains both correspond to half an oxygen atom. The Ce₂Zr₂O_{7.5} is also cubic and has a space group of $F\bar{4}3m$ and is grey in colour – this is referred to in this work as the intermediate phase.

If a considerably high temperature, ~1500 K, is used to reduce the pyrochlore, strong ordering of the κ -phase along the $\langle 100 \rangle$ plane can be achieved. This is because the high reduction temperature introduces a significant amount of O-vacancies which facilitate the mobility of the cations and therefore the cationic sublattice. The κ -phase is actually a fairly distorted system even though it is so ordered, this is due to it being at the limit of oxygen present around the cations; this will be demonstrated later in section 4.3.7. Ce₂Zr₂O₈ is bright yellow in colour, is cubic and has the space group $P2_13$. In the κ -phase the Zr cation is too small to accommodate 8 oxygen atoms in its first coordination sphere and so it displaces one of the coordinating oxygen's to a nonbonding distance. It is this structural, yet consistent, non-uniformity that leads to the greatly enhanced OSC capabilities of this system. These weak bonds have been predicted by Gupta *et. al.* [49] by using DFT to show that weaker Zr-O bonds are generated when transitioning from Ce₂Zr₂O₇ to Ce₂Zr₂O₈.

4.2 Materials and Methods

4.2.1 Materials and ¹⁷O enrichment

In this chapter a disordered and an ordered ceria-zirconia solid solution are investigated. The disordered system, Ce_{0.5}Zr_{0.5}O₂ was bought in from a commercial supplier and then provided to me by Johnson Matthey. The synthesis details of this system are unknown.

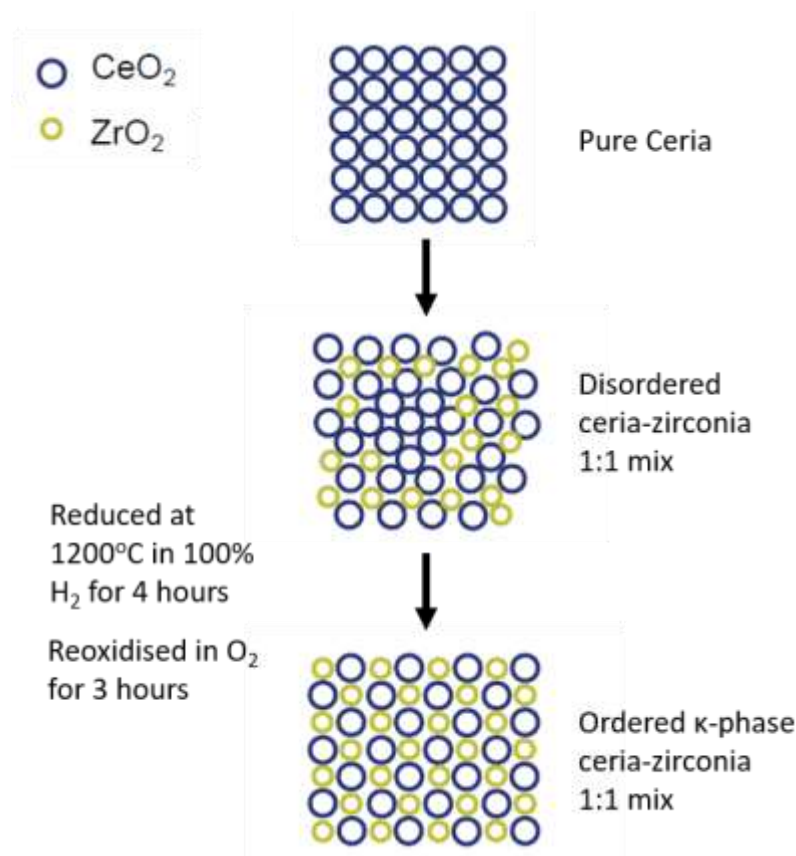


Figure 4.2 The three step process to producing ordered ceria-zirconia. The step from pure ceria to the disordered solid-solution is unknown but by reducing the disordered system and reoxidising; the ordered κ -phase system can be synthesised.

The ordered ceria-zirconia system was made using the disordered $\text{Ce}_{0.5}\text{Zr}_{0.5}\text{O}_2$ as the starting material, Figure 4.2. By reducing this solid-solution at 1200°C in 100% H_2 for 4 hours and then reoxidising in O_2 for 3 hours, the ordered κ -phase system can be synthesised. This κ -phase is the as prepared system that will be seen in later sections.

Three 1 L O_2 gas canisters with a 99.9% purity and isotope composition of ^{17}O (71%), ^{16}O (25.6%) and ^{18}O (3.3%) were bought from Cortecnet (France), this the $^{17}\text{O}_2$ gas used in the labelling of the ceria-zirconia samples in this work. The 0.1% impurities are from: CO , CO_2 , H_2 and N_2 .

4.2.2 Methods

4.2.2.1 $^{17}\text{O}_2$ Straight Exchange and $^{17}\text{O}_2$ Redox Experiments

The $^{17}\text{O}_2$ labelling procedures used here build from previous work done by Maria Vlachou (Johnson Matthey) [50]. The methods have been adapted slightly: in later

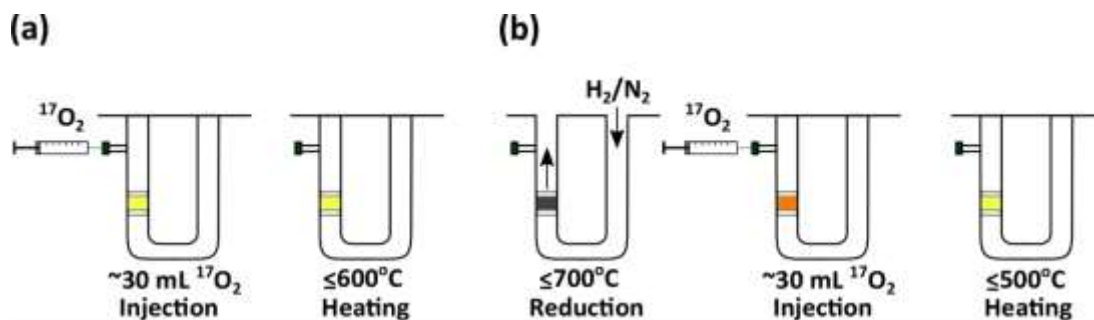


Figure 4.3 The two $^{17}\text{O}_2$ gas labelling experiments used on the ordered and disordered ceria-zirconia samples. a) is the straight exchange method and b) the redox method.

samples straight exchange labelling used shorter temperature hold times after the oxygen injection; the maximum reoxidation temperature used in the redox experiments was also increased up to 500°C (previously 300°C).

0.3 g of the materials mentioned in Section 4.2.1 were placed in a quartz three-port U-tube reactor supported between pieces of ultra-fine grade quartz wool. The top two ports were connected in a through flow fashion to a Quantachrome Autosorb-iQ-C Analyser. The third port, see Figure 4.3, is positioned to the left side of the reactor in this setup and is sealed with a rubber septum (each septum is replaced after a labelling experiment). Two labelling procedures were used on these samples, one in which the samples were reduced and then reoxidised with $^{17}\text{O}_2$ ($^{17}\text{O}_2$ Redox) and another were the $^{17}\text{O}_2$ is directly exchanged with the samples ($^{17}\text{O}_2$ straight exchange).

The $^{17}\text{O}_2$ straight exchange method, Figure 4.3a, is described below. The system was purged with He, a short evacuation then occurs achieving $\sim 0.1 \text{ mmHg}$. The temperature was then increased to 40°C , 30 mL of $^{17}\text{O}_2$ was injected into the system to achieve an average pressure of $\sim 0.7 \text{ atm}$ (read out from the pressure sensor) and a temperature ramp of $20^\circ\text{C}/\text{min}$ increased up to the desired temperature, temperatures used were between 200°C and 500°C . In early experiments the temperature would be held overnight ($\sim 18\text{--}22$ hours), however later tests showed that a 3 hour hold time could achieve the same degree of labelling. This change meant that in later experiments, two samples couple be labelled per day.

The $^{17}\text{O}_2$ redox method, Figure 4.3b, is described below. The system was purged with He, and a temperature ramp of $20^\circ\text{C}/\text{min}$ increased up to the desired temperature,

temperatures used were between 300 °C and 700 °C. A H₂/N₂ gas mix (5%/95%) was flowed in eight incremental injections from 0 to 760 mmHg over the course of ~ 2 hours. The H₂/N₂ flow was removed and the system was evacuated for 20 mins to remove residual H₂ and the system was then cooled back to room temperature. Both sets of samples used here have a characteristic yellow which changes to dark grey/black after this reduction. 30 mL of ¹⁷O₂ was injected into the system to achieve an average pressure of ~0.7 atm and then heated to either 300 °C or 500 °C for an overnight (~18-22 hours) soak.

After either method, the reactors were briefly evacuated to remove the oxygen atmosphere and backfilled with Ar. The reactors were then sealed and transferred to an Ar glovebox where they were packed into NMR rotors and sample vials – all of which were then sealed up with Parafilm for transportation. There is one sample, 700 °C 500 °C redox blue, that for an unknown reason did not uptake much oxygen when being labelled.

Higher labelling temperatures were not used here for two reasons: the rig has a safety limiter at 800 °C and the cell pressure cannot be measured whilst injecting ¹⁷O₂, so risking anything much greater could cause the sealed ports to blowout.

4.2.2.2 Solid-state NMR and other characterisation techniques

Powder XRD was carried out on a Panalytical X-Pert Pro MPD K_{α1} with a Cu source. A 2θ range of 5° to 130° was used with increments of 0.125°. The data was processed using Highscore plus to correct the baselines of the spectra and remove additional noise. TOPAS was used for Rietveld refinements of the ordered ceria-zirconia XRD spectra. Scripts were written in J-edit and included fitting to the κ-phase and intermediate structures produced using scXRD from Urban *et. al.* [48].

Raman spectra were measured on a Renishaw inVia Raman microscope using a 532 nm wavelength DPSS laser operating over a 300 – 4000 cm⁻¹ wavenumber range. A Renishaw CCD using an automated sample stage was used for detection. A x50 Olympus objective lens was used to focus the beam onto the sample, the system was calibrated using a silicon reference. A diffraction grating of 1200 l/mm was used. Each

scan had a 10 s exposure time and 10 scans were recorded for each sample at 10% laser power. The raw data was baselined and fitted using Origin 2019b.

^{17}O single pulse, Hahn echo and T_1 NMR measurements were carried out on a Bruker Avance III HD spectrometer operating at 9.05 T, with the ^{17}O Larmor frequency at 54.24 MHz. Single pulse and Hahn echo measurements were obtained using either a Bruker HX 2.5 mm probe, a Bruker HX 3.2 mm probe or a Bruker HX 4 mm probe with spinning speeds of 30 – 33 kHz, 20 kHz and 12 kHz respectively. $\pi/2$ pulse widths of 2.33 μs and a recycle delay of 45 s were used; 2000 scans were acquired. For the Hahn echo experiments an echo delay of 100 μs was used. For later measurements using the 3.2 mm probe recycle delays of 505 s were used to obtain quantitative data, acquiring 500 scans. ^{17}O T_1 saturation recovery measurements used the same experimental parameters but also used a train of 100 $\pi/2$ pulses followed by a variable τ delay and subsequent $\pi/2$ pulse of 2.33 μs . Delay times between 0.01 and 300 s were used. All ^{17}O chemical shifts were externally referenced against ^{17}O labelled water (H_2^{17}O), $\delta_{\text{iso}} = 0$ ppm for ^{17}O) relative to TMS. All data was processed in Topspin using 100 to 200 Hz of line broadening.

^{91}Zr multi-field measurements were acquired on a Bruker Avance III HD, a Bruker Avance III and a Bruker Avance Neo operating at 400, 500 and 600 MHz with a ^{91}Zr Larmor frequency of 31.20 MHz, 46.49 MHz and 55.79 MHz respectively. A solid-echo experiment was used with a $\pi/2$ pulse of 6 μs , a recycle delay of 0.5 s and an echo delay of 30 μs . 85000 scans were acquired. The samples were loaded into glass tubes fashioned from solution NMR tubes, these tubes were sealed with Parafilm to minimise exposure to air and to keep the sample from falling out into the probe. These tubes were used to avoid background NMR signal from standard Bruker rotors as they are made of zirconia. All data was processed in Topspin using 400 Hz of line broadening.

The DFT calculations utilised the CASTEP17 code which employ a set of plane wave basis sets and Ultrasoft on-the-fly (OTF) pseudopotentials [15]. The calculations performed here used Perdew, Burke and Ernzerhof (PBE) exchange functionals, a k-point spacing of 0.05 and a 900 eV kinetic energy cut-off. This set of parameters allowed convergence of the final energy for single point calculations which can then

be used for geometry optimisation to fully relax the system within its unit cell constraints. The optimised cell is then utilised to obtain NMR shielding tensors, shifts and electric field tensor values via the ‘Magres’ task that resides within the CASTEP17 code [51–53].

4.3 Results

Both the disordered and ordered ceria-zirconia systems have been labelled with $^{17}\text{O}_2$ gas in order to record ^{17}O NMR spectra. To ascertain the effect of replacing a large amount of ^{16}O with ^{17}O a range of characterisation techniques other than ^{17}O NMR must be used. Raman, pXRD and SAXS measurements of the labelled samples and the as prepared samples were compared to glean information on structural changes that may have occurred as a result of the $^{17}\text{O}_2$ labelling experiments. This data will be discussed in the following sections first, before the ^{17}O NMR. The samples are named according to their $^{17}\text{O}_2$ gas labelling conditions. For a redox sample the reduction and

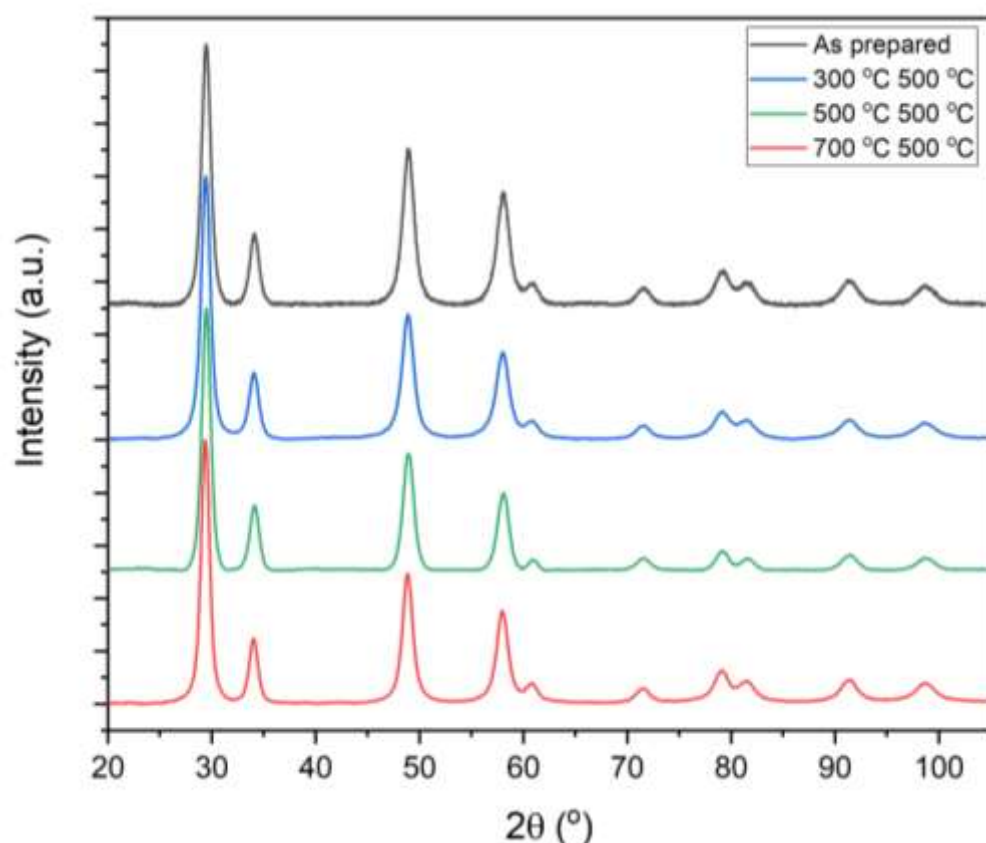


Figure 4.4 PXRD of the as prepared disordered ceria-zirconia and the 300 °C 500°C, 500 °C 500 °C and 700 °C 500 °C $^{17}\text{O}_2$ redox labelled samples.

Table 4.1 Particle size and particle distribution values taken from fits to SAXS data for the as prepared and various redox $^{17}\text{O}_2$ labelled ceria-zirconias.

Sample	Average particle size (nm) \pm 0.3 nm	Particle size distribution (nm) \pm 0.2 nm
CeZrO ₂ as prepared	4.6	2.5
CeZrO ₂ 300°C 500°C	4.4	1.7
CeZrO ₂ 500°C 500°C	4.3	1.7
CeZrO ₂ 700°C 500°C	4.9	2.7

reoxidation temperatures are given i.e. 300 °C 500 °C redox. For a straight exchange sample, the single temperature used is given i.e. 500 °C exchange.

4.3.1 PXRD and SAXS studies of disordered ceria-zirconia

PXRD gives information about the long-range structure of a system and can help identify any major structural changes that may have occurred due to the $^{17}\text{O}_2$ labelling process. Figure 4.4 shows the pXRD spectra of the as prepared disordered CeZrO₂ and the 300 °C 500°C, 500 °C 500 °C and 700 °C 500 °C $^{17}\text{O}_2$ redox labelled samples measured between 20° and 105° 2 θ . Major reflections at 29°, 34°, 49° and 58° 2 θ are present in all of the samples with no alteration in width or position. This would suggest that the labelling process has not affected the bulk structure of the system.

SAXS measurements were also taken to determine the average particle size and particle size distribution across the system. Table 4.1 shows that the average particle size varies randomly within error from 4.6 nm for the as prepared sample, down to 4.3 nm for the 500 °C 500 °C redox labelled sample and up to 4.9 nm for the 700 °C 500 °C redox sample (SAXS fits can be found in Figure A.7). There is no clear pattern in these variations, this data therefore agrees with the pXRD in that $^{17}\text{O}_2$ labelling of the disordered CeZrO₂ does not affect the bulk structure.

4.3.2 Raman studies of disordered ceria-zirconia

The Raman spectra of the as prepared disordered CeZrO₂ and a series of $^{17}\text{O}_2$ redox labelled samples are shown in Figure 4.5. Two significant regions are marked out, both of which give an indication to the small structural changes caused by the $^{17}\text{O}_2$ labelling process. The F_{2G} band represents the symmetrical stretching of the CeO₈ cube

and for the as prepared sample is observed at 474 cm^{-1} . In pure fluorite phase CeO_2 it is observed at 464 cm^{-1} [29]. This blue shift in the solid-solution is a result of the average particle size decrease as Cerium has a van der Waals radius of 0.181 nm whereas Zirconium has a radius of 0.16 nm . In the labelled disordered CeZrO_2 samples a red shift of the $\text{F}_{2\text{G}}$ band by 8 cm^{-1} to 466 cm^{-1} is observed. This indicates an increase in the presence of Ce^{3+} i.e. an increase in average particle size, Ce^{3+} radius is 0.114 nm whereas Ce^{4+} radius is 0.097 nm . This alludes that the samples have not fully

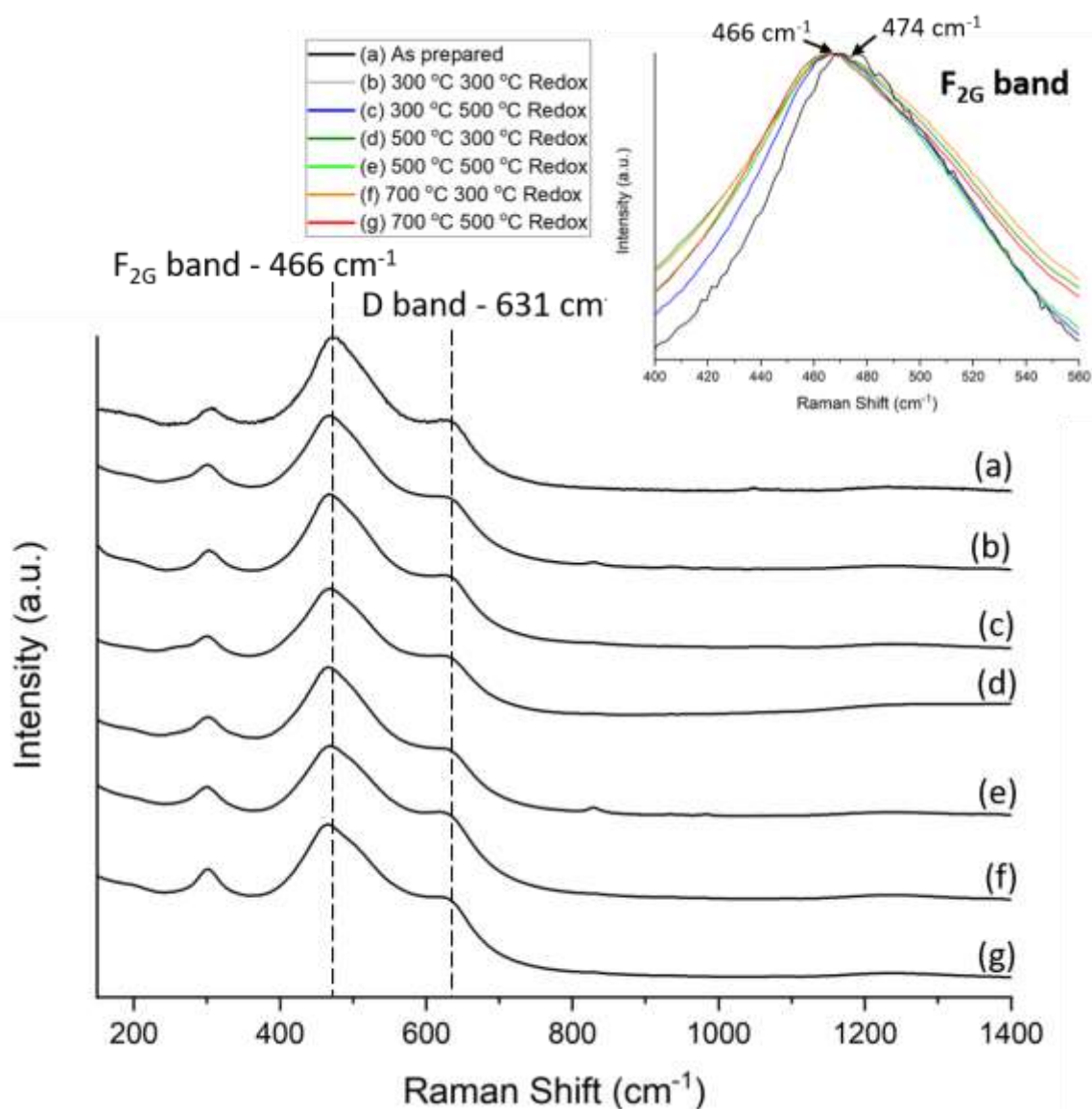


Figure 4.5 Raman spectra of the as prepared sample of (a) the as prepared disordered CeZrO_2 and a series $^{17}\text{O}_2$ redox labelled CeZrO_2 (b) $300\text{ }^{\circ}\text{C}$ $300\text{ }^{\circ}\text{C}$, (c) $300\text{ }^{\circ}\text{C}$ $500\text{ }^{\circ}\text{C}$, (d) $500\text{ }^{\circ}\text{C}$ $300\text{ }^{\circ}\text{C}$, (e) $500\text{ }^{\circ}\text{C}$ $500\text{ }^{\circ}\text{C}$, (f) $700\text{ }^{\circ}\text{C}$ $300\text{ }^{\circ}\text{C}$ and (g) $700\text{ }^{\circ}\text{C}$ $500\text{ }^{\circ}\text{C}$. The inset shows the expanded region of the $\text{F}_{2\text{G}}$ band.

reoxidised after the labelling process. There is also an average broadening of the F_{2G} band after $^{17}\text{O}_2$ labelling. The as prepared sample has a FWHM of 89 cm^{-1} whereas there is an average FWHM of 113 cm^{-1} for the redox labelled samples, this is likely also a result of the increased amount of Ce^{3+} . An average FWHM had to be measured for all the labelled samples as there is no consistent broadening trend across the series.

The other marked out region in the Raman spectra is the defect or D-band. This band represents vibrations from oxygen vacancies [54,55], intrinsic Frenkel defects [33,54,56,57] and other extrinsic defects [57]. In fluorite phase ceria this region usually spans between $540\text{--}600\text{ cm}^{-1}$ [58]. Again a blue shift of this region is seen in the solid solution CeZrO_2 . In the $^{17}\text{O}_2$ labelled samples no shift of this band is seen, however an average broadening of the D-band by $\sim 10\text{ cm}^{-1}$ is observed which is a result of an increase in defect concentration, this agrees with there being an increase in Ce^{3+} as shown by the shift of the F_{2G} band. These changes to the defect concentration and amount of Ce^{3+} have little impact on the overall structure of the system, it is therefore reasonable to treat the labelled disordered CeZrO_2 as similar if not the same as the unlabelled sample when discussing the ^{17}O NMR.

4.3.3 ^{17}O MAS NMR studies of disordered ceria-zirconia

As the previous two sections have shown, $^{17}\text{O}_2$ labelling using the redox method does not cause any major structural changes to the disordered CeZrO_2 . To test which regions of the CeZrO_2 structure exchange oxygen first, a series of redox experiments were done, using $300\text{ }^\circ\text{C}$, $500\text{ }^\circ\text{C}$ and $700\text{ }^\circ\text{C}$ reduction steps and $300\text{ }^\circ\text{C}$ and $500\text{ }^\circ\text{C}$ reoxidation steps. Figure 4.6 shows the ^{17}O NMR spectra of these experiments along with the spectrum of an empty rotor for comparison. The rotor resonance appears at 389 ppm which coincides with the zirconia region of the disordered CeZrO_2 . In all of the ^{17}O NMR spectra the rotor will be contributing to the signal of this region, however in the samples that have better labelling this contribution will be far less significant. At the lowest redox temperature, $300\text{ }^\circ\text{C}$, very little if any ^{17}O uptake is observed, however as the reoxidation temperature is increased to $500\text{ }^\circ\text{C}$ multiple resonances become visible. The resonance at 389 ppm is assigned to zirconium coordinated oxygen, the two very broad central resonances at 551 ppm and 688 ppm are assigned to oxygen coordinated to 3 zirconium and 1 cerium, and 1 zirconium and

3 cerium respectively. The final distinct resonance at 857 ppm is assigned to cerium coordinated oxygen. The relative broadness of these resonances arises from the total disorder of these systems, this is highlighted in the central region where many variations of cerium and zirconium coordination's as well as their adjacent coordination combinations are present.

By reducing the reoxidation temperature back down to 300 °C and increasing the reduction temperature to 500 °C an assessment of which regions of the system release oxygen first can be determined. The ^{17}O labelling is much improved compared to the 300 °C 300 °C redox sample, the zirconium coordinated oxygen region is far more prominent and evidence of a portion of the mixed cerium-zirconium coordinated region can be seen. This occurs because the higher reduction temperature opens up

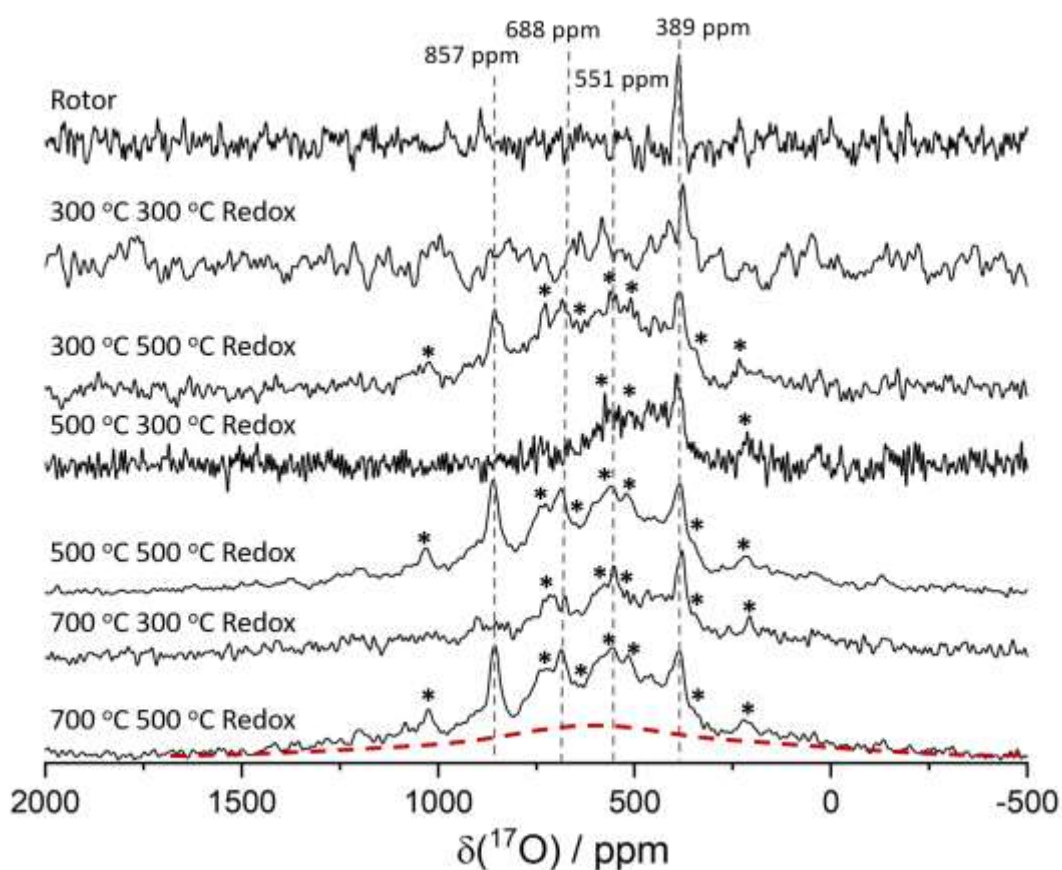


Figure 4.6 ^{17}O MAS NMR of a range of $^{17}\text{O}_2$ redox labelled disordered CeZrO_2 . A 4 mm zirconium rotor spectrum has been added for comparison with the zirconium coordinated oxygen region of the samples. These data were acquired in a 4 mm zirconia rotor with $\nu_r = 14 \text{ kHz}$ on a spectrometer operating at 14.1 T. Asterisks (*) denote spinning sidebands. The red dashed line marks out the broad Ce^{3+} site.

additional oxygen sites. The spectrum mostly contains zirconium coordinated oxygen sites, even when reoxidising at 300 °C the ^{17}O is taken up by these sites which now readily accept oxygen. This is a key property of a material that has an OSC, particularly when used in a catalytic converter. After being exposed to the high temperature of the gasses from the engine, in oxygen rich conditions the CeZrO_2 will reabsorb the oxygen as demonstrated in the 500 °C 300 °C redox spectrum. Increasing the reoxidation temperature to 500 °C produces a similar spectrum to the 300 °C 500 °C redox spectrum. The key difference here is that the S/N is greatly improved as a considerable amount of ^{17}O has been incorporated into the sample.

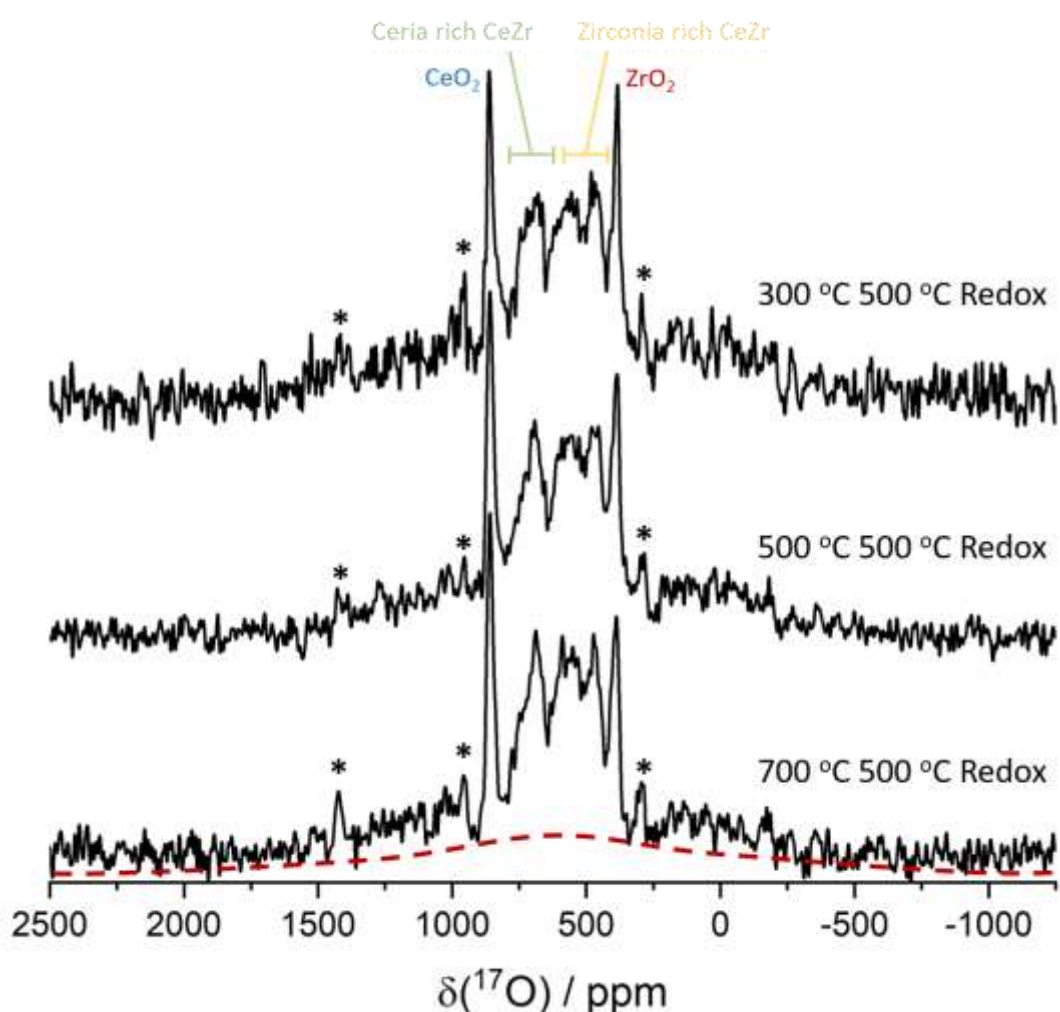


Figure 4.7 ^{17}O MAS NMR of $^{17}\text{O}_2$ redox labelled disordered CeZrO_2 . These data were acquired in a 2.5 mm zirconia rotor with $\nu_r = 31 \text{ kHz}$ on a spectrometer operating at 9.4 T. Asterisks (*) denote spinning sidebands. The red dashed line marks out the broad Ce^{3+} site.

For the highest reduction temperature, 700 °C, at the 300 °C reoxidation step a similar result is seen to the 500 °C 300 °C experiment. However, this time more of the mixed coordination oxygen has exchanged, the S/N is also vastly improved. The final redox step, 700 °C 500 °C, shows an almost identical spectrum to the 500 °C 500 °C spectrum. This indicates that while using a high temperature reduction step to reduce the oxygen sites in the system is important for ^{17}O uptake, the limiting factor is the reoxidation temperature. This is consistent with temperature programmed reduction (TPR) studies [59,60]. At the higher combinations of $^{17}\text{O}_2$ redox labelling, 500 °C 500 °C and 700 °C 500 °C, a broad site spanning ~2000 ppm between 1500 ppm and -500 ppm becomes visible. This can be tentatively assigned to Ce^{3+} as its paramagnetic nature would lead to a very broad resonance.

The majority of the spectra in Figure 4.6 are obscured by spinning sidebands making it difficult to be certain as to whether an assignment is genuine or just a sideband of one of the more prominent resonances. This was combatted by switching to a 2.5 mm probe, spinning at 31 kHz and acquiring the data at a weaker magnetic field (9.4 T) such that the sidebands now appear on the sides of the main resonances. Figure 4.7 shows the result of these changes. The CeO_2 and ZrO_2 resonances are still very prominent, but what is seen now is that there is a distinct mixed region in the centre. The resonances about ~ 700 ppm correspond to ceria rich oxygen coordination's and the resonances about ~550 ppm correspond to zirconia rich oxygen coordination's. This is due deshielding from the larger Cerium nuclei and shielding due to the smaller Zirconium nuclei.

4.3.4 PXRD and SAXS studies of ordered ceria-zirconia

The pXRD of the κ -phase ceria-zirconia and a range of $^{17}\text{O}_2$ straight exchange labelled samples are shown in Figure 4.8. It is in stark contrast to Figure 4.4, the reflections are far narrower which indicates a considerably more crystalline structure. The major indicator for this system being in the κ -phase is the presence of the superstructure [61] reflections seen at 36.7° and $45.8^\circ 2\theta$. For the straight exchange process there appears to be very little change to the reflections and therefore structure of the κ -phase ceria-

Table 4.2 Particle size and particle distribution values taken from fits to SAXS data, Figure A.8, for the as prepared and various straight exchange $^{17}\text{O}_2$ labelled κ -phase ceria-zirconia. The two columns indicate the two different size distributions present in the material.

Sample	Average particle size (nm) \pm 0.3 nm		Particle size distribution (nm) \pm 0.2 nm	
κ -phase as prepared	40.3	12.6	24.3	18.3
κ -phase 200 °C exchange	39.0	13.7	23.9	17.2
κ -phase 300 °C exchange	39.7	11.8	25.3	19.7
κ -phase 350 °C exchange	39.6	10.2	25.4	18.0
κ -phase 400 °C exchange	37.6	14.9	26.7	18.4

zirconia. The SAXS data echoes this conclusion. Table 4.2 shows the average particle size and particle distribution of the κ -phase ceria-zirconia and the labelled samples. Two distributions and sizes are present in the κ -phase, the smaller average particle size likely belonging to more zirconium coordinated sites and the larger containing

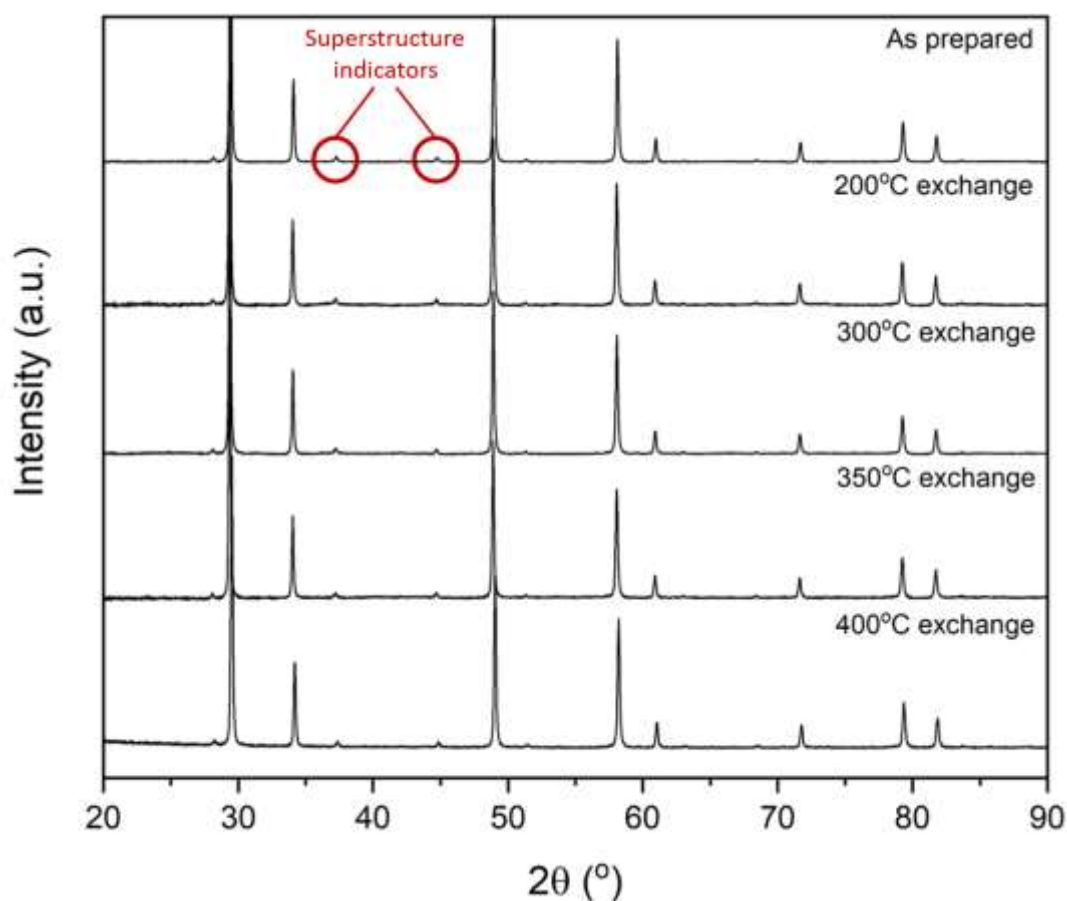


Figure 4.8 PXRD of the as prepared κ -phase ceria-zirconia and the 200 °C, 300°C, 350 °C and 400 °C $^{17}\text{O}_2$ straight exchanged labelled samples.

sites with more cerium. There is no clear trend for the changes in either the particle size or size distribution, as the systems are designed to experience temperatures in excess of 1000 °C this is to be expected. Much like the disordered systems there is likely no major structural change after the $^{17}\text{O}_2$ labelling process. The average particle size does show that the κ -phase is $\sim 10\times$ larger than the disordered system, this is a result of the high temperatures it has been exposed to during synthesis. This loss of surface area and therefore OSC is however outweighed by the ordering process, thus the κ -phase still possesses superior OSC.

A feature unique to the SAXS spectrum of the κ -phase ceria-zirconia is a small ‘peak’ at $\sim 0.08 \text{ \AA}^{-1}$, Figure 4.9. It is hypothesized to be a Bragg peak coming from a plane of the κ -phase structure and is analogous to corrugated oxygen rows seen in V_2O_5 gels and intermediate phase ceria-zirconia [47,62,63]. By investigating the predicted pXRD spectrum of the κ -phase crystal structure [48] this Bragg peak can be attributed to the $\langle 011 \rangle$ reflection plane. The pXRD reflection is not visible due to its low 2θ angle of 2° and very low predicted intensity.

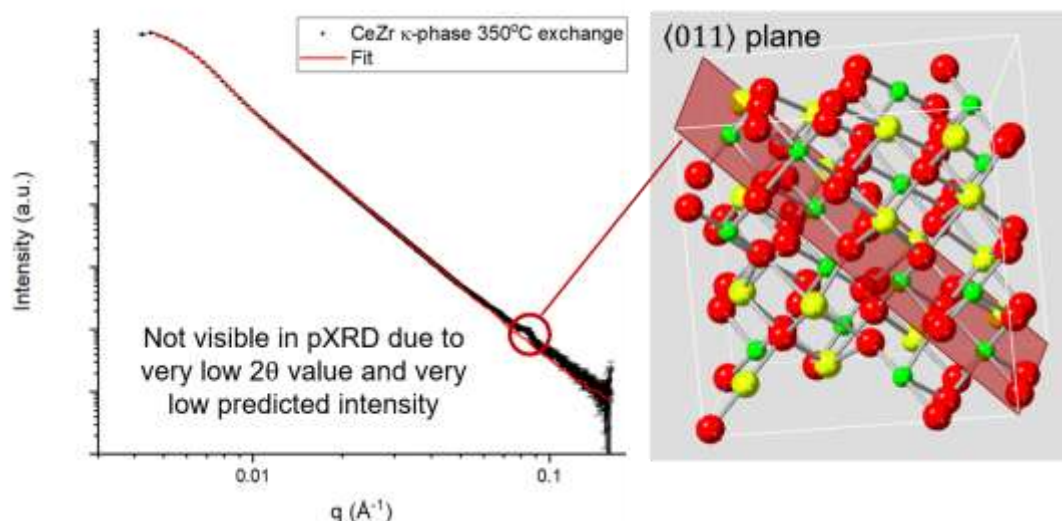


Figure 4.9 A SAXS spectrum of the 350 °C $^{17}\text{O}_2$ straight exchanged sample highlighting the Bragg peak at $\sim 0.08 \text{ \AA}^{-1}$. The right of the figure shows the plane that this peak is attributed to.

4.3.5 Raman study of straight exchange labelled κ -phase $\text{Ce}_2\text{Zr}_2\text{O}_8$

The ordered κ -phase $\text{Ce}_2\text{Zr}_2\text{O}_8$ system also has a very different Raman spectrum to that of the disordered system. Figure 4.10 shows a comparison of the two, what is immediately noticeable is that when conducting the experiment the S/N of the κ -phase $\text{Ce}_2\text{Zr}_2\text{O}_8$ is far greater compared to the ordered system. This is a result of the increased coherence of energy changes the photons experience, leading to more coherent and stronger stokes and anti-stokes scattering. The κ -phase $\text{Ce}_2\text{Zr}_2\text{O}_8$ has a far more resolved spectrum and as a result the $\text{F}_{2\text{G}}$ and defect band have been resolved into multiple bands. This data has therefore been normalised to the band at 274 cm^{-1} . The increased resolution and narrower bands occur due to the increased crystallinity of the κ -phase $\text{Ce}_2\text{Zr}_2\text{O}_8$ which is analogous to the pXRD data. The bands at 274 cm^{-1} , 440 cm^{-1} and 600 cm^{-1} are indicative of the κ -phase [64–66]. In a pure κ -phase system, containing 96 atoms per unit cell, 144 active modes are expected 24A_g , 24E_g , 24E_g

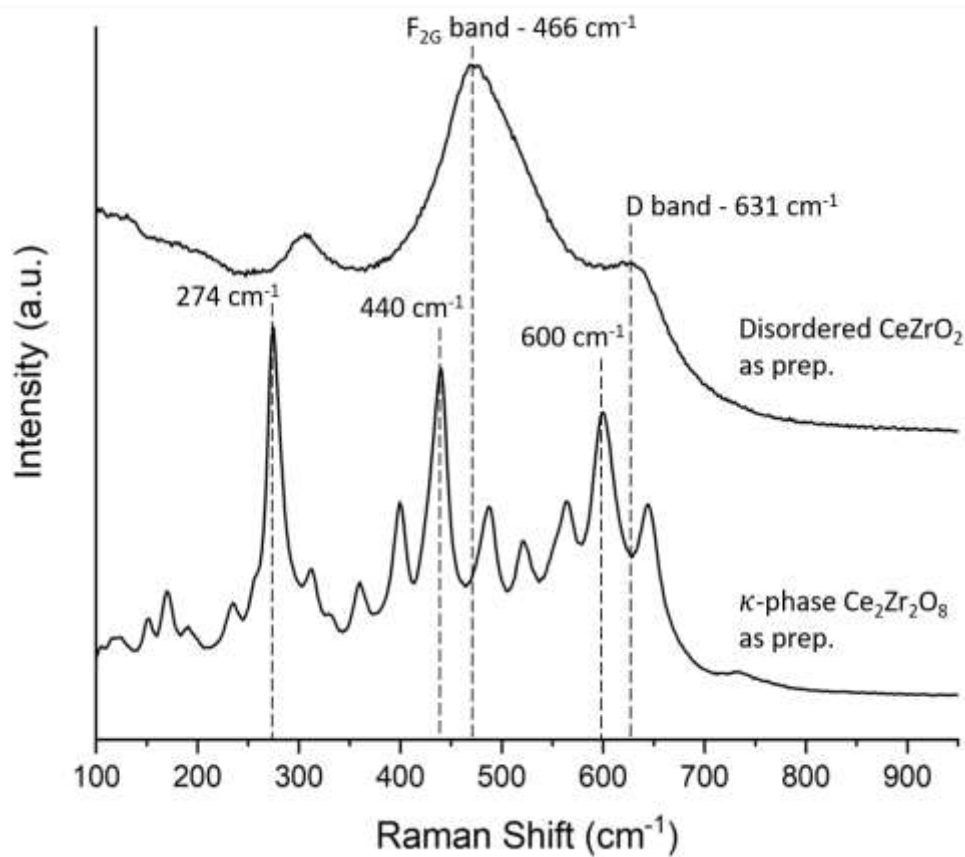


Figure 4.10 Comparison of Raman spectra of the disordered CeZrO_2 and the ordered κ -phase $\text{Ce}_2\text{Zr}_2\text{O}_8$.

and 72F. However due to similar species within the unit cell there is significant overlap of these bands [67–69].

The changes to the κ -phase $\text{Ce}_2\text{Zr}_2\text{O}_8$ must also be investigated by Raman spectroscopy. Figure 4.11 shows the difference spectrum of the as prepared sample with $^{17}\text{O}_2$ straight exchange labelled samples. For the 200 °C labelled sample it can be seen that all of the Raman bands have narrowed by an average of $\sim 3 \text{ cm}^{-1}$. The narrowing is likely a result of the labelling treatment very slightly increasing the crystallinity of the system. As the temperature the system is exposed to increases this narrowing becomes more prominent with peak width reducing by 4 cm^{-1} , 5 cm^{-1} and 6 cm^{-1} for 300 °C, 350 °C and 400 °C respectively. None of the major Raman bands disappear or are altered substantially so it can be said that the straight exchange method maintains the κ -phase structure.

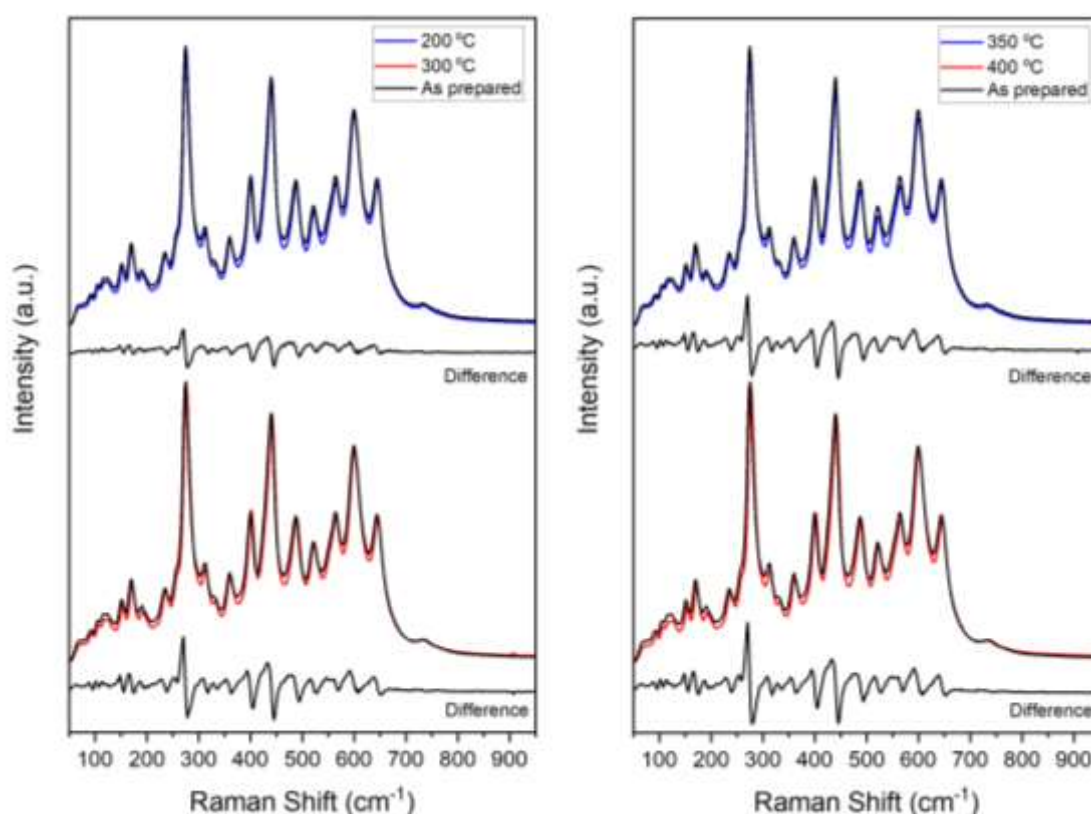


Figure 4.11 Comparison of the as prepared κ -phase $\text{Ce}_2\text{Zr}_2\text{O}_8$ against a range of $^{17}\text{O}_2$ straight exchange labelled samples using temperatures of 200 °C, 300 °C, 350 °C and 400 °C.

4.3.6 ^{17}O MAS NMR studies of κ -phase $\text{Ce}_2\text{Zr}_2\text{O}_8$

A comparison of the ^{17}O MAS NMR of the disordered CeZrO_2 and the κ -phase $\text{Ce}_2\text{Zr}_2\text{O}_8$ is shown in Figure 4.12. This figure is purely to give a direct comparison of the analogues between the two systems. The individual regions will be investigated in greater detail in later sections. The κ -phase system also has the three distinct regions observed in the disordered system, the ceria, ceria-zirconia and zirconia region. Due to the very ordered κ -phase structure however the resonances are far narrower and individual peaks are now resolved in each region.

The initial ^{17}O MAS NMR of the low temperature straight exchange κ -phase $\text{Ce}_2\text{Zr}_2\text{O}_8$ were acquired in a 4 mm rotor as a way to combat the poor S/N. To avoid spinning

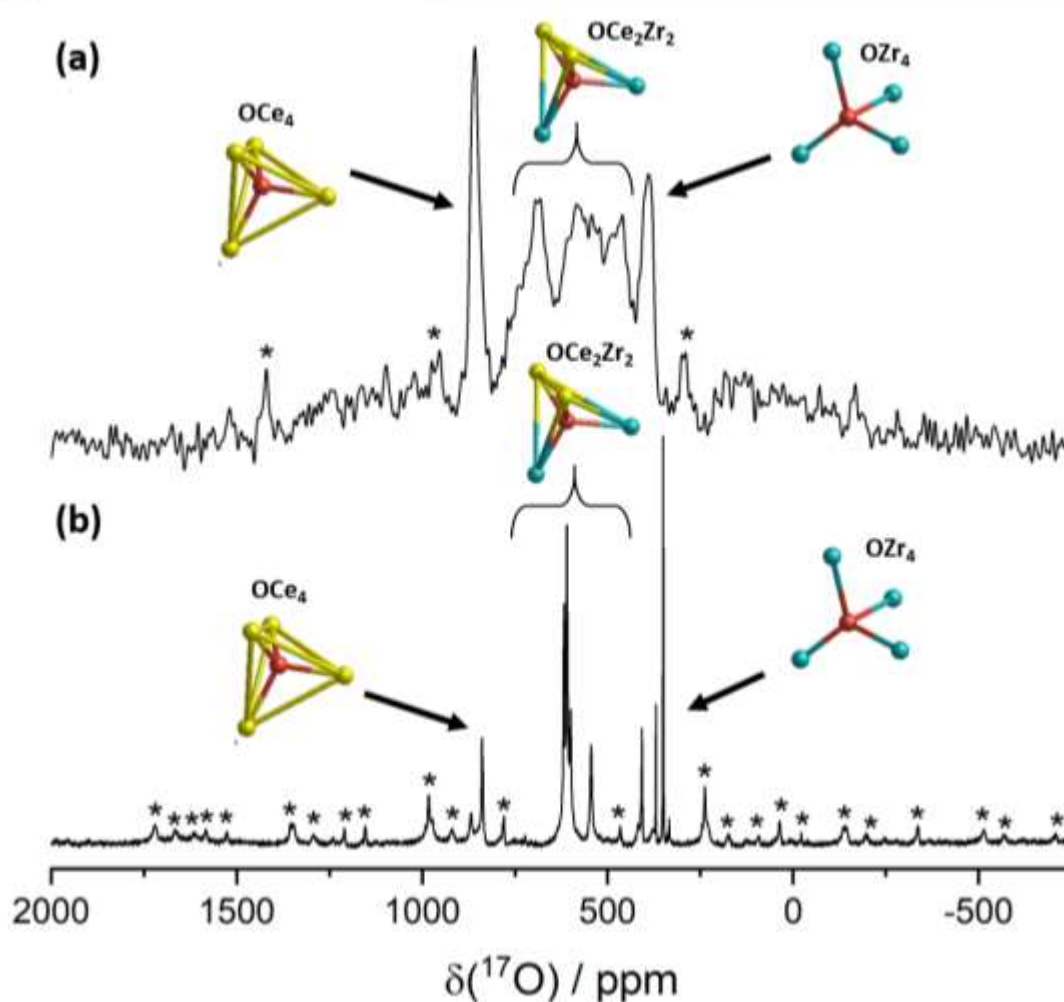


Figure 4.12 ^{17}O MAS NMR comparison of (a) the disordered CeZrO_2 and (b) the κ -phase $\text{Ce}_2\text{Zr}_2\text{O}_8$. Each spectrum was measured at 9.4 T but (a) was acquired in a 2.5 mm rotor spinning at 31 kHz and (b) in a 3.2 mm rotor spinning at 20 kHz.

sidebands overlapping with primary resonances a relatively slow spinning speed of 8 kHz has been used. Later experiments used spinning speeds of 20 kHz or greater.

A series of low temperature straight exchange κ -phase $\text{Ce}_2\text{Zr}_2\text{O}_8$ ^{17}O MAS NMR spectra are shown in Figure 4.13, these experiments were done to assess the way in which oxygen is incorporated into the system. As is to be expected from TPR measurements [70] at lower labelling temperatures only a small amount ^{17}O is incorporated into the system, this is reflected in the poor S/N. As the labelling temperature is increased from 200 °C all the way up to 400 °C the S/N increases. What is important to note is that there is negligible variation of the relative intensities of each resonance across the three regions. This means that there is non-selective oxygen

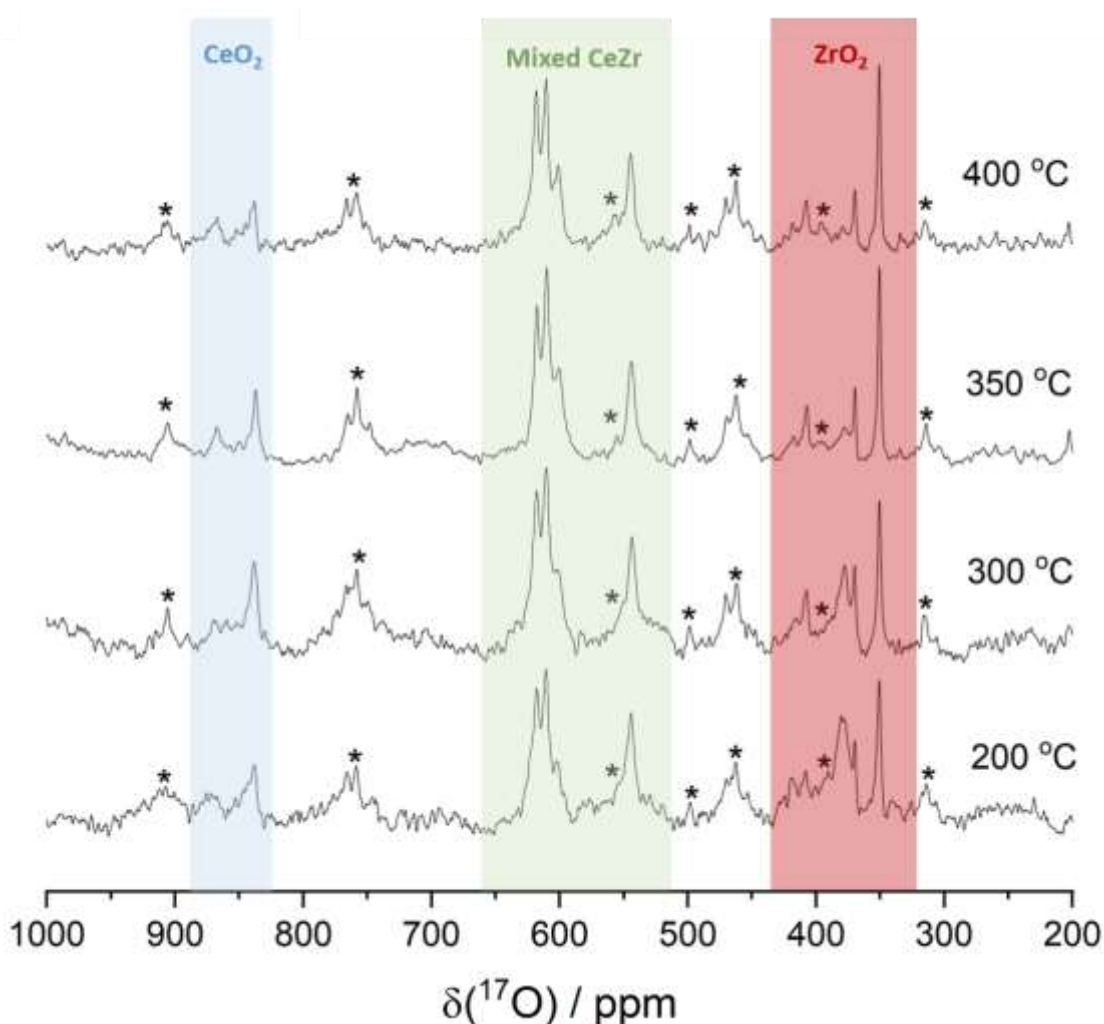


Figure 4.13 ^{17}O MAS NMR spectra of $^{17}\text{O}_2$ straight exchange labelled κ -phase $\text{Ce}_2\text{Zr}_2\text{O}_8$. These were acquired in a 4 mm rotor spinning at 8 kHz in a 9.4 T field. A recycle delay of 45 s was used. Asterisks denote spinning sidebands.

incorporation at low labelling temperatures and therefore at lower temperatures in a catalytic converter. This implies that as oxygen is absorbed at the material surface it is drawn into the structure and spreads out evenly, thus allowing further oxygen incorporation.

4.3.7 ^{17}O MAS NMR studies of redox labelled κ -phase $\text{Ce}_2\text{Zr}_2\text{O}_8$

The previous section shows that at lower labelling temperatures the κ -phase $\text{Ce}_2\text{Zr}_2\text{O}_8$ non-selectively incorporates ^{17}O , however at higher temperatures this behaviour changes. In Figure 4.14 three spectra, focussed about the ceria region, of labelled samples are shown at temperatures of 500 °C 500 °C redox, 600 °C straight exchange and 700 °C 500 °C redox. A notable change is seen as the temperature increases; there is the increase of intensity of an additional resonance at 840 ppm. This is evidence that

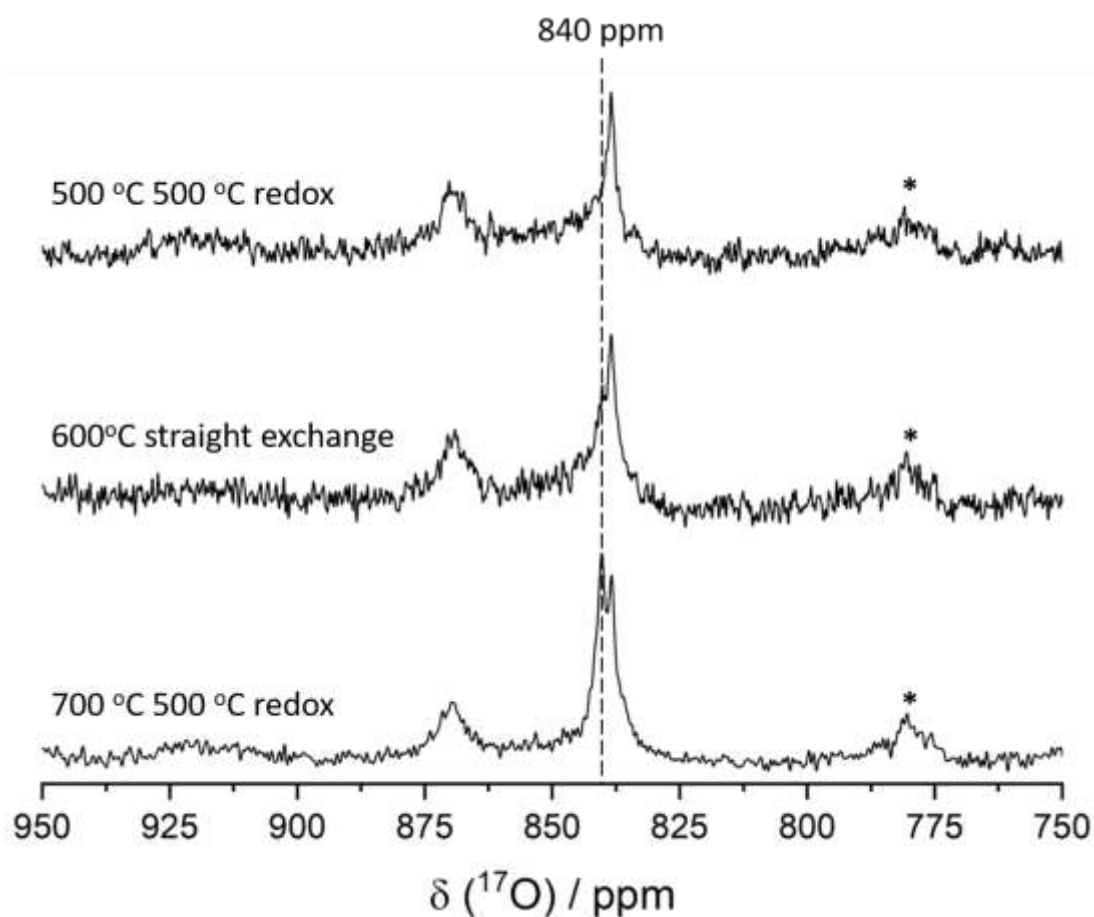


Figure 4.14 The ceria region of the κ -phase $\text{Ce}_2\text{Zr}_2\text{O}_8$ showing the increasing intensity of the resonance at 840 ppm. This was acquired on a spectrometer operating at 9.4 T in a 3.2 mm rotor with spinning speeds of 20 kHz. Asterisks denote spinning sidebands.

one of the ceria sites is more tightly bound in the structure and thus exchanges last. There are two unique OCe_4^+ sites in the κ -phase $\text{Ce}_2\text{Zr}_2\text{O}_8$ crystal structure with average Ce-O bond lengths of 2.23 Å and 2.36 Å. The former site is now ascribed to the resonance at 840 ppm.

The rest of this section will more completely investigate the resonances seen in the κ -phase $\text{Ce}_2\text{Zr}_2\text{O}_8$ spectrum. Figure 4.15 shows a 700 °C 500 °C redox labelled κ -phase $\text{Ce}_2\text{Zr}_2\text{O}_8$ along with simulations of each resonance and black bars showing isotropic shift positions predicted from DFT calculations. The calculations in this case employed Hubbard +U corrections. This was to ensure that the overestimation of the covalency of the Ce-O bond was avoided. This overestimation arises from over hybridisation of the Ce 4f orbitals. This method has been seen throughout the literature [71–73] and effectively alters the energy shift for Ce. The new on-the-fly (OTF) pseudopotentials are shown below:

Ce 2|2.1|9|10|11|50U:60:51:43:52L(qc=6)

Ce 2|2.1|9|10|11|50U:60:51:43U@0.41435U@0.41435:52L(qc=6)

the unmodified potentials are at the top and the modified at the bottom. The Hubbard correction of 0.41435 Ha that was used, comes from a calibration against 4 purely diamagnetic systems, ZnO, SiO₂, Na₂WO₄ and Na₂MoO₄ [74]. This model was then applied to the ideal κ -phase system CIF file produced by Urban *et. al.* [48].

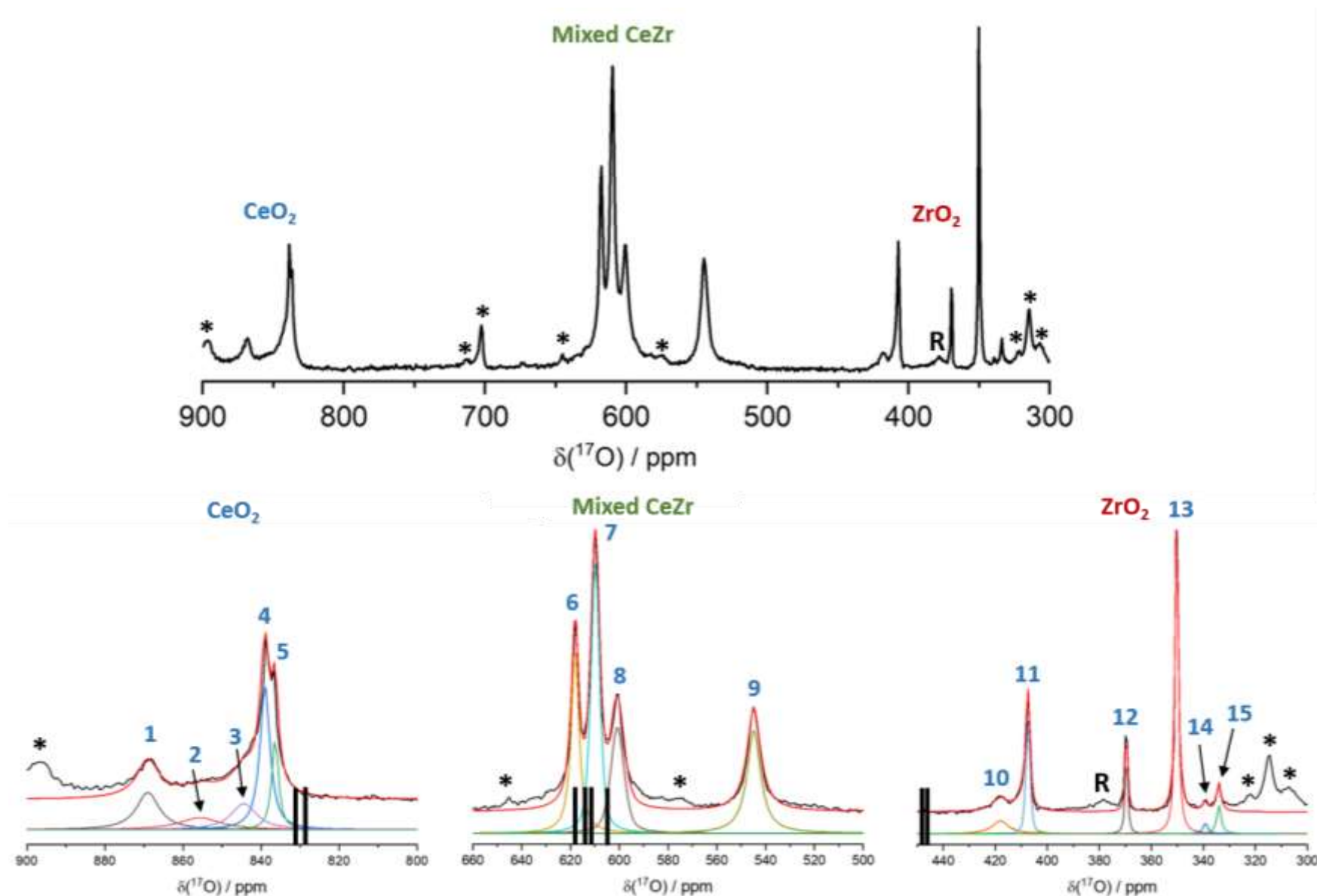


Figure 4.15 (Top) ^{17}O MAS NMR spectrum of $^{17}\text{O}_2$ 700 $^\circ\text{C}$ 500 $^\circ\text{C}$ redox labelled κ -phase $\text{Ce}_2\text{Zr}_2\text{O}_8$. (Bottom) The ceria, mixed ceria-zirconia and zirconia regions of the κ -phase spectrum with DMfit simulations in red and the convolutions of these simulations in various colours offset below. This spectrum was obtained in a 3.2 mm rotor spinning at 20 kHz at a field of 9.4 T. The black bars are predicted isotropic shifts from DFT calculations. Asterisks denote spinning sidebands and the **R** is the signal from the rotor.

Resonance no.	Resonance region	δ_{iso} (ppm)	Calculated shift (ppm)	T_1 (s)
1	Ceria	869	-	94 ± 20
2	Ceria	856	-	-
3	Ceria	844	-	-
4	Ceria	840	833	60 ± 6
5	Ceria	838	828	69 ± 7
6	Ceria-zirconia	618	619	71 ± 6
7	Ceria-zirconia	610	614	62 ± 6
8	Ceria-zirconia	601	612	57 ± 6
9	Ceria-zirconia	545	606	92 ± 11
10	Zirconia	418	450	23 ± 6
11	Zirconia	407	450	100 ± 7
12	Zirconia	370	-	84 ± 8
13	Zirconia	350	-	71 ± 7
14	Zirconia	339	-	-
15	Zirconia	334	-	60 ± 6

Table 4.3 A list of the δ_{iso} , calculated shifts from DFT and relaxation times of the resonances from the κ -phase $\text{Ce}_2\text{Zr}_2\text{O}_8$. The resonance numbers match to the numbers seen in Figure 4.15.

In the ceria region of the spectrum only two unique ceria sites are predicted, these closely match the two sites at 840 ppm and 838 ppm, Table 4.3. These resonances are narrow at ~ 2 ppm, this is a result of the low variation in Ce-O bond lengths, see Figure

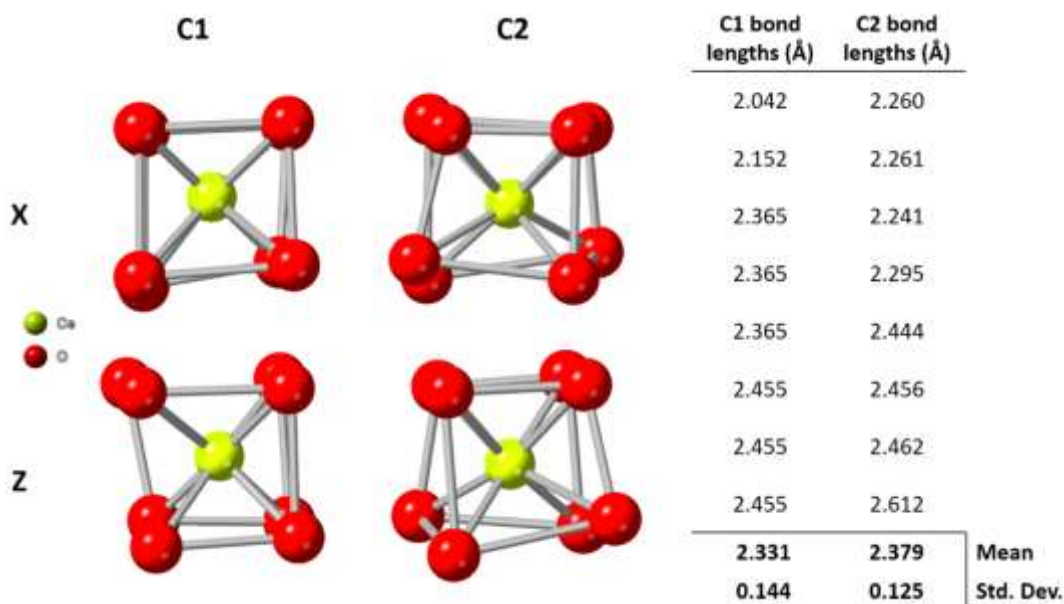


Figure 4.16 The two unique ceria sites, C1 and C2, in the κ -phase structure. The top row shows the x-axis orientation and the bottom row the z-axis. The table on the right shows the Ce-O bond lengths as well as the mean and standard deviation of each site.

4.16. The additional resonances at 869, 856 and 844 ppm are not predicted and are likely to arise from interstitial oxygen defects within the structure. The ceria-zirconia region has 4 resonances present at 618, 610, 601 and 545 ppm. Four shifts are predicted and the former 3 very closely agree at 619, 614 and 612 ppm. The fourth prediction however is at 606 ppm, similar to the other three but 61 ppm away from the experimental value. This implies that there is a greater coordination of zirconia around this oxygen on average throughout the system. The other three resonances differ by ~ 9 ppm which can be attributed to differences in the average bond length of these unique sites. The zirconia region accounts for the majority of the resonances in this spectrum. The calculated shifts don't agree with any of the experimental shifts which is likely a result of the +U corrections. Only two shifts are predicted similarly to the

κ -phase $\text{Ce}_2\text{Zr}_2\text{O}_8$

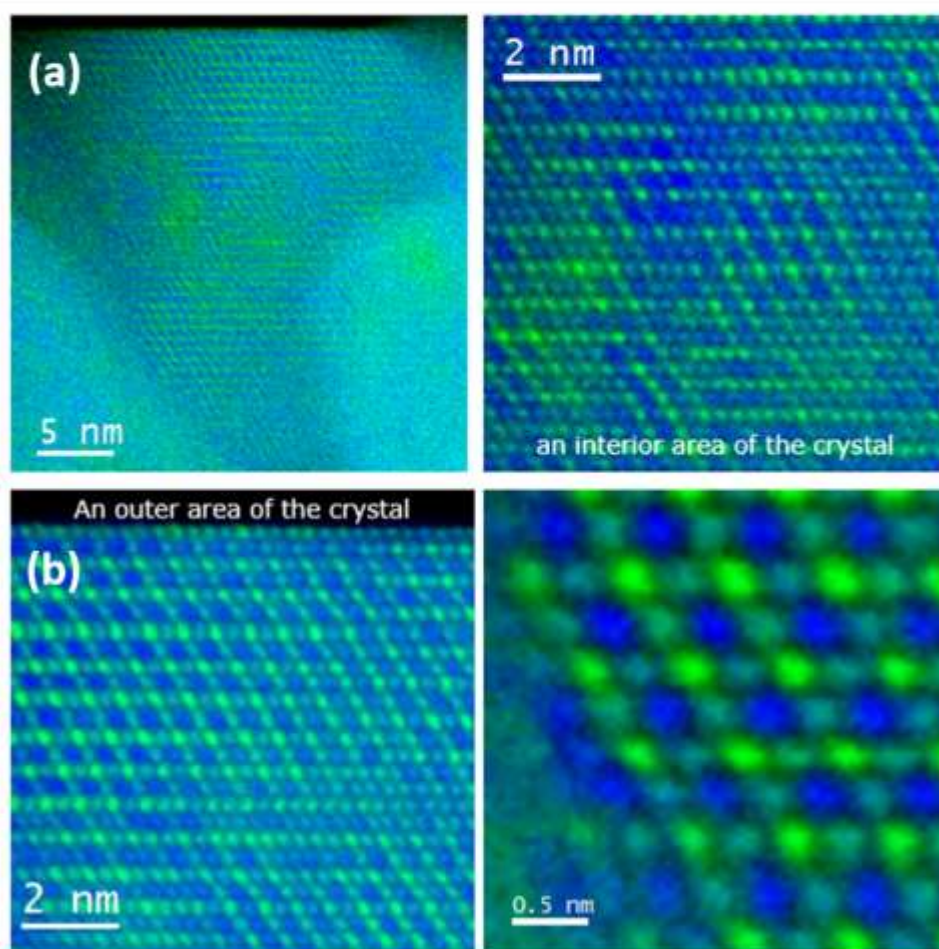


Figure 4.17 EELS images of the κ -phase $\text{Ce}_2\text{Zr}_2\text{O}_8$. (a) shows the interior of the crystal (b) shows the exterior.

ceria region, whereas 6 resonances are present in the spectrum. The difference in shifts are quite large ~ 50 and 20 ppm between them. These shift differences likely arise from the zirconia coordinated oxygen presenting different morphology like structure within the system. This means that some of these sites behave similarly to tetragonal, cubic or monoclinic zirconia. It is not reasonable to assign the morphologies to any individual resonance as they may only appear to have these structures randomly throughout the system. There are also smaller shift differences in two cases, the 11 ppm difference between the resonances at 418 ppm and 407 ppm and the 5 ppm difference between the resonances at 339 ppm and 334 ppm. These smaller shifts are analogous to the ceria region and are the result of interstitial oxygen defects. This phenomena of the less intense zirconia resonances having an accompanying defect site may also occur with the resonance at 370 ppm, however this cannot be confirmed due to the overlapping signal from the rotor.

T_1 relaxation times for the majority of the resonances in the κ -phase $\text{Ce}_2\text{Zr}_2\text{O}_8$ are shown in Table 4.3. As might be expected for such an ordered system the relaxation times are relatively long, ranging from 23 - 100 s. There doesn't appear to be any notable trend across the three regions of the system with regard to relaxation, this may be due to the oxygen mobility being fairly uniform in the system.

Some of the additional resonances in the spectrum may also be explained with electron energy loss spectroscopy (EELS). EELS is a technique by which a material is hit with an incident beam of electrons with a narrow range of known kinetic energies. The electrons will undergo inelastic scattering and the energy loss can then be measured via an electron spectrometer. When this technique is used on the κ -phase $\text{Ce}_2\text{Zr}_2\text{O}_8$ it would be expected that a uniform image is produced that would represent each OCe_4 and OZr_4 oxygen coordination. In Figure 4.17 (b) this uniformity can be seen for the exterior of the system, however in (a) the interior is not uniformly ordered. This is likely due to the reduction temperature used to make the κ -phase $\text{Ce}_2\text{Zr}_2\text{O}_8$ not being high enough to achieve a pure κ -phase like that seen in work by Achary *et. al.* [47]. In their work they used a temperature of 1673 K whereas here 1200 K was used. This lack of total uniformity explains the additional zirconia and ceria resonances as now many very stable regions that are richer in either cerium or zirconium coordinated

Table 4.4 The percentage contribution from the two structures used in Rietveld refinements of a series of κ -phase $\text{Ce}_2\text{Zr}_2\text{O}_8$ with varying levels of oxidation.

κ -phase Sample	Rietveld refinement	
	κ -phase	Intermediate
As prepared (Yellow)	96.7	3.3
600 °C straight exchange (Yellow)	91.8	8.2
700 °C 500 °C (Green)	75.1	24.9
Reduced 700 °C 500 °C (Blue)	52.0	48.0

oxygen are present. This will also be addressed when analysing pXRD spectra via Rietveld refinements in the next section.

4.3.8 Oxidation comparison of ordered ceria-zirconia

It has been recorded by Urban *et. al.* [48] that the κ -phase $\text{Ce}_2\text{Zr}_2\text{O}_8$ system is yellow and that the pyrochlore $\text{Ce}_2\text{Zr}_2\text{O}_7$ is black. These colours are consistent with a series of samples with different levels of oxidation, Figure 4.18. Unlike the disordered system, a stable reduced κ -phase can be produced as high temperatures are required for the system to incorporate oxygen even when left in a normal atmosphere. The colours give a good indication of the oxidation state; however, a more rigorous approach to determine the amount of oxygen present in this system can be better achieved using Rietveld refinements of pXRD.

A Rietveld refinement of the 700 °C 500 °C redox blue κ -phase $\text{Ce}_2\text{Zr}_2\text{O}_8$ is shown in Figure 4.19. This was a two phase refinement and uses the crystal structures of the pure κ -phase and the intermediate phase, $\text{Ce}_2\text{Zr}_2\text{O}_{7.5}$ from Urban *et. al.* The difference

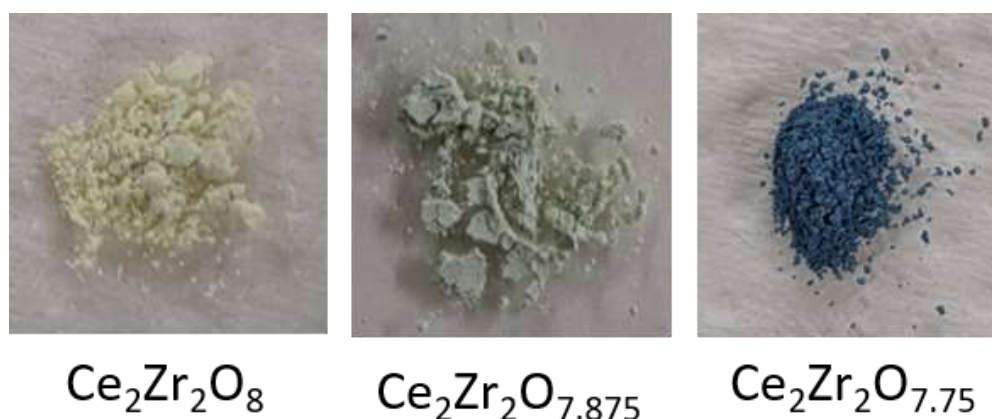


Figure 4.18 Photos of various oxidation states of the κ -phase $\text{Ce}_2\text{Zr}_2\text{O}_8$ powder.

spectrum shows that this fit is suitable, the main issue is the slightly underestimated intensities which is common with this type of refinement. The intermediate phase contributes a broad component to each reflection that can be very clearly seen in the inset which shows some of the greater 2θ peaks. Using this method, the percentage contribution of each crystal structure can be determined and therefore a loose estimate of the amount of oxygen in each system can be attained. This data can be seen in Table 4.4. The blue sample has roughly a 1:1 ratio of each phase so it can be thought of as $\text{Ce}_2\text{Zr}_2\text{O}_{7.75}$, whereas the 700 °C 500 °C redox green has a 3:1 ratio and would therefore be $\text{Ce}_2\text{Zr}_2\text{O}_{7.875}$. Interestingly the yellow samples, the as prepared and 600 °C exchange, are not 100% κ -phase as the ^{17}O NMR spectra and EELS images suggest. The as prepared sample may be within error of the refinement but the labelled sample

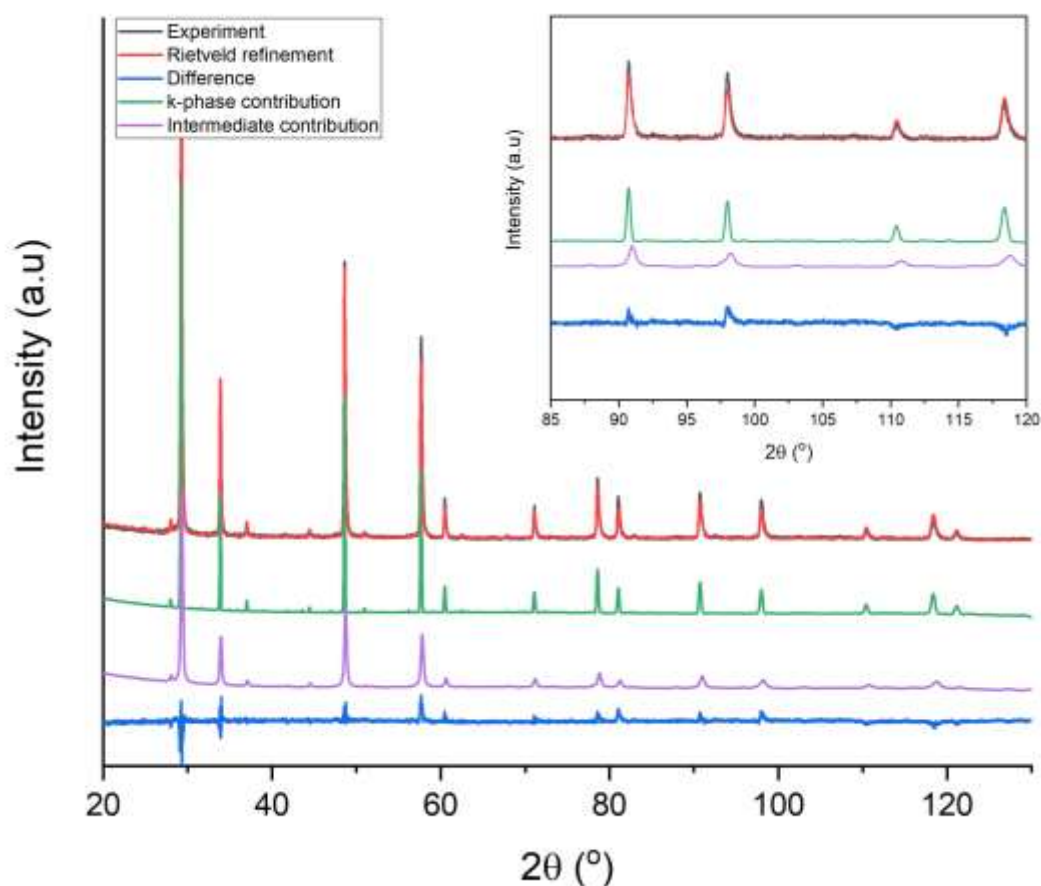


Figure 4.19 pXRD of the reduced κ -phase $\text{Ce}_2\text{Zr}_2\text{O}_8$ and a two phase Rietveld refinement. The blue line shows the difference between the refinement and the experimental data.

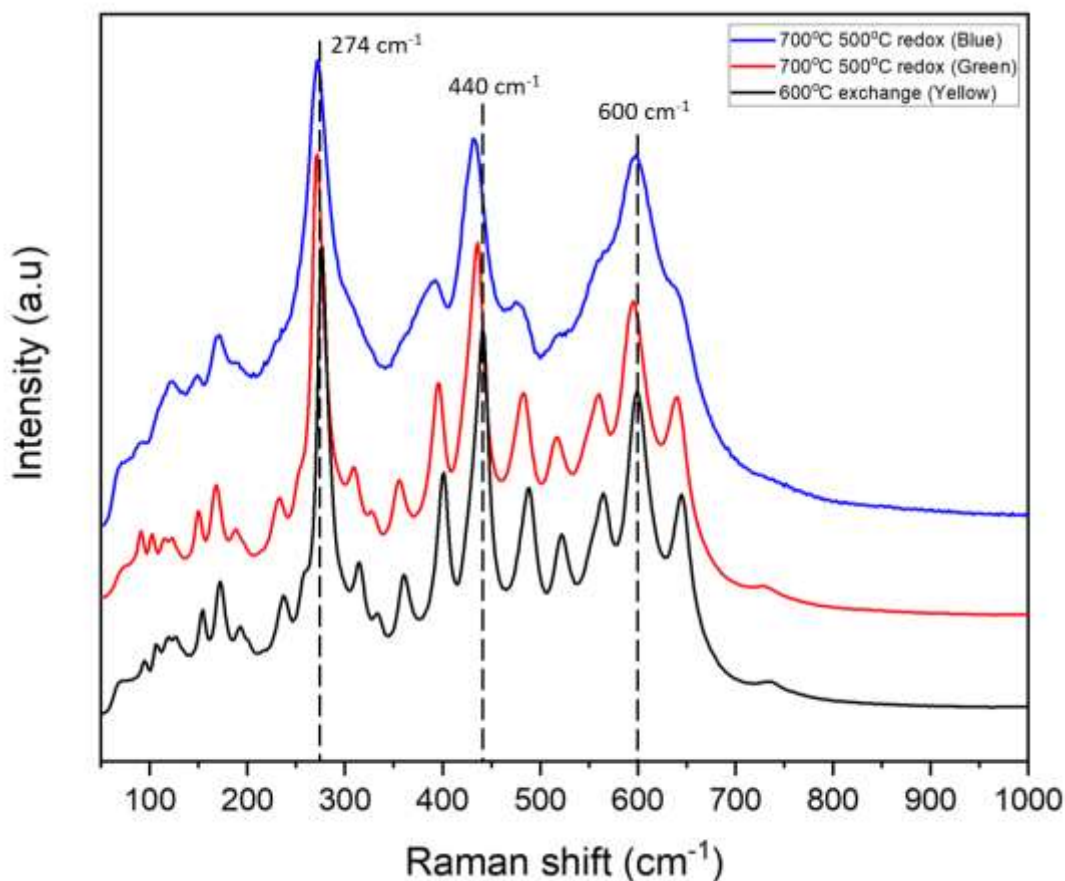


Figure 4.20 Raman spectra of the 700 °C 500 °C redox blue and green ordered ceria-zirconia samples as well as the 600 °C exchange sample.

has a definite contribution from the intermediate phase. This is a result of the high exposure temperature only being sufficient to alter the disordered structure most of the way toward the κ -phase.

Raman spectroscopy, as seen in previous sections, is also a good probe for small changes in the crystal structure of the κ -phase. For the 700 °C 500 °C redox green sample the indicative κ -phase bands at 274 cm^{-1} , 440 cm^{-1} and 600 cm^{-1} have all redshifted to 272 cm^{-1} , 436 cm^{-1} and 597 cm^{-1} respectively, Figure 4.20. As seen in Figure 4.5 this redshift is a result of the increased amount of Ce^{3+} present. The bands however show no evidence of broadening. The 700 °C 500 °C redox blue sample however displays considerable broadening and band overlap as well as redshifted bands. The broadening is a product of disorder as the system is now a mixed phase of

the κ -phase and the intermediate as demonstrated by the pXRD data. The further redshift of the bands is again due to even more Ce^{3+} being present in the system.

Whilst the Rietveld refinements and Raman spectroscopy can quite readily show the changes in oxidation state between the three different coloured systems, NMR cannot. Figure 4.21 shows an ^{17}O NMR comparison of a blue, green and yellow ordered ceria-zirconia. The yellow and green samples are identical apart from the additional intensity of the ceria site at 840 ppm. This site is not a structural difference however; it is a result of the high reduction temperature exposing this site more before reoxidation. This similarity implies that there is a threshold point where the system is stressed enough, due to lack of oxygen, to reconfigure from the κ -phase superstructure into a more mixed phase. As the spectrum for the blue sample is very different to the

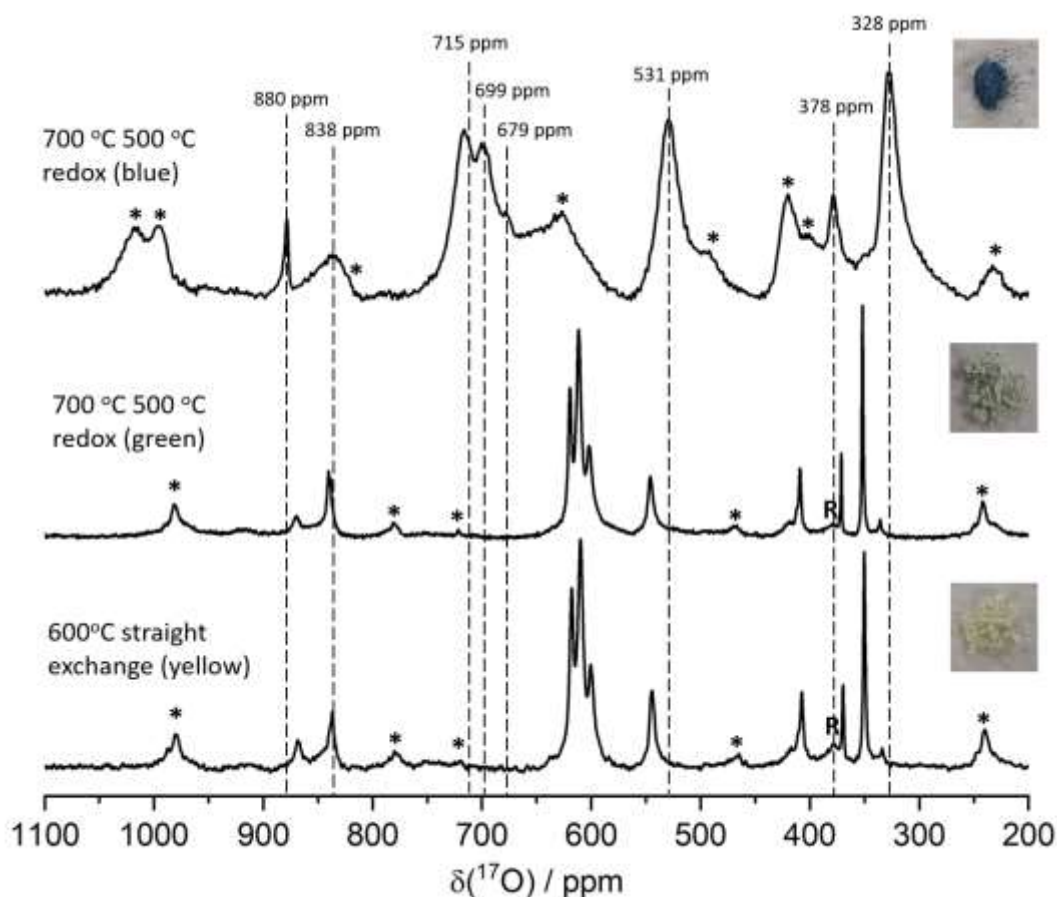


Figure 4.21 ^{17}O NMR comparison of the three different coloured ordered ceria-zirconia samples. The blue sample was measured on a spectrometer operating at 11.7 T, the other two at 9.4 T. All samples were in a 3.2 mm rotor spinning at 20 kHz. The blue sample required 13000 scans due to very low S/N. Asterisks denote spinning sidebands.

green and yellow, that point is somewhere between the 75% and 52% κ -phase contribution. The blue sample clearly has a very different structure to the other two. The resonances present are far broader than the systems maintaining the κ -phase structure, there have also been shifts both up and down field in all regions. The ceria region contains two resolved resonances, a very narrow one at 880 ppm and a broader one at 838 ppm. The site at 838 ppm likely contains the two unique OCe_4 coordination's seen in the κ -phase, but due to the distortion of the crystal lattice they have broadened out. The 880 ppm resonance is unique to this system and can tentatively be attributed to the single OCe_4 site present in the intermediate phase crystal structure which has a uniform O-Ce bond length of 2.24 Å, this would also explain why the resonance is relatively narrow at 4.5 ppm FWHM. The central ceria-zirconia region has shifted ~100 ppm downfield, a result of deshielding caused by the reduction of the system. The three OCe_2Zr_2 sites formerly at 618, 610 and 601 ppm can still be resolved at 715, 699 and 679 ppm. These resonances are significantly broader again due to the distortion of the crystal lattice. The final ceria-zirconia resonance is very slightly shielded and appears at 531 ppm a 16 ppm shift upfield from the 545 ppm resonance in the κ -phase structure. The zirconia region of the spectrum is littered with spinning sidebands so only two resonances can be confidently assigned. The first at 378 ppm may be entirely the signal from the rotor, as this spectrum required 13000 scans, therefore due to poor S/N it would contribute significantly. The second resonance at 328 ppm is likely an amalgamation of all the OZr_4 resonances seen in the κ -phase and just slightly shielded and broadened. What is clear from these three spectra is that the κ -phase system can form stable reduced phases and simply by heating in an oxygen rich atmosphere can readily revert back to a fully oxidised state. This property is the backbone of the vast OSC of these types of catalyst supports and why ordered κ -phase ceria-zirconia is at the forefront of catalytic converter and catalyst support materials.

4.3.9 ^{91}Zr static NMR studies of ordered and disordered ceria-zirconia

The final comparison to be made for the three different coloured systems is for the ^{91}Zr static measurements. Figure 4.22 shows the ^{91}Zr NMR spectra of a series of ordered ceria-zirconias as well as the as prepared disordered ceria-zirconia and the

BaZrO₃ reference. The reference material, as would be expected, is very narrow even in the static regime due to its high crystallinity. The κ -phase 600 °C exchange, Figure 4.22d, is also highly crystalline however still produces a broad resonance when compared to the reference. This spectrum consists of a highly ordered resonance

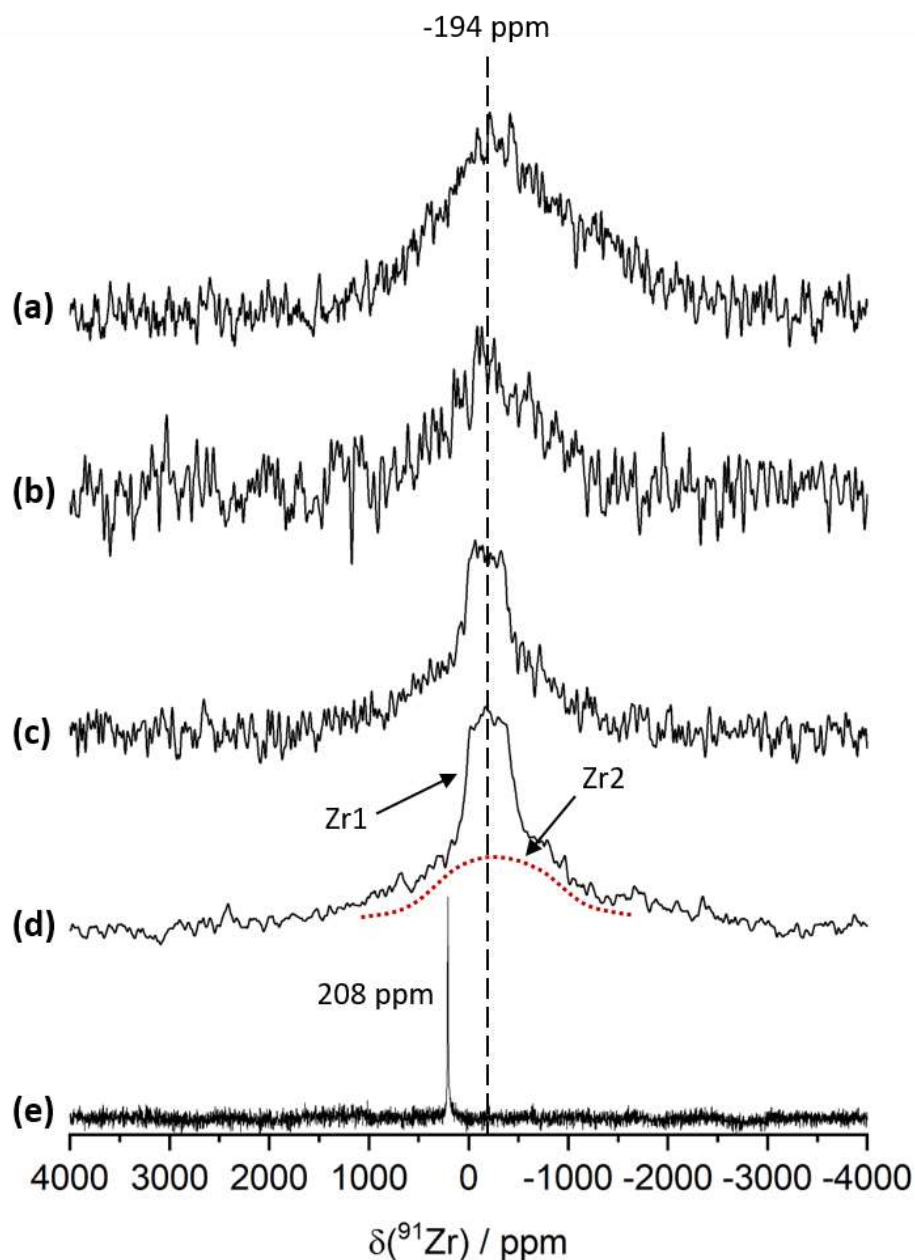


Figure 4.22 ^{91}Zr NMR spectra of (a) the disordered CeZrO₂, (b) the 700 °C 500 °C redox blue ordered sample, (c) the 700 °C 500 °C redox green ordered sample, (d) the 600 °C straight exchange ordered sample and (e) the BaZrO₃ reference. All measurements were static and recorded on an 11.7 T spectrometer apart from (a) which was on a spectrometer operating at 9.4 T.

at -194 ppm that can be attributed to one of the unique Zr sites with average bond length of 2.17 Å and standard deviation of 0.13 Å. The broader underlying component can be attributed to the other Zr site that has a much wider range of bond lengths with average bond length 2.24 Å and standard deviation of 0.27 Å. Figure 4.23 shows the two zirconia sites, Z1 and Z2, it is apparent that Z1 has little variation in its bond lengths and therefore represents the narrower resonance seen in the ^{91}Zr spectrum. Z2 however has a very distinct variation in bond length and therefore an orientation dependence in a static NMR measurement. This dependence means that this site has a large CSA which leads to the broad nature of the second resonance that spans ~4000 ppm. The 700 °C 500 °C redox sample spectrum, Figure 4.22c, has the same features as the 600 °C exchange. This is analogous to the ^{17}O spectra in Figure 4.21, even though the redox sample is mixed phase the structure still displays κ -phase features in the NMR data. It isn't until the structure becomes a 1:1 mixed phase of the κ -phase and the intermediate that the ordered resonance at -194 ppm vanishes. In the blue sample, Figure 4.22b, the ^{91}Zr spectrum now consists of a single broad feature, the mixed phase leads to very irregular bond lengths throughout the system, thus the CSA is very large and causes a broad resonance. The spectrum for the blue sample is

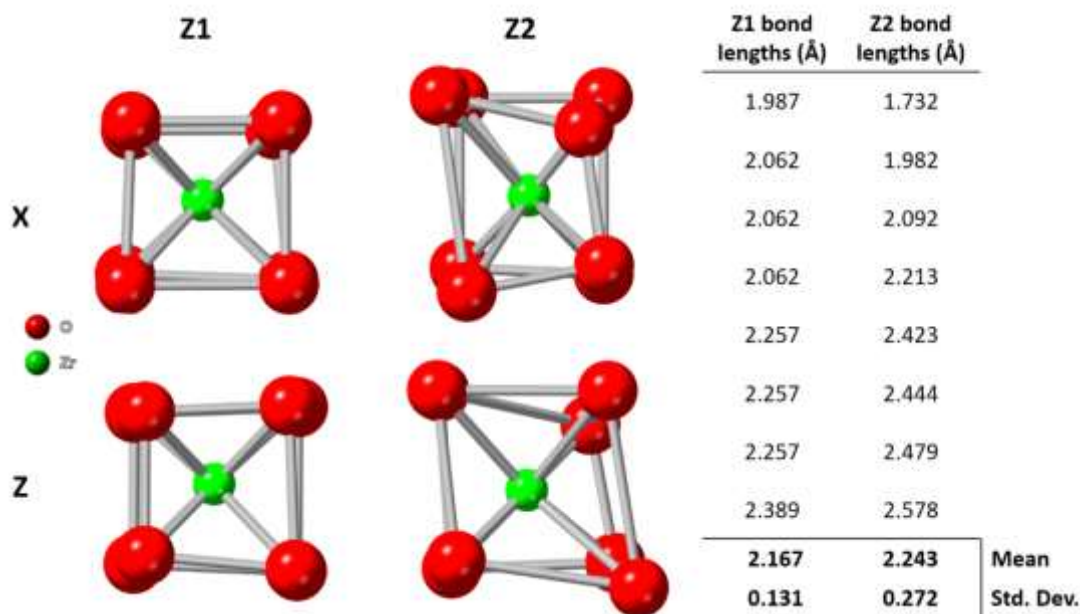


Figure 4.23 The two unique zirconia sites, Z1 and Z2, in the κ -phase structure. The top row shows the x-axis orientation and the bottom row the z-axis. The table on the right shows the Zr-O bond lengths as well as the mean and standard deviation of each site.

comparable to the disordered ceria-zirconia spectrum, Figure 4.22a. The single broad feature is indicative of disorder and is to be expected.

4.4 Conclusion

A disordered and ordered 1:1 ceria-zirconia solid solution have been characterised by a number of methods, including SAXS, pXRD, Raman spectroscopy and ^{17}O and ^{91}Zr solid state NMR. These systems were labelled with $^{17}\text{O}_2$ gas in order to conduct the ^{17}O NMR, due to this labelling many of these techniques were also used to ensure that the system did not undergo severe structural changes, thus resulting in unreliable data.

The pXRD of the disordered CeZrO_2 does not elucidate any changes after ^{17}O labelling, however the $\text{F}_{2\text{G}}$ band (representing the CeO_8 stretching) in the Raman spectrum shows a distinct and consistent redshift from 474 cm^{-1} to 466 cm^{-1} in all labelled samples. This is to be expected due to the increase in average particle size from the greater amount of Ce^{3+} present. This alludes to the samples not being fully reoxidised, but the change is small enough that the t' tetragonal phase is still maintained. The SAXS measurements of the disordered system also showed no obvious trend across the as prepared sample and the labelled samples, this is another indicator that the system has retained its structure.

Using ^{17}O NMR it was found that at lower reduction and reoxidation temperatures, $300\text{ }^\circ\text{C}$ $300\text{ }^\circ\text{C}$, that oxygen exchange was not occurring due to the stability of the solid-solution. As the reoxidation temperature was increased to $500\text{ }^\circ\text{C}$ there was oxygen exchange for all sites, this is consistent with TPR data from the literature. When $500\text{ }^\circ\text{C}$ $300\text{ }^\circ\text{C}$ redox is done, only the zirconia sites and some mixed CeZr sites exchange. This is to be expected as the Zr-O bonds are longer and therefore weaker in this system and a higher reoxidation temperature is required to exchange with the oxygen coordinated cerium. This is shown when $500\text{ }^\circ\text{C}$ $500\text{ }^\circ\text{C}$ redox is done, the entirety of the system now exchanges oxygen. Finally, at the highest labelling temperatures $700\text{ }^\circ\text{C}$ $500\text{ }^\circ\text{C}$ redox there again is excellent oxygen exchange. What this shows it that the reoxidation temperature is the limiting step, unfortunately higher temperatures could not be used due to the limit of the labelling rig. The ^{17}O NMR shows clear regions present in the system, zirconium coordinated oxygen, cerium

coordinated oxygen and a mixed CeZr coordinated region. The centre region can be roughly assigned to regions with a greater amount of Ce coordination at greater isotropic shift and greater amount of Zr coordination at lower shifts. The broad nature of the resonances in these spectra are to be expected due to the great amount of disorder in the system.

The stark difference in ^{17}O NMR between the disordered CeZrO_2 and the κ -phase is telling as to the differences in the structural order. The very narrow resonances of the κ -phase are a product of the very uniform sites seen in the crystal structure from Urban *et. al.* [48]. This order is also highlighted in the pXRD of the κ -phase, the very narrow reflections and the presence of the superstructure peaks are consistent with the literature. The Raman spectrum when compared to the disordered system shows far greater resolution and S/N, the resolution however is still not great enough to resolve all 144 active modes. The labelling process for the lower straight exchange temperatures shows little effect on the structure in the pXRD but in the Raman narrowing of the bands by between 3 and 6 cm^{-1} is seen, this is due to a slight increase of the crystallinity of the sample after being exposed to temperatures between 200 °C and 400 °C. These are only very minor changes so it can be said that for these labelling conditions the structure has not altered.

The ^{17}O NMR of the κ -phase is analogous to the disordered system, with three regions being present for the cerium, zirconium and CeZr coordinated oxygen. Again the resonances are very narrow, but the important result from the low temperature labelling is that the system labels non-selectively. Meaning that the oxygen when exchanging is distributed equally throughout the system. This however is not the case at labelling temperatures exceeding 500 °C, as an additional Ce coordinated oxygen begins to exchange and at the most extreme labelling condition of 700 °C 500 °C redox this resonance is very prominent. This is consistent with the Ce-O bond lengths as this site has an average bond length of 2.331 Å and the other site has an average length of 2.379 Å.

When scrutinising the ^{17}O of the κ -phase it is apparent that the predicted isotropic shifts from CASTEP calculations and the number of resonances present, do not match the experimental data. There are certainly a greater number of Ce and Zr resonances.

This can be explained with the use of both EELS data and Rietveld refinements which shows that the system is not in fact purely κ -phase. The EELS data reveals that only the surface is homogeneously ordered and that the bulk of the system is not entirely. The Rietveld refinements show a discrepancy of 8% in the 600 °C straight exchange sample (which based on its colour appears fully oxidised) that can be attributed to the intermediate phase ordered ceria-zirconia. This is a result of the labelling temperature used being too low, the literature advises using ~ 1500 °C in the reduction step, here 1200 °C was used.

Different levels of oxidation of the κ -phase have been investigated using all previous techniques. Initially these three different systems were identified by their colours, yellow being fully oxidised and then green and blue demonstrating less and less oxygen in the structure. The pXRD Rietveld refinements give a good indication as to the amount of oxygen present, leading to two new stable structures being identified $\text{Ce}_2\text{Zr}_2\text{O}_{7.875}$ (green) and $\text{Ce}_2\text{Zr}_2\text{O}_{7.75}$ (blue). This was done by using the intermediate and the κ -phase crystal structures. There is a consistent theme that the blue system has evidence of disorder across the Raman, ^{17}O and ^{91}Zr NMR. This is largely seen in the broadening and loss of resolution of the individual resonances (NMR) and vibrational modes (Raman). This is a result of the blue system being a mixed phase of the intermediate and the κ -phase, and is one of the steps that the κ -phase structure would go through when oxidising exhaust emissions. This process is reversible and is one of the major useful properties of ceria-zirconia materials. The change to a mixed phase only occurs at some threshold point as the $\text{Ce}_2\text{Zr}_2\text{O}_{7.875}$ (green) Raman and NMR data are almost identical to that of a yellow sample. This shows that the κ -phase structure is robust and can maintain the cubic structure even when a great amount of oxygen has been removed.

The final result comes from the ^{91}Zr static NMR which concisely demonstrates the two different Zr sites, one a site with mostly uniform bond lengths (std. dev. 0.131 Å) that appears as a fairly narrow resonance for a static measurement and the other is a broad resonance caused by the large CSA of the site, which has a much wider range of bond lengths (std. dev. 0.272 Å).

In further work smaller increments of the reduction temperatures could be used to assess the full range of oxidation levels of the κ -phase, this would allow the chance to pinpoint the exact moment the κ -phase no longer maintains its cubic structure. The 1:1 system could also be compared to 1:3 and 3:1 ratio ordered ceria-zirconia's, to assess how the oxygen mobility might change and how the structures react to different levels of oxidation.

Knowing that at low temperatures, oxygen non-selectively moves through the κ -phase and having evidence that there is a threshold point for the κ -phase may be beneficial in the design of ordered ceria-zirconia supports for the new generation of catalytic converters used in autocatalysis.

Chapter 5: An investigation of hybrid perovskites used as LEDs

5.1 Introduction

Electrical lighting accounts for 20% of the world's energy consumption [75]. Since the inception of electrical lighting designs have moved from simple filament based bulbs to LED devices that can emit the full range of visible light. In recent years, hybrid lead halide perovskites have been shown to have broadband emitting properties which are used to emit white light in white light emitting diodes (WLEDs) [76,77]; the ease of manufacture and high colour rendering index of these systems puts them ahead of their down-converting phosphor analogues in a commercial environment [10,78]. A series of WLED <100>-oriented 2D hybrid perovskites have been produced by Hu *et al.* that contain robust organic structures which allow fine-tuning of their bandgap and photoluminescence properties [76].

The effect of water interacting with hybrid perovskites has been studied greatly. In some cases, such as solar cell thin films, the amount of water the systems are exposed to can determine the resulting efficiency of the system [79,80]. It has also been shown how this efficiency increase can be due to atmospheric water aiding in thin film formation [81] and that these perovskites can be both hydrated and stable [82].

Hydration of the crystals and thin films has been shown to be reversible, but can also lead to degradation of the system into lead iodide (PbI_2) [83]. Exposing these perovskite solar cell systems to both rain and atmospheric water leads to degradation [84,85], the highly hygroscopic nature of the amine salts in these perovskites are to blame for this behaviour [86]. The method by which water intercalation in methylammonium lead iodide (MAPI) leads to degradation of the systems, thus reducing the lifespan of the devices, has additionally been investigated. Largely, however, the actual degradation pathways are studied by *ab initio* calculations and are purely theoretical [87–89].

Excitons are the driving force behind the photoluminescence, phosphorescence and many of the other properties hybrid perovskites possess [90,91]. Excitons are quasiparticles that consist of an electron and a hole that are bound together, Figure 5.1a. Thus they are electrostatically neutral. There are two main types of exciton, free and self-trapped. Typically, a self-trapped exciton has a longer lifetime than the free exciton and these longer lifetime excitons can lead to emission of multiple wavelengths of light [75,92]. The self-trapped excitons can be excited into the free exciton level and vice versa, this exchange can lead to an effective increase in exciton lifetime which can significantly alter the emission properties of a hybrid perovskite [76], Figure 5.1b.

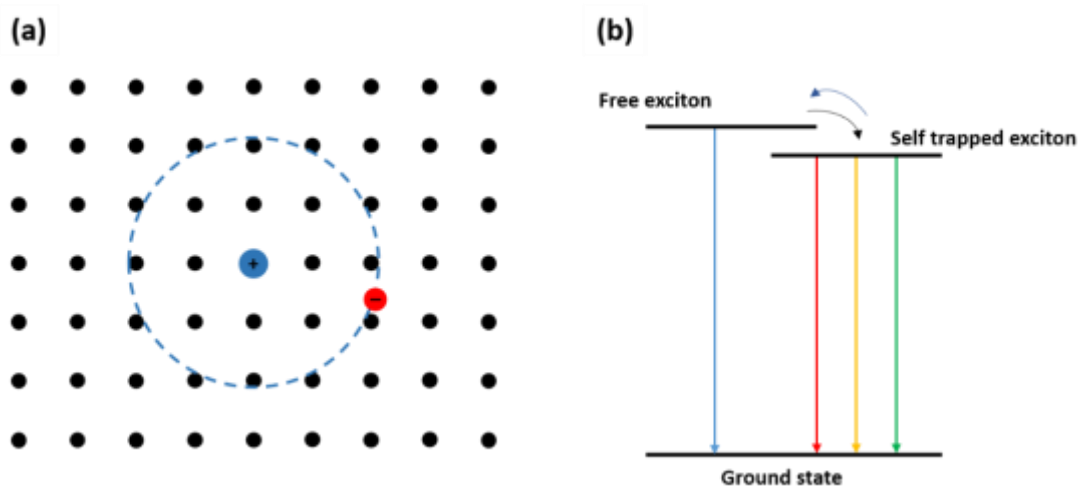


Figure 5.1 (a) a basic representation of an exciton and (b) an energy level diagram showing how free and self-trapped excitons can exchange before the energy emission back to the ground state. Adapted from Hu. *et. al.* [89].

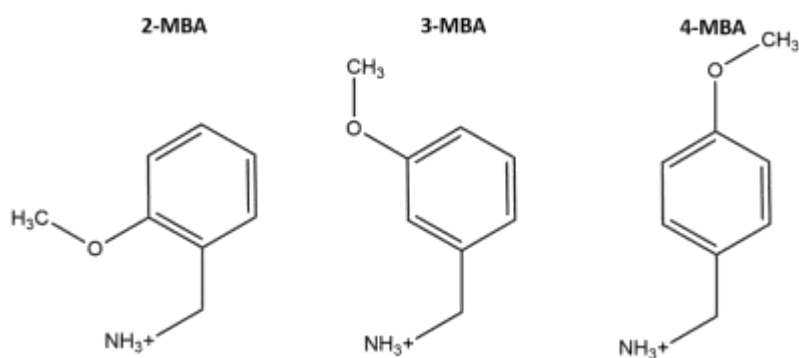


Figure 5.2 Schematics of the organic MBA molecules placed in the inorganic lead bromide lattice.

Hu *et al.* [93] discuss the concept of self-trapped excitons leading to the broadband emission properties of methoxybenzylammonium (MBA) and lead bromide based organic-inorganic hybrid perovskites, Figure 5.2. The intrusion of the methoxy group of the organic into the inorganic framework causes varying amounts of dihedral titling. It is asserted that this titling may determine the photoluminescent properties in these LED materials. The three systems, denoted 2-MOP, 3-MOP and 4-MOP, all exhibit strong excitonic absorption; as is typical in 2D hybrid perovskites. They differ in that the 2-MOP system exhibits a broader and red shifted bound exciton peak in its photoluminescence (PL) spectrum compared to that of 3-MOP and 4-MOP. The PL emission from 2-MOP spans the entire visible wavelength range and is therefore a WLED. It is hypothesised by Hu *et al.* that the formation of these strongly bound excitons, which lead to this broadband emission, are the results of the distorted inorganic octahedra. This is supported by previous studies that also relate structural distortion about the inorganic framework in WLEDs to strongly bound self-trapped excitons [94–96].

Hybrid perovskite systems are commonly investigated using single-crystal and powder XRD, photoluminescence and Fourier transform infrared (FTIR) spectroscopy. Such techniques, combined with device performance studies only infer the presence of H₂O within the structures [77,93,97]. The use of techniques such as XRD will only provide long-range structural information about a system; consequently, no information is elucidated on the position or relative abundance of the

water molecules within the crystal structure. NMR is used to investigate the local structure in a system by observing individual nuclei, and it has been demonstrated that individual H₂O molecules are visible in ¹H NMR [98–100]. Gun'ko and Turov [98] show how different chemical shifts for hydrogen bonded water can appear in ¹H NMR spectra based on nearby electron density, and the degree of bonding to the surface of varying oxides. Ladizhansky *et al.* [99] have used 1D NMR and 2D NMR correlation methods to show how water binds to CdS nanoparticles; the resonances in their spectra are attributed to both hydrogen-bonded and free water.

This study aims to show that the presence of water in these systems is not deleterious to their photophysical properties, so far as to say that these water molecules may actually mediate these properties. By use of similar 1D and 2D NMR experiments, it has been revealed in the tuneable perovskite systems investigated in this study that water is indeed present within the structure. In these systems the NMR data shows two distinct sites for water in two of the systems and one site for the final system. The former is likely due to different degrees of hydrogen bonding between the present waters. Unlike the solar cell MAPI counterparts, there are no signs of degradation in the systems to PbBr₂ as demonstrated by 1D ²⁰⁷Pb NMR. By coupling multinuclear MAS NMR, AIRSS and DFT calculations it can be shown that there exist hybrid perovskites containing large amounts of water in their bulk system, that remain stable and can be used as cheap and efficient WLEDs.

5.2 Materials and Methods

5.2.1 Materials

Methoxybenzylammonium (MBA) bromides were synthesized by adding HBr (48wt% in water) into 2-methoxybenzylamine, 3-methoxybenzylamine, or 4-methoxybenzylamine in ethanol at 0 °C (molar ratio of amine to HBr = 1:1.2). The crude product was obtained by slowly evaporating the solvent under reduced pressure. Then the resultant white precipitate was dissolved in ethanol and recrystallized by slowly adding diethyl ether. The small crystals were further washed with diethyl ether several times before drying them in a vacuum oven. After drying overnight, all

samples were sealed under nitrogen and transferred into a nitrogen-filled glove box for further use.

5.2.2 Methods

Powder XRD was carried out on a Panalytical X-Pert Pro MPD $K_{\alpha 1}$ with a Cu source. A 2θ range of 5° to 130° was used with increments of 0.125° . The data was processed using Highscore plus to correct the baselines of the spectra and remove additional noise.

Single crystal X-ray diffraction was undertaken using a Bruker SMART APEX-II system. The system uses a Mo sealed tube source along with a graphite monochromator to produce X-rays of wavelength 0.71073 \AA . Data was solved using SHELXT and refined on F2 using SHELXL in the program suite WinGX.3-5

All FTIR data were collected on a Thermo Fisher iS50R FT-IR spectrometer equipped with a Golden Gate ATR manufactured by Specac. A KBr beamsplitter and a Teflon DGTS detector leading to a spectral resolution of 4cm^{-1} . Spectra were recorded between 600 cm^{-1} and 3500 cm^{-1} .

Raman spectra were measured on a Renishaw inVia Raman microscope using a 785 nm wavelength DPSS laser operating over a $300 - 4000\text{ cm}^{-1}$ wavenumber range. A Renishaw CCD using a manual sample stage was used for detection. A x50 Olympus objective lens was used to focus the beam onto the sample, the system was calibrated using a silicon reference. A diffraction grating of 1200 l/mm was used. Each scan had a 10 s exposure time and 10 scans were recorded for each sample at 10% laser power.

The raw data for both the Raman and FTIR were baselined and fitted using Origin 2019b.

^1H , ^{13}C and $^1\text{H } T_1$ NMR measurements were carried out on a Bruker Avance III HD spectrometer operating at 18.8 T , with ^1H and ^{13}C Larmor frequencies at 800 MHz and 201.2 MHz respectively. Both one and two dimensional ^1H , $^1\text{H } T_1$ and ^{13}C MAS spectra were obtained using a Bruker HXY 0.7 mm probe with spinning speeds of 110 kHz . $\pi/2$ pulse widths of $0.8\text{ }\mu\text{s}$ for ^1H were used with a recycle delay of 20 s to ensure quantitative data. For the ^{13}C cross-polarisation with MAS (CPMAS) a ^1H - ^{13}C contact time of 1.1 ms , a 35% CP ramped pulse, and a recycle delay of 30 s were used.

A total of 8096 scans were acquired. All ^1H and ^{13}C chemical shifts were externally referenced against alanine's methyl (CH_3) group ($\delta_{\text{iso}} = 1.1$ ppm for ^1H) ($\delta_{\text{iso}} = 20.5$ ppm for ^{13}C) relative to TMS.

^1H T_1 saturation recovery measurements were taken using a train of 100 $\pi/2$ pulses followed by a variable τ delay and a subsequent $\pi/2$ pulse of 0.8 μs . Delays ranging from 0.01 – 20 s were used to ensure complete relaxation. ^{13}C $T_{1\rho}$ measurements were acquired on a Bruker Avance III HD spectrometer operating at 9.4 T using a Bruker HX 4 mm probe with spinning speeds of 12 kHz. For the $T_{1\rho}$ measurement, ^1H magnetization was excited by a $\pi/2$ pulse of 2.5 μs then spin-locked at varied time periods and transferred to the ^{13}C via CP for detection.

For the NOESY sequences $\pi/2$ pulse lengths of 0.8 μs are used as well as a varied mixing times ranging from 100 ms to 500 ms. Exchange correlation spectroscopy (EXSY) was also employed here. This is a series of NOESY experiments with varied mixing times going all the way up to a relatively long mixing time, in this case 2 s. EXSY experiments reveal the degree of interaction between individual spins.

In the HETCOR sequence, ^{13}C CPMAS were observed by RAMP-CP with contact times of 2ms, $\pi/2$ pulse widths of 0.8 μs are used for both ^1H and ^{13}C . The BABA sequences also had $\pi/2$ pulse lengths of 0.8 μs and used 1 or 2 loops for the pulse trains.

^{207}Pb NMR spectroscopy was carried out on both a Bruker Avance II+ and Bruker Avance III HD spectrometer operating at 14.1 T and 7.05 T with ^{207}Pb Larmor frequencies of 125.6 kHz and 62.8 kHz respectively. One dimensional Hahn echo ^{207}Pb MAS spectra were obtained using a Bruker HX 2.5 mm probe with spinning speeds of 24 kHz and 30 kHz. $\pi/2$ pulse widths of 2.5 μs with a recycle delay of 3 s, echo delay of 120 μs and 14000 scans were typically used. All ^{207}Pb chemical shifts were externally referenced against 1 M PbNO_3 solution, $\delta_{\text{iso}} = -2976$ ppm relative to neat $(\text{CH}_3)_4\text{Pb}$.

CASTEP (version 21.1) [15], a plane-wave pseudopotential DFT package, was used to carry out electronic structure and geometry relaxation calculations for the pristine and hydrated MOP structures. The rSCAN meta-generalised gradient

functional [101,102] was used to model the exchange-correlation energy term. CASTEP's built in on-the-fly generated pseudopotentials of the "C19" suite were used throughout in the calculations. Dispersion interactions were modelled using the many-body dispersion scheme. [16]

Geometry relaxations, including those performed with AIRSS [16–18], used an electronic cutoff energy of 600 eV for the plane-wave basis set, and the Brillouin zone (BZ) was sampled using a 1x2x2 Monkhorst-Pack grid [103]. Only the atomic positions were relaxed, to a tolerance of 0.05 eV/Å in the atomic forces.

NMR parameters were computed using the GIPAW method [52,53], implemented in CASTEP with tighter convergence settings, at 800 eV cutoff energy for the plane-wave basis set and 2x4x4 Monkhorst-Pack grid for the BZ sampling.

5.3 Results

This series of <100>-oriented 2D hybrid perovskites are referred to as 2,3 and 4-MOP. The naming convention arises from the para, meta and ortho positions of the methoxy groups attached to the benzylammonium in the organics. These organics are named 2, 3 and 4-MBA and when placed in the hybrid perovskites are then subsequently referred to as 2, 3 and 4-MOP. The long-range structure of these systems have all been investigated via scXRD previously carried out by by Hu *et al.* [76].

5.3.1 FTIR, Raman, single-crystal and powder XRD studies

FTIR and Raman spectra of 2-MOP, 3-MOP and 4-MOP were recorded to determine if H₂O is present in the three systems. Figure 5.3b and Figure 5.3c show Raman spectra measured with a 785 nm laser. H₂O would have been seen as either a stretching of the H-O-H bond at 1635 cm⁻¹ and/or stretching of O-H bond in a broad band between 3200 cm⁻¹ and 3400 cm⁻¹ [104]. The band at 1635 cm⁻¹ could be present in this case, however if it is, then vibrational modes from the organic are obscuring it. The broad O-H band is entirely absent in the Raman spectra; this could simply mean that due to the position of the H₂O molecules in the octahedral PbBr₄ lattice there isn't enough freedom for them to have observable vibrational modes. This assertion is supported

by the FTIR spectra, Figure 5.3a. Much like the Raman spectrum, H-O-H bending would be observed at $\sim 1600\text{ cm}^{-1}$ and O-H stretching between 3100 and 3500 cm^{-1} in FTIR [104]. Again the H-O-H bending is obscured by vibrations originating from the organics in the hybrid perovskite. A broad band is however observed in the FTIR. The bands present from $\sim 2800\text{ cm}^{-1}$ to 3000 cm^{-1} can be attributed to single bond C-H and N-H stretching [105], but the less intense region from 3000 cm^{-1} to 3200 cm^{-1} likely

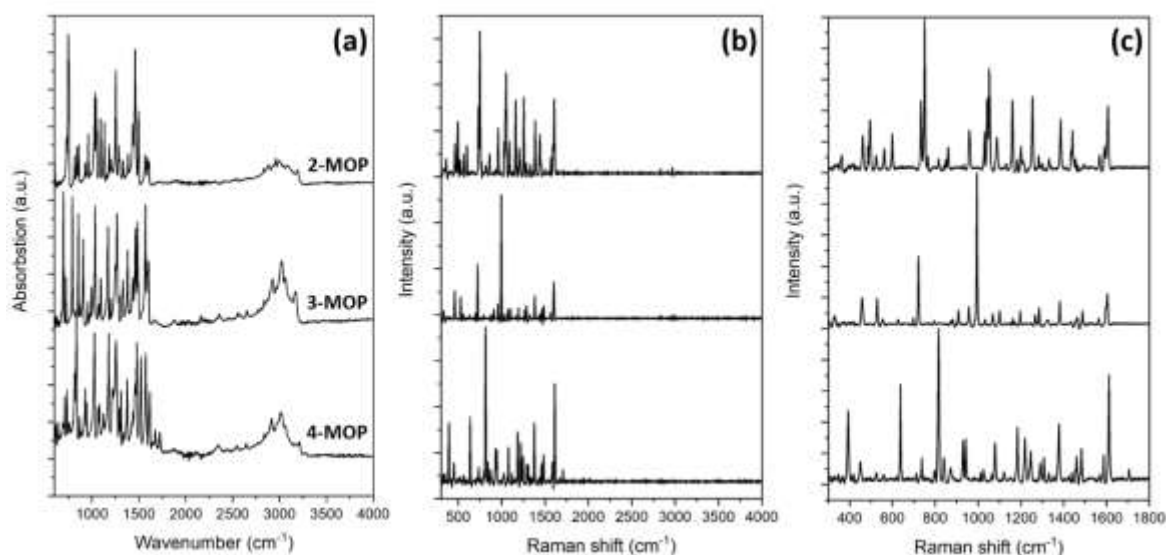


Figure 5.3 Raman and FTIR spectra of the 2-MOP, 3-MOP and 4-MOP systems. Section a) FTIR of all three systems, showing the fingerprint region and stretching region of N-H and O-H, b) a Raman spectra showing the full range from the prominent organics up to the O-H stretching region, and c) zoomed in spectra showing only the prominent vibrational modes from the organic region.

stems from O-H stretching. There are no O-H bonds present in any of the organics in

the MOP systems, so this can tentatively be attributed to O-H stretching in H₂O

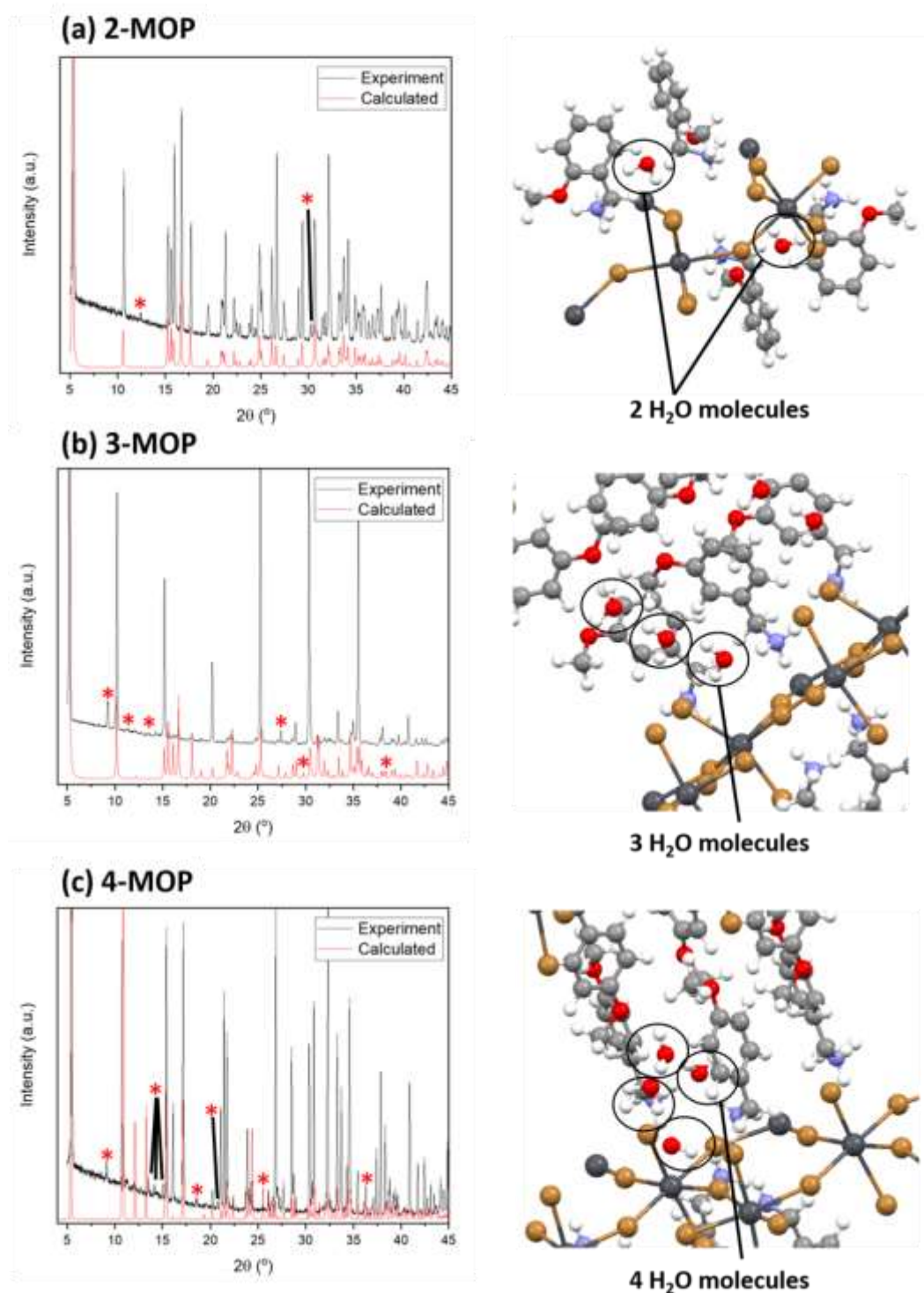


Figure 5.4 A comparison of experimental pXRD patterns and calculated powder patterns from scXRD for (a) 2-MOP, (b) 3-MOP and (c) 4-MOP. These data suggest that the content of the single-crystal data is not entirely accounted for, discrepancies are shown with a red asterisk. AIRSS modelling has been used to add the missing water molecules to each crystal structure (see crystal structures to the right).

molecules within the framework of each system. The lower relative amount of intensity present in this region for the 2-MOP system could be attributed to a there being less H₂O relative to the organic molecule present.

Comparing pXRD data with diffraction patterns calculated from the MOP single-crystal XRD can be used to indicate the completeness of the single-crystal data. Figure 5.4a, b and c show a comparison of these experimental and calculated patterns. For 2-MOP (Figure 5.4a) the majority of reflections are consistent between the two data sets, there is however a noticeable additional major reflection in the experimental data at $2\theta = 12.4^\circ$. This could indicate that some structural facet of the scXRD is missing, likely due to the complicated nature of detecting and resolving smaller atoms and molecules. There are significant differences between the calculated and experimental powder patterns in 3-MOP and 4-MOP (Figure 5.4b and Figure 5.4c). Numerous major reflections are absent in the calculated pattern, and the shift of many reflections seem to differ by $1-2^\circ 2\theta$. It is therefore clear that in these cases, there is a substantial amount of missing information in the single-crystal data. Pairing this with FTIR would suggest that water molecules have not been detected or modelled in the single-crystal XRD. These can however be added retroactively added using additional modelling techniques.

Table 5.1 Single crystal XRD cell parameters of the three MOP systems. The parameters excluding water are from experiment and the parameters including water are from the structures generated by AIRSS.

	2-MOP		3-MOP		4-MOP	
	Excluding water	Including water	Excluding water	Including water	Excluding water	Including water
Empirical formula	C ₁₆ H ₂₄ Br ₄ N ₂ O ₂ Pb	C ₁₆ H ₂₆ Br ₄ N ₂ O ₃ Pb	C ₁₆ H ₂₄ Br ₄ N ₂ O ₂ Pb	C ₁₆ H ₂₇ Br ₄ N ₂ O _{3.5} Pb	C ₁₆ H ₂₄ Br ₄ N ₂ O ₂ Pb	C ₁₆ H ₂₈ Br ₄ N ₂ O ₄ Pb
Crystal system	Monoclinic	Monoclinic	Monoclinic	Monoclinic	Monoclinic	Monoclinic
Space group	P2 ₁ /c	P1	P2 ₁ /c	P1	P2 ₁ /c	P1
Unit cell dimensions	a = 16.9280 Å	a = 16.9280 Å	a = 17.7662 Å	a = 17.7662 Å	a = 17.1963 Å	a = 17.1963 Å
	b = 8.0054 Å	b = 8.0054 Å	b = 8.0375 Å	b = 8.0375 Å	b = 8.2080 Å	b = 8.2080 Å
	c = 8.5533 Å	c = 8.5533 Å	c = 8.2585 Å	c = 8.2585 Å	c = 8.4360 Å	c = 8.4360 Å
	α = 90°	α = 90°	α = 90°	α = 90°	α = 90°	α = 90°
	β = 98.742°	β = 98.742°	β = 94.639°	β = 94.639°	β = 104.152°	β = 104.152°
Volume	γ = 90°	γ = 90°	γ = 90°	γ = 90°	γ = 90°	γ = 90°
	1145.638 Å ³	1145.638 Å ³	1175.416 Å ³	1175.416 Å ³	1154.580 Å ³	1154.580 Å ³
Density	2.3283 g cm ⁻³	2.3805 g cm ⁻³	2.2693 g cm ⁻³	2.3457 g cm ⁻³	2.3103 g cm ⁻³	2.4139 g cm ⁻³
Z	2	2	2	2	2	2

5.3.2 AIRSS modelling and DFT calculations

If water is present in these structures, then the initial single-crystal XRD data is incomplete. By using AIRSS and finding the most energetically favourable structure containing H₂O molecules, a step towards completing the crystal structures can be taken. Figure 5.4a, Figure 5.4b and 5.4c show the most energetically favourable cells containing water for the three MOP systems.

The calculations predict that there are 2, 3 and 4 H₂O molecules present in 2, 3 and 4-MOP respectively. Figure 5.5 shows the binding energies of each water molecule after it is added to the system. For 2-MOP and 3-MOP the greatest binding energies correspond to two and three water molecules respectively. In 4-MOP however, four waters were the chosen amount to be added even though that water molecule has a lower binding energy than that of the 2nd, 3rd and 5th added molecule. This is because the latter molecules produced calculated NMR isotropic shifts that did not correspond to the real system, whereas adding four molecules did.

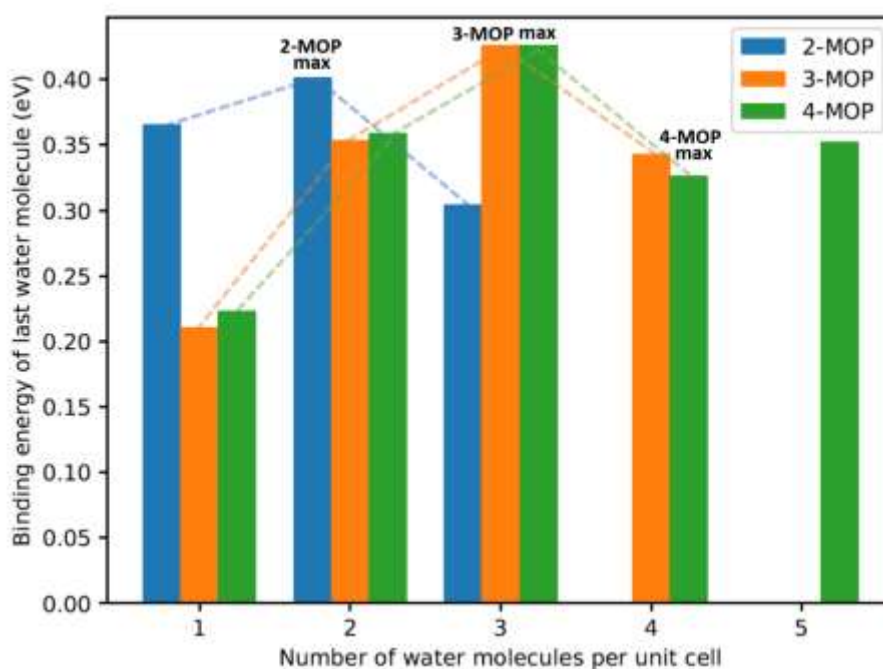


Figure 5.5 The binding energy of the last added water molecule using AIRSS is shown here, the water molecules are added sequentially before the systems are relaxed.

From these more complete cells, DFT calculations using rSCAN can be used to determine theoretical NMR shift parameters and can then be compared against the experimental ^1H and ^{13}C NMR data. This is then compared to calculations of the systems in their incomplete state without the H_2O present, Table 5.1 and 5.2.

5.3.3 1D ^1H and ^{13}C MAS NMR studies

In order to confirm that these complete structures contain H_2O , 1D ^1H and ^{13}C NMR along with 2D HETCOR experiments (aided by NOESY and BABA data) are used. This 2D NMR data allows for the determination of the positions of single ^1H s with respect to carbons present in the system.

Initially, single pulse ^1H spectra were measured. In Figure 5.6 we see that the CH_3 and NH_3 groups for each system are clearly visible and show a quantitative 3:1 ratio of ^1H 's present (each proton has relative intensity of $\sim 7\%$ in 3-MOP and 4-MOP and $\sim 8\%$ in 2-MOP, see Table 5.2). As these groups appear in a single site it can be assumed that these protons are rotating about their respective C or N atom, and thus share indistinguishable chemical shifts. In contrast, the CH_2 ^1H 's can be resolved individually in all three systems; these ^1H 's are fixed and are exposed to different electron densities due to either: proximity to the intramolecular O atom, or to electron density from neighbouring molecules.

In the 3-MOP system (Figure 5.6b) all of the aromatic ^1H 's appear in a single region; these ^1H 's are experiencing the same electron density perturbation throughout the crystal structure. In 2-MOP (Figure 5.6a) and 4-MOP (Figure 5.6c), however, there is a splitting of the aromatic site. 2-MOP has both a more shielded and more deshielded aromatic ^1H site at 5.8 ppm and 7.3 ppm respectively, and in 4-MOP there is a single more shielded aromatic site at 5.4 ppm. This is due to the proximity of the CH_3 group attached to the O atom ~ 2.0 Å away and also likely from additional shielding from neighbouring H_2O molecules. In 2-MOP, the deshielded peak can be attributed to the proximity of the intramolecular O atom ~ 2.7 Å away. The more shielded peak, like in 3-MOP, is also due to a proximal CH_3 group (~ 3.7 Å away), but from a neighbouring molecule rather than from within its own molecule.

The similarity of 3-MOP and 4-MOP (and their subsequent difference to 2-MOP), in terms of ^1H spectra, can be compared to the degree of tilting in their respective crystal structures. Hu *et al.* explains how titling of the PbBr_6 octahedra may be the cornerstone of the self-trapped exciton states present in the system. This tilting is caused by the O atom in the organic structure repelling the proximal bromine atoms in the inorganic octahedra. The largest degree of titling present is in 2-MOP (17.6°), it is much smaller in 3-MOP and 4-MOP which have similar amounts of tilting (3.1° and 5.1° respectively). This minimal tilting would allow for sufficient space in the crystal structure in which multiple H_2O molecules can reside. The ^1H spectra show a clear

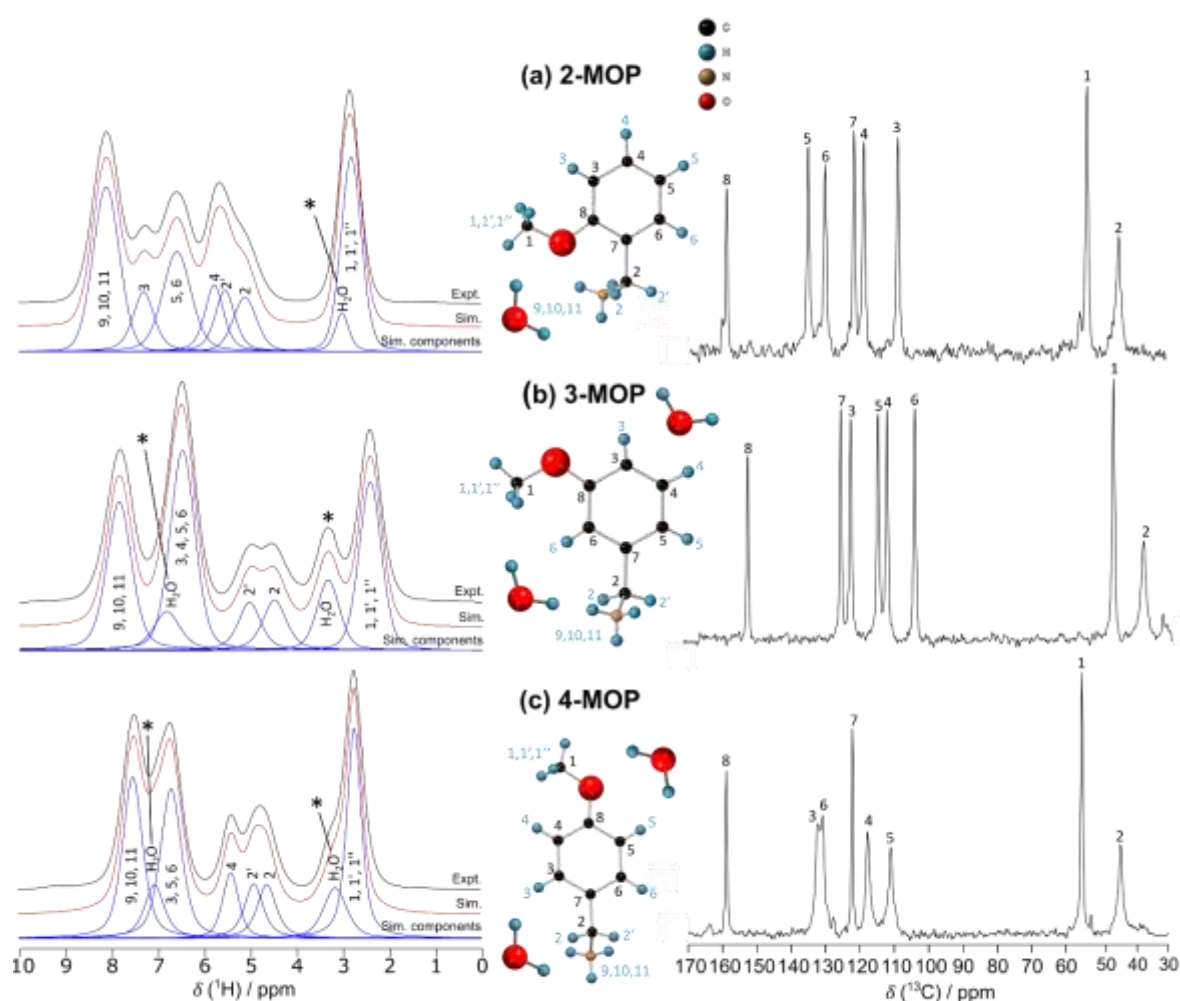


Figure 5.6 1D ^1H and ^{13}C NMR of (a) 2-MOP (b) 3-MOP and (c) 4-MOP. Each ^1H spectrum has an associated simulation and deconvolution showing the individual sites which match up with the adjacent schematic molecules. H_2O is present in all three systems, but 2-MOP does not have a resonance at ~ 7 ppm like 3-MOP and 4-MOP.

Table 5.2 ^1H T_1 relaxation times for 2-MOP, 3-MOP and 4-MOP taken on 600 MHz and 800 MHz spectrometers. In general, the T_1 times increase when increasing in field strength. Also shown are the relative intensities of the ^1H simulations shown in Figure 5.6.

System	Resonance no.	Functional Group	^1H δ_{iso} (ppm)	^1H Calculated Resonance H_2O excluded (ppm)	^1H Calculated Resonance H_2O included (ppm)		Relative Intensity (% \pm 1 %)	^1H T_1 (s) 600 MHz	^1H T_1 (s) 800 MHz
					1	2			
2-MOP	1, 1', 1''	CH_3	2.8	0.1, 1.8, 3.0	1.6, 1.7, 2.6	2.7, 2.9, 3.5	25	3.0 ± 0.4	3.9 ± 0.5
	2	CH_2	5.1	4.3	4.4	3.7	8	1.7 ± 0.2	2.3 ± 0.4
	2'	CH_2	5.6	5.0	4.5	4.4	8	1.6 ± 0.2	2.2 ± 0.4
	4	Aromatic	5.8	6.2	5.6	4.9	8	1.5 ± 0.2	2.1 ± 0.3
	5,6	Aromatic	6.6	4.8, 5.7	5.9, 7.1	5.8, 6.4	16	1.2 ± 0.2	1.5 ± 0.3
	3	Aromatic	7.3	6.0	7.5	6.3	8	0.8 ± 0.1	1.1 ± 0.1
	9, 10, 11	NH_3	8.1	8.8, 7.5, 6.3	6.0, 7.5, 8.0	6.3, 6.9, 8.3	25	0.7 ± 0.1	0.7 ± 0.1
	-	H_2O	3.0	-	-1.5, 1.8	-1.5, 1.8	3	1.1 ± 0.1	3.0 ± 0.2
3-MOP	1, 1', 1''	CH_3	2.4	0.3, 1.8, 2.4	1.1, 2.9, 3.2	1.2, 2.6, 3.1	21	1.5 ± 0.2	2.0 ± 0.3
	2	CH_2	4.5	3.7	5.4	3.8	7	0.9 ± 0.2	1.7 ± 0.5
	2'	CH_2	5.0	4.4	4.3	4.8	7	0.8 ± 0.2	1.7 ± 0.5
	3, 4, 5, 6	Aromatic	6.5	5.6, 5.7, 5.4, 5.8	5.9, 5.9, 6.2, 6.6	6.2, 6.3, 6.5, 5.8	28	0.8 ± 0.1	1.4 ± 0.2
	9, 10, 11	NH_3	7.9	6.6, 7.7, 7.9	6.4, 7.0, 9.0	6.6, 7.1, 8.5	21	0.4 ± 0.1	0.7 ± 0.1
	-	H_2O	3.4	-	0.4, 0.6^a		9	0.8 ± 0.2	2.7 ± 0.5
	-	H_2O	6.9	-	4.5, 4.5, 4.6, 4.8^a		6	1.4 ± 0.4	1.6 ± 0.3
4-MOP	1, 1', 1''	CH_3	2.8	2.0, 2.3, 2.4	2.2, 2.3, 2.9	2.1, 2.3, 3.1	21	1.2 ± 0.1	1.3 ± 0.1
	2	CH_2	4.6	3.8	4.2	4.8	7	1.1 ± 0.1	1.2 ± 0.1
	2'	CH_2	4.9	4.8	4.6	4.3	7	1.1 ± 0.1	1.2 ± 0.1
	4	Aromatic	5.4	6.6	6.3	6.4	7	1.1 ± 0.1	1.2 ± 0.1
	3, 5, 6	Aromatic	6.7	6.3, 5.8, 5.4	5.4, 6.3, 7.3	6.2, 6.4, 6.8	21	1.3 ± 0.1	1.3 ± 0.1
	9, 10, 11	NH_3	7.5	5.4, 8.5, 5.7	5.2, 7.1, 9.0	6.0, 6.3, 10.3	21	1.0 ± 0.1	1.1 ± 0.1
	-	H_2O	3.2	-	-1.3, 1.1, 1.3^b		8	2.9 ± 0.4	3.1 ± 0.4
	-	H_2O	7.1	-	4.7, 5.1, 5.9, 6.0, 7.5_b		8	1.2 ± 0.1	1.2 ± 0.1

^a The calculated H_2O resonances belong to 3 unique H_2O molecules that have been separated into distinct regions, the shifts in ppm for each molecule are: (4.5, 4.8), (4.6, 0.4), (4.5, 0.6)

^b The calculated H_2O resonances belong to 4 unique H_2O molecules that have been separated into distinct regions, the shifts in ppm for each molecule are: (-1.3, 4.7), (1.1, 5.9), (5.9, 6.0), (1.3, 7.5)

H_2O site in 2-MOP, 3-MOP and 4-MOP at 3.0 ppm, 3.4 ppm and 3.2 ppm respectively.

For quantitative measurements such as these, the relative intensities of each site should match 1:1 across a spectrum (see Table 5.2). If the protons present in the organic molecule are the only ones accounted for, then the quantitation of each spectrum does not match in this case. The addition of one H₂O molecule corrects the 2-MOP spectrum but that is only half the story in 3-MOP and 4-MOP; the spectra still exhibit intensity which is unaccounted for at ~7 ppm. H₂O resonances can be seen between the aromatic and amine sites at 6.9 ppm and 7.1 ppm for 3-MOP and 4-MOP respectively. The relative amounts across the three systems predict a single H₂O molecule to be present in 2-MOP, 3 to be present in 3-MOP and 4 to be present in 4-MOP.

These H₂O resonances from experiment can be compared to those predicted from the DFT calculations ran on the complete water containing MOP cells. In 2-MOP, 2 H₂O molecules were predicted using AIRSS. Whilst this is not consistent with the experiment (which only shows one), it is likely that certain dynamics are not accounted for in the DFT as these calculations assume 0 K conditions and these measurements were taken at room temperature. In a dynamic system there may be sufficient motion in either the cell or the water molecules themselves meaning that only a single molecule can be present. The predicted shift of the two molecules is (-1.5, 1.8) ppm for both. This again is a little shielded compared to the experiment but it does show that there is a single resonance at lower shift which corroborates the assertion that this additional resonance is water.

In the 3-MOP, AIRSS predicts 3 H₂O molecules, the calculations this time showed that the two regions at higher and lower shift don't arise from separate molecules but from the degree of hydrogen bonding on the individual protons of each water. The shifts for each molecule are (4.5, 4.8) ppm, (4.6, 0.4) ppm and (4.5, 0.6) ppm. The higher shifts are caused by either hydrogen bonding to the bromine ions of the inorganic lattice, to other adjacent water molecules or in the case of the third molecule to the oxygen atom in the organic MBA. There are two discrepancies that once again can be explained by additional dynamics at room temperature. One is that the isotropic shifts for both regions are shielded by ~2 ppm, but again we are seeing two distinct regions which is consistent with the ¹H NMR. The other point is that the ratio of highly shifted and low shifted protons is 2:1 whereas the NMR clearly shows it is 1:2.

Dynamic spinning water molecules at room temperature would likely cause the majority of the protons in the water molecules to experience an effective increase in electron density thus causing increased shielding and thus a lower isotropic shift. These three water molecules effectively form a bridge between the inorganic and organic parts of the perovskite. Hydrogen bonding between the bromine ions, then each other and then the oxygen of the organic. This additional relaxation pathway would not only lead to faster T_1 and $T_{1\rho}$ relaxation but also may hinder the formation of strongly bound excitons in 3-MOP. This pathway is not present in 2-MOP which may explain why it can so easily form these strongly bound states and therefore produce luminescence across the visible light region.

A similar phenomenon occurs in 4-MOP; AIRSS this time predicts that 4 water molecules are present. The shifts for each water molecule are (-1.3, 4.7) ppm, (1.1, 5.9) ppm, (5.9, 6.0) ppm and (1.3, 7.5) ppm. The hydrogen bonding for the greater isotropic shifts again arise from either bonding to adjacent water molecules or the organic bromine ions. A single proton is near the oxygen of the organic but it is not close enough to experience significant deshielding as the predicted shift is 1.3 ppm. The same arguments for dynamics at room temperature not being accounted for in the calculations of the isotropic shift positions can be applied in this case, and again the ratios of protons at each shift experimentally is 1:1 whereas here it is 5:3. The water molecules again form a network, hydrogen bonding between the inorganic octahedral, themselves and then the organic and thus hindering the formation of strongly bound excitonic states.

Table 5.3 ^{13}C NMR isotropic shifts and comparative DFT values from the incomplete MOP structures and the complete, water containing, structures. $T_{1\rho}$ relaxation times were also measured for 2-MOP, 3-MOP and 4-MOP. The relaxation times for the 2-MOP system is on average three times slower than its narrowband LED counterparts.

System	Resonance no.	Functional Group	^{13}C δ_{iso} (ppm)	^{13}C Calculated Resonance H_2O excluded (ppm)	^{13}C Calculated Resonance H_2O included (ppm)		^1H $T_{1\rho}$ (s)
					1	2	
2-MOP	1	CH_3	54	50	56	56	0.33 ± 0.03
	2	CH_2	45	40	49	47	0.35 ± 0.09
	3	Aromatic	108	103	106	107	0.35 ± 0.06
	4	Aromatic	134	113	131	127	0.37 ± 0.06
	5	Aromatic	118	130	113	115	0.33 ± 0.09
	6	Aromatic	130	126	131	133	0.40 ± 0.12
	7	Aromatic	121	116	118	116	0.30 ± 0.05
	8	Aromatic	158	155	157	155	0.25 ± 0.07
3-MOP	1	CH_3	48	50	56	56	0.09 ± 0.02
	2	CH_2	38	40	46	48	0.12 ± 0.01
	3	Aromatic	124	117	116	114	0.09 ± 0.02
	4	Aromatic	113	106	127	126	0.12 ± 0.02
	5	Aromatic	116	125	119	118	0.09 ± 0.02
	6	Aromatic	105	128	108	110	0.09 ± 0.02
	7	Aromatic	127	114	133	132	0.10 ± 0.02
	8	Aromatic	154	156	155	157	0.09 ± 0.03
4-MOP	1	CH_3	56	62	59	58	0.07 ± 0.02
	2	CH_2	45	45	49	45	0.06 ± 0.01
	3	Aromatic	133	109	131	130	0.06 ± 0.01
	4	Aromatic	118	120	107	110	0.07 ± 0.01
	5	Aromatic	111	137	113	114	0.06 ± 0.01
	6	Aromatic	131	135	127	130	0.07 ± 0.01
	7	Aromatic	122	127	120	120	0.06 ± 0.01
	8	Aromatic	159	161	155	155	0.07 ± 0.01

Another strong case for these complete cells being closer in structure to the real system lies in the accuracy of the calculated ^{13}C isotropic shifts when compared to the ^{13}C NMR. On average each resonance is within 2-3 ppm of the experimental data, whereas DFT from the incomplete structures are on average 6-7 ppm away, see Table 5.3.

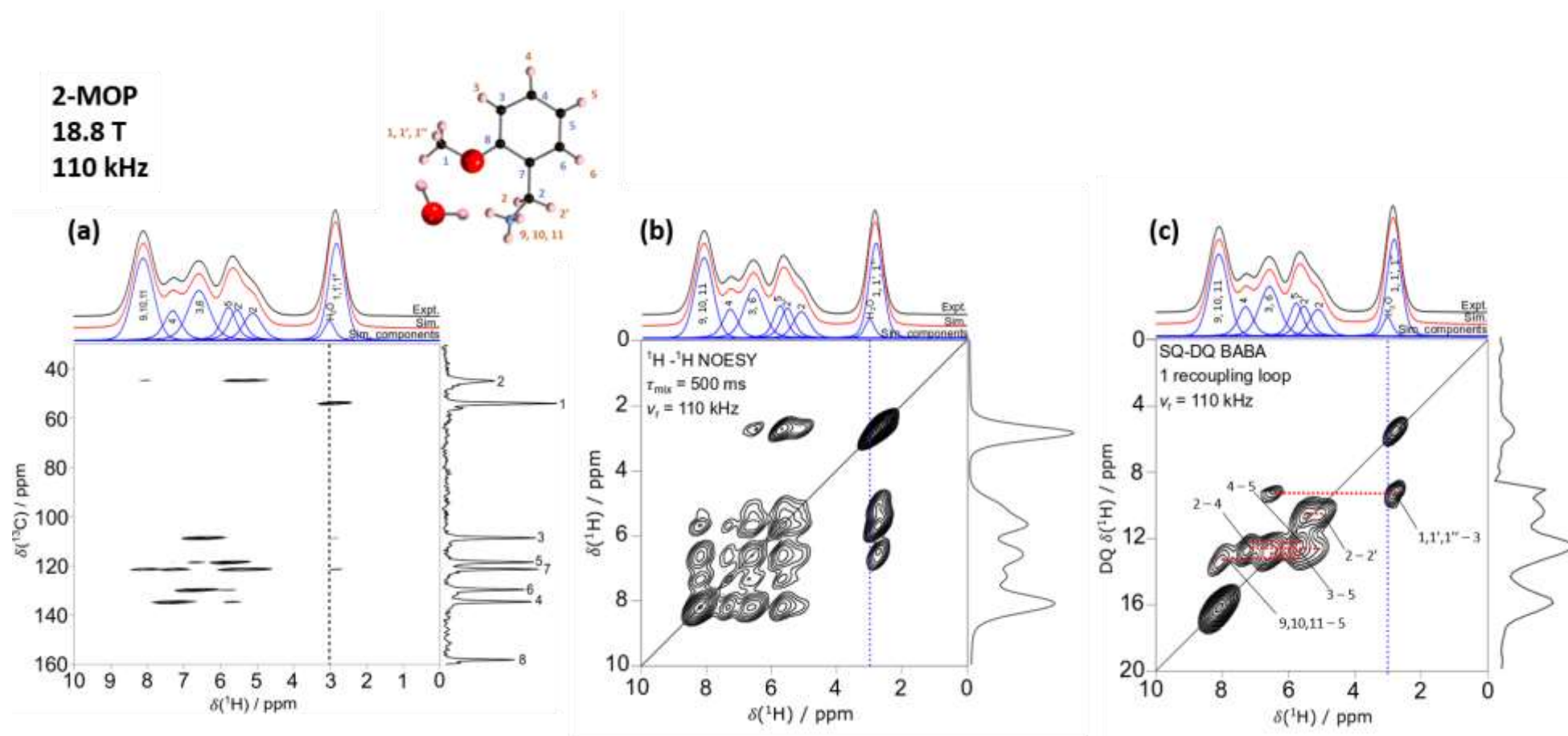


Figure 5.7 2-MOP 2D spectra (a) ^1H - ^{13}C HETCOR using 2 ms contact times, (b) ^1H - ^1H NOESY using a contact time of 500 ms and (c) SQ-DQ BABA using 1 recoupling loop. The black dotted line in (a) is used as a guide to indicate a lack of major correlations and the blue dotted lines in (b) and (c) show the same.

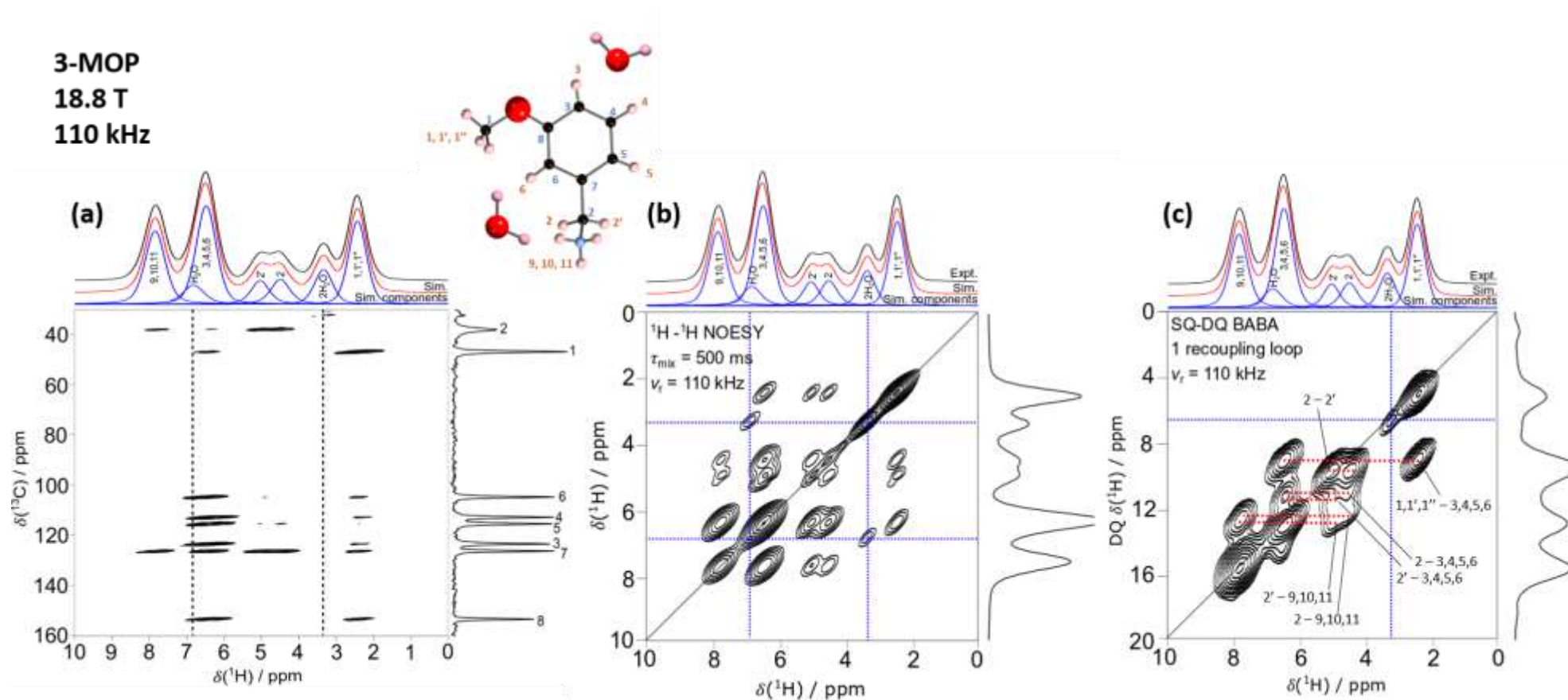


Figure 5.8 3-MOP 2D spectra (a) ^1H - ^{13}C HETCOR using 2 ms contact times, (b) ^1H - ^1H NOESY using a contact time of 500 ms and (c) SQ-DQ BABA using 1 recoupling loop. The black dotted line in (a) is used as a guide to indicate a lack of major correlations and the blue dotted lines in (b) and (c) show water-water correlations.

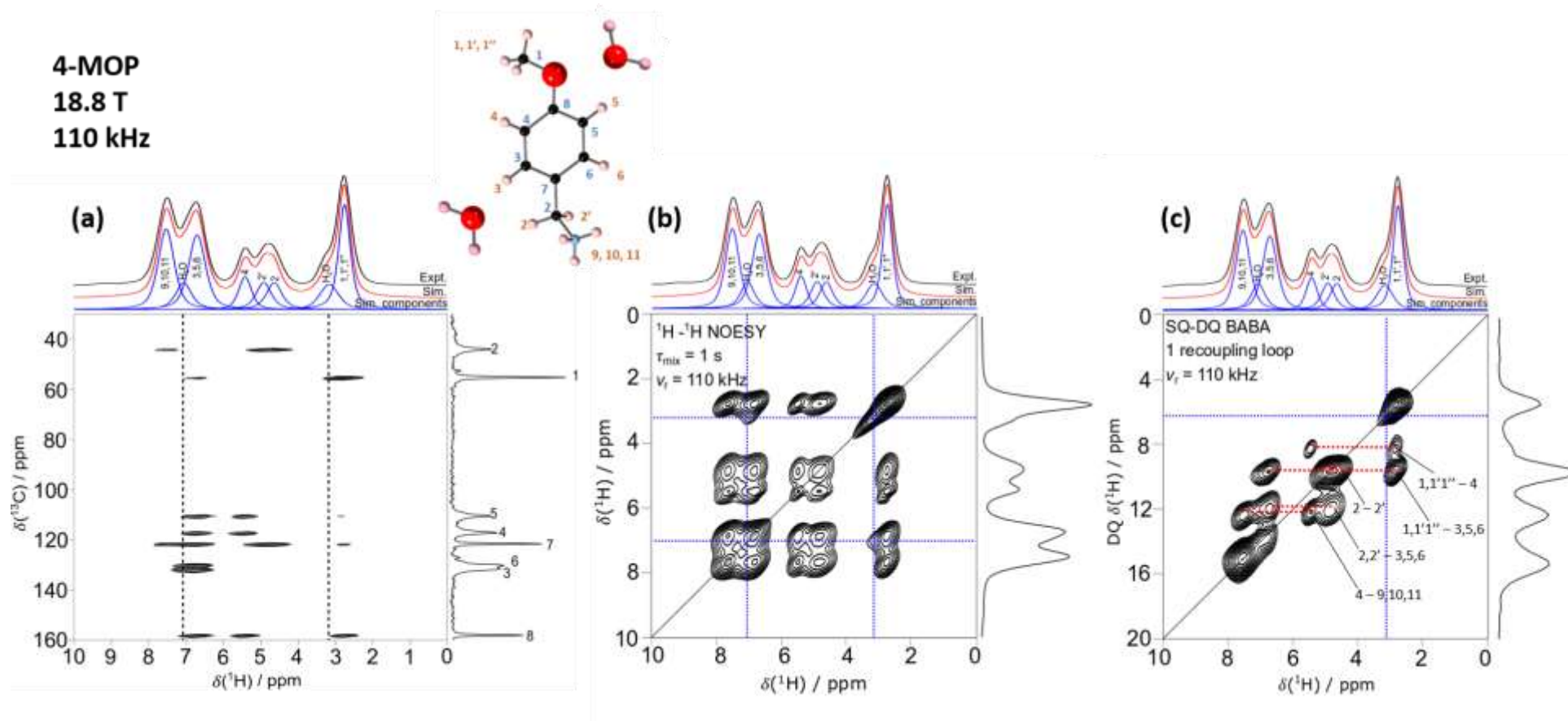


Figure 5.9 4-MOP 2D spectra (a) ^1H - ^{13}C HETCOR using 2 ms contact times, (b) ^1H - ^1H NOESY using a contact time of 1 s and (c) SQ-DQ BABA using 1 recoupling loop. The black dotted line in (a) is used as a guide to indicate a lack of major correlations and the blue dotted lines in (b) and (c) show water-water correlations.

5.3.4 HETCOR, BABA and NOESY studies

The assignments asserted in Figure 5.6 have all been verified using the correlations seen in the 2D HETCOR data, with the aid of 2D ^1H - ^1H NOESY and SQ-DQ BABA data (Figure 5.7, Figure 5.8 and Figure 5.9). The HETCOR spectra support the assignment of the non-hydrogen bonded H_2O sites in 3-MOP and 4-MOP, due to the lack of any major correlations to any carbon sites. The hydrogen bonded H_2O resonances may have some overlap of correlations with certain aromatic carbon regions however there is no further compelling evidence for or against this.

The SQ-DQ BABA in all three systems do not show any correlations for the low shifted H_2O resonance. BABA spectra show through-bond interactions, so the assertion here is that these water molecules are not directly bonded to the organic or another water molecule.

The ^1H - ^1H NOESY data for 3-MOP (Figure 5.8b) does however confirm the presence of the second H_2O resonance since, at a higher mixing time of 500 ms, the only cross-peak correlation observed for the low shifted H_2O is with the hydrogen bonded site, indicating that it is the only molecule close in space to it. This same correlation is seen in the 4-MOP system for the corresponding NOESY data with a 1 s mixing time, Figure 5.9b. This H_2O - H_2O correlation is not seen in the 2-MOP NOESY spectrum, further supporting the lack of any strongly hydrogen bonded H_2O molecules being present in the system.

5.3.5 T_1 , $T_{1\rho}$ relaxation and ^{207}Pb MAS NMR studies

^1H T_1 and $T_{1\rho}$ measurements (Table 5.2 and Table 5.3) have been measured to assess the dynamics of the MOP systems and how that may affect their properties. The T_1 times for 3-MOP and 4-MOP, taken at 14.1 T and 18.8 T, (Table 5.2) are very similar for all sites except for the non-hydrogen bonded H_2O sites, which are on average 3 times longer than the other resonances, (2.7 ± 0.5) s and (3.1 ± 0.4) s respectively. 2-MOP on average has longer T_1 times owing to its more rigid structure which is caused by the greater degree of octahedral tilting present in the organic, when compared to the other systems. It does however share similar relaxation times for the

non-hydrogen bonded H₂O at (3.0 ± 0.2) s, see Figure 5.10. The non-hydrogen bonded H₂O molecules likely have longer T_1 times due to the lack of any significant bonding, thus they have fewer relaxation pathways.

There are significant differences in the $T_{1\rho}$ relaxation times (Table 5.3 and Figure 5.10) across the three systems, as 3-MOP and 4-MOP have an average relaxation time of 0.1 s whilst in 2-MOP they have a far longer average relaxation time of 0.3 s. This is to be expected since the ¹H 1D NMR indicates there is a similar amount of H₂O in 3-MOP and 4-MOP that is significantly greater than the amount present in the 2-MOP measurements. The shorter $T_{1\rho}$ times of 3-MOP and 4-MOP can be attributed to weak dipolar coupling between the H₂O and the organic molecule, which in turn facilitates faster relaxation. This increased molecular motion enabled by the presence of bridging H₂O may also be the cause of the high free exciton to self-trapped exciton ratio seen in 3-MOP and 4-MOP, resulting in their narrow band emission properties. Conversely, 2-MOP has $T_{1\rho}$ values three times longer than that of its counterparts, this indicates slower molecular motion and the lack of the additional coupling facilitated by water may be the reason there is an increased number of self-trapped excitons in the system, ultimately leading to the broadband emission properties it possesses.

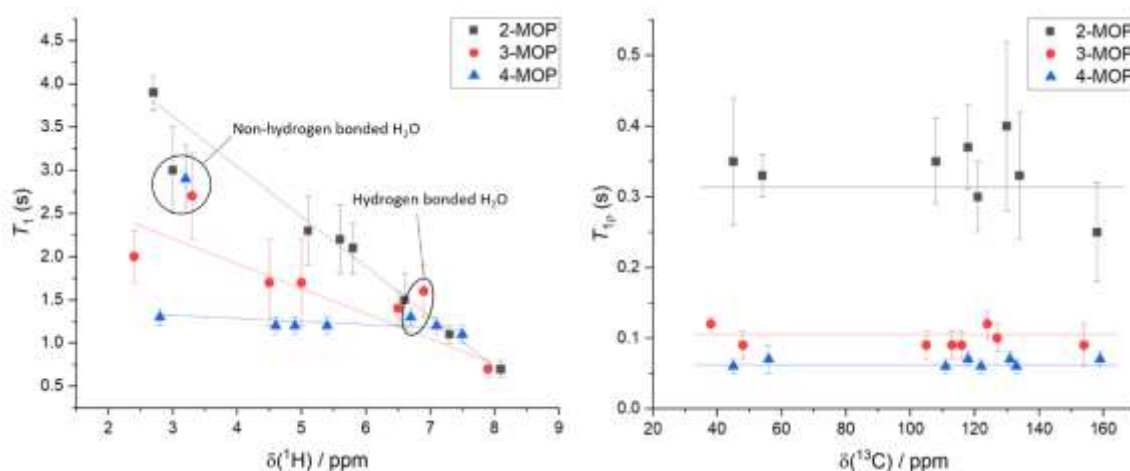


Figure 5.10 T_1 and $T_{1\rho}$ data for 2-MOP, 3-MOP and 4-MOP, the lines going through each data set are guides to show the difference in times clearly and are not lines of best fit.

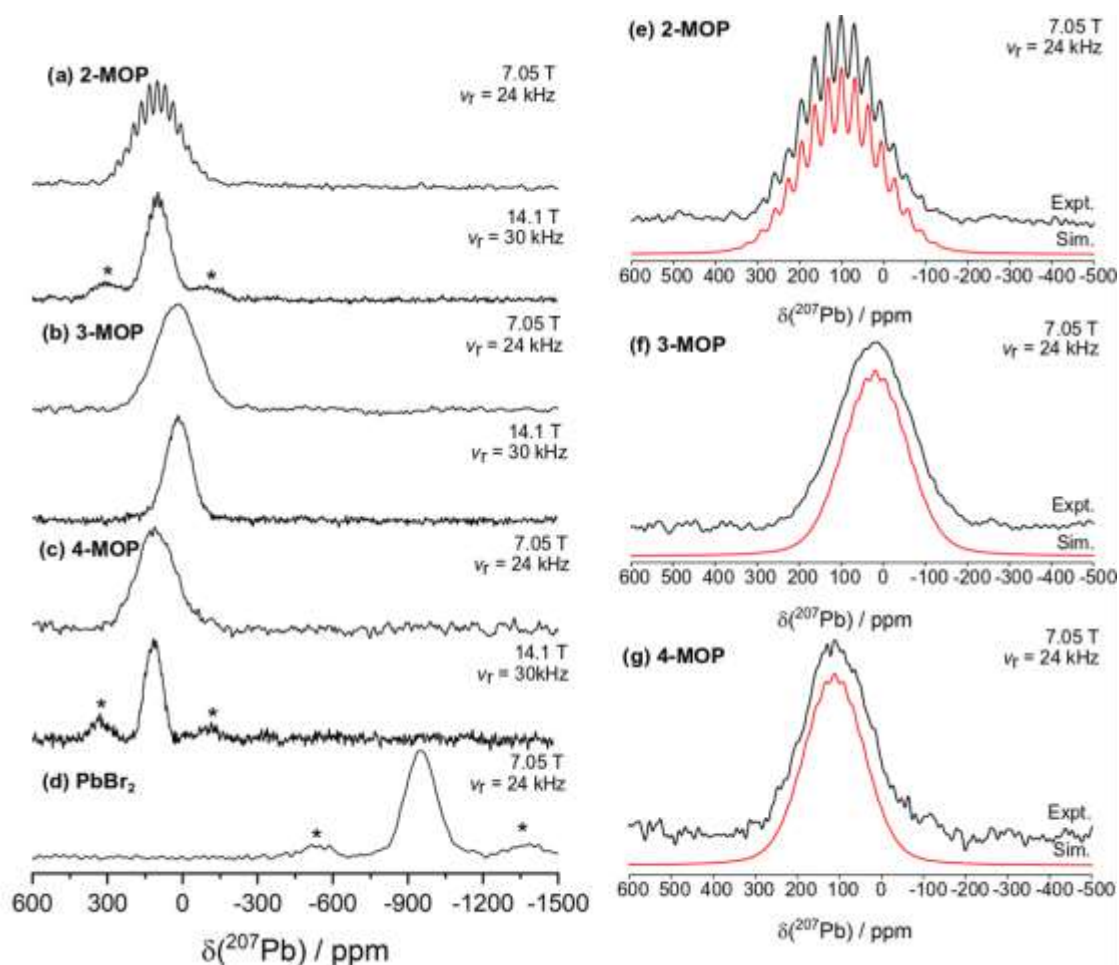


Figure 5.11 ^{207}Pb NMR spectra of the MOP series at 14.1 T and 7.05 T. At higher field a faster spinning speed was employed as the spinning sidebands are more visible. Due to the J -coupling present in 2-MOP the sidebands could not be displaced from the central transition (marked with an asterisk). The 7.05 T spectra have been magnified to better display the extent of J -coupling present; a J -manifold has been fitted for each.

The ^{207}Pb NMR further highlights the slower dynamics of 2-MOP. Due to the titled, yet very ordered, structure J -coupling is observed, Figure 5.11a and 5.11e. This phenomenon in ^{207}Pb NMR has been seen in numerous studies of hybrid perovskites [106–108]. J -coupling gives important information about the covalency and directionality of the Pb-Halide bonding structure in hybrid perovskites, these bonds, and how they are affected by the structure, have been verified using band structure calculations by Goesten and Hoffman [109].

Table 5.4 J -manifold parameters from the ^{207}Pb NMR measurements.

System	δ_{iso} (ppm)	Width (Hz \pm 100 Hz)	J -coupling (Hz \pm 100 Hz)	Average Pb-Br distance (Å)	Average Pb-H distance (Å)
2-MOP	102	1500	2000	3.03	4.47
3-MOP	23	2400	2000	2.99	4.17
4-MOP	113	2200	1400	3.00	4.19
PbBr ₂	-949	-	-	-	-

This J -coupling would likely arise from the bromines coupling to the lead; using the $2nI+1$ rule, where n is the number of coupled atoms and I is the associated spin of said nucleus, we would expect a splitting of 19 peaks (bromine spin = $3/2$ and 6 bromines are present in the octahedral structure). When fitting the 2-MOP spectrum with a J -manifold that includes 19 peaks there arises excellent agreement between the simulation and experimental data. From the simulation, the J -coupling parameter is calculated to be $J(^{207}\text{Pb}, ^{79}\text{Br}) = 2000 \pm 100$ Hz (Table 5.4). This coupling strength is comparable to those reported by Aebli *et. al.* [107] in their Pb and Cs based hybrid perovskites. It has been proposed that extreme tilting in the Pb-X-Pb bonds can obscure J -coupling in these systems, as this would lead to orbital overlap [110,111]. However, the opposite is the case here. Leading from this, it has also been shown that a wide range of bond lengths would also reduce the coupling strength to the individual halides in the octahedra [112]. In the case of the three MOP systems however, the Pb-Br bond lengths are almost entirely uniform, with each possessing two unique but similar distances. These are 2.981 Å and 3.053 Å for 2-MOP, 2.988 Å and 3.000 Å for 3-MOP and 2.998 Å and 3.002 Å for 4-MOP. What is supported is that a near perfect PbX_6 octahedron would produce narrow J -coupling lines compared to a distorted one [108], this is a phenomena present in the 2-MOP spectrum.

No evidence of this coupling is seen for 3-MOP and 4-MOP, it stands to reason that the lack of visible coupling between the lead and bromine is due to their faster dynamics as seen in the T_1 and $T_{1\rho}$ relaxation data. This faster relaxation may be facilitated by the additional hydrogen bonded H_2O molecules and the network they form in the structure. It could also be a result of increased rotational freedom of the organic cations, due to the small degree of titling in the octahedra, this has been shown before via pair distribution function analysis [113]. Liquid like motion, potentially

brought about by the water molecules present, is another factor in the increased dynamics of 3-MOP and 4-MOP. This would cause fast deformation dynamics and therefore inhomogeneously broadened lines, again obscuring the pattern [109].

A few points of similarity for the three systems in the ^{207}Pb NMR is that each peak appears between 0 ppm and 100 ppm which is typical for structures with PbBr_6 octahedrons present. PbBr_2 (Figure 5.11d), the product of these octahedra degrading, appears at -949 ppm which agrees with the literature value [12]. It can therefore be safely assumed that these systems have not degraded even though they show the presence of H_2O molecules. A final point is that the visibility of the spinning sidebands is generally increased at higher fields, but in some samples 3-MOP and 4-MOP in particular, they could not be seen at all due to low intensity.

5.3.6 EXSY studies

As mentioned above, EXSY experiments are used to investigate the exchange rate between individual spins or resonances within a system. Chemical exchange spectroscopy (CEST) is another way to directly measure exchange rates, but in this case they are used to analyse chemical exchange and not just the dipolar exchange seen in an EXSY experiment. EXSY measures rates from $\sim (0.2 - 100) \text{ s}^{-1}$ [114] whereas CEST is the most efficient between $\sim (10 - 300) \text{ s}^{-1}$ [115].

Figure 5.12 and Table A.1 show the exchange rates of the three MOP systems, the correlation labels correspond to the resonances from the ^1H spectra. What is evident is that the majority of the exchange between spins falls only within the EXSY regime, thus there is only dipolar exchange occurring and not chemical exchange. Importantly this is true for the exchanging waters, only dipolar interactions are present. There are some notable exceptions, the 3,5,6 – 9,10,11; 3,5,6 – 4 and 3,5,6 – 2,2' in 4-MOP. These correlations all have exchange rates significantly exceeding the 10 s^{-1} CEST cut-off range. This is likely due to the nature of the arrangement of the 4-MOP organic, the unit cell contains two MBA molecules very close in space with some intermolecular ^1H - ^1H distances being as short as 1.249 \AA . Therefore, the aromatic ring (^1H 's 3,4,5,6) has some degree of chemical exchange between molecules.

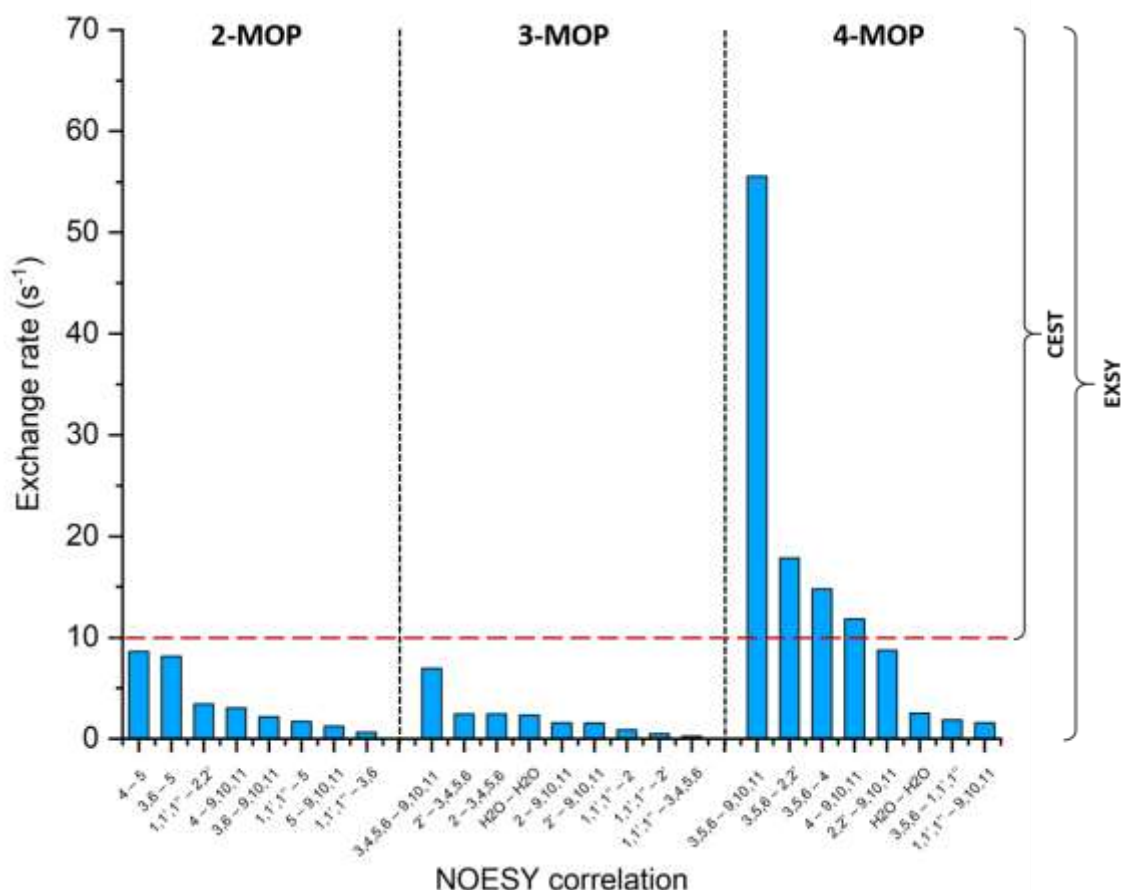


Figure 5.12 Exchange rates calculated from EXSY experiments. The red dotted line shows the starting rate for efficient CEST experiments. The x-axis labels show the NOESY correlations taken from experiment, see Table A.1.

5.4 Conclusion

The MOP series of organic-inorganic hybrid perovskites that possess photoluminescent properties have been characterised using a range of spectroscopic and computational techniques. FTIR spectroscopy shows that there is a band present between 3000 cm⁻¹ to 3200 cm⁻¹ that likely stems from O-H stretching which arises from some form of water in the system. Comparing the pXRD of the powder samples to the simulations from the scXRD shows that there are reflections present that are not predicted by the structures taken from the literature. This is all evidence that points towards the crystal structures being incomplete.

AIRSS was then used to insert water molecules into the unit cell of each system, ensuring that the number of molecules chosen was the most energetically favourable

for the structure. Comparing this with the experimental results from 1D ^1H NMR the final water molecule count for 2-MOP was 2 for 3-MOP 3, and for 4-MOP 4. These final structures were then used for DFT calculations to predict isotropic chemical shifts, the predicted shifts matched excellently with the ^1H NMR spectra and also predicted two regions of hydrogen-bonded and non-hydrogen-bonded water. These combined studies are strong evidence for the presence of crystallographic water in hybrid perovskites; in which, the systems have not degraded. Further evidence comes from the 2D ^1H - ^1H NOESY NMR, the spectra for 3-MOP and 4-MOP clearly show a singular correlation between the two water resonances and no correlations to any part of the organic molecule. In tandem the NOESY spectra of 2-MOP confirms the presence of only a single water resonance residing close to the CH_3 group of the organic. Again showing the distinct differences between the three hybrid perovskites as 2-MOP is a broadband emitter whereas 3-MOP and 4-MOP produce narrowband emissions.

Relaxation studies further support these differences as the average of both the T_1 and $T_{1\rho}$ times are longer for 2-MOP. This is particularly prominent in the $T_{1\rho}$ times as they are ~ 3 times longer than 3-MOP and 4-MOP. The faster relaxation in 3-MOP and 4-MOP is likely a result of the large amount of dipolar exchanging water molecules in the structure, thus providing additional relaxation pathways. This additional relaxation likely causes there to be shorter lived self-trapped excitons in the system and therefore narrowband emission. This is also supported by ^{207}Pb NMR, which in addition shows that the systems have not degraded to PbBr_2 based on their isotropic shifts. Only 2-MOP displays J -coupling, and as the bond lengths are reasonably uniform across the three systems, this is due to the more rigid structure and slower dynamics. Again the lack of this coupling in 3-MOP and 4-MOP is solely due to the increased dynamics, which reduce the coupling strength and broaden any present coupling, thus the J -manifold is not resolved.

Whilst the EXSY data does not provide any additional structural information, it does give an indication as to the nature of the H_2O - H_2O interactions. They are likely solely undergoing dipolar exchange and not chemical exchange.

In summary, 2-MOP, 3-MOP and 4-MOP are a series of hybrid perovskites that contain crystallographic water but have not degraded into PbBr_2 . The exchanging water in 3-MOP and 4-MOP causes faster dynamics than in 2-MOP and likely facilitate shorter self-trapped exciton lifetimes, thus narrowband emission. 2-MOP is a rigid, slow relaxing structure that does not possess exchanging water molecules and thus has a much higher self-trapped to free exciton ratio and therefore has broadband emission properties.

1D and 2D solid state NMR have proved a valuable tool in probing the local structure of these hybrid perovskites. Even going as far as to aid in completing crystal structures and investigating the dynamics in such a way to explain their emission properties. This suite of NMR techniques paired with the other characterisation methods will be a useful approach to investigating other hybrid perovskites in the future.

Chapter 6: An investigation of hybrid perovskites with optoelectronic properties

6.1 Introduction

A great amount of interest has recently been taken in metal halide perovskites as light-harvesting or light-capturing semiconductors due to their superior optical and electrical properties, ease of fabrication, relatively low processing cost, and ease of bandgap tuning [116–119]. Popular applications include photovoltaics, solar-to-fuel energy conversion devices, quantum dots and LEDs [92,120–123]. Metal halide perovskites based on organic cations provide a viable option for the latter since they are easily solution-processed, they require no high-temperature heating, and they have an optical bandgap that is tuneable in the visible to infrared regions by altering chemical composition [124–127]. The photoluminescent property is thought to be the result of a balance between free and self-trapped exciton emissive states which produce either broad or narrow band emission in 1D, 2D and 3D hybrid perovskites [128,129]. Hu *et. al.* [93] reported the existence of room temperature phosphorescence (RTP) from the triplet states of the organic cations in a hybrid perovskite with mixed cations, and S. Yang *et. al.* [130] also showed highly efficient RTP from organic fluorophores used as the cations in 2D hybrid perovskites. The confirmation of RTP reveals a whole new field of research into hybrid perovskites that might benefit from these emissive properties of the organics – such as broad band emission and long-lived RTP [131].

Previous studies on the hybrid halide perovskite $\text{CH}_3\text{NH}_3\text{PbI}_3$ have revealed that orientation of the organic cation plays a fundamental role in determining the material's electronic properties via distortion of the PbI_6 octahedral cage [132]. Such molecular rotations induce a dynamical change of the band structure that may partially account for the perovskite's unique properties of slow carrier recombination and high conversion efficiency [133].

Du and Mitzi *et. al.* [134,135] highlight the versatility and robust nature of hybrid organic-inorganic perovskites. For 2D structures using organics that typically are employed for their photoluminescent and phosphorescent properties, $(\text{PMA})_2\text{PbCl}_4$, $(\text{PEA})_2\text{PbCl}_4$ (Figure 6.1d and 6.1e), they demonstrate their additional piezoelectric properties. In the piezoelectric context these systems can be used as low-cost solution-processed Complementary Metal-Oxide Semiconductor (CMOS)- compatible Micro-Electro-Mechanical Systems (MEMS). They also investigate structures containing a double benzene ring molecule, 1-(2-naphthyl)methan ammonium (here referred to as NMA-2) and 2-(2-naphthyl)ethan ammonium (NEA) – Figure 6.1b and Figure 6.1c. These are an excellent example of how a small alteration to the organic can affect the

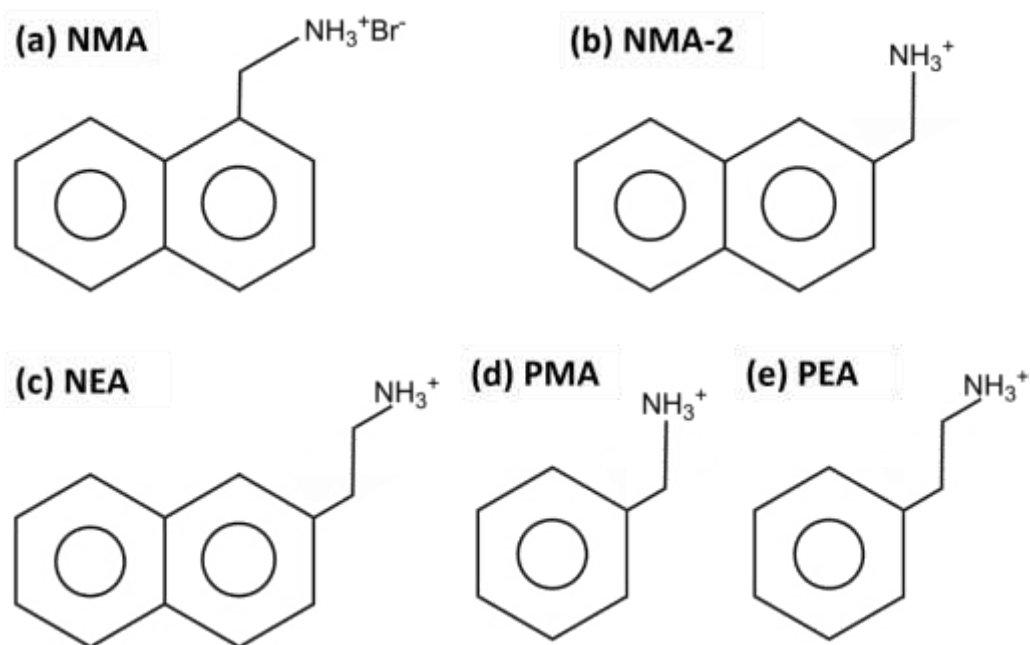


Figure 6.1 Organics used in hybrid perovskite systems (a) the NMA organic used by Hu *et. al.*, (b) the NMA organic used by Du *et. al.* (c) the NEA organic, (d) the PMA organic and (e) the PEA organic.

properties of these systems. They show that the molecules have varying effects on the distortion of the lead-halide octahedral lattice which leads to changes in the width of the valence and conduction bands – thus altering the band gap size. The small structural difference between NMA-2 and NEA leads to the NMA-2 producing a broadband (or white) emission whereas NEA produces a narrowband emission. The NMA-2 is an excellent example and comparison to the work presented in this thesis of fine tuning a material to alter its properties

This study centres around a newly developed lead bromide perovskite based on a naphthalenemethylammonium (NMA) cation, Figure 6.1a, denoted $(\text{NMA})_2\text{PbBr}_4$. Initial phosphorescence studies on an NMA based lead halide perovskite showed three distinct emission peaks ranging from blue to green regions. This emission range means the compound is an excellent emitter of sky-blue light. Also observed are long lifetime photoluminescent properties which suggest the feasibility of applications in data storage and security [93]. Despite the discovery of such properties, little is known about the local structure of this system. Relating structure to properties not only allows one to understand dynamics within these materials, but also to predict new perovskite structures with high performance [136]. Due to a high-level of disorder within this crystal system long-range spectroscopic techniques, such as scXRD, cannot provide any useable data. Solid-state NMR, which provides information about the local structure, is the primary spectroscopic technique used in this study. 2D NMR correlation methods are used in order to gain dynamic stereographic information [137] and hence support the presence of organic cation conformers within the crystal structure. Comparisons are drawn to the organic bromide salt NMABr, Figure 6.1a, which adopts a monoclinic P_{21} space group and possesses a high-level of long-range order such that X-ray diffraction techniques are useful.

6.2 Materials and Methods

6.2.1 Materials

Naphthalenemethylammonium bromide (NMABr) was synthesized by adding HBr (48wt% in water) into naphthalenemethylamine in ethanol at 0 °C (molar ratio of amine to HBr = 1:1.2). The crude product was obtained by slowly evaporating the solvent under reduced pressure. The white precipitate was then dissolved in ethanol

and recrystallized by slowly adding diethyl ether. The precipitate was further washed with diethyl ether several times before drying them in a vacuum oven. After drying overnight, they were all sealed under nitrogen and transferred into a nitrogen-filled glove box for further use.

The perovskite precursor (1 M) was prepared by mixing PbBr_2 with NMABr (1:2 molar ratio) in anhydrous dimethylformamide (DMF). The $(\text{NMA})_2\text{PbBr}_4$ fast preparation was prepared by dropping the precursor solutions into toluene (1:10 volume ratio) followed by centrifugation at 8000 rpm for 15 minutes. The powder was collected and dried in a nitrogen-filled glove box and further annealed at 110 °C for 30 minutes. The $(\text{NMA})_2\text{PbBr}_4$ slow preparation was prepared by dropping the precursor into a glass petri dish and then heated at 80 °C to allow the slow evaporation of the DMF solvent. The completely dried powder was then further annealed at 110 °C for 30 minutes.

6.2.2 Methods

Powder XRD was carried out on a Panalytical X-Pert Pro MPD $\text{Cu K}\alpha_1$ (1.54 Å). A 2θ range of 5° to 130° was used with increments of 0.125°. The data was processed using Highscore plus to correct the baselines of the spectra and remove additional noise.

Single crystal X-ray diffraction was undertaken using a Bruker SMART APEX-II system. The system uses a Mo sealed tube source along with a graphite monochromator to produce X-rays of wavelength 0.71073 Å. Data was solved using SHELXT and refined on F2 using SHELXL in the program suite WinGX.3-5

All FTIR data were collected on a Thermo Fisher iS50R FT-IR spectrometer equipped with a Golden Gate ATR manufactured by Specac. A KBr beamsplitter and a Teflon DGTS detector leading to a spectral resolution of 4 cm^{-1} were used. Spectra were recorded between 600 cm^{-1} and 3500 cm^{-1} .

Raman spectra were measured on a Renishaw inVia Raman microscope using a 785 nm wavelength DPSS laser operating over a 300 – 4000 cm^{-1} wavenumber range. A Renishaw CCD using a manual sample stage was used for detection. A x50 Olympus objective lens was used to focus the beam onto the sample, the system was calibrated

using a silicon reference. A diffraction grating of 1200 l/mm was used. Each scan had a 10 s exposure time and 10 scans were recorded for each sample at 10% laser power.

All 1D and 2D NMR measurements used the same parameters as those in chapter 5.

The DFT calculations utilised the CASTEP17 code which employ a set of plane wave basis sets and Ultrasoft on-the-fly (OTF) pseudopotentials [15]. The calculations performed here used Perdew, Burke and Ernzerhof (PBE) exchange functions, a k-point spacing of 0.05 and a 900 eV kinetic energy cut-off. This set of parameters allowed convergence of the final energy for single point calculations which can then be used for geometry optimisation to fully relax the system within its unit cell constraints. The optimised cell is then utilised to obtain NMR shielding tensors, shifts and electric field tensor values via the ‘Magres’ task that resides within the CASTEP17 code [51–53].

6.3 Results

The NMABr organic has been measured via scXRD, which provides a long-range crystallographic description of the structure, based on average atomic positions over a large number of repeating crystal cells. However, this technique is unable to elucidate short-range atomic interactions, and systems which exhibit even the slightest amount of disorder are unable to be fully characterised. Solid-state NMR offers a viable option for short-range characterisation of such systems, including even singular ^1H 's in complex organic systems. Furthermore, 2D NMR techniques can detect nuclear interactions between proximate nuclei, which reveals stereographic structural information. Acquiring accurate scXRD data also enables the use of DFT calculations, which output theoretical NMR parameters for every nucleus in the unit cell. In the case of the NMABr organic crystal both techniques were used to rigorously characterize the system. As for the $(\text{NMA})_2\text{PbBr}_4$ hybrid perovskite samples, crystals sufficiently large and/or stable enough could not be grown, hence there is a lack of both long-range crystallographic data (via scXRD) and DFT data. Consequently, characterisation of the hybrid perovskite systems in this chapter is solely dependent on NMR, and the scrutiny of the NMR data for these systems must be carefully

considered, and compared with both each other and the starting organic crystal if the conclusions from the data are to be deemed credible.

6.3.1 FTIR and Raman Spectroscopy

FTIR and Raman spectra of the NMABr organic crystal and the 2 preparations of the NMA based hybrid perovskites were recorded to determine the presence of H₂O within the structures. The Raman spectra are analogous to those seen in Chapter 5.3.1 for the MOP series. Figure 6.2b and 6.2c show a zoomed in region of the Raman spectrum around 400 cm⁻¹ and 2000 cm⁻¹ and the full Raman spectra between 400 cm⁻¹ and 3200 cm⁻¹ respectively. Neither spectrum shows the characteristic H-O-H stretching at 1635 cm⁻¹ or the broad O-H stretching that normally is seen between 3200 cm⁻¹ and 3400 cm⁻¹. Much like in the MOP systems, if water is present in the two perovskites then the position of those molecules may lack enough freedom to have observable vibrational modes. The FTIR data, Figure 6.2a, does however show the broad O-H stretching that normally appears between 3100 cm⁻¹ and 3500 cm⁻¹ in the two hybrid perovskites systems. This stretching is also present in the NMABr organic however to

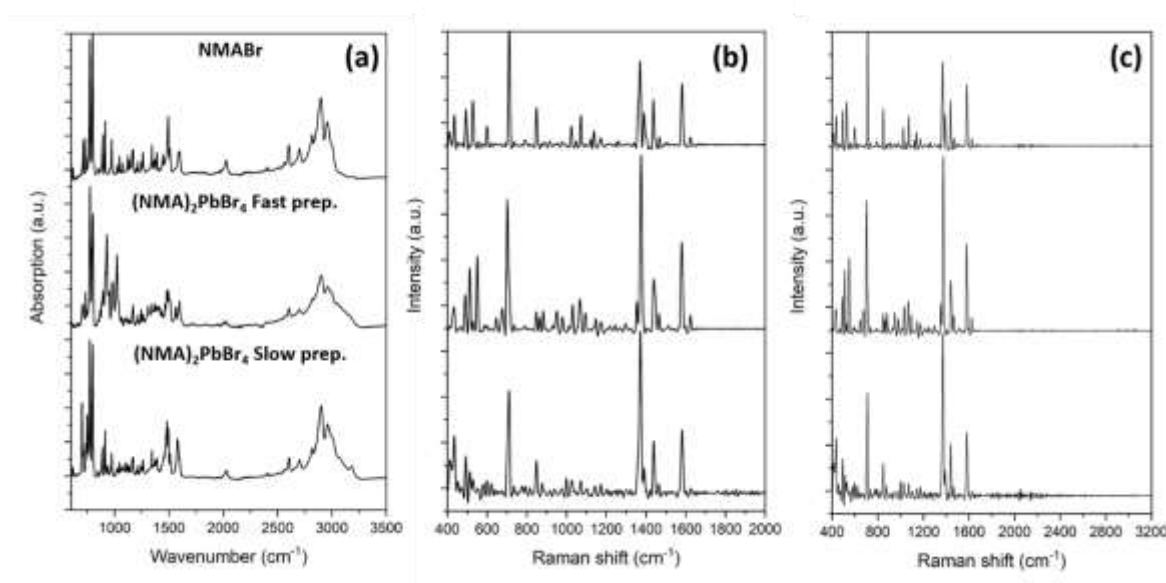


Figure 6.2 Raman and FTIR spectra of the NMABr organic and the slow and fast preparation NMA based perovskites systems. Section a) FTIR of all three systems, showing the fingerprint region and stretching region of N-H and O-H, b) zoomed in spectra showing only the prominent vibrational modes from the organic region c) a Raman spectra showing the full range from the prominent organics up to the O-H stretching region.

a much lesser extent, this indicates that there is water within the system but far less relative to the perovskites.

6.3.2 1D ^1H MAS NMR studies

The assignments for the following ^1H NMR were chosen based on expected shifts of ^1H 's of this type as well as considerable guidance from 2D HETCOR, NOESY and BABA data as well as DFT calculations– this will be presented in the following section.

The ^1H NMR spectra of the three NMA systems, Figure 6.3, all share a characteristic resonance that arises from the NH^{3+} section of the organic, these are labelled as Am1, Am2 and Am3. The narrower resonances seen in the perovskites for this amine group indicate that they have faster dynamics compared to the NMABr organic. As there is no scXRD data for the two perovskites, the packing structures can only be inferred, in the case of the slow preparation the average of the proton shifts is deshielded compared to the fast preparation. This could be a result of a tighter packing structure that causes the organic to be closer to the Br ions in the inorganic lattice.

Table 6.1. ^1H NMR shifts of the NMABr organic and the two NMA based perovskite structures. Also included are the ^1H shifts from DFT calculations of the NMABr, the T_1 times for all three systems and the relative intensity of the simulation components.

System	Resonance no.	Functional Group	Measured Resonance (ppm)	Calculated Resonance (ppm)	Relative Intensity (% $\pm 1\%$)	$^1\text{H } T_1$ (s) 800 MHz	T_1 ratios
NMABr	1	CH_2	2.8	2.6	8	269 ± 16	-
	1'	CH_2	3.4	3.0	8	255 ± 12	-
	4,8	Aromatic	4.7	4.1, 4.8	16	265 ± 10	-
	7	Aromatic	6.1	5.8	8	260 ± 12	-
	3,5	Aromatic	7.1	7.1, 6.8	16	250 ± 9	-
	2	Aromatic	7.5	7.3	8	240 ± 9	-
	6	Aromatic	8.0	7.7	8	242 ± 9	-
	Am1, Am2, Am3	NH_3	9.1	9.1, 8.9, 9.5	24	265 ± 5	-
	-	H_2O	4.3	-	3	265 ± 11	-
$(\text{NMA})_2\text{PbBr}_4$ fast prep.	1	CH_2	2.7	-	9	0.8 ± 0.1 5.2 ± 0.6	4:1
	1', 4, 5	CH_2 , Aromatic, Aromatic	3.2	-	24	0.7 ± 0.1 3.7 ± 0.3	2:1
	2	Aromatic	4.8	-	6	1.2 ± 0.1 14.6 ± 2.0	2:1
	3	Aromatic	3.9	-	7	1.0 ± 0.1 7.7 ± 0.9	3:1
	6	Aromatic	6.7	-	7	3.0 ± 0.3 8.6 ± 0.9	2:1
	7	Aromatic	7.3	-	7	2.6 ± 0.2 6.9 ± 0.6	1:1
	8	Aromatic	8.7	-	9	2.7 ± 0.3 5.5 ± 0.3	1:1
	Am1, Am2, Am3	NH_3	7.7	-	22	3.0 ± 0.4 5.1 ± 0.6	1:1
	-	H_2O	2.3	-	9	0.8 ± 0.1 8.8 ± 1.6	3:1
$(\text{NMA})_2\text{PbBr}_4$ slow prep.	1	CH_2	4.1	-	8	6.3 ± 0.4	-
	1', 4, 5	CH_2 , Aromatic, Aromatic	5.1	-	25	6.2 ± 0.4	-
	2	Aromatic	5.8	-	8	5.3 ± 0.3	-
	7	Aromatic	6.4	-	9	1.2 ± 0.2 5.8 ± 0.4	2:5
	8,3	Aromatic	7.1	-	17	1.0 ± 0.2 5.6 ± 0.3	1:1
	6	Aromatic	7.8	-	8	0.7 ± 0.1 4.9 ± 0.3	2:1
	Am1, Am2, Am3	NH_3	8.3	-	23	0.6 ± 0.1 3.6 ± 0.2	2:1
	-	H_2O	4.6	-	2	6.9 ± 0.4	-

A H₂O resonance has been added when creating the ¹H simulations. This is to account for missing intensity after all of the components of the organic have been accounted

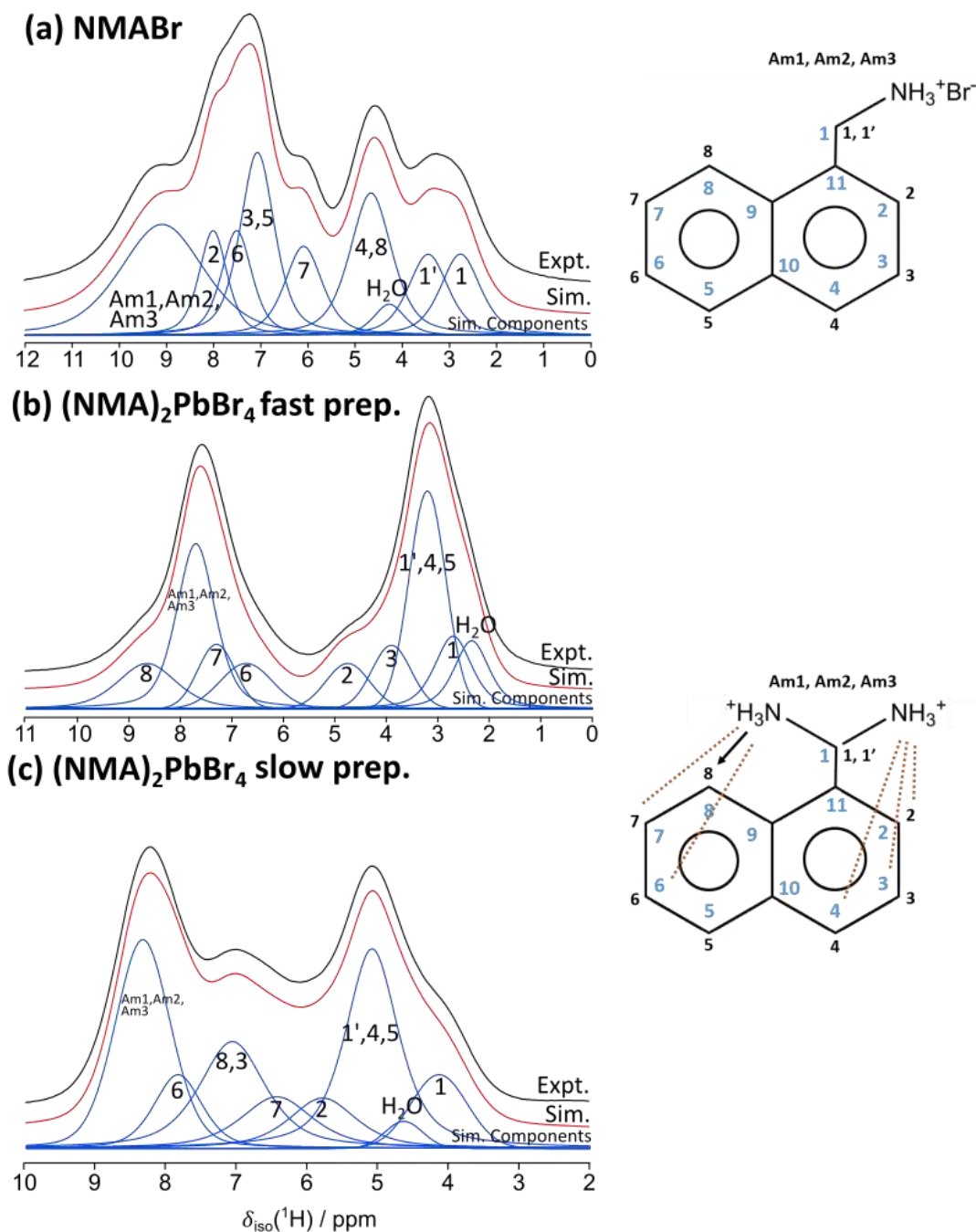


Figure 6.3 1D ¹H NMR of a) the NMABr organic, b) the fast preparation perovskite and c) the slow preparation perovskite. The red lines show the simulated spectra from DmFit and the blue lines are the components of those simulations. The two molecules shown are the NMABr organic (top) and the NMA organic in the perovskites (bottom). The perovskite organic has two NH³⁺ groups to indicate that it displays conformerism.

for. The relative intensity of the H₂O in the NMABr is only 3% and has a shift of 4.3 ppm. It is common for powder samples to adsorb water onto their surfaces when exposed to air, so this resonance could either be from adsorbed water or H₂O introduced during synthesis. The slow preparation perovskite also has a relatively small water contribution to the ¹H spectrum at only 2% and has a shift of 4.6 ppm, it is likely that this resonance is analogous to the one seen in the NMABr organic. The water resonance in the fast preparation however has a relative intensity of 9% and a shift of 2.3 ppm. The near stoichiometric relative intensity and lower shift indicates that this is crystallographic water that is somewhere in the unit cell. The greater amount of water present could also be an explanation for the increased average shielding of the ¹H shifts and why the fast preparation perovskite has narrower resonances compared to the slow preparation.

The nature of these water species will be further investigated in the following section using 2D NMR techniques.

6.3.3 HETCOR studies

Figure 6.4, Figure 6.5 and Figure 6.6 show the HETCOR data for the NMABr organic, and the slow and fast preparation NMA based perovskites respectively. The left section of each figure shows the aliphatic region of the spectrum and the right section the aromatic region. In Figure 6.4 the evidence for the presence of water in the NMABr can be clearly seen. Unlike the MOP series there is a noticeable correlation between the water and part of the organic, in this case the carbon from the CH₂ group. Based on this it can be said that the water, if it is within the crystal structure, is situated very close in space to the CH₂ site. The ¹³C spectra of the NMABr has a region with numerous aromatic carbons that greatly overlap, leading to the aromatic section of the HETCOR being difficult to resolve. To ensure that all of the important correlations can be identified a fairly high floor level has been presented, at this level a great deal of long range correlations can also be identified and are shown with red asterisks. As one would expect the NMABr organic shows only 1-to-1 correlations for each of the ¹H's and ¹³C's.

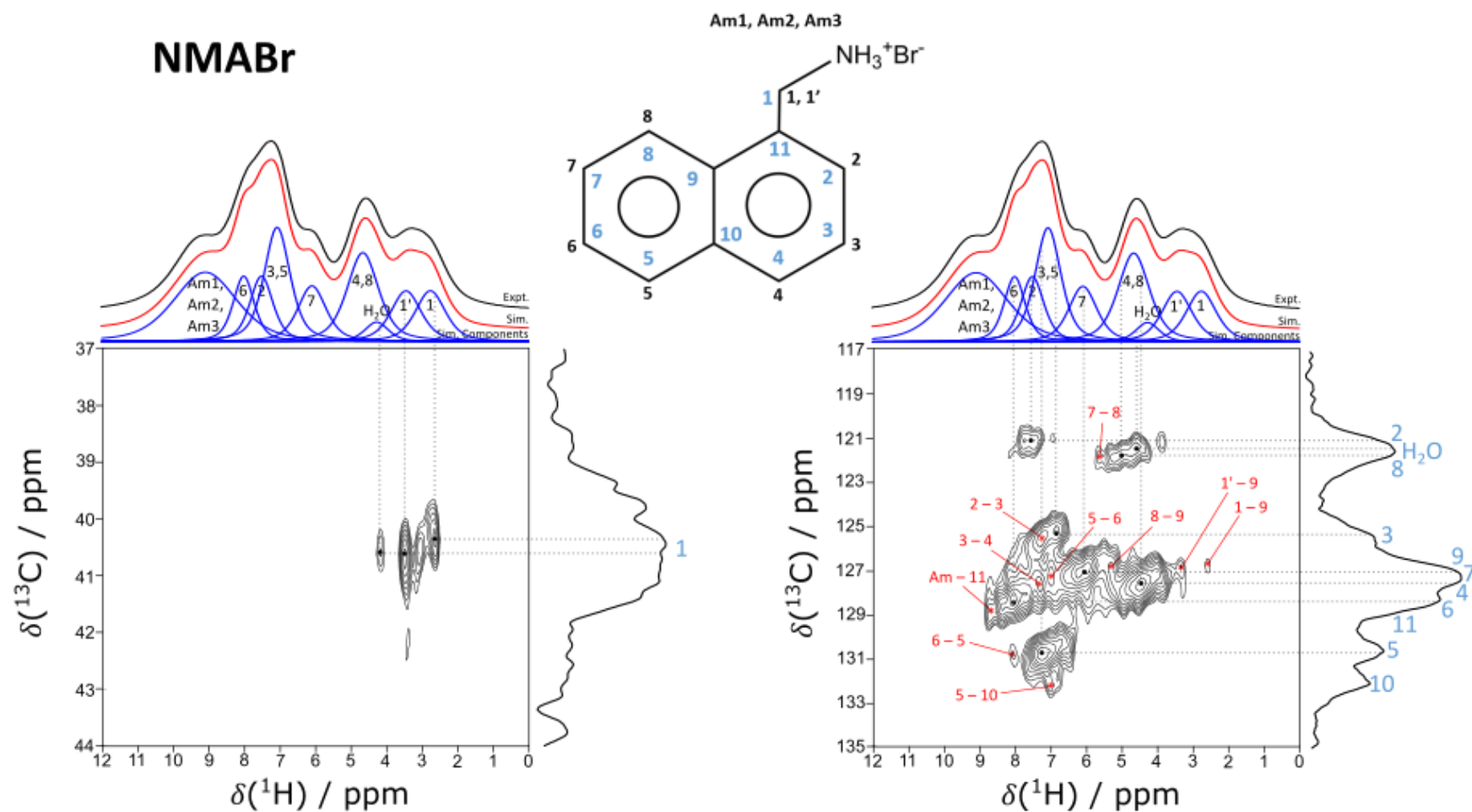


Figure 6.4 HETCOR spectra of the NMABr organic. The left diagram is focussed around the aliphatic region and the right is focussed on the aromatic region. Black dots denote direct correlations between the protons and carbons whereas the red asterisks denote long range correlations.

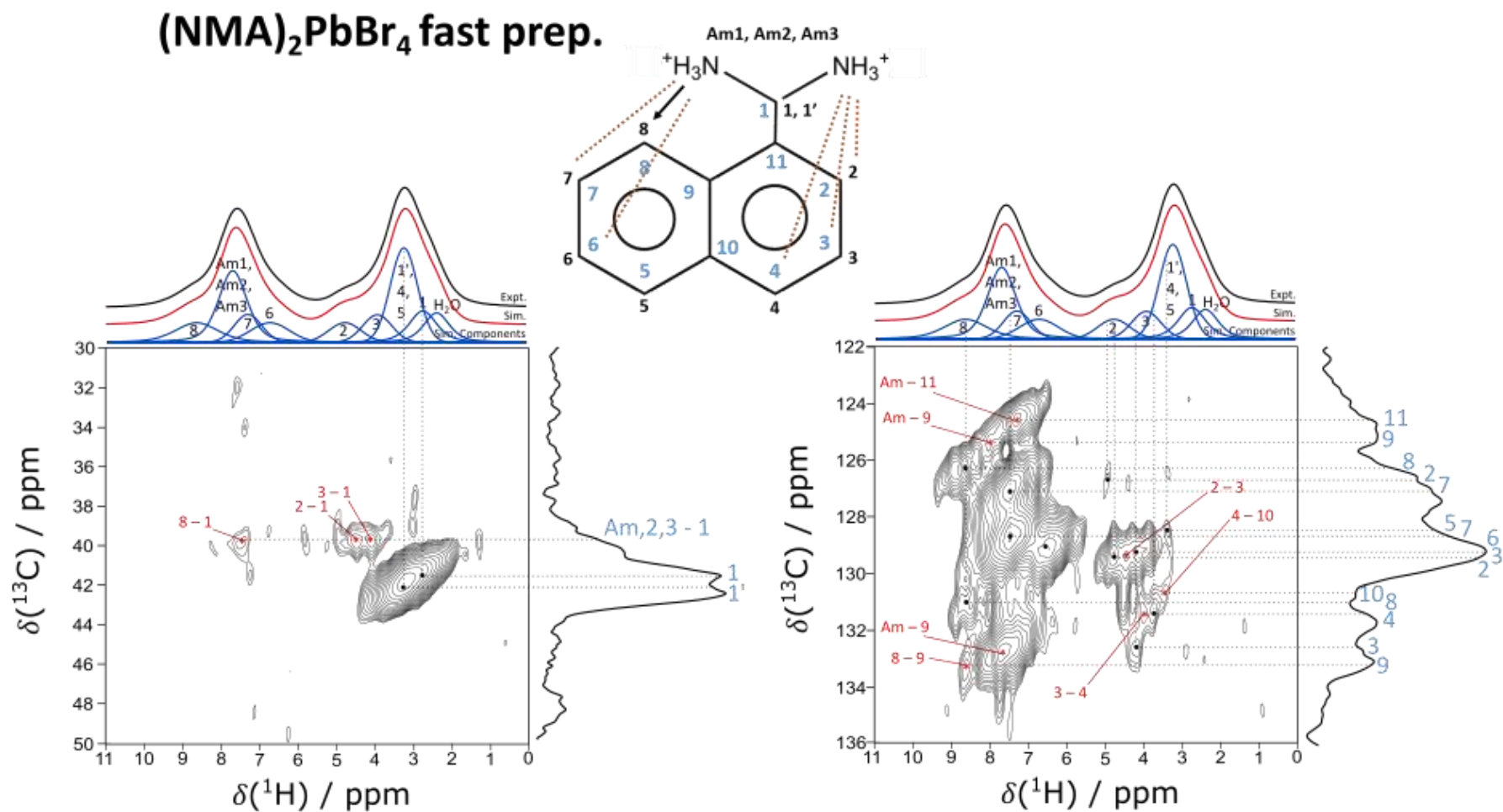


Figure 6.5 HETCOR spectra of the (NMA)₂PbBr₄ fast preparation perovskite. The left diagram is focussed around the aliphatic region and the right is focussed on the aromatic region. Black dots denote direct correlations between the protons and carbons whereas the red asterisks denote long range correlations.

(NMA)₂PbBr₄ slow prep.

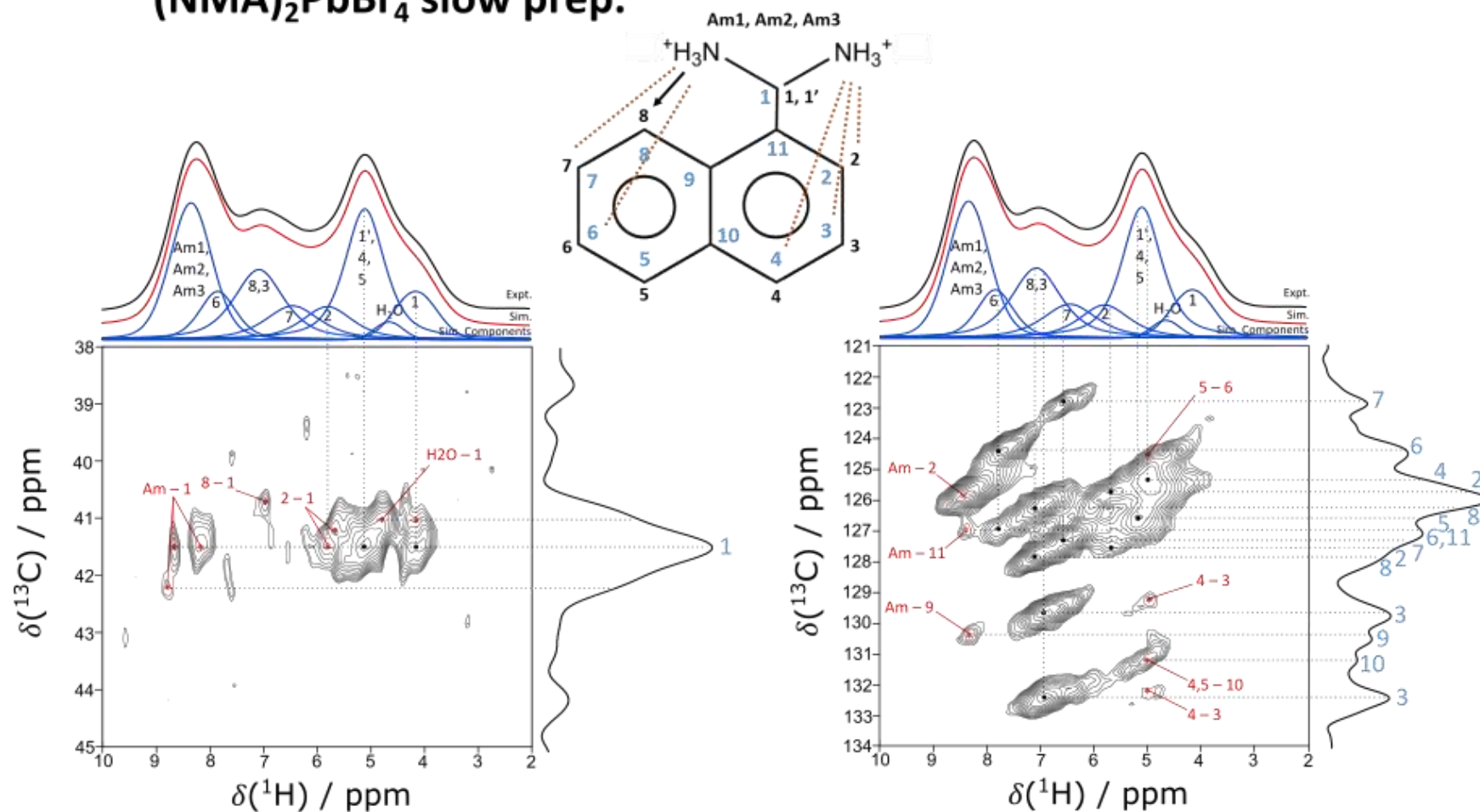


Figure 6.6 HETCOR spectra of the (NMA)₂PbBr₄ slow preparation perovskite. The left diagram is focussed around the aliphatic region and the right is focussed on the aromatic region. Black dots denote direct correlations between the protons and carbons whereas the red asterisks denote long range correlations.

The long range correlations in all of these HETCOR figures proved very useful in identifying the carbon resonances that have no attached ^1H 's. These correlations indicate which ^1H 's are the closest in space and therefore the next carbon along can be identified.

In Figure 6.5 for the fast preparation NMA based perovskite the aliphatic region of the HETCOR shows some long range correlations but also more importantly that there are two slightly differently shifted CH_2 carbon resonances visible at 41.7 ppm and 41.2 ppm. This is likely a product of conformerism of the organic within the perovskite structure. This conformerism is of the NH_3^+ group attached to the CH_2 likely pointing in at least two different directions, as seen in the schematic of the organic in the figure. The influence of this conformerism can be further demonstrated in the aromatic region of the HETCOR. Aromatic ^1H 's 2,3,7 and 8 all show two distinct carbon correlations. These aromatic ^1H 's would be the closest in space within the molecule to the NH_3^+ group and having a significant shift in its position would lead to very different electron densities perturbing these ^1H 's.

Figure 6.6 shows the slow preparation NMA based perovskites HETCOR spectrum. The aliphatic region shows the potential evidence for a secondary carbon site for the CH_2 group, alluding to conformerism. The water resonance, like in the NMABr organic, can also be seen to have a long range correlation with the CH_2 carbon, thus indicating that the molecule is present in space somewhere near this section of the organic within the perovskite. Similarly, to the fast preparation the slow preparation shows two distinct carbon correlations for ^1H 's 2,3,6,7 and 8. Again sizeable shifts of 2-4 ppm between these duplicate correlations are seen. The presence of this conformerism in both the fast and slow preparations is certainly an indicator as to why stable crystals could not be grown for use in scXRD. The conformerism is likely a direct result of placing a relatively large organic within an inorganic perovskite structure, causing the NH_3^+ group to shift from its usual position as seen in the NMABr organic structure.

6.3.4 NOESY and BABA studies

In the NMABr organic, DFT calculations were a prominent aid in assigning the resonances of the ^1H and ^{13}C spectra. As using predicted shifts from DFT was not an option for the perovskite systems, the NOESY and BABA data was vital to assignments alongside the use of the HETCOR spectra.

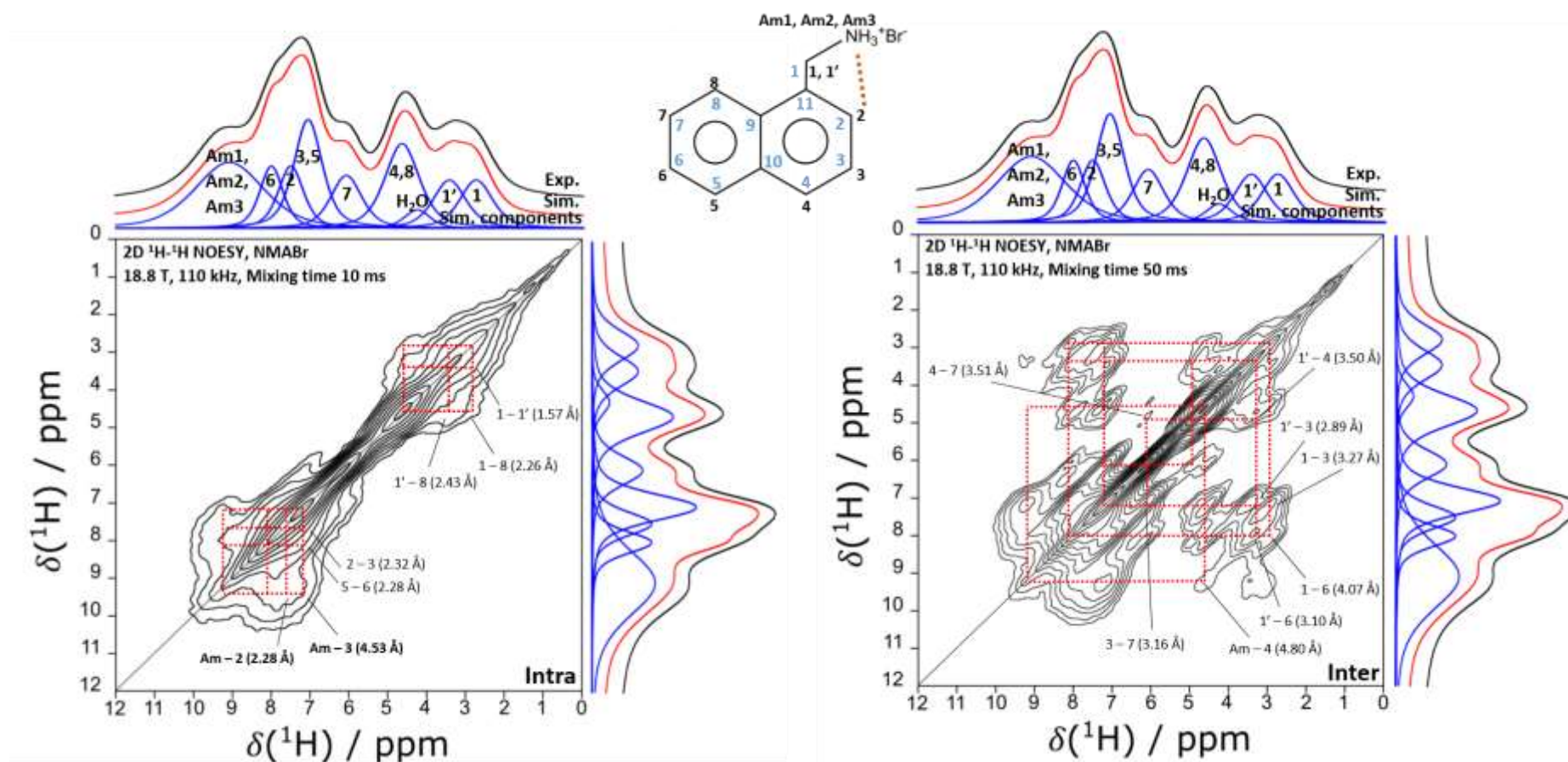


Figure 6.7 NOESY spectra of the NMABr organic. The left spectrum uses a 10 ms mixing time and the right a 50 ms mixing time. Red dotted lines indicate correlations between resonances and the distances in brackets are the distances in space between atoms from the NMABr crystal structure.

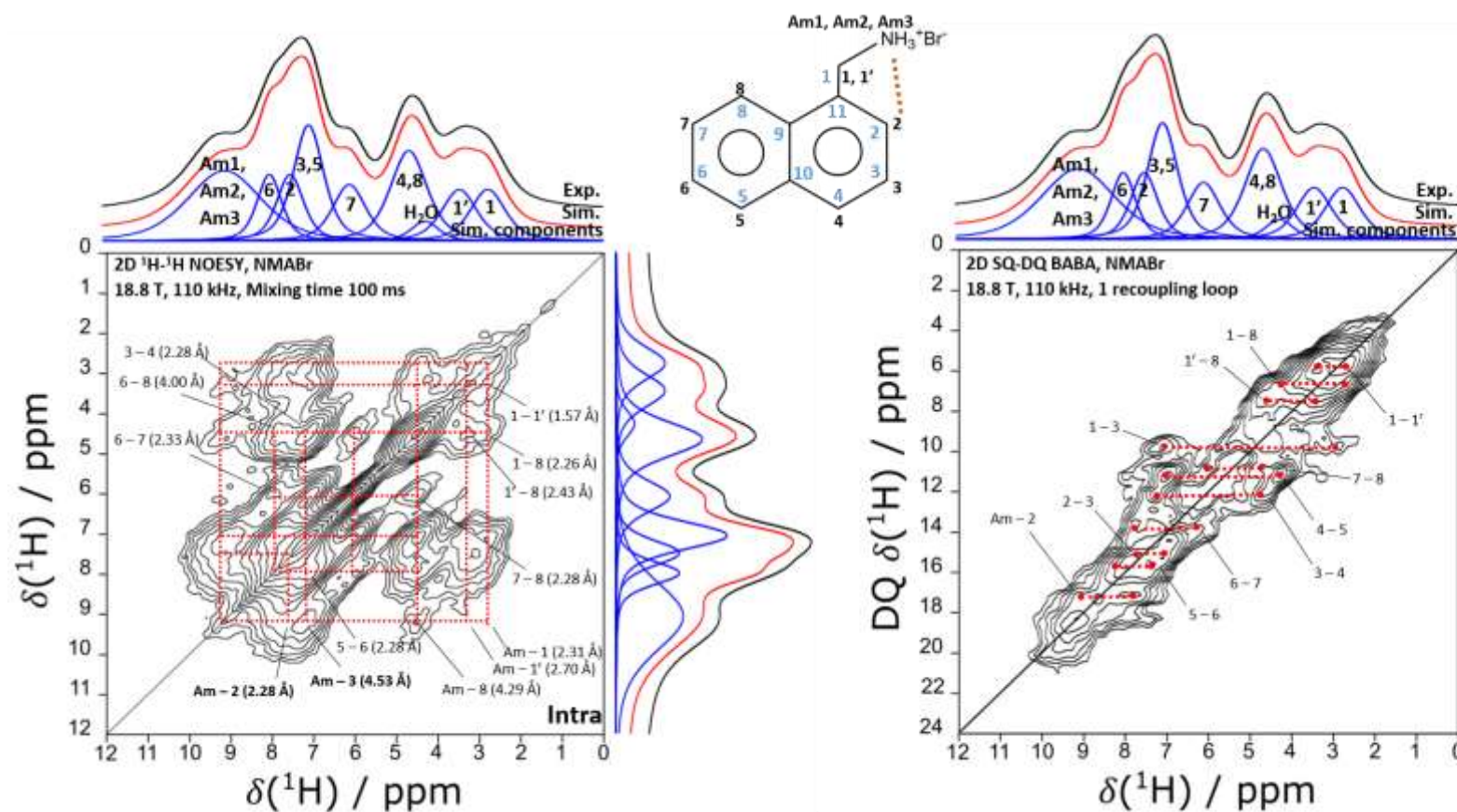


Figure 6.8 NOESY (Left) and BABA (Right) spectra of the NMABr organic. The NOESY uses a 100 ms mixing time and the BABA uses 1 recoupling loop. Red dotted lines indicate correlations between resonances and the distances in brackets are the distances in space between atoms from the NMABr crystal structure.

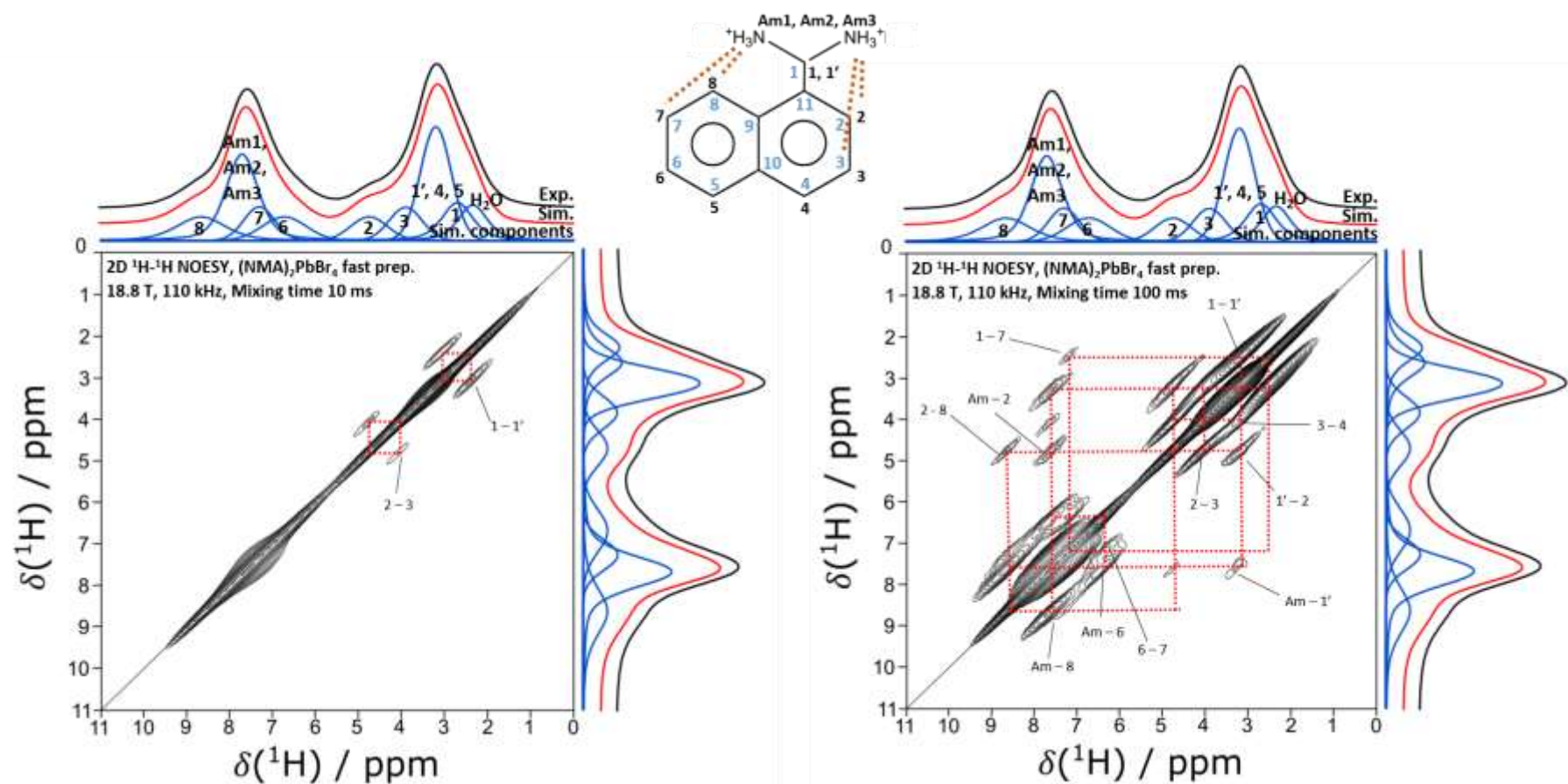


Figure 6.9 NOESY spectra of the $(\text{NMA})_2\text{PbBr}_4$ fast preparation. The left spectrum uses a 10 ms mixing time and the right a 100 ms mixing time. Red dotted lines indicate correlations between resonances.

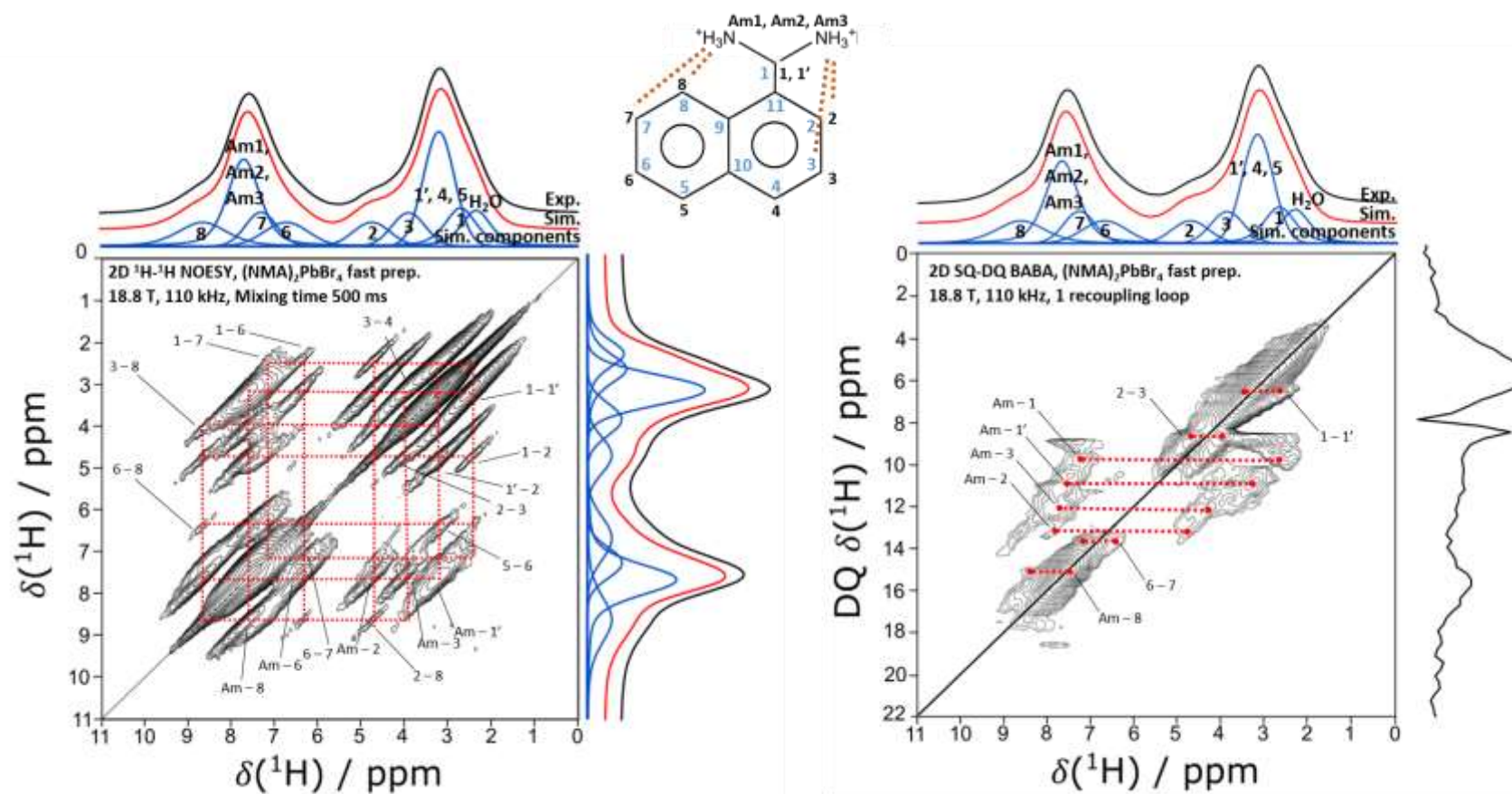


Figure 6.10 NOESY (Left) and BABA (Right) spectra of the $(\text{NMA})_2\text{PbBr}_4$ fast preparation. The NOESY uses a 500 ms mixing time and the BABA uses 1 recoupling loop. Red dotted lines indicate correlations between resonances.

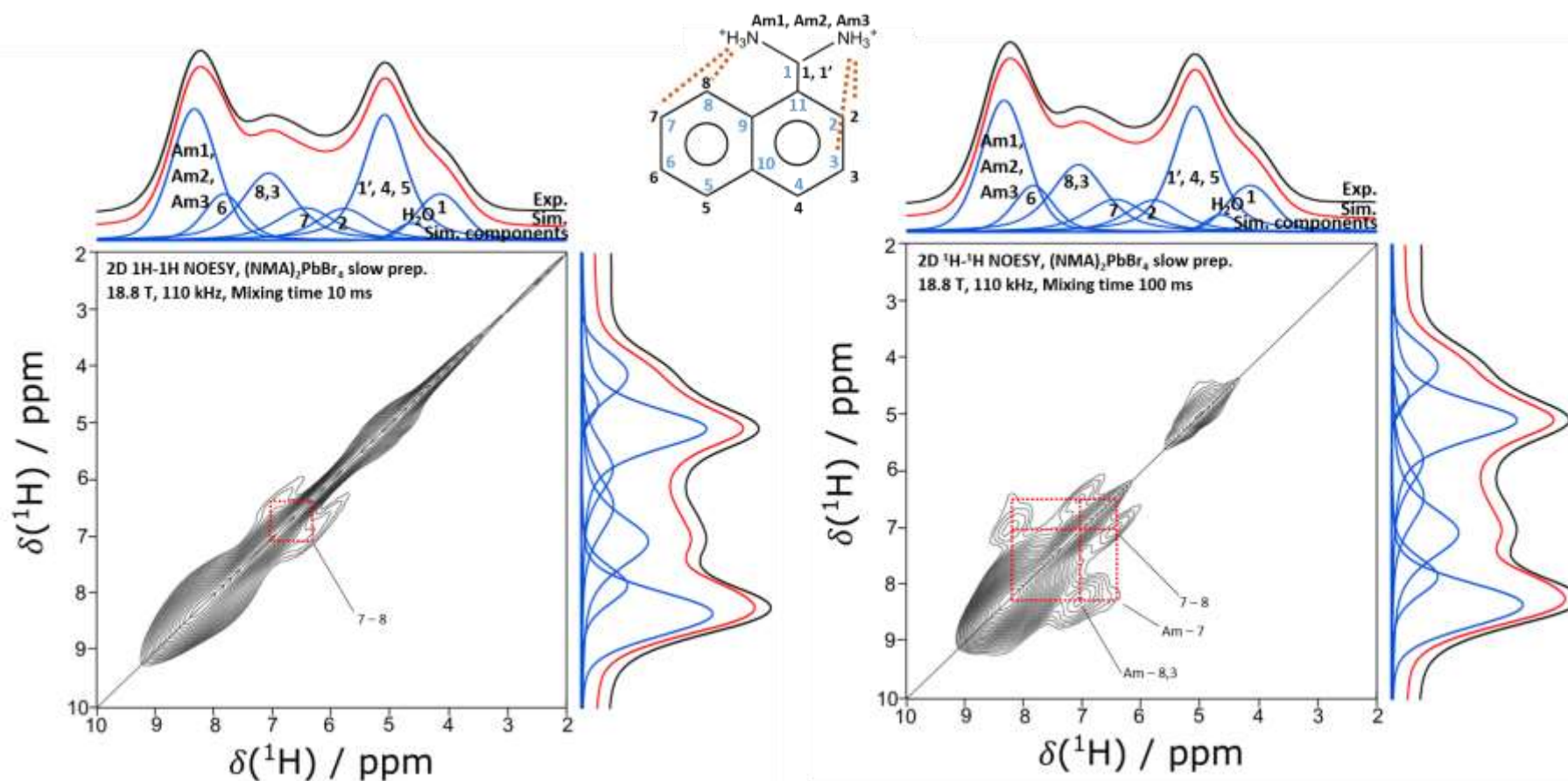


Figure 6.11 NOESY spectra of the $(\text{NMA})_2\text{PbBr}_4$ slow preparation. The left spectrum uses a 10 ms mixing time and the right a 100 ms mixing time. Red dotted lines indicate correlations between resonances.

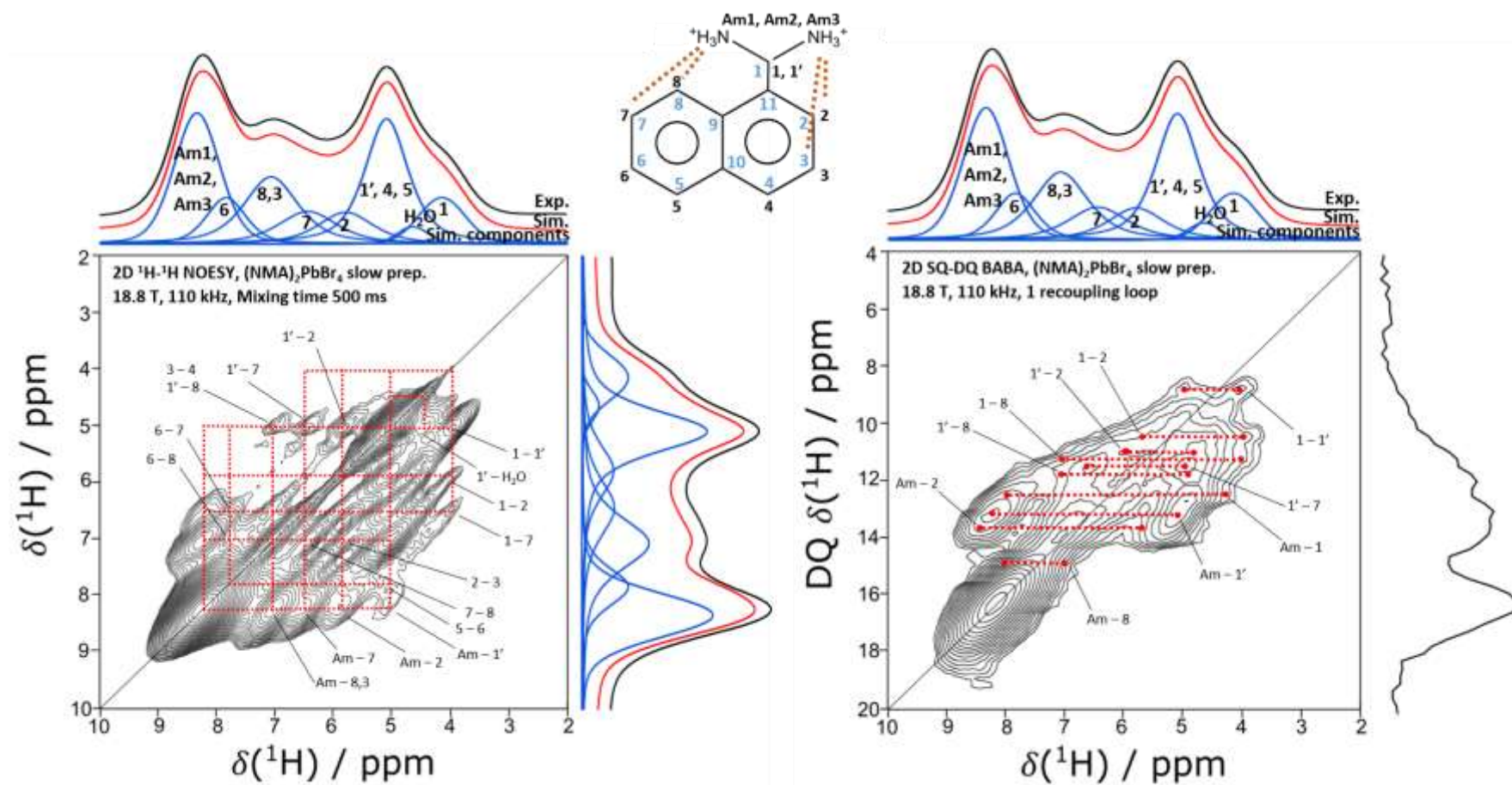


Figure 6.12 NOESY (Left) and BABA (Right) spectra of the $(\text{NMA})_2\text{PbBr}_4$ slow preparation. The NOESY uses a 500 ms mixing time and the BABA uses 1 recoupling loop. Red dotted lines indicate correlations between resonances.

The ^1H - ^1H distances taken from the NMABr organic matched very well with the early NOESY correlations that are seen in Figure 6.7 for the 10 ms mixing time. Notably, intramolecular adjacent ^1H 's correlate at these low mixing times such as 1-1' (1.57 Å), 2-3 (2.32 Å), 5-6 (2.28 Å) and 1,1'-8 (2.26 Å, 2.43 Å). There are also some intermolecular correlations between adjacent molecules within the unit cell at a mixing time of 50 ms. Examples of these correlations are Am-4 (4.80 Å), 3-7 (3.16 Å) and 1-6 (4.07 Å). The closest ^1H in space for these correlations is the next molecule in the unit cell; the intramolecular distances are far greater and will only begin to contribute to the correlation at longer mixing times. In Figure 6.8 the BABA spectrum agrees with these assignments as it only shows correlations within ~ 3.5 Å. The furthest correlation that is seen in the BABA is 1-3 which have a distance of 3.27 Å. None of these correlations suggest the presence of conformers as would be expected in the standalone organic system.

Looking at the 10 ms mixing time NOESY for the fast preparation NMA based perovskite in Figure 6.9 only very proximate nuclei (using the NMABr crystal structure as a guide) correlate. The correlations are between 1-1' and 2-3 so the assignments for these resonances can be assumed to be correct. As the mixing time is increased to 100 ms other nuclei that would be expected to be close are also seen i.e. 3-4 and 6-7. What is also seen at this relatively short mixing time is the amine group correlating with both aromatic ^1H 2 and 8. This is further evidence that there is a conformer of the amine group that faces in at least two different directions, one close to ^1H 2 and the other to ^1H 8. A frequent occurrence in NOESY spectra is that at sufficiently long mixing times there is enough time for the diffusion of magnetisation, such that all of the ^1H 's in a system will correlate with all of the others ^1H 's. The 500 ms NOESY spectrum in Figure 6.10 is an example of this. The BABA spectrum of the fast preparation perovskite also confirms the amine group conformer as both Am-8 and Am-2,3 correlations are present. The average distance between the amine group and ^1H 8 is 4.43 Å which would not be visible in the BABA spectrum without that conformer being present.

The NOESY spectra for the slow preparation NMA based perovskite behave slightly differently to the previous two systems. For the 10 ms mixing time NOESY, Figure 6.11 the first and only correlation that is seen is 7-8 and there is no trace of the 1-1' correlation. This is also the case in the 100 ms NOESY, it is likely that the proximity

of these ^1H 's is so close that the magnetisation has completely diffused before the spectrum is recorded. A strong correlation is seen between the amine group and the 8 and 3 aromatic proton resonance, this resonance cannot be resolved so there is uncertainty as to which, if not both, ^1H the amine is correlating too. There is some supporting evidence that it is ^1H 8 as the Am-7 correlation is seen, albeit weakly. At a 500 ms mixing time, Figure 6.12, the 1-1' correlation is seen as well as the Am-2 correlation, along with all previously mentioned correlations. Since this is a relatively long mixing time it could be inferred that the 1-1' and Am-2 correlation are intermolecular rather than intramolecular. The BABA spectrum does offer some unambiguous support of the conformer in the slow preparation perovskite, both Am-2 and Am-8 are present. Once again however, it must be noted that ^1H 8 could in fact be ^1H 3 in this correlation. To further support the evidence of conformers or lack thereof in these systems the relaxation data must be investigated.

6.3.5 Relaxation studies

T_1 measurements of the NMABr and the two hybrid perovskite preparations have been taken on an 800 MHz spectrometer and are presented in Figure 6.13 (T_1). The T_1 times for the NMABr organic further demonstrate that it has no conformers present, relative to the perovskite systems, the T_1 times are both very long, $T_{1\text{avg.}} = (256 \pm 10)$ s, and single component. The long relaxation times indicate a rigid system with very few additional relaxation pathways.

The two preparations of the NMA based hybrid perovskites have considerably shorter T_1 relaxation times, $T_{1\text{avg.}} = (4.6 \pm 0.5)$ s for the fast preparation and $T_{1\text{avg.}} = (4.0 \pm 0.3)$ s for the slow preparation. This is because the presence of the Pb mediates the dipole interactions between the ^1H 's in the organic part of the system thus creating more efficient relaxation pathways and therefore considerably shorter average T_1 times when compared to the long times of the NMABr organic. Another major difference in the T_1 times is that for all of the fast preparation T_1 plots a two component

Table 6.2 ^{13}C shifts for the NMABr organic and the fast and slow $(\text{NMA})_2\text{PbBr}_4$ preparations. NMABr has comparative values from the DFT calculations using CASTEP17.

System	Resonance no.	Functional Group	δ_{iso} (ppm)	Calculated Resonance (ppm)	$^1\text{H } T_{1\rho}$ (s)
NMABr	1	CH ₂	40.5	39.8	0.0040 ± 0.0010
	2	Aromatic	121.3	120.5	0.0028 ± 0.0002
	3	Aromatic	125.4	125.7	0.0031 ± 0.0004
	4	Aromatic	128.4	126.7	0.0035 ± 0.0002
	5	Aromatic	130.6	131.1	0.0034 ± 0.0003
	6	Aromatic	127.3	128.1	0.0034 ± 0.0002
	7	Aromatic	126.7	126.5	0.0033 ± 0.0002
	8	Aromatic	121.8	121.3	0.0027 ± 0.0002
	9	Aromatic	128.4	127.2	0.0035 ± 0.0002
	10	Aromatic	132.0	130.5	0.0037 ± 0.0007
	11	Aromatic	127.3	127.5	0.0034 ± 0.0002
$(\text{NMA})_2\text{PbBr}_4$ fast prep.	1	CH ₂	42.1	-	0.13 ± 0.02
	2	Aromatic	126.6 129.3	-	0.11 ± 0.01 0.20 ± 0.03
	3	Aromatic	129.2 132.6	-	0.12 ± 0.01 0.42 ± 0.17
	4	Aromatic	131.5	-	0.26 ± 0.03
	5	Aromatic	128.6	-	0.18 ± 0.01
	6	Aromatic	129.1	-	0.16 ± 0.01
	7	Aromatic	127.0 128.7	-	0.13 ± 0.01 0.18 ± 0.01
	8	Aromatic	126.1 131.0	-	0.20 ± 0.01 0.40 ± 0.17
	9	Aromatic	133.2	-	0.042 ± 0.002
	10	Aromatic	130.6	-	0.12 ± 0.02
	11	Aromatic	123.6	-	0.18 ± 0.02
$(\text{NMA})_2\text{PbBr}_4$ slow prep.	1	CH ₂	41.5	-	0.036 ± 0.002
	2	Aromatic	125.9 127.7	-	0.018 ± 0.004 0.020 ± 0.003
	3	Aromatic	129.8 132.5	-	0.024 ± 0.002 0.012 ± 0.002
	4	Aromatic	125.5	-	0.019 ± 0.002
	5	Aromatic	126.5	-	0.017 ± 0.002
	6	Aromatic	124.5 127.0	-	0.007 ± 0.002 0.021 ± 0.003
	7	Aromatic	122.9 127.3	-	0.022 ± 0.002 0.023 ± 0.003
	8	Aromatic	126.2 128.0	-	0.019 ± 0.002 0.038 ± 0.002
	9	Aromatic	130.4	-	0.016 ± 0.004
	10	Aromatic	131.2	-	0.022 ± 0.006
	11	Aromatic	127.0	-	0.021 ± 0.003

fit was required and in the slow preparation half of the plots required two component fits (see Figure A.4, Figure A.5 Figure A.6).

Focussing first on the fast preparation it can be seen that there is a fast relaxing component and a slow relaxing component, relative to the perovskite systems.

Generally, the faster relaxing component contributes more to the fit, with ratios of 4:1 for the CH₂ relaxation, ¹H 1, 3:1 for the water resonance and aromatic ¹H 3 and 2:1 for aromatic protons 2, 4, 5 and 6 and the CH₂ proton 1'. All the other aromatic protons and the amine group have a 1:1 ratio for their relaxation times. These ratios may be an indication to the prominence of each conformer in the unit cell. Having two contributing relaxation components is another strong indicator for the presence of conformers in the amine group of the organic. It is evidence that two very different electron densities and therefore dipole interactions are present where one dipole interaction is more efficient than the other leading to one relaxation time being considerably shorter than the other.

Much like in the NOESY and BABA spectra, the *T*₁ times for the slow preparation hybrid perovskite are similar but with some notable differences. Four of the resonances, aromatic ¹H's 7, 8, 3 and 6 as well as the amine group, display two component relaxation curves. The difference between the fast and slow relaxing components and their ratios is similar to those in the fast preparation. The ratio for aromatic ¹H 7 however is 2:5 in favour of the slower relaxation pathway. All of the

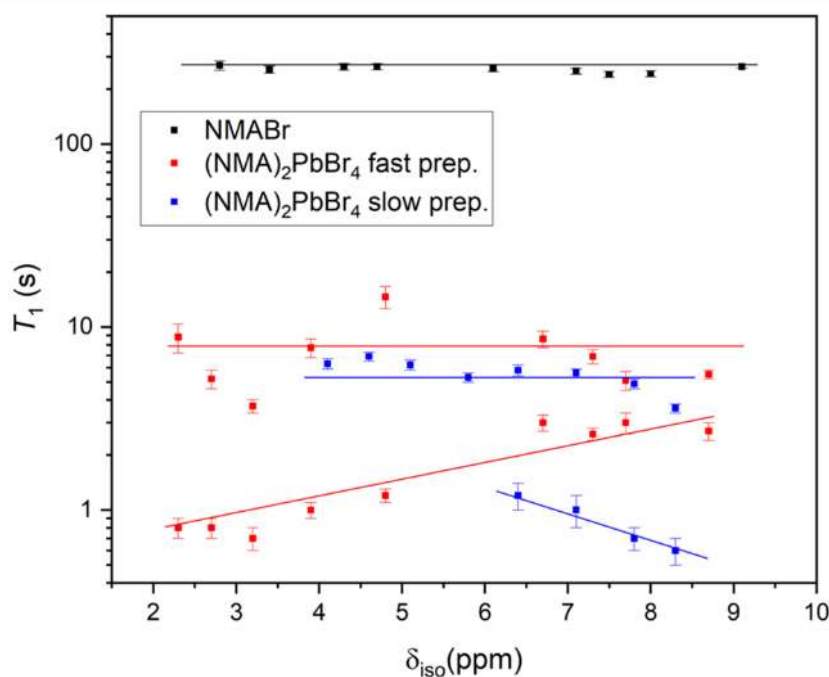


Figure 6.13 *T*₁ and times of the NMABr organic and the fast and slow prep. (NMA)₂PbBr₄ perovskites. The lines through the data are used to guide the eye and are not lines of best fit.

two component relaxation times occur on the ‘left’ benzene ring of the NMA molecule which indicates that the position of the amine conformer is different to that of the schematic shown, which is likely the orientation that is seen in the fast preparation hybrid perovskite.

6.3.6 ^{207}Pb NMR studies

^{207}Pb NMR of the fast and slow preparations of $(\text{NMA})_2\text{PbBr}_4$ were conducted. Each show distinct ^{207}Pb sites at -409 ppm and -85 ppm, Figure 6.14. The fast preparation sample is shielded by 325 ppm with respect to the slow preparation, thus the fast preparation has comparatively higher surrounding electron density. This may be a result of the greater amount of H_2O molecules present in the system.

Each spectrum exhibits prominent sidebands which appear at multiples of the spinning speed used in the experiment (in this case 24 kHz). The intensity of the sidebands in a

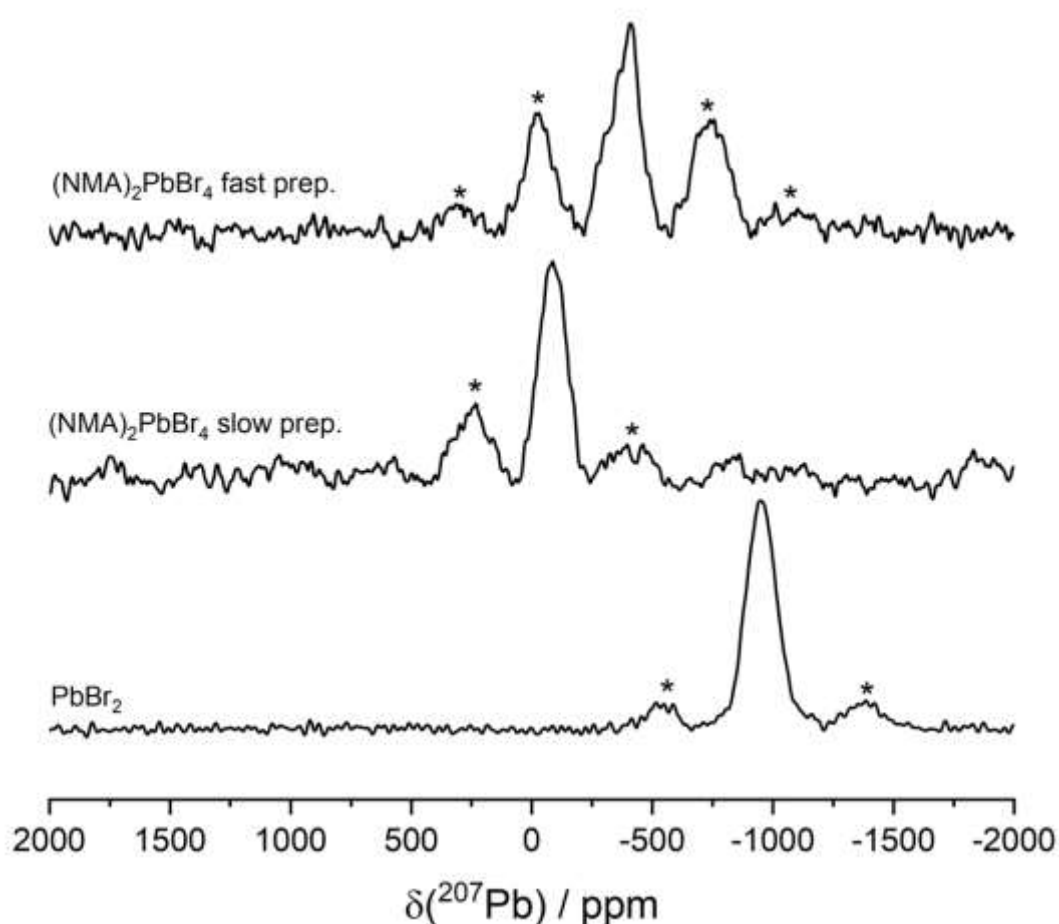


Figure 6.14 ^{207}Pb MAS NMR of the fast and slow prep. $(\text{NMA})_2\text{PbBr}_4$ perovskites and PbBr_2 . The asterisks denote spinning sidebands.

solid state NMR spectrum are closely related to the chemical shift anisotropy (CSA) of the observed nucleus. By inspection it is apparent that each system has sufficiently different anisotropic interactions, this again will arise from the different amounts of water in the system and the packing structure of the cell. This larger CSA, not seen in the MOPs in Chapter 5, could be further evidence for the non-uniform structure caused by multiple conformers.

As it has been shown that water molecules are present in the two perovskite preparations it is important to note that, just like the MOP systems in the previous chapter, these systems have not degraded to PbBr_2 . Thus another series of lead-halide hybrid perovskites has been found that contain crystallographic water.

6.4 Conclusion

The series of the NMABr organic and the fast and slow preparations of $(\text{NMA})_2\text{PbBr}_4$ hybrid perovskites have been fully investigated using 1D and 2D NMR methods and relaxometry data.

The NMABr organic structure from scXRD has been confirmed using ^1H and ^{13}C 1D NMR and the assignments of those spectra have been confirmed with DFT calculations via CASTEP to predict the ^1H and ^{13}C isotropic chemical shifts. This confirmation was also aided by HETCOR, NOESY and BABA experiments; these spectra also show that there are no conformers present in the NMABr organic.

The fast and slow preparations of $(\text{NMA})_2\text{PbBr}_4$ required more detailed analysis of the 2D NMR spectra as no structural data from scXRD was available. This analysis showed that in both systems certain ^1H 's correlated to multiple ^{13}C resonances in their HETCOR spectrum indicating the presence of conformers. The NOESY and BABA data then showed that this conformer is from the change in orientation of the NH_3^+ group that anchors the organic to the inorganic lead-bromide octahedra. This is evidenced by the presence of the Am-2 and Am-8 correlation in the NOESY data at short mixing times and the BABA data. The BABA data is particularly compelling as these spectra only show correlations for a distance of $\sim 3.5 \text{ \AA}$, and yet the Am-2 and Am-8 correlations are still present, despite the distances from the scXRD structure of

NMABr showing that Am-8 should not be seen. The T_1 data of the two perovskite preparations is also further evidence of this conformer as for all of the fast preparation times and half of the slow preparation times there are two components contributing to the relaxation. The reason single-crystals of sufficient size or stability could not be grown is likely a result of these conformers.

Finally, as seen in the MOP systems, the organic and the two perovskites show that structural water is present and yet, in the case of the perovskites, the ^{207}Pb NMR shows that the systems have not degraded.

Knowing now that water is within the structures and that the fast and slow preparations of $(\text{NMA})_2\text{PbBr}_4$ have conformers within their structure will aid in designing more resilient phosphorescent materials. Since the NMABr is actually a better phosphorescent material than the perovskites, this knowledge may improve their properties if they can be synthesised with only a single conformer in the structure.

Chapter 7: Summary

Solid-state NMR, paired with Raman spectroscopy, pXRD and DFT calculations provided a useful combination of techniques in analysing and interpreting the properties of both hybrid perovskite systems and ceria-zirconia supports. The methods used supported each other in making up for the shortfalls that they possess, this was particularly prominent in the ceria-zirconia investigation. The following section will provide a brief summary of each study.

7.1 An investigation of ordered and disordered ceria-zirconia

The first result of this chapter was the confirmation of the weaker Zr-O bonds that facilitate the improved reducibility of ceria-zirconia solid solutions. This was shown in the ^{17}O solid-state NMR. For both the ordered and disordered system, Raman, pXRD and SAXS measurements confirm that the structure did not majorly alter due to the $^{17}\text{O}_2$ gas labelling.

The ordered system showed a non-selective oxygen exchange at sub 500 °C labelling conditions. Above this temperature a final OCe_4 site began to exchange. This again agrees with the literature that the Zr-O bonds are weaker and facilitate the improved OSC and that, based on the crystal structure the Ce-O bonds only exchange at higher temperatures.

Different oxidative states of the κ -phase were investigated and here the strengths of each technique used were highlighted. The pXRD data and Rietveld refinements showed the mixed phase nature of yellow, green and blue samples. Each sample representing a different level of oxidation. The NMR and Raman spectra showed that there was a threshold point at which the κ -phase lost its cubic structure and became mixed phase.

Having knowledge of the oxygen mobility of each system and knowing how the κ -phase behaves in oxygen rich or lean conditions would be key to designing a more efficient catalyst support in catalytic converters.

7.2 An investigation of hybrid perovskites used as LEDs

The MOP series of hybrid perovskites are novel, tuneable, materials that are used as components in LEDs. 2-MOP possess broadband emission properties whereas 3-MOP and 4-MOP do not. FTIR and 1D ^1H NMR revealed that there may be crystallographic water present in each system, this was then confirmed using AIRSS (paired with DFT calculations) and 2D ^1H - ^1H NOESY measurements. A hydrogen-bonded and non-hydrogen-bonded site are present and are seen to be exchanging in 3-MOP and 4-MOP, but only a single site is present in 2-MOP. These exchanging waters explain the faster $T_{1\rho}$ relaxation times in 3-MOP and 4-MOP and thus their lack of J -coupling in the ^{207}Pb NMR. This can be used to explain the smaller ratio of self-trapped to free excitons in these systems, which leads to their narrow emission. 2-MOP is a rigid structure with no exchanging water molecules and thus has the broadband emission property.

A series of hybrid perovskites with crystallographic water in their structure has been characterised and shown not to have degraded, based on ^{207}Pb NMR data. The presence of water is now known to effect the emission properties of these systems, future materials with potential uses as LED materials can now be designed with this knowledge in mind.

7.3 An investigation of hybrid perovskites with optoelectronic properties

In this chapter another series of hybrid perovskites, this time with RTP properties, has been shown to contain conformers. The conformers only appear in the hybrid perovskite NMA systems and not the organic molecule on which they are based. Solid-state NMR has been the key to identifying these conformers, the HETCOR spectra showed multiple ^1H - ^{13}C correlations for ^1H 's near the NH_3^+ group whilst the NOESY data showed correlations at short mixing times which could only be present if these species were close in space – which the crystal structure for the organic only allows if the NH_3^+ group can have multiple orientations. These conformers are also alluded to in the relaxometry study, two-component T_1 fits imply the presence of at least two different electron densities which would lead to different relaxation pathways for the system.

Knowing that these conformers are present can aid in designing new more efficient hybrid perovskites as in this case, the perovskites don't perform as well as the lone NMA organic.

References

-
- [1] K. J. D. MacKenzie and M. E. Smith, *Multinuclear Solid-State NMR of Inorganic Materials* (Pergamon, Oxford, 2002).
 - [2] V. I. Bakhmutov, *Solid-State NMR in Materials Science: Principles and Applications* (CRC Press, New York, 2016).
 - [3] D. C. Apperley, R. K. Harris, and P. Hodgkinson, *Solid-State NMR: Basic Principles and Practice* (Monument Press, 2012).
 - [4] M. E. Rose, *Elementary Theory of Angular Momentum* (Wiley, New York, 1957).
 - [5] U. Haeberlen, *High Resolution NMR in Solids : Selective Averaging / Ulrich Haeberlen* (Academic Press, New York, 1976).
 - [6] K. Jurga, E. Reynhardt, and S. Jurga, *Meas. Sci. Technol.* **5**, 27 (1994).
 - [7] M. Feike, D. E. Demco, R. Graf, J. Gottwald, S. Hafner, and H. W. Spiess, *J. Magn. Reson. - Ser. A* **122**, 214 (1996).
 - [8] C. Jäger, P. Hartmann, R. Witter, and M. Braun, *J. Non. Cryst. Solids* **263**, 61 (2000).
 - [9] P. M. C. Po and A. Cedex, **12**, (2001).
 - [10] M. Feike, C. Jäger, and H. W. Spiess, *J. Non. Cryst. Solids* **223**, 200 (1998).
 - [11] M. Tüsar, L. Tüsar, S. Bohanec, and J. Zupan, *J. Chem. Inf. Comput. Sci.* **32**, 299 (1992).
 - [12] S. M. Kaasz and L. Angeles, *Tetrahedron* **30**, 641 (1989).
 - [13] J. K. Baker, *Spectrosc. Lett.* **25**, 31 (1992).
 - [14] W. Kohn and L. J. Sham, *Phys. Rev.* **140**, A1133 (1965).
 - [15] S. J. Clark, M. D. Segall, C. J. Pickard, P. J. Hasnip, M. I. J. Probert, and K. Refson, **220**, 567 (2005).
 - [16] A. Ambrosetti, A. M. Reilly, R. A. Distasio, and A. Tkatchenko, *J. Chem. Phys.* **140**, (2014).
 - [17] C. J. Pickard and R. J. Needs, *J. Phys. Condens. Matter* **23**, (2011).
 - [18] C. J. Pickard and R. J. Needs, *Phys. Rev. Lett.* **97**, 1 (2006).
 - [19] C. J. Pickard and R. J. Needs, *Nat. Mater.* **9**, 624 (2010).
 - [20] G. Schusteritsch, R. Ishikawa, A. R. Elmaslmane, K. Inoue, K. P. McKenna, Y.

- Ikuhara, and C. J. Pickard, *Nano Lett.* (2021).
- [21] A. J. Morris, C. J. Pickard, and R. J. Needs, *Phys. Rev. B - Condens. Matter Mater. Phys.* **80**, 1 (2009).
 - [22] B. B. Harrison, A. F. Diwell, and C. Hallett, *Platin. Met. Rev.* 73 (1988).
 - [23] J. C. Martínez-Munuera, M. Zoccoli, J. Giménez-Mañogil, and A. García-García, *Appl. Catal. B Environ.* **245**, 706 (2019).
 - [24] A. F. N. Abdul-Manan, H. W. Won, Y. Li, S. M. Sarathy, X. Xie, and A. A. Amer, *Appl. Energy* **267**, (2020).
 - [25] D. Petitjean, L. Bernrdini, C. Middlemass, and S. Shahed, *SAE Tech. Pap.* **1**, (2004).
 - [26] T. Montini, M. Melchionna, M. Monai, and P. Fornasiero, *Chem. Rev.* **116**, 5987 (2016).
 - [27] J. Gagnon, M. J. D. Clift, D. Vanhecke, D. A. Kuhn, P. Weber, A. Petri-Fink, B. Rothen-Rutishauser, and K. M. Fromm, *J. Mater. Chem. B* **3**, 1760 (2015).
 - [28] Z. Tian, J. Li, Z. Zhang, W. Gao, X. Zhou, and Y. Qu, *Biomaterials* **59**, 116 (2015).
 - [29] S. Saitzek, J. F. Blach, S. Villain, and J. R. Gavarri, *Phys. Status Solidi Appl. Mater. Sci.* **205**, 1534 (2008).
 - [30] P. Jasinski, T. Suzuki, and H. U. Anderson, *Sensors Actuators, B Chem.* **95**, 73 (2003).
 - [31] A. Trovarelli, *Catalysis by Ceria and Related Materials* (Imperial College Press, London, 2002).
 - [32] E. Aneggi, M. Boaro, S. Colussi, C. de Leitenberg, and A. Trovarelli, *Handbook on the Physics and Chemistry of Rare Earths* (2016).
 - [33] Z. Wu, M. Li, J. Howe, H. M. Meyer, and S. H. Overbury, *Langmuir* **26**, 16595 (2010).
 - [34] S. Agarwal, X. Zhu, E. J. M. Hensen, L. Lefferts, and B. L. Mojet, *J. Phys. Chem. C* **118**, 4131 (2014).
 - [35] E. Mamontov and T. Egami, *Structural Defects in a Nano-Scale Powder of CeO₂ Studied by Pulsed Neutron Diffraction* (2000).
 - [36] E. Mamontov, T. Egami, R. Brezny, M. Koranne, and S. Tyagi, *J. Phys. Chem. B* **104**, 11110 (2000).

- [37] T. X. T. Sayle, S. C. Parker, and C. R. A. Catlow, *Surf. Sci.* **316**, 329 (1994).
- [38] R. Grau-Crespo, N. H. De Leeuw, S. Hamad, and U. V. Waghmare, *Proc. R. Soc. A Math. Phys. Eng. Sci.* **467**, 1925 (2011).
- [39] M. Sugiura, *Catal. Surv. from Asia* **7**, 77 (2003).
- [40] M. Yashima, K. Morimoto, N. Ishizawa, and M. Yoshimura, *J. Am. Ceram. Soc.* **2773** (1994).
- [41] M. Yashima, K. Morimoto, N. Ishizawa, and M. Yoshimura, *J. Am. Ceram. Soc.* (1991).
- [42] M. Yashima, K. Morimoto, N. Ishizawa, and M. Yoshimura, *J. Am. Ceram. Soc.* **76**, 2865 (1993).
- [43] P. Fornasiero, E. Fonda, R. Di Monte, G. Vlaic, and J. Kaspar, *J. Catal.* **185**, 177 (1999).
- [44] G. Vlaic, P. Fornasiero, S. Geremia, J. Kašpar, and M. Graziani, *J. Catal.* **168**, 386 (1997).
- [45] S. Lemaux, A. Bensaddik, A. M. J. Van Der Eerden, J. H. Bitter, and D. C. Koningsberger, *J. Phys. Chem. B* **105**, 4810 (2002).
- [46] S. Otsuka-Yao-Matsuo, T. Omata, N. Izu, and H. Kishimoto, *J. Solid State Chem.* **138**, 47 (1998).
- [47] S. N. Achary, S. K. Sali, N. K. Kulkarni, P. S. R. Krishna, A. B. Shinde, and A. K. Tyagi, *Chem. Mater.* **21**, 5848 (2009).
- [48] S. Urban, P. Dolcet, M. Möller, L. Chen, P. J. Klar, I. Djerdj, S. Gross, B. M. Smarsly, and H. Over, *Appl. Catal. B Environ.* **197**, 23 (2016).
- [49] A. Gupta, A. Kumar, U. V. Waghmare, and M. S. Hegde, *J. Phys. Chem. C* **121**, 1803 (2017).
- [50] M. C. Vlachou, *17O Solid State NMR Study of Ceria Systems*, University of Warwick, 2017.
- [51] M. Profeta, F. Mauri, and C. J. Pickard, *J. Am. Chem. Soc.* **125**, 541 (2003).
- [52] C. J. Pickard and F. Mauri, *Phys. Rev. B* **63**, 245101 (2001).
- [53] J. R. Yates, C. J. Pickard, and F. Mauri, *Phys. Rev. B* **76**, 24401 (2007).
- [54] T. Taniguchi, T. Watanabe, N. Sugiyama, A. K. Subramani, H. Wagata, N. Matsushita, and M. Yoshimura, *J. Phys. Chem. C* **113**, 19789 (2009).
- [55] L. Li, F. Chen, J. Q. Lu, and M. F. Luo, *J. Phys. Chem. A* **115**, 7972 (2011).

- [56] Y. Lee, G. He, A. J. Akey, R. Si, M. Flytzani-Stephanopoulos, and I. P. Herman, *J. Am. Chem. Soc.* **133**, 12952 (2011).
- [57] M. Dosa, M. Piumetti, S. Bensaid, T. Andana, C. Novara, F. Giorgis, D. Fino, and N. Russo, *Catal. Letters* **148**, 298 (2018).
- [58] S. Loridant, *Catal. Today* **373**, 98 (2021).
- [59] T. Kuznetsova, V. Sadykov, L. Batuev, E. Moroz, E. Burgina, V. Rogov, V. Kriventsov, and D. Kochubey, *J. Nat. Gas Chem.* **15**, 149 (2006).
- [60] P. Kumar, Y. Sun, and R. O. Idem, *Energy and Fuels* **21**, 3113 (2007).
- [61] T. A. Lee, C. R. Stanek, K. J. McClellan, J. N. Mitchell, and A. Navrotsky, *J. Mater. Res.* **23**, 1105 (2008).
- [62] S. Arai, S. Muto, J. Murai, T. Sasaki, Y. Ukyo, K. Kuroda, and H. Saka, *Nippon Kinzoku Gakkaishi/Journal Japan Inst. Met.* **68**, 264 (2004).
- [63] S. Arai, S. Muto, T. Sasaki, K. Tatsumi, Y. Ukyo, K. Kuroda, and H. Saka, *Solid State Commun.* **135**, 664 (2005).
- [64] M. Glerup, O. F. Nielsen, and F. W. Poulsen, *J. Solid State Chem.* **160**, 25 (2001).
- [65] Y. Ding, Z. Wang, Y. Guo, Y. Guo, L. Wang, and W. Zhan, *Catal. Today* **327**, 262 (2019).
- [66] Y. Sun, C. Li, I. Djerdj, O. Khalid, P. Cop, J. Sann, T. Weber, S. Werner, K. Turke, Y. Guo, B. M. Smarsly, and H. Over, *Catal. Sci. Technol.* **9**, 2163 (2019).
- [67] D. Errandonea, R. S. Kumar, S. N. Achary, O. Gomis, F. J. Manjn, R. Shukla, and A. K. Tyagi, *J. Appl. Phys.* **111**, (2012).
- [68] X. Wang, K. Jiang, and L. Zhou, *J. Nucl. Mater.* **458**, 156 (2015).
- [69] T. Masui, Y. Peng, K. I. Machida, and G. Y. Adachi, *Chem. Mater.* **10**, 4005 (1998).
- [70] T. Masui, T. Ozaki, K. I. Machida, and G. Y. Adachi, *J. Alloys Compd.* **303–304**, 49 (2000).
- [71] M. Profeta, M. Benoit, F. Mauri, and C. J. Pickard, *J. Am. Chem. Soc.* **126**, 12628 (2004).
- [72] G. Shao, **113**, 6800 (2009).
- [73] M. F. M. Taib, D. T. Mustaffa, N. H. Hussin, M. H. Samat, A. M. M. Ali, O.

- H. Hassan, and M. Z. A. Yahya, *Mater. Res. Express* **6**, 0 (2019).
- [74] B. C. Shih and J. R. Yates, *Phys. Rev. B* **96**, 1 (2017).
- [75] Z. Xia and Q. Liu, *Prog. Mater. Sci.* **84**, 59 (2016).
- [76] H. Hu, S. A. Morris, X. Qiao, B. Chen, E. M. Chia, and Y. Ming, *J. Mater. Chem. C* **6**, 10301 (2018).
- [77] Z. Wu, C. Ji, Z. Sun, S. Wang, S. Zhao, W. Zhang, L. Li, and J. Luo, *J. Mater. Chem. B* **6**, 1171 (2018).
- [78] Z. Yuan, C. Zhou, J. Messier, Y. Tian, Y. Shu, J. Wang, Y. Xin, and B. Ma, *Adv. Opt. Mater.* **4**, 2009 (2016).
- [79] C. Mu, T. Glaser, M. Plogmeyer, M. Sendner, S. Do, A. A. Bakulin, C. Brzuska, R. Scheer, M. S. Pshenichnikov, W. Kowalsky, A. Pucci, and R. Lovrinc, *Chem. Mater.* **27**, 7835 (2015).
- [80] J. Huang and P. D. Lund, *R. Soc. Chem.* **10**, 2284 (2017).
- [81] A. Halder, D. Choudhury, S. Ghosh, A. S. Subbiah, and S. K. Sarkar, *J. Phys. Chem. Lett.* **6**, 3180 (2015).
- [82] B. Nicholson, S. Verma, P. Med, and S. S, *Science (80-.)*. **345**, 542 (2014).
- [83] L. Ama, Y. Hu, A. Mi, W. Oj, P. Azarhoosh, W. Mt, T. Bein, J. Nelson, P. Docampo, B. Prf, A. Leguy, Y. Hu, M. Campoy-quiles, M. I. Alonso, and O. J. Weber, **27**, 3397 (2016).
- [84] B. Hailegnaw, S. Kirmayer, E. Edri, G. Hodes, and D. Cahen, *J. Phys. Chem. Lett.* **6**, 1543 (2015).
- [85] D. B. Khadka, Y. Shirai, M. Yanagida, and K. Miyano, *J. Mater. Chem. C* **6**, 162 (2017).
- [86] N. Tripathi, M. Yanagida, Y. Shirai, T. Masuda, L. Han, and K. Miyano, *J. Mater. Chem. A* **3**, 12081 (2015).
- [87] G. N. Hall, M. Stuckelberger, T. Nietzold, J. Hartman, J. Park, B. Niesen, M. L. Cummings, V. Rose, C. Ballif, M. K. Chan, D. P. Fenning, and M. I. Bertoni, *J. Phys. Chem. C* **121**, 25659 (2017).
- [88] L. Zhang and P. H. L. Sit, *J. Phys. Chem. C* **119**, 22370 (2015).
- [89] A. Kakekhani, R. N. Katti, and A. M. Rappe, *APL Mater.* **7**, 041112 (2019).
- [90] S. Sanguinetti, M. Guzzi, and M. Gurioli, in edited by C. B. T.-C. of S. H. and N. Lamberti (Elsevier, Amsterdam, 2008), pp. 175–208.

- [91] B. P. Zakharchenya and S. A. Permogorov, in edited by F. Bassani, G. L. Liedl, and P. B. T.-E. of C. M. P. Wyder (Elsevier, Oxford, 2005), pp. 171–179.
- [92] S. Zhang, X. Yang, Y. Numata, and L. Han, *Energy Environ. Sci.* **6**, 1443 (2013).
- [93] H. Hu, F. Meier, D. Zhao, Y. Abe, Y. Gao, B. Chen, T. Salim, E. E. M. Chia, X. Qiao, C. Deibel, and Y. M. Lam, *Adv. Mater.* **30**, 1 (2018).
- [94] M. D. Smith, A. Jaffe, E. R. Dohner, A. M. Lindenberg, and H. I. Karunadasa, *Chem. Sci.* **8**, 4497 (2017).
- [95] L. Mao, Y. Wu, C. C. Stoumpos, B. Traore, C. Katan, J. Even, M. R. Wasielewski, and M. G. Kanatzidis, *J. Am. Chem. Soc.* **139**, 11956 (2017).
- [96] L. Mao, Y. Wu, C. C. Stoumpos, M. R. Wasielewski, and M. G. Kanatzidis, *J. Am. Chem. Soc.* **139**, 5210 (2017).
- [97] B. A. Rosales, L. Men, S. Cady, M. P. Hanrahan, A. J. Rossini, and J. Vela, *Chem. Mater.* **28**, 6848 (2016).
- [98] V. M. Gun and V. V. Turov, *Am. Chem. Soc.* 6405 (1999).
- [99] V. Ladizhansky, G. Hodes, S. Vega, and V. Reho, *J. Phys. Chem. B* **104**, 1939 (2000).
- [100] W. Makulski, M. Wilczek, and K. Jackowski, *Phys. Chem.* **20**, 22468 (2018).
- [101] A. P. Bartók and J. R. Yates, *J. Chem. Phys.* **150**, 1 (2019).
- [102] J. Sun, A. Ruzsinszky, and J. Perdew, *Phys. Rev. Lett.* **115**, 1 (2015).
- [103] H. J. Monkhorst and J. D. Pack, *Phys. Rev. B* **13**, (1976).
- [104] B. M. Auer and J. L. Skinner, *J. Chem. Phys.* **128**, (2008).
- [105] P. J. Larkin, *IR and Raman Spectra–Structure Correlations* (2018).
- [106] G. M. Bernard, R. E. Wasylishen, C. I. Ratcliffe, V. Terskikh, Q. Wu, J. M. Buriak, and T. Hauger, *J. Phys. Chem. A* **122**, 1560 (2018).
- [107] M. Aebli, L. Piveteau, O. Nazarenko, B. M. Benin, F. Krieg, R. Verel, and M. V. Kovalenko, *Sci. Rep.* **10**, 1 (2020).
- [108] C. Martineau, F. Fayon, C. Legein, J. Y. Buzaré, G. Silly, and D. Massiot, *Chem. Commun.* **1**, 2720 (2007).
- [109] M. G. Goesten and R. Hoffmann, *J. Am. Chem. Soc.* **140**, 12996 (2018).
- [110] R. X. Yang, J. M. Skelton, E. L. Da Silva, J. M. Frost, and A. Walsh, *J. Phys. Chem. Lett.* **8**, 4720 (2017).

- [111] J. S. Bechtel and A. Van der Ven, *Phys. Rev. Mater.* **2**, 25401 (2018).
- [112] J. Autschbach and B. Le Guennic, *J. Chem. Educ.* **84**, 156 (2007).
- [113] A. Bernasconi and L. Malavasi, *ACS Energy Lett.* **2**, 863 (2017).
- [114] I. R. Kleckner and M. P. Foster, *Biochim. Biophys. Acta* **1814**, 942 (2011).
- [115] V. P. Tiwari and P. Vallurupalli, *J. Biomol. NMR* **74**, 443 (2020).
- [116] T. W. Lee, *Adv. Mater.* **31**, 1 (2019).
- [117] M. Kim, *Opt. Photonics News* **31**, 32 (2020).
- [118] Z. Song, C. L. McElvany, A. B. Phillips, I. Celik, P. W. Krantz, S. C. Watthage, G. K. Liyanage, D. Apul, and M. J. Heben, *Energy Environ. Sci.* **10**, 1297 (2017).
- [119] M. Antonietta Loi and J. C. Hummelen, *Nat. Mater.* **12**, 1087 (2013).
- [120] M. K. Nazeeruddin, E. Baranoff, and M. Grätzel, *Sol. Energy* **85**, 1172 (2011).
- [121] S. Mathew, A. Yella, P. Gao, R. Humphry-Baker, B. F. E. Curchod, N. Ashari-Astani, I. Tavernelli, U. Rothlisberger, M. K. Nazeeruddin, and M. Grätzel, *Nat. Chem.* **6**, 242 (2014).
- [122] M. K. Nazeeruddin, A. Kay, E. Miüller, P. Liska, N. Vlachopoulos, M. Gratzel, C.- Lausanne, and R. April, *J. Am. Chem. Soc.* **115**, 6382 (1993).
- [123] W. Zhang, G. E. Eperon, and H. J. Snaith, *Nat. Energy* **1**, (2016).
- [124] G. E. Eperon, S. D. Stranks, C. Menelaou, M. B. Johnston, L. M. Herz, and H. J. Snaith, *Energy Environ. Sci.* **7**, 982 (2014).
- [125] Y. H. Kim, H. Cho, and T. W. Lee, *Proc. Natl. Acad. Sci. U. S. A.* **113**, 11694 (2016).
- [126] C. C. Stoumpos, C. D. Malliakas, and M. G. Kanatzidis, *Inorg. Chem.* **52**, 9019 (2013).
- [127] J. H. Noh, S. H. Im, J. H. Heo, T. N. Mandal, and S. Il Seok, *Nano Lett.* **13**, 1764 (2013).
- [128] F. Deschler, M. Price, S. Pathak, L. E. Klintberg, D. D. Jarausch, R. Higler, S. Hüttner, T. Leijtens, S. D. Stranks, H. J. Snaith, M. Atatüre, R. T. Phillips, and R. H. Friend, *J. Phys. Chem. Lett.* **5**, 1421 (2014).
- [129] L. C. Schmidt, A. Pertegás, S. González-Carrero, O. Malinkiewicz, S. Agouram, G. Mínguez Espallargas, H. J. Bolink, R. E. Galian, and J. Pérez-Prieto, *J. Am. Chem. Soc.* **136**, 850 (2014).

- [130] S. Yang, D. Wu, W. Gong, Q. Huang, H. Zhen, Q. Ling, and Z. Lin, *Chem. Sci.* **9**, 8975 (2018).
- [131] M. Komura, T. Ogawa, and Y. Tani, *Chem. Sci.* **12**, 14363 (2021).
- [132] C. Motta, F. El-Mellouhi, S. Kais, N. Tabet, F. Alharbi, and S. Sanvito, *Nat. Commun.* **6**, (2015).
- [133] Y. Zhao and K. Zhu, *Chem. Soc. Rev.* **45**, 655 (2016).
- [134] K. Z. Du, Q. Tu, X. Zhang, Q. Han, J. Liu, S. Zauscher, and D. B. Mitzi, *Inorg. Chem.* **56**, 9291 (2017).
- [135] B. Saparov and D. B. Mitzi, *Chem. Rev.* **116**, 4558 (2016).
- [136] H. Hongwei, *Science (80-.)*. **63**, 1 (2014).
- [137] R. Willem, *Prog. Nucl. Magn. Reson. Spectrosc.* **20**, 1 (1988).

Appendix

Table A.1 EXSY exchange rate data from ^1H - ^1H NOESY correlations of 2,3 and 4-MOP.

System	Interacting ^1H 's	Functional groups	Cross-peak position – x,y (ppm)	Exchange time (ms)	Exchange rate (s^{-1})	Average Exchange Rate (s^{-1})
2-MOP	4 – 5	Aromatic – aromatic	5.8, 7.3	116 ± 11	8.62 ± 0.82	3.6 ± 0.1
	3,6 – 5	Aromatic – aromatic	6.6, 5.8	123 ± 12	8.16 ± 0.80	
	1,1',1'' – 2,2'	Methyl – methylene	2.8, 5.4	292 ± 23	3.43 ± 0.27	
	4 – 9,10,11	Aromatic – amine	7.3, 8.1	330 ± 50	3.03 ± 0.45	
	3,6 – 9,10,11	Aromatic – amine	6.6, 8.1	461 ± 47	2.17 ± 0.21	
	1,1',1'' – 5	Methyl – aromatic	2.8, 5.8	582 ± 65	1.72 ± 0.19	
	5 – 9,10,11	Aromatic – amine	5.8, 8.1	813 ± 101	1.23 ± 0.14	
	1,1',1'' – 3,6	Methyl – aromatic	2.8, 6.6	1466 ± 308	0.68 ± 0.15	
3-MOP	3,4,5,6 – 9,10,11	Aromatic – amine	6.5, 7.9	144 ± 6	6.97 ± 0.29	2.1 ± 0.2
	2' – 3,4,5,6	Methylene – aromatic	5.0, 7.5	408 ± 15	2.45 ± 0.09	
	2 – 3,4,5,6	Methylene – aromatic	4.5, 6.5	409 ± 16	2.45 ± 0.09	
	$\text{H}_2\text{O} - \text{H}_2\text{O}$	-	3.3, 6.9	430 ± 41	2.33 ± 0.22	
	2 – 9,10,11	Methylene – amine	4.5, 7.9	628 ± 55	1.59 ± 0.14	
	2' – 9,10,11	Methylene – amine	5.0, 7.9	648 ± 56	1.54 ± 0.14	
	1,1',1'' – 2	Methyl – methylene	2.4, 4.5	1126 ± 195	0.89 ± 0.15	
	1,1',1'' – 2'	Methyl – methylene	2.4, 5.0	1987 ± 572	0.50 ± 0.15	
	1,1',1'' – 3,4,5,6	Methyl – aromatic	2.4, 6.5	3593 ± 986	0.28 ± 0.08	
4-MOP	3,5,6 – 9,10,11	Aromatic – amine	6.7, 7.5	18 ± 3	55.56 ± 6.93	11.8 ± 1.7
	3,5,6 – 2,2'	Aromatic – methylene	6.7, 4.8	56 ± 5	17.86 ± 1.69	
	3,5,6 – 4	Aromatic – aromatic	6.7, 5.4	68 ± 23	14.81 ± 5.07	
	4 – 9,10,11	Aromatic – amine	5.4, 7.5	85 ± 9	11.83 ± 1.33	
	2,2' – 9,10,11	Methylene – amine	4.8, 7.5	115 ± 9	8.73 ± 0.69	
	$\text{H}_2\text{O} - \text{H}_2\text{O}$	-	3.2, 7.1	397 ± 64	2.52 ± 0.40	
	3,5,6 – 1,1',1''	Aromatic – methyl	6.7, 2.8	536 ± 17	1.87 ± 0.06	
	1,1',1'' – 9,10,11	Methyl - amine	2.8, 7.5	634 ± 72	1.58 ± 0.18	
	1,1',1'' – 2,2''	Methyl – methylene	2.8, 4.8	717 ± 45	1.40 ± 0.08	
	1,1',1'' – 4	Methylene – aromatic	2.8, 5.4	947 ± 164	1.06 ± 0.18	

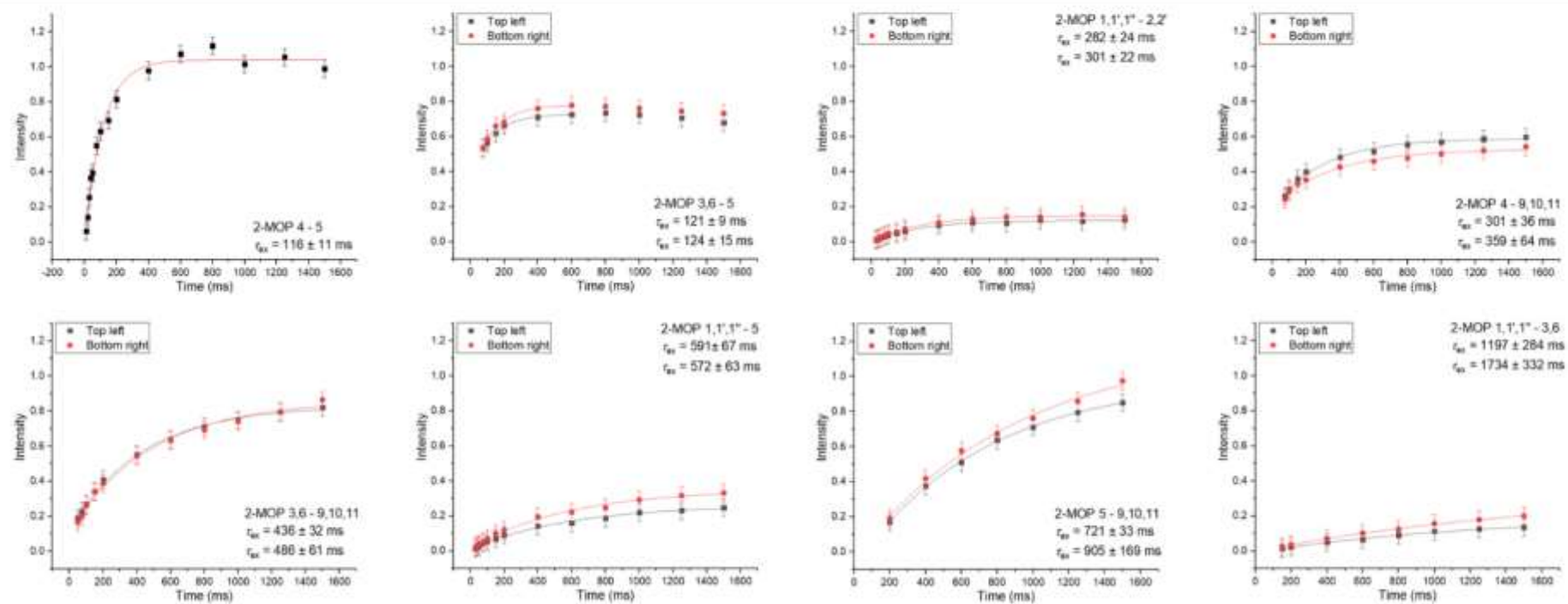
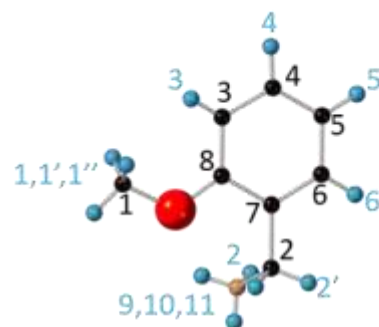


Figure A.1 EXSY fits used to produce exchange rates for 2-MOP.

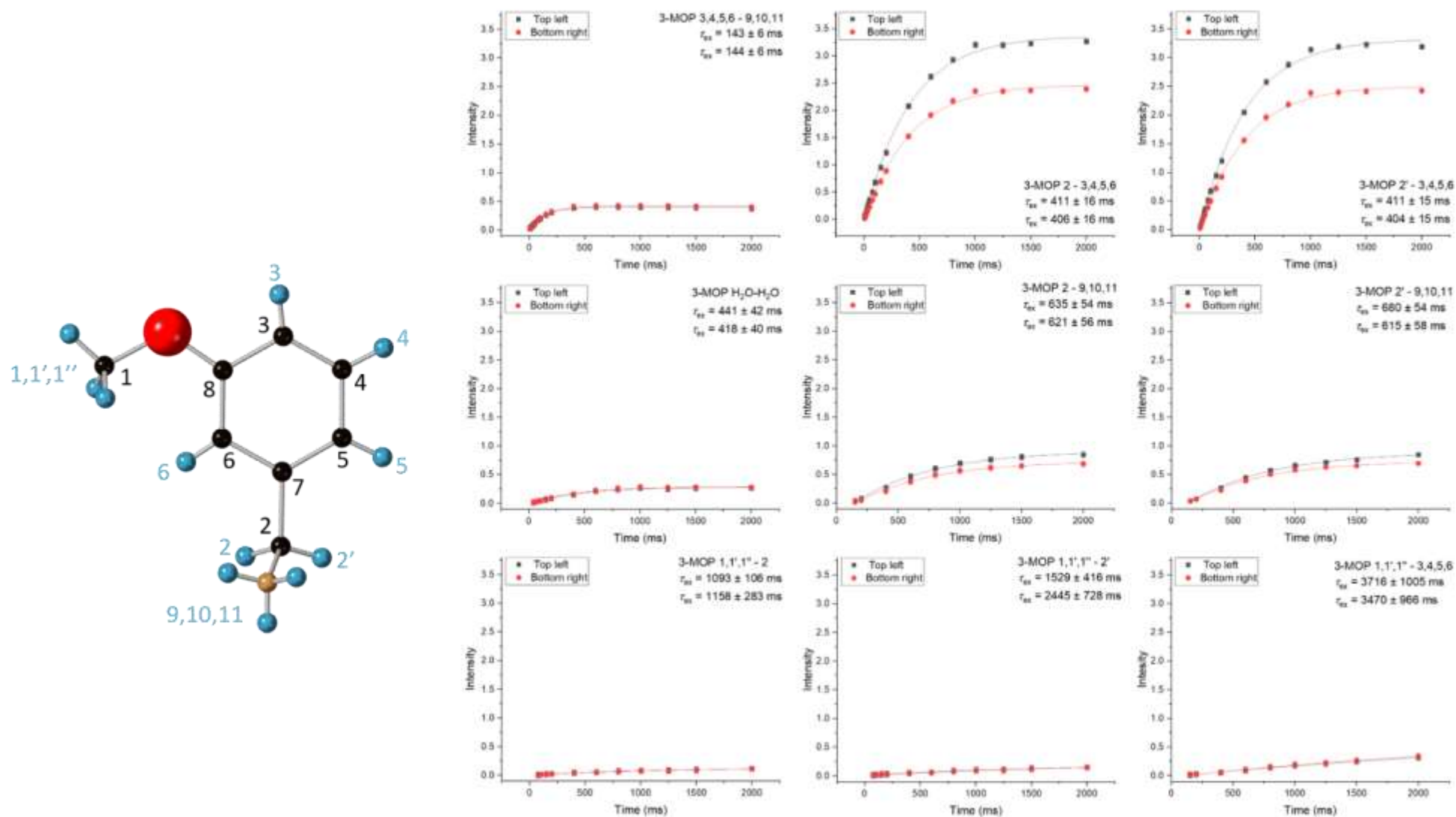


Figure A.2 EXSY fits used to produce exchange rates for 3-MOP.

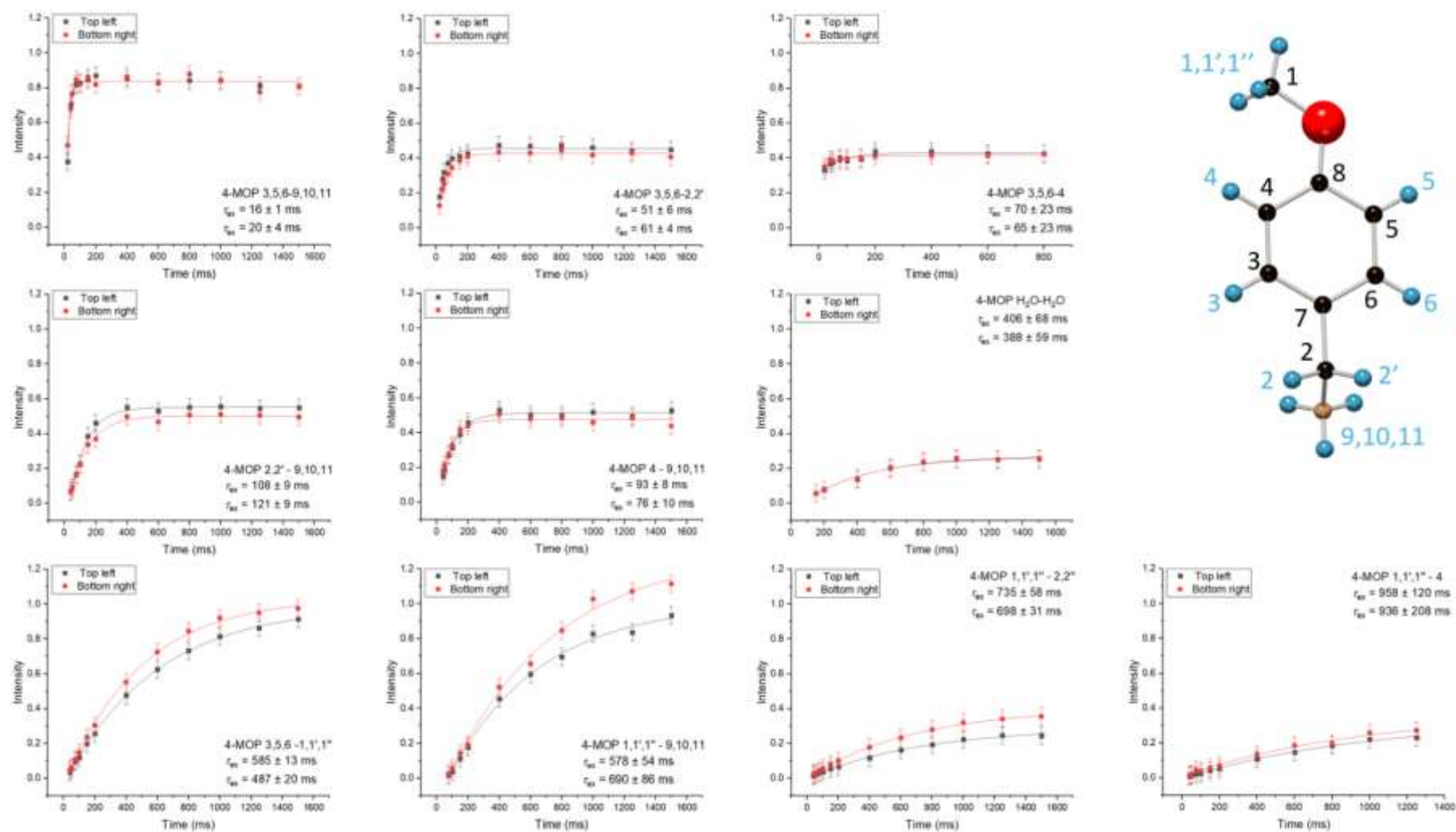


Figure A.3 EXSY fits used to produce exchange rates for 4-MOP.

NMABr T_1 – 800 MHz

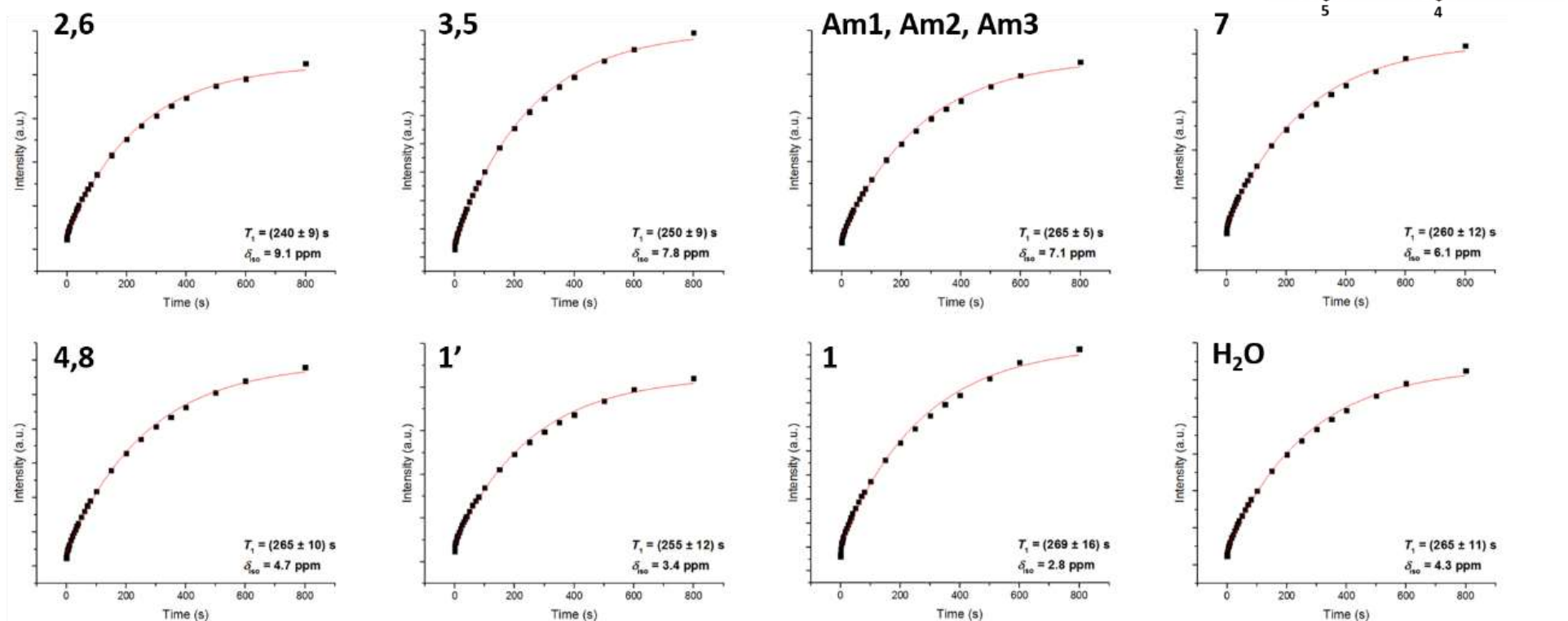


Figure A.4 T_1 fits for NMABr organic.

(NMA)₂PbBr₄ T_1 fast prep.– 800 MHz

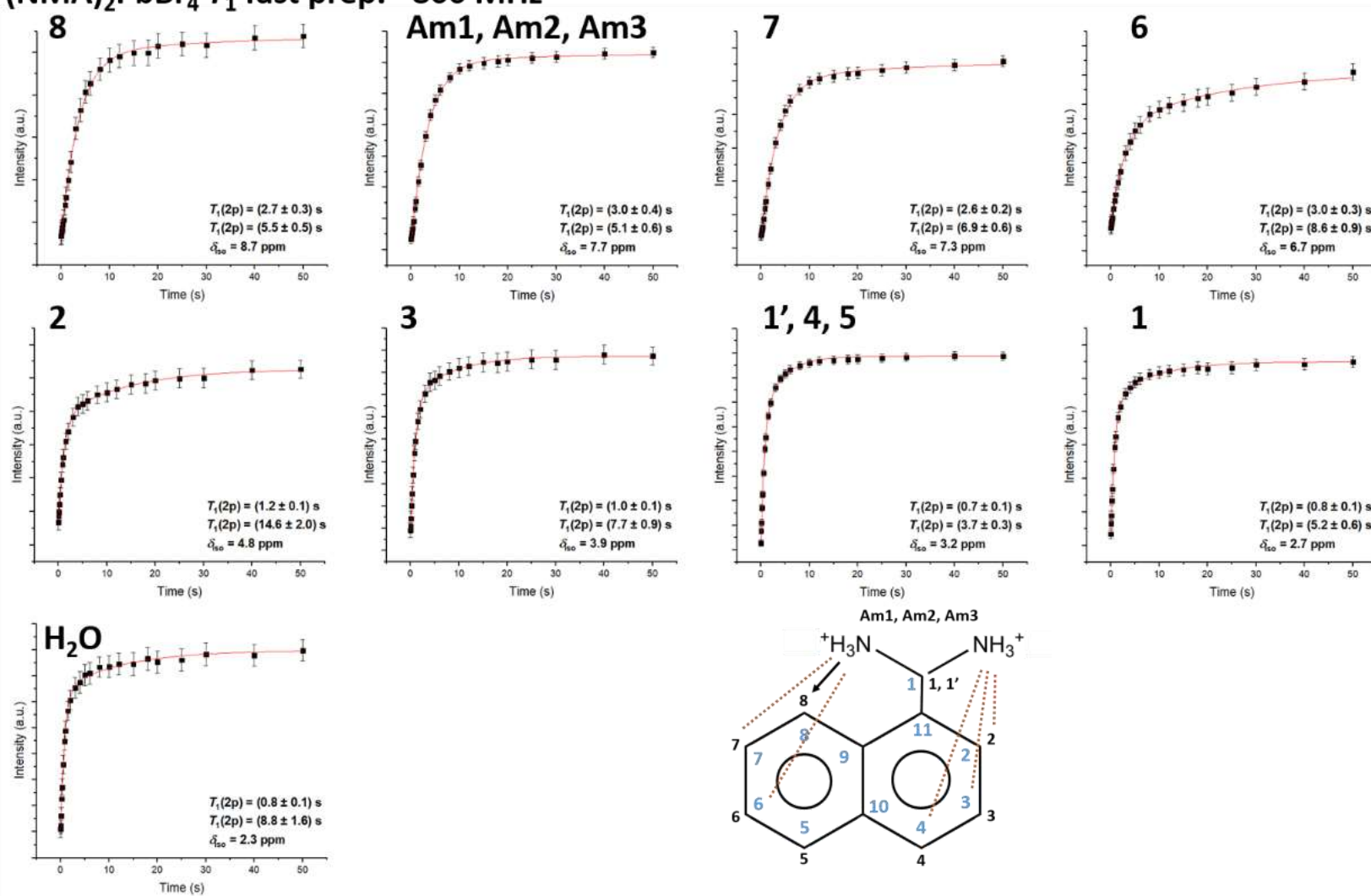


Figure A.5 T_1 fits for (NMA)₂PbBr₄ fast preparation perovskite.

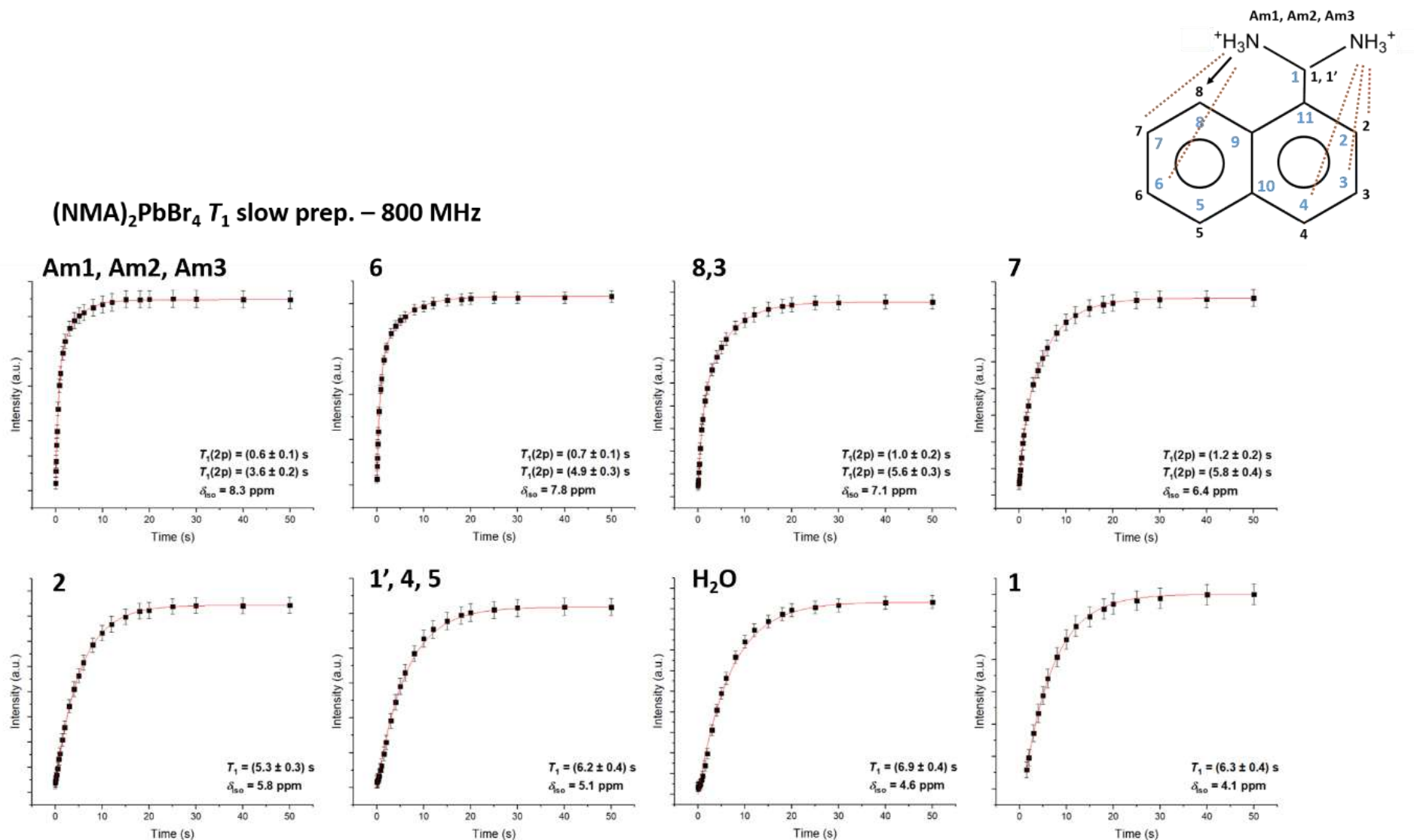


Figure A.6 T_1 fits for (NMA)₂PbBr₄ slow preparation perovskite.

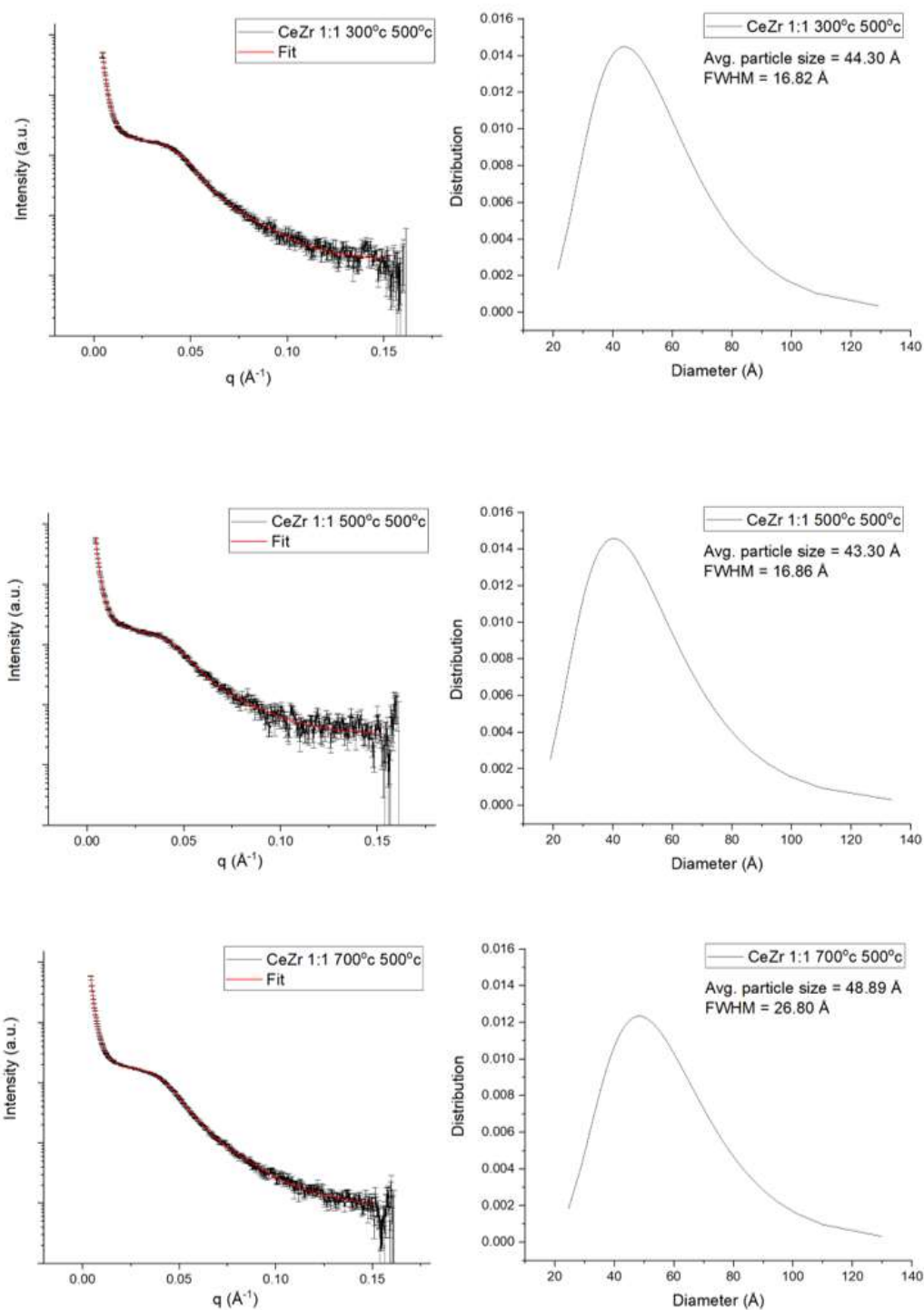


Figure A.7 SAXS measurements and fits including particle size distribution data of the disordered ceria-zirconia system.

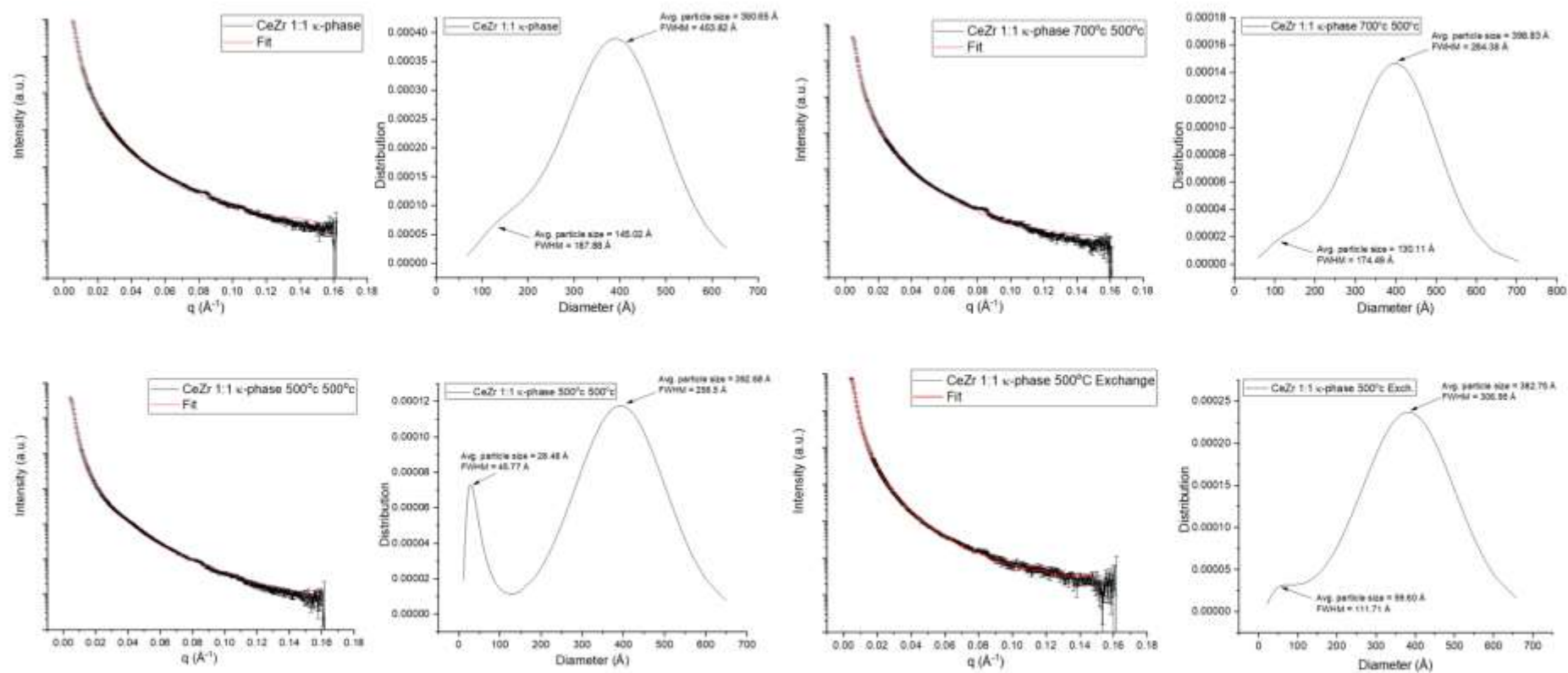


Figure A.8 SAXS measurements and fits including particle size distribution data of the κ -phase ceria-zirconia.

